Roles for Rab7 in Endocytic Trafficking and in Response to Endo-lysosomal Stress

Ryan J Mulligan

Jacksonville, Florida

B.S., Biochemistry, University of Florida

A dissertation presented to the Graduate Faculty of the University of Virginia in Candidacy for the Degree of Doctor of Philosophy

Department of Cell Biology
University of Virginia
May 2024

Table of Contents

Acknowledgements

First and foremost, I would like to thank my mentor, Dr. Bettina Winckler for her guidance and support over the past four years. I joined the lab at the onset of the COVID-19 pandemic, which brought its own unique challenges to graduate studies. You were a beacon of understanding, compassion, and support during the times where I did not yet have a project, was not permitted to come into lab, and was limited to reading papers at home for months on end. From those moments onward, I felt anything was surmountable under your wing. Throughout my studies, you have continued to display understanding and the importance of prioritizing health, without which I do not think I would have been this successful. Thank you for instilling in me an attention to detail and scientific rigor, which have made me a better scientist. Thank you for providing the right amount of guidance, criticism, and praise for me, and for allowing me to always pursue what I found interesting and exciting, even if we as a lab were not experts in it. And thank you for bringing me gluten-free snacks, and for saying hello and goodbye to me each day we were both in lab---the little things quickly add up. Thank you to my committee members Drs. Jim Casanova, Noelle Dwyer, Anne Kenworthy, and Xiaowei Lu, whose feedback, criticisms and guidance were instrumental in the completion of this work. Thank you to my collaborator Dr. Stefanie Redemann, for your willingness to work together, to teach me new techniques and spend hours of your time at the electron microscope with me.

Thank you to all Winckler lab members past and present: Dr. Chan Choo Yap, Laura Digilio, Lloyd McMahon, Dr. Ashley Mason, Jonanthon Sewell, Isaiah Swann, and Abigail Lamison. To Chan Choo, thank you for being a guiding light, for your broad knowledge and expertise, and for your matter-of-fact critiques. I knew once I had convinced you of something with my data, I was good to go! To Laura, thank you for keeping the lab afloat, for performing the countless dissections necessary for this work, for always checking in on me to see how I am doing or how may weekend went, and for having great music taste. To Lloyd, thanks for teaching me all there was to know about Imaris, and for having a keen eye and ear when I needed technical help with experiments. To Ashley, thanks for being an incredible bench mate and friend for the better part of four years, for inspiring me with your attention to detail and criticisms of

others work, and for always having an open ear to chat about anything. To Jonathon, thanks for being an incredible lab mate, a reliable friend, and for inspiring me with you organizational skills. To Isaiah, thanks for being an amazing bench mate, friend, inspiring me with both your passion for neuroscience and novel ideas, and your ability to balance so much. To Abigail, though we were not in lab together long, thanks for being a supportive and productive lab member, and your willingness to learn and help. I have also been fortunate enough to receive funding in the form of an F30 Predoctoral Fellowship from the National Institute of Aging, and be appointed to T32 Medical Scientist Program and Cell and Molecular Biology Training grants. It is through these modes of support I was able to complete this work.

Thank you to the UVA Department of Cell Biology and the Cell and Developmental Biology Graduate program, for your collaboration, intellectual prowess and intellectual stimulation for the past four years. I have consistently felt supported by the welcoming and collegial environment. Thank you to the faculty in the department, for their consistent willingness to chat about any or everything. Special thanks to Drs. Anne Sutherland and Ray Keller, for supporting me through your travel award. Thank you to the staff of the department, in particular Mary, Keith, Jamie, and Phillis, for ensuring everything was always squared away when it came to registration, scheduling, or grants. Thank you to my fellow graduate students for being friends, confidantes, and collaborators, of which there are many. Special thanks to Magda for your collaboration and willingness to help with electron microscopy experiments. Also special thanks to the Annex lab members, especially Gustavo, Tien, Holly, and Chris for the numerous lunches, collaborative efforts, and willingness to exchange reagents or ideas.

Thank you to my undergraduate and post-baccalaureate mentor, Dr. Edgar Rodriguez, for seeing a spark and promise in me, and encouraging me to pursue a PhD. Thank you to my graduate student mentors and friends from that time, Brittney and Rachna, for your guidance and friendship both then and now.

Thank you to the UVA MSTP, and especially my cohort--Greg, Gustavo, Blair, Wei, and Niket--whom I started with in 2018, for your ongoing support and sense of community throughout the past six years. Thank you to my medical school friends,

especially Greg, Lydia, Jake, Jacqueline, David, and Kyle, for being there for me through the constant ups and downs, even after you departed for residency. And thank you to my lifelong hometown friends, Chris, Tam, Al, Liz, Kevin, Nate and Nick, for the many nights of gaming (both board and video alike), frank discussions about life, and for being by my side since this journey started in high school many years ago.

Finally, I would like to thank my family for their unending support throughout the course of my training. I would like to thank my in-laws, Jim, Stephanie, Jay and MB, for your constant interest in my work and support of my career and dreams. To my dad, who always pushed me for academic success, fostered a love for STEM, and who I know would have loved to see the accomplishments I have made. To my brother Jayson, and my sister Madison, for being my best friends, always understanding me, and being sources of love and support. To my mom, for your hard work, love, and incredible ability to balance so much, which granted me the opportunities I have been afforded today. Your unwavering support and interest in my pursuits have lifted me to the person and scientist I am. Thank you for always checking up on me and for your wisdom. Last, to my wife Caroline, who has been by my side since the start of this journey, for your unending support and love. Thank you for always keeping me calm and helping me see the positives in everything. Thanks for caring for me throughout this process, whether it be meal prepping on the weekend while I'm at lab, or making dinner on late nights, listening to me, and buying me mints and Jolly Ranchers so I could get this thesis done. Thank you for showing me there is more to life than work and for helping me grow as a person. I could not have done this without you.

Chapter I. Endosomal Trafficking and Mechanistic Cellular Responses to Lysosomal Stress

1.1 An Introduction to the Endosomal System and Lysosomal Biogenesis

The endosomal-lysosomal system is the principal intracellular organelle network responsible for the sorting, recycling and degradation of cargoes, most notably membrane proteins like signaling receptors. The system is broadly composed of endosomes, membrane bound vesicle-like organelles which come in many flavors and functions, and lysosomes, highly acidic and degradative organelles classically thought of as the end-point for cargo fated for degradation (Elkin et al., 2016).

Material, including signaling receptors, that is taken up from the extracellular space via endocytosis is first internalized into early (or sorting) endosomes. Early endosomes represent a unique step in endocytic trafficking, as many fate decisions, notably recycling versus degradation, take place here. Through cargo-specific mechanisms, cargo is sorted into domains by endosomal- and cytoplasm-localized machinery for either recycling back to the plasma membrane or for degradation in lysosomes (**Figure 1**) (Cullen and Steinberg, 2018). Cargo destined for return to the plasma membrane can either directly recycle from the early endosome, or first traffic to a different class of endosomes, recycling endosomes, then to the plasma membrane (O'Sullivan and Lindsay, 2020). Degradation-fated cargo is trafficked through the late endosome and to the lysosome. Cargos which are membrane-bound and degradation-fated are also internalized into small, intraluminal vesicles (ILVs) through inward budding of endosomal membranes (Cullen and Steinberg, 2018). Late endosomes contain many ILVs and are thus also referred to as multi-vesicular bodies (or MVBs), which often lead to their classification at an ultrastructural level (Klumperman and Raposo, 2014).

Endosomal trafficking and functions are under the control of multiple regulatory proteins. Some of the best understood among those are the Ras-associated binding (Rab) family of small-GTPases. Rabs are often considered master regulators of membrane traffic and exert control via unique associations with particular endosomal subtypes and recruitment of specific "effector" proteins unique to the Rab (Hutagalung and Novick, 2011). As such, endosomal subtypes (i.e., early, late, recycling) are often defined by which Rab is associated, and Rabs are used as markers for endosomes in

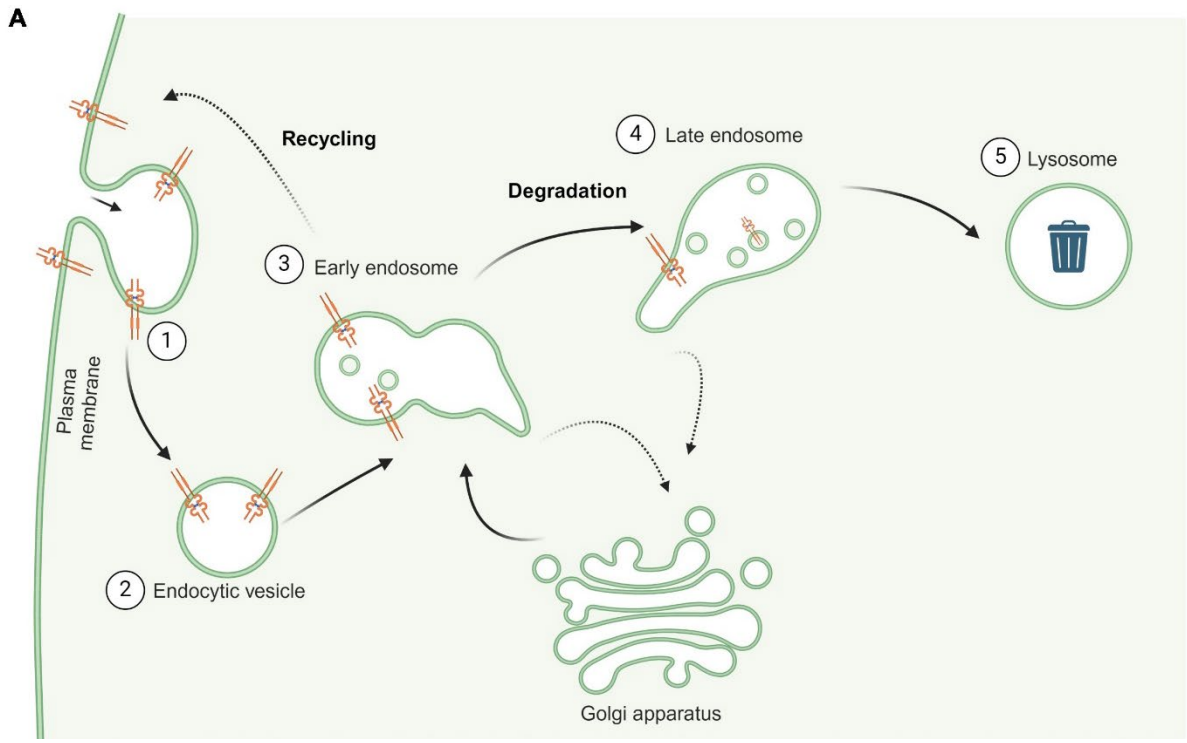

Figure 1 Endocytic processes control signaling receptor recycling or degradation.

(A) Schematic demonstrating the endocytosis of a generic signaling receptor (*orange*). (1) Invagination of the plasma membrane generates endocytic carrier vesicles (2), which carry cargo intracellularly. Topologically, the endocytosed receptor's cytosolic tail remains in the cytosol. (3) Intracellular membrane trafficking of the receptor delivers it to the early endosome. At the early, or sorting endosome, fate decisions are made, and the receptor is selectively sorted either for recycling back to the plasma membrane (either directly or through recycling endosomes), or fated for degradation (4). Within the degradative pathway, receptors traffic through late endosomes, where they are internally sequestered on intraluminal vesicles. Upon maturation into lysosomes or fusion with lysosomes (5) the receptors are degraded.

experimental studies (Grosshans et al., 2006). Specific effector proteins which rely on the presence of particular Rabs, can similarly be utilized as markers for particular endosomal subtypes. For instance, early endosomes are Rab5-positive, and recruit effector proteins like the tether early endosome antigen-1 (EEA1), such that Rab5 and/or EEA1 are used experimentally as early endosome markers (Wandinger-Ness and Zerial, 2014). Recycling endosomes are typically Rab11-positive, whereas direct early endosome to plasma membrane recycling is typically a Rab4-driven process (O'Sullivan and Lindsay, 2020). Late endosomes are Rab7-positive and recruit many diverse effectors (a major topic of this dissertation and which is discussed more at length in Chapter 2). Lysosomes are also Rab7-positive along with other small GTPase class members like ADP-Ribosylation Factor-like 8a/b (Arl8a/b) (Khatter et al., 2015). In

total, some 60 Rab proteins currently identified each have specific intracellular localization and function that confer specificity to endosomes and other compartments and aid in overall control of membrane traffic (Homma et al., 2021).

Rabs are cytosolic small GTPases that can become membrane-associated in a manner dependent on their GTP binding. In an inactive (GDP-bound) form, Rabs are cytosolic and retained by the GDP-dissociation inhibitor (GDI) family of proteins (GDI1/2 in humans) which maintain their solubility and serve as cytoplasmic shuttling complexes (Müller and Goody, 2018). Cytosolic, GDI-bound Rabs are prenylated on C-terminal cysteine residues by a complex of Rab escort protein (REP) and Rab geranylgeranyl transferase (RabGGT). Geranylgeranyl modifications are required for Rab membrane association. In the active (GTP-bound) form, Rabs are membrane-associated (Müller and Goody, 2018). Only in the active and membrane bound form can they then recruit effector proteins. The conversion from inactive to active Rab forms involves directed nucleotide exchange from GDP to GTP at the membrane by guanine exchange factor (GEF) proteins. Inactivation (GTP to GDP conversions) is result of GTP hydrolysis by GTPase activating proteins (GAPs) (Lamber et al., 2019). GEFs and GAPs are specific to individual Rabs. The Rab7 GEF and GAPs are discussed more at length in Chapter 2. Thus, the localization and downstream effector functions of Rabs are controlled through GTP/GDP binding.

Given that different Rabs preferentially associate with different endosomal subtypes, it is inherently implied that endosomes must switch Rab identities in order to perform different functions or recruit new effector proteins. Rab switching is best exemplified in the conversion between Rab5 and Rab7, and hence an early to late endosome switch (or transition) (Poteryaev et al., 2010; Rink et al., 2005). In this process, the Rab5-mediated recruitment of the Rab7 GEF drives both the displacement of the Rab5 GEF and the recruitment of the Rab5 GAP, thus simultaneously activating Rab7 while inactivating Rab5 (Stroupe, 2018). This conversion is thought to take place rapidly, on the order of minutes in some cell types (Rink et al., 2005). The Rab5 to Rab7 transition also raises a unique concept in the relationship between endosomes: that of endosomal maturation (Huotari and Helenius, 2011). To this point, endosomes have

been presented as separate, identifiable entities, unique in their Rab protein composition. In reality, these compartments exist much more like a maturational, dynamic gradient with multiple intermediary steps. For example, a conversion from a Rab5-positive early endosome to Rab7-positive late endosome contains an intermediary Rab5- and Rab7-double positive transitioning early endosome. Take this and multiply it by the 60 known Rabs and it can easily be seen how numerous intermediates with many Rab combinations may arise, which do not unambiguously align with definitive “early” or “late” endosomal pools.

Endosomal maturation is not only defined by Rab transitions, but also through changes in many other endosomal properties and function (Huotari and Helenius, 2011). This is again best exemplified by the degradative arm of the endocytic pathway, concerning trafficking between early endosomes, late endosomes, and lysosomes. This can perhaps more easily be conceptualized as a question: *how do early endosomes maturationally become lysosomes?* As endosomal maturation takes place, there are Rab conversion (such as from Rab5 to Rab7), as discussed above which redefine the effectors and function of the endosome. Only when Rab7 is present can late endosomes acquire more “mature” properties akin to those of lysosomes. These include changes to morphology, lipid composition, fusion capability, motility, and the luminal content of the endosome (Huotari and Helenius, 2011). While early endosomes are highly tubular with many adaptor subdomains necessary for sorting and budding (D’Souza et al., 2014), the morphology of late endosomes are larger, more ovular, and they undergo ILV-based sorting mechanisms through ESCRT family proteins. Early endosomes are enriched in the phosphoinositide PI3P (Gillooly et al., 2000), while late endosomes contain PI(3,5)P2 following a phosphorylation event by the PI-kinase PIKFYVE (Ikonomov et al., 2001). Rab and phosphoinositide conversion are often very tightly interlinked, as PI(3,5)P2 production also contributes to the recruitment of Rab7 and its cognate GEF (Stroupe, 2018). The presence of PI(3,5)P2 may further shape the maturational landscape through activation of other late-endosomal ion channels, like TRPML1 (Dong et al., 2010). The presence of different Rabs also influences the recruitment of different membrane tethers, fusion complexes, and SNARE proteins, thus altering potential homo- and hetero-typic fusion capability (Balderhaar and Ungermann,

2013; Huotari and Helenius, 2011). Perhaps most notably, endosomal maturation involves acquiring luminal properties most characteristic of lysosomes including both progressive acidification and increasing degradative capacity. Lysosomes are most acidic (pH~4.5) while late endosomes (pH~5-5.5) and early endosomes (pH~6.2-6.3) are less so (Maxfield and Yamashiro, 1987). Degradative lysosomal hydrolases like cathepsins frequently are increasingly active at lower pH (Yadati et al., 2020), thus establishing a pH and degradation gradient along endosomal maturational steps.

How do cathepsins get to lysosomes in the first place? This question raises one final important point regarding endosomes. That is, they represent unique crossroads between endocytic cargo sorting and degradation (discussed above), and the biosynthetic generation and trafficking of native endosomal and lysosomal proteins necessary for their function. This includes the lysosomal hydrolase family of cathepsins, other degradative enzymes such as lipases, plus other lysosomal resident membrane proteins like LAMPs, LIMPs, and lysosomal membrane pumps, channels or transporters. The array of lysosomal resident proteins is further unified under a common transcriptional network, termed the Coordinated Lysosomal Expression and Regulation (CLEAR) network. CLEAR network genes are controlled by the MiT/TFE subfamily transcription factor EB (TFEB) (Palmieri et al., 2011; Sardiello et al., 2009). In settings of increased lysosomal demand (such as discussed in the latter half of this chapter), TFEB-mediated CLEAR network transcription can kick off *de novo* lysosomal biogenesis and trafficking.

Of the steps in lysosomal biogenesis, cathepsin trafficking is the best studied (**Figure 2**) (Yadati et al., 2020). Cathepsins are synthesized as pre-procathepsins and deposited into the ER lumen via co-translational cleavage events as procathepsins. Procathepsins are trafficked to the Golgi where late Golgi-based carbohydrate modifications expose mannose-6-phosphate (M6P) residues, which are recognized by Golgi-resident mannose-6-phosphate receptors (M6PRs). Procathepsin-M6PR complexes are sorted in the trans-Golgi network by the GGA family protein into AP-1 and clathrin-coated carrier vesicles (Doray et al., 2002; Ghosh et al., 2003). Trans-Golgi derived carrier vesicles deliver cathepsin-M6PR to early and late endosomes, where pH

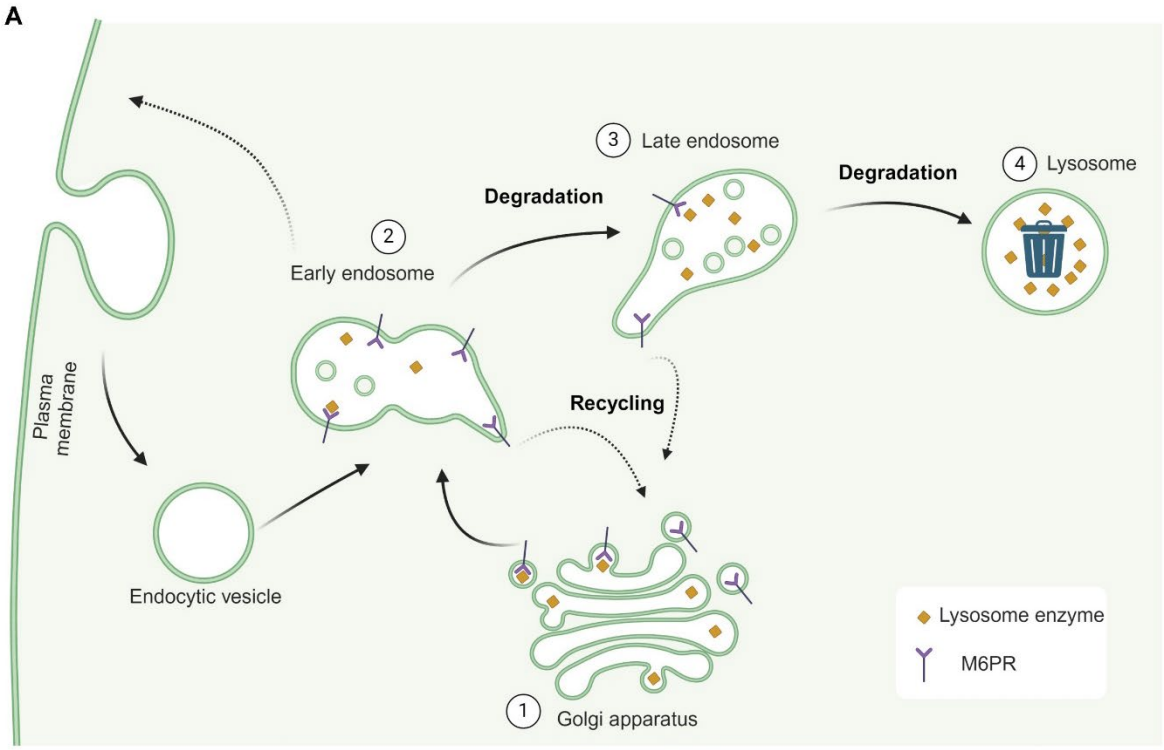

Figure 2 Biosynthetic trafficking of cathepsin-B involves cyclical recycling of mannose-6-phosphate receptors and maturation of degradative endosomes.

(A) Schematic demonstrating the biosynthetic trafficking of lysosomal enzymes, specifically cathepsin-B (*gold diamond*). Biosynthesis of new cathepsin-B begins with translation of preprocathepsins in the endoplasmic reticulum (not shown), and trafficking to the Golgi apparatus (1) where carbohydrate moieties on now procathepsins are modified. Upon exposure of mannose-6-phopshate moieties, cathepsins are recognized by mannose-6-phosphoate receptors (M6PRs, *purple*) in the trans-Golgi network (TGN). Cathepsin-M6PR complexes are sorted into carrier vesicles in the TGN and trafficked to early endosomes. (2) In early endosomes, and subsequently late endosomes (3), M6PRs release cathepsins due to structural changes arising from the more acidic lumen of endosomes as compared to the TGN. M6PR is then sorted and recycled from endosomes back to the TGN in carrier vesicles by retromer complex dependent and independent mechanisms (*not shown*). Conversely, liberated cathepsin-B enzymes traffick from early endosomes (3), through late endosomes (4) and ultimately to lysosomes (5). Auto-cleavage events by procathepsins in the midly acidic environment of endosomes generates mature cathepsin enzymzes, which are most proteolytically active in the highly acidic lumen of lysosomes (5).

changes in the luminal environment release pro-cathepsins from M6PR (Olson et al., 2008). Procathepsins then mature into active cathepsins in decreasing pH environments, in many cases due to auto-activation and auto-cleavage events (Verma et al., 2016). This process has been intimately linked to endosomal maturation, as cathepsins move through early and late endosomes to lysosomes as cargo, maturing to active enzymes as pH drops. Indeed, disruptions to Rab7 function led to failed maturation of cathepsins (Press et al., 1998). M6PR on the other hand is recycled from

endosomes back to the trans Golgi network for re-use (Ghosh et al., 2003). In some cell types, this has been shown to be dependent on the retromer complex, which identifies, sorts, and tubulates M6PR from early or late endosomes (Arighi et al., 2004; Seaman, 2004). In other cell types, M6PR retrieval was retromer-independent, speaking to cell type specificity and redundancy in M6PR trafficking (Cui et al., 2019; Seaman, 2018). For instance, Rab9 and TIP47 also contribute to M6PR recycling, specifically from late endosomes (Díaz and Pfeffer, 1998). I explore the necessity for Rab7 in maturation, M6PR retrieval and lysosomal biosynthesis in Chapter 5.

1.2 An Introduction to Lysosomal Dysfunction, Stress, and Damage: defining terms and relevance

The canonical role for lysosomes has been degradation of macromolecules which entered the cell via endocytic pathways (as discussed in the previous section) and degradation of intracellular cargos through macroautophagy (autophagy). It is becoming increasingly apparent that lysosomes also serve as important metabolic and immune signaling platforms in nutrient regulation, and for exocytosis (Settembre and Perera, 2023). Under this broad spectrum of functions, it is abundantly clear that maintaining a healthy lysosomal pool is essential for cellular health. *Lysosomal dysfunction,* which I define here as a general lack of the ability to degrade cargo but may also apply to the lack of signaling or exocytic competency, underlies the pathology of many diseases, particularly those of the nervous system and cancer (Kallunki et al., 2013; Lakpa et al., 2021). Mutations in endosomal or lysosomal genes that cause lysosomal dysfunction are often causative for neurodegenerative disorders (Malik et al., 2019; Winckler et al., 2018). Despite the broad implications and impact on human health that lysosomal dysfunction provides, the mechanistic understands of cellular responses to such dysfunction is not yet completely understood. The field of lysosomal quality control is a young and still developing field, as compared to similar fields of ER or mitochondrial dysfunction which have been investigated for decades (Lakpa et al., 2021).

Much of the attention in the field around lysosomal dysfunction has turned to specifically investigating *lysosomal membrane permeabilization (LMP)*, interchangeably used with *lysosomal damage*, in which the limiting membrane of the lysosome is physically disrupted. In LMP, luminal lysosomal content (e.g., ions, lytic enzymes, reactive oxygen species) leaks into the cytosol as a result of membrane damage (Wang et al., 2018). LMP falls under a broader category of *lysosomal stress* which has been systematically defined as a combination of any of the following elements: increased lysosomal pH, increased lysosomal size, LMP, ionic efflux, lysosomal repositioning, protein aggregation, LDL accumulation, redox catastrophe, or bioenergetic crises (Lakpa et al., 2021). The terminology used in the literature is often not specific and not standardized, but for the purposes of this dissertation, dysfunctional lysosomes are under stress, which may be due to LMP. As stated above, much of the attention in the field has turned toward the understanding of LMP for the study of lysosomal quality control and homeostasis. This is due to a growing body of evidence that (1) LMP, causing clear detriment to lysosomal function, occurs in physiologic processes, in pathophysiology, and due to therapeutics which can precipitate cell death, and (2) LMP can be modeled in the lab.

LMP and cathepsin release-driven cell death occurs in the physiologic processes of mammary gland involution (Arnandis et al., 2012; Kreuzaler et al., 2011; Sargeant et al., 2014), spermatogonial cyst resolution(Yacobi-Sharon et al., 2013), and programmed neutrophil death (Loison et al., 2014). This mechanism is effective because certain cathepsins (e.g., cathepsin-B) maintain degradative capability at more neutral pH and can cleave cytosolic pro-apoptotic proteins like Bax and Bid, which promote traditional apoptotic pathways (Serrano-Puebla and Boya, 2016).

In the central nervous system, which is particularly susceptible to lysosomal dysfunction (Lie and Nixon, 2019; Malik et al., 2019), reperfusion following a stroke (Windelborn and Lipton, 2008) initiates a glutamate excitotoxicity-calcium-calpain axis mediated neuronal death. Calpain cleavage of Hsp70 downstream of excess calcium influx destabilizes the lysosomal membrane leading to LMP and cell death. Neurotoxic aggregates of amyloid, tau, synuclein or Huntington proteins (Htt) have the capability to

directly rupture lysosomal membranes (Flavin et al., 2017). Endosomal disruption and escape of tau fibrils can precipitate its pathologic spread from one cell to another (Polanco and Götz, 2022; Polanco et al., 2018; Polanco et al., 2021). Low basal levels of LMP in wild-type neurons may also lead to increased susceptibility of synuclein seeding and spread (Sanyal et al., 2024). Lysosomal storage disorders that impact the nervous system, like Gaucher, Niemann Pick A (NPA), and C (NPC), have lysosomal lipid homeostatic disruptions which then precipitate LMP and cathepsin-mediated cell death and neurodegeneration (Serrano-Puebla and Boya, 2016). In NPC, introduction of Hsp70 is protective against LMP and cell death, linking its protective role to that seen in ischemia (Kirkegaard et al., 2010).

Weak base amine compounds can rapidly accumulate in lysosomal lumens in a manner dependent on protonation, i.e. they are lysososomotropic, and cause lysosomal stress. There are many classes of lysosomotropic compounds. Of note are particular compounds termed cationic ampiphilic drugs (or CADs) which contain hydrophobic ring structures with hydrophilic side chains and charged cationic amine groups that allow them to readily diffuse across membranes. Upon encountering the acidic lumen of the lysosome, they become protonated and trapped. Many classes of drugs used in the clinic are CADs, including anti-histamines, anti-depressants, anti-malarial and anti-tumor agents (Berg et al., 2022),which have all been shown to collapse lysosomal pH at particular concentrations (Kuwahara et al., 2020). As an example, the anti-depressant fluoxetine (Prozac), of the selective serotonin reuptake inhibitor (SSRI) family of anti-depressant drugs, is a CAD that collapses lysosomal pH at a concentration of 6.5μM *in vitro* (Kuwahara et al., 2020). Steady state measurements of circulating levels of racemic fluoxetine in patient serum and brains has been measured as greater than 1mM and 15 μM, respectively, suggesting that fluoxetine is present in the body at above minimum concentrations necessary to cause lysosomal stress (Henry et al., 2005). In our own hands, fluoxetine collapses pH and disrupts protein degradation in the absence of lysosomal membrane rupture (R.M. and J.S., unpublished, data not shown).

Conversely, drugs like anti-tumor agents may also be lysosomotropic, but have cytosolic or nuclear mechanisms of action necessary for therapeutic benefit. Such

lysosomal trapping may be contributory towards chemoresistance (Hraběta et al., 2020). Purposeful, directed disruption of endo-lysosomes would therefore play an advantageous role in therapeutic design and efficacy in these cases (Lönn et al., 2016). As evidence of this, combinatorial approaches that include a lysosomal disrupting agent achieve greater knockdown of cytosolic GFP compared to controls in an experiment where an anti-GFP siRNA is trapped in endosomes (Du Rietz et al., 2020). This suggests that treatment efficacy and resistance of currently used drugs may be improved by causing LMP.

Finally, the properties of lysosomotropic weak base compounds have been used advantageously in the lab to study LMP and lysosomal membrane rupture. In particular, the small dipeptide L-Leucyl-L-Leucine-O-Methyl Ester (LLOMe) has been widely used, and similarly to CADs, accumulates in acidic lysosomes via free diffusion and protonation, and at high concentrations can neutralize pH like other dipeptides (Goldman and Kaplan, 1973; Thiele and Lipsky, 1990). Though the lytic mechanism of LLOMe is actively debated, foundational studies in human and mouse lymphocytes suggest LLOMe works through a cathepsin-C mediated acyl-transferase reaction that creates membranolytic polymer species >3 LLOMe subunits in length (Thiele and Lipsky, 1990; Uchimoto et al., 1999). Cells that have higher levels of cathepsin-C are reported to be more susceptible to LLOMe-mediated lysosomal damage (Kavčič et al., 2020). Nevertheless, studies utilizing LLOMe as a lysosomal disrupting agent (nearly all the studies discussed in the following section) have greatly advanced the understanding of lysosomal quality control and have established LLOMe as a well-accepted tool in the field.

Taken collectively, by broadly understanding the underlying cell biologic mechanisms by which cells address LMP, we can gain greater understanding into targetable pathways to prevent and promote cellular death.

1.3 Cellular Mechanisms of Lysosomal Quality Control

Given the now broad recognition that maintaining lysosomes is essential for cellular health, as further evidenced by lysosomal-based cell death pathways in disease, significant progress has been made in elucidating mechanisms by which cells monitor and address lysosomal quality. Quality control mechanisms can broadly be summarized into three major groups (repair, removal, or replacement) (**Figure 3**), which differ on their temporal nature and the extent of lysosomal damage that they can address. Each of these will be presented individually in the following subsections.

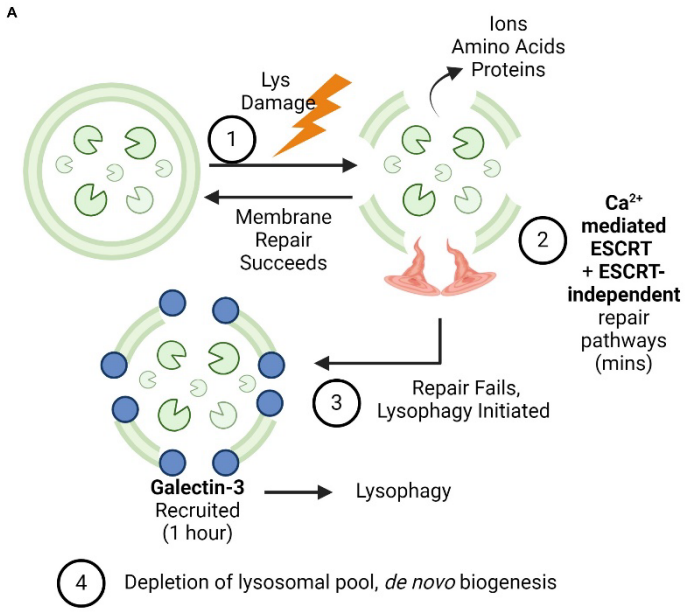

Figure 3 Known lysosomal quality control pathways are diverse and temporally different.

(A) Lysosomes may be damaged by a number of insults (1). Following damage, luminal contents of lysosomes including ions, amino acids, and degradative enzymes leak out into the cytosol. Membrane damage thus permits bidirectional communication between luminal and cytosolic content. (2) Shortly following membrane damage calcium dependent repair mechanisms, including ESCRT and phosphoinositide-based mechanisms, begin to attempt to directly repair membranes. If successful, functional lysosomes can be acutely re-established (1). If this fails, if initial damage is too extensive or membrane ruptures are too large, lysosomal specific autophagy, or lysophagy is initiated (3). In lysophagy, cytosolic lectins called galectins recognize the inner glycocalyx of lysosomes. Following recognition, galectins coordinate the recruitment of ubiquitin ligases and autophagy conjugation machinery for the removal of damaged lysosomes *en masse*. (4) Following damage and after depletion of damaged lysosomes, lysosomes are replaced *de novo* through a dedicated transcriptional network and biosynthetic trafficking.

a) Mechanisms of Direct Membrane Repair

By far the quickest mechanism to control lysosomal quality are direct repair mechanisms. In these mechanisms, small holes or disruptions in the membrane are directly addressed by machineries that are recruited to the sites of damage. The first described of these is the endosomal sorting complex required for transport (ESCRT) mediated repair pathways (Radulovic et al., 2018; Skowyra et al., 2018). ESCRT proteins have diverse roles in the cell that center around cargo sorting and membrane remodeling (Vietri et al., 2020). They are best understood in the context of cargo recognition and inward budding of endosomal membranes to form ILVs. ESCRT protein family members can be broken down into a number of subgroups, including ESCRT-0, -I, -II, -III complexes and ESCRT-associated proteins. In general, for membrane remodeling, ESCRT function is achieved through sequential recruitment of sub-complexes. That is, ESCRT-0 recruits ESCRT-I which recruits ESCRT-II, then ESCRT-III. Only after assembly of ESCRT-III lattices does ATPase activity drive membrane remodeling, scission, and inward vesicular budding away from the cytosol. The recruitment of ESCRTs in LMP is rapid (within minutes) and dependent on the release of Ca^{2+} from the lysosomal lumen (Bohannon and Hanson, 2020). In a manner akin to plasma membrane repair (Jimenez et al., 2014; Scheffer et al., 2014), lysosomal Ca^{2+}efflux is recognized by the protein ALG2, which recruits ESCRT-I protein Tsg101 and/or ESCRT-associated protein ALIX (Skowyra et al., 2018). Reconstituted ALG2, even in the absence of damage, is sufficient to nucleate ESCRT complexes (Shukla et al., 2022). ALG2 recruitment of Tsg101 and ALIX ultimately drives the downstream assembly of ESCRT-III proteins, which the drive inward budding of damaged membrane and ultimately repair of the limiting lysosomal membrane. As evidence of this, knockout of both Tsg101 and ALIX abrogates ESCRT-III subunit recruitment and significantly delays lysosomal repair and recovery following LLOMe treatment (Radulovic et al., 2018; Skowyra et al., 2018).

The role for ESCRT in lysosomal damage repair has now been validated across many studies. However, it was recently highlighted that in these studies, despite double knockout of Tsg101/ALIX, there was only a partial delay in the recovery of lysosomal function, suggesting that there were additional redundant repair pathways (Tan and

Finkel, 2022). As such, multiple ESCRT-independent membrane repair mechanisms have been elucidated, which share the underlying feature of being Ca^{2+} dependent. The first of these is dependent on members of the annexin family of proteins, which were previously shown to also have roles in Ca^{2+}-dependent plasma membrane repair (Lennon et al., 2003; Sønder et al., 2019). Annexins can promote healing of membrane disruptions by forming aggregates and vesicular complexes around damage sites to promote healing (Lennon et al., 2003). Annexins A1/2 are rapidly recruited to LLOMe ruptured endo-lysosomes, preferentially to those with membrane wounds of a larger size (Scharf et al., 2012; Yim et al., 2022), and knockdown of A1/A2 delays lysosomal repair (Yim et al., 2022). A separate group showed that another annexin, Annexin A7, is similarly recruited in an ESCRT-independent mechanism following LLOMe damage, and that knockout of A7 sensitizes lysosomes to damage and delays lysosomal repair (Ebstrup et al., 2023). A7 was proposed to promote curvature induction and crosslinking the membrane which would better facilitate membrane resealing. Collectively, the annexin family of proteins provide additional redundancy to lysosomal repair mechanisms by inducing local membrane changes.

Membrane contact sites and lipid exchange were also recently described to play a role in facilitating membrane repair, independent of ESCRTs. In the described phosphoinositide-initiated membrane tethering and lipid transport (PITT) pathway (Tan and Finkel, 2022), lysosomal damage drives the recruitment of the phosphoinositide kinase PI4K2α to damaged membranes within minutes, which phosphorylates PI to PI4P. High levels of PI4P on the damaged lysosomal membrane contribute to the formation of ER-lysosomal contact sites, mediated by ORP family protein members OSBP and ORP9/10/11 and ER-resident membrane proteins VAP-A/B. OSBP exchanges lysosomal PI4P for ER cholesterol, with cholesterol then providing membrane stability to damaged lysosomes (Radulovic et al., 2022; Tan and Finkel, 2022). A heterodimer of ORP9 with ORP10 or 11 also exchanges lysosomal PI4P with ER phosphatidylserine (PS), which recruits and activates ATG2. ATG2 drives lipid transfer from the ER into the damaged membrane directly contributing to membrane repair. Similarly, Ca^{2+}-dependent lipid scrambling exposes sphingomyelin, normally on the luminal leaflet, to the cytosolic face where it is cleaved by neutral-sphingomyelinase

to generate ceramide (Niekamp et al., 2022). Ceramide is known to induce membrane curvature and inward budding (as in ILV formation). Thus, in addition to ESCRTs, lipid modifications and composition have emerging, diverse roles in coordinating direct membrane repair of damaged endo-lysosomes.

b) Flavors of lysosome-specific autophagy (Lysophagy)

Macroautophagy (herein autophagy) is a highly conserved pathway in which either bulk cytosolic components (non-selective) or specific cargos (selective) are sequestered in double membraned structures (autophagosomes), which then fuse with the lysosome for degradation (Yamamoto et al., 2023). Selective autophagy involves countless adaptor proteins which specifically recognize cargoes and link them to a growing phagophore. In the case of lysosomes, selective autophagy is referred to as lysophagy, first reported roughly a decade ago (Hung et al., 2013; Maejima et al., 2013). Temporally, lysophagy of LLOMe-damaged lysosomes (on the order of ~30 minutes to hours) is slower than direct membrane repair mechanisms, and is generally used for bulk removal of extensively damaged lysosomes. That is, lysophagy-based clearance of damaged structures is initiated on damaged lysosomes which are unable to be directly repaired. Lysosomes with this extent of damage have holes large enough for exchange of proteins in and out of the lysosomal lumen to the cytosol. Most notably, a family of cytosolic lectin proteins, called galectins, can enter the damaged lysosome and bind to the now exposed, heavily glycosylated inner leaflet serving as surveillance signals (Hoyer et al., 2022). Of these, galectin-3 is best studied and is now canonically used as a marker of lysosomal damage and lysophagy. The autophagy field is extensive, and this dissertation does not dive extensively into lysophagy mechanism, so this subsection will only broadly present what is known regarding two sub-classes of lysophagy, canonical and non-canonical.

Canonical Lysophagy: In canonical lysophagy, damaged lysosomes are removed in a manner consistent with other forms of selective autophagy, via a common, redundant mechanism with different combinations of molecular players. First, surveillance proteins, mainly galectins, mark damaged lysosomes (Johannes et al., 2018). Galectins facilitate the recruitment of E3-ubiquitin ligase complexes which poly-

ubiquitinate lysosomal proteins (Hoyer et al., 2022). Currently identified E3 ubiquitin ligases for lysophagy include TRIM16 (Chauhan et al., 2016; Kumar et al., 2017), UBE2QL1 (Koerver et al., 2019), CUL4A (Teranishi et al., 2022) and FBX-O2 or -O27 (Liu et al., 2020; Yoshida et al., 2017) . Poly-ubiquitinated proteins are then recognized by particular autophagy adaptor proteins, including optineurin (OPTN) (Eapen et al., 2021), SQSTM1/p62 (Gallagher and Holzbaur, 2023; Papadopoulos et al., 2017), and TAX1BP1 (Eapen et al., 2021). Autophagy adaptors link poly-ubiquitin chains with core autophagy machinery necessary for the production of ATG8 family member (LC3 and GABARAP) conjugated phagophores around the damaged structure (Hoyer et al., 2022). Knockout of such conjugation machinery, including ATG4 or ATG5, delays lysophagy progression and leads to persistent Gal3 puncta (Maejima et al., 2013).

Non-canonical Lysophaghy: In non-canonical lysophagy, ATG8 family proteins LC3 and GABARAPs are directly conjugated to the damaged lysosomal membrane, in the absence of poly-ubiquitination and autophagy adaptors. This was first described in infection with *Salmonella typhimurium* (Xu et al., 2019). In this paradigm, the bacterium-containing vacuole is damaged which led to increased assembly of the endosomal-lysosomal V-ATPase. This multi-subunit, membrane-bound pump is responsible for luminal acidification of endosomes and lysosomes. V-ATPase assembly directly recruits the autophagy machinery protein ATG16L1 to the damaged vacuole, which leads to direct LC3 lipidation. This was similarly dependent on ATG12 and ATG5 machinery, but not the ULK complex which is responsible for initiation of canonical lysophagy. Non-canonical autophagy dependent on the V-ATPase/ATG161L axis was also demonstrated more recently in phagocytosis (Hooper et al., 2022) and lysosomal damage with LLOMe (Cross et al., 2023b), similarly independent of canonical lysophagy initiation. More recently, an alternative direct LC3 conjugation pathway via the E3-ubiquitin ligase TECPR1 was also discovered (Boyle et al., 2023; Corkery et al., 2023). TECPR1 senses cytoplasm-facing sphingomyelin (Niekamp et al., 2022) and recruits ATG5/ATG12 for LC3 conjugation (Florey, 2023).

c) Lysosomal Biogenesis

Aside from direct repair or whole clearance of damaged lysosomes, the alternative is to simply make more. As compared to the other mechanisms, *de novo* lysosomal biogenesis takes considerable time, given it involves transcriptional and translational steps. As previously discussed, lysosomal biogenesis is under the control of a transcriptional network (CLEAR network) and the master transcription factor TFEB (Palmieri et al., 2011; Sardiello et al., 2009). TFEB nuclear translocation is controlled by phosphorylation by the lysosome-localized mammalian target of rapamycin complex 1 (mTORC1). mTORC1 is a master sensor of lysosomal health, nutritional status, and fed state, and thus, tunes TFEB phosphorylation based on lysosomal health (Liu and Sabatini, 2020). Under states which mTORC1 is active, TFEB is phosphorylated and interacts with 14-3-3 proteins in the cytosol. Under states which mTORC1 is inactive, TFEB is rapidly de-phosphorylated and is translocated to the nucleus for transcription initiation of the CLEAR network (Martina et al., 2012; Roczniak-Ferguson et al., 2012). Various forms of lysosomal stress, including LMP, are sufficient to inactivate mTORC1 and drive TFEB nuclear translocation (Jia et al., 2020a; Zhitomirsky et al., 2018). In some instances, this was demonstrated to be dependent on the presence of LC3 (Nakamura et al., 2020).

d) Roles for Rab GTPases?

Of relevance to this dissertation are a few instances in which Rab proteins have been implicated in lysosomal damage responses. In one study, the complete knockout of Rab8 or inhibition of the kinase LRRK2 leads to deficits in ESCRT and galectin-3 recruitment, suggesting LRRK2-based phosphorylation and/or Rab8 are essential for both membrane repair and lysophagy (Herbst et al., 2020). Subsequently, more clear roles for LRRK2 and Rabs have been elucidated in studies of lysosomal tubulation following damage, in which portions or proteins of the damaged lysosomal membrane are sequestered and tubulated off into new carriers. This specific process of reformation in the context of damage is related to a larger field of lysosomal reformation (or ALR), in which prolonged starvation leads to the reformation of functional lysosomes from existing ones by phosphoinositide dependent mechanisms (Nanayakkara et al., 2023; Yu et al., 2010).

An early study of reformation in the context of LLOMe-induced LMP described that the lysosomal protein LAMP2 is released to the cytosol in small carrier vesicles in a manner dependent on lysophagy progression (Eriksson et al., 2020). Around the same time, LRRK2 was reported to be recruited to damaged lysosomes (Bonet-Ponce et al., 2020). At damaged lysosomes, LRRK2 phosphorylates Rabs 10 and 35. Phospho-Rab10 then recruits the microtubule motor adaptor protein JIP4, which generates tubules devoid of lysosomal markers. JIP4+ carrier vesicles form from the tubules emanating from damaged lysosomes and go on to fuse with LAMP1-positive compartments. Importantly, JIP4 tubulation is dependent on Rab10 or Rab35 phosphorylation. JIP4 vesicle generation was subsequently linked to ER mediated constriction of the tubules from damaged lysosomes (Bonet-Ponce and Cookson, 2022). Rab12 activity was recently shown to be even more upstream of LRRK2 recruitment and phospho-Rab10 generation on damaged lysosomes (Wang et al., 2023b) as was the lipid transfer protein Vps13C (Schröder et al., 2024). Finally, a separate tubulation event was described in LLOMe conditions, in which the lysosomal membrane protein LIMP2 binds LC3 and facilitates the recruitment of the Rab7 GAP TBC1D15 (Bhattacharya et al., 2023). The activity of the LIMP2-LC3-TBC1D15 complex depletes the membrane of active Rab7 at long timepoints following LLOMe, which permits the assembly of scaffolds for the generation of LAMP1 tubules and carriers.

1.4 Conclusions and Central Goals of this Dissertation

This chapter has highlighted the general principles of endosomal trafficking, endosomal maturation, lysosomal biogenesis, and lysosomal quality control. The clear emphasis in the literature regarding lysosomal quality control is on mechanisms that take place at the lysosomal limiting membrane itself (e.g., repair, lysophagy, tubulation). Such narrow view of this cellular problem clearly ignores other major organelles (endosomes) and processes (maturation, trafficking) that ultimately contribute to lysosomal function. The take-away from this is that the field currently knows little about how lysosomal damage ultimately impairs upstream trafficking, or whether endosomes play protective, compensatory roles in states of lysosomal stress. Thus, the goal of this

dissertation is to broadly explore the currently unknown connections, impacts and/or functions of upstream endosomal trafficking and maturation in the context of lysosomal damage states. Given my lab's expertise in endosomal trafficking, neuronal cell biology, and Rab7 function, I have more explicitly explored the role of Rab7 in wild-type lysosomal biosynthesis and lysosomal damage states across cell types.

In the subsequent introduction chapter (*Chapter 2*), I more closely explore what is currently known in the literature regarding Rab7 control of endocytic trafficking in neurons, especially with regard to a prototypical cargo (TrkA) and the Rab7-driven disease Charcot-Marie Tooth 2B (CMT2B). In *Chapter 3*, I explore upstream Rab7-driven lysosomal damage responses in non-neuronal cells. I discovered a novel stress response in late endosomes dependent on Rab7 activation and association with the V-ATPase, that subsequently controls biosynthetic trafficking receptors. In *Chapter 4*, I explore a similar question and probe endocytic trafficking during lysosomal damage in neurons, which have unique spatial and trafficking demands. I find that lysosomal damage differentially impacts Rab7 compartments in the soma and dendrite. In the dendrite specifically, endosomal maturation and trafficking of lysosomal-fated cargo out of the dendrite is perturbed. In *Chapter 5*, I take a step back and attempt to definitively outline the steps in lysosomal biosynthesis that require Rab7, a question currently muddled with conflicting data. Finally, in *Chapter 6*, I draw some brief conclusions, caveats, and future directions related to the findings presented.

Chapter II. Regulation of Endosomal Trafficking by Rab7 and Its Effectors in Neurons: Clues from Charcot–Marie–Tooth 2B Disease

This chapter is published as “Regulation of Endosomal Trafficking by Rab7 and Its Effectors in Neurons: Clues from Charcot–Marie–Tooth 2B Disease.” Ryan J. Mulligan, Bettina Winckler. Regulation of Endosomal Trafficking by Rab7 and Its Effectors in Neurons: Clues from Charcot-Marie-Tooth 2B Disease. Biomolecules. 2023 Sep 16;13(9):1399. doi: 10.3390/biom13091399. PMID: 37759799; PMCID: PMC10527268.

2.A Abstract

Intracellular endosomal trafficking controls the balance between protein degradation and synthesis, i.e. proteostasis, but also many of the cellular signaling pathways that emanate from activated growth factor receptors after endocytosis. Endosomal trafficking, sorting, and motility are coordinated by the activity of small GTPases, including Rab proteins, whose function as molecular switches direct activity at endosomal membranes through effector proteins. Rab7 is particularly important in the coordination of the degradative functions of the pathway. Rab7 effectors control endosomal maturation and properties of late endosomal and lysosomal compartments, such as coordination of recycling, motility, and fusion with downstream compartments. The spatiotemporal regulation of endosomal receptor trafficking is particularly challenging in neurons because of their enormous size, their distinct intracellular domains with unique requirements [dendrites vs. axons], and their long lifespans as postmitotic, differentiated cells. In Charcot Marie Tooth 2B disease (CMT2B), familial missense mutations in Rab7 cause alterations in GTPase cycling and trafficking leading to an ulcero-mutilating peripheral neuropathy. The prevailing hypothesis to account for CMT2B pathologies is that CMT2B-associated Rab7 alleles alter endocytic trafficking of the neurotrophin NGF and its receptor TrkA and thereby disrupt normal trophic signaling in the peripheral nervous system, but other Rab7-dependent pathways are also impacted. Here, using TrkA as a prototypical endocytic cargo, we review physiologic Rab7 effector interactions and control in neurons. Since neurons are among the largest cells in the body, we place particular emphasis on the temporal and spatial regulation of endosomal sorting and trafficking in neuronal processes. We further discuss current findings in CMT2B mutant Rab7 models, the impact of mutations on effector interactions or balance, and how this dysregulation may confer disease.

2.1 Introduction

Charcot Marie Tooth (CMTs) diseases (also known as hereditary motor and sensory neuropathies, or HMSNs) are a group of heterogeneous peripheral neuropathies that often present in adolescence or early adulthood. They are classified into subtypes (CMT1-4, X) by their genetic inheritance pattern, underlying pathophysiology, and clinical presentation, all of which are exceptionally diverse. In total, roughly 60 genetic loci have been linked to all forms of CMT, with varying inheritance patterns (Azzedine et al., 2012; Hoyle et al., 2015), which collectively are estimated to affect 1 in 2,500 individuals (Züchner and Vance, 2006). Typical symptomatic features of CMT in patients include distal muscle weakness and wasting, foot deformities like pes cavus, distal sensory deficits, and reduced or absent tendon reflexes (Harding and Thomas, 1980). Charcot Marie Tooth Type 2B (CMT2B) is a rare autosomal dominant, axonal CMT subtype (CMT2). The CMT2B phenotype is marked by predominant distal sensory loss with normal motor neuron conduction velocity, skin changes, and ulceration and infection complications which often necessitate digit amputation (Auer-Grumbach, 2004; Barisic et al., 2008). Genetic loci consistent with CMT2B phenotypes were first identified in a family with ten affected members (Kwon et al., 1995). Additional families were later identified to carry mutations at the same genetic loci with similar phenotypic features (Auer-Grumbach, 2004; Auer-Grumbach et al., 2000; De Jonghe et al., 1997). The original classification of the disorder as CMT2B has been debated, as it shares predominant clinical features with hereditary sensory neuropathy type 1 (HSN1) (Vance et al., 1996). However, the lack of sensory pain (typical of HSN1) and presence of distal muscle weakness (typical of CMT) has generally led to its acceptance in classification as CMT2B (Auer-Grumbach, 2004). To this point, there are no current cures for any CMT subtype and medical treatment is purely symptom management. Molecular genetic studies later revealed that the genetic locus causative for CMT2B encodes the endosomal small GTPase Rab7 and identified two missense mutations (L129F, V162M) associated with the disease (Verhoeven et al., 2003). Four additional missense mutations (K126R, K157N, N161T, N161I) have since been identified (Houlden et al., 2004; Meggouh et al., 2006; Saveri et al., 2020; Verhoeven et al., 2003; Wang et al., 2014).

Rabs are a family of small GTPases considered the master controllers of intracellular membrane traffic since they coordinate the behavior of membrane bound organelles, including endosomes (Grosshans et al., 2006; Homma et al., 2021; Wandinger-Ness and Zerial, 2014). Collectively, endosomes facilitate the sorting and trafficking necessary to either degrade or recycle endocytosed cargo (Cullen and Steinberg, 2018). Rab7 functions principally within the degradation arm, and so its activity is integral for controlling levels of degradative fated cargos, many of which are signaling receptors. Thus, Rab7 activity can modulate levels of intracellular signaling and signaling duration. This includes the signaling downstream of tyrosine-receptor kinase complexes like EGF-EGFR (Ceresa and Bahr, 2006) or NGF-TrkA (Saxena et al., 2005). NGF-TrkA provides critical trophic signaling within the peripheral nervous system and is thus highly relevant to CMT diseases.

Specific Rabs are characteristic of particular endosomal compartments and provide unique functions to such compartments through effector proteins (Grosshans et al., 2006; Homma et al., 2021; Wandinger-Ness and Zerial, 2014). For example, Rab5 is associated with early endosomes, while Rab7 is associated with late endosomes. In fact, Rab5 to Rab7 transitions are required for early to late endosomal maturation, and subsequently permit the new association of Rab7 effectors to direct late endosomal behavior (Poteryaev et al., 2010; Rink et al., 2005). On late endosomes, multiple effectors interact with active Rab7 to facilitate a process of late endosomal maturation: late endosomes acquire degradative capacity, motility, acidity, and fusion machinery that makes them functionally more similar to and capable of fusing with lysosomes. Lysosomes, and often autophagosomes, are also Rab7-positive and associated with Rab7 effectors (**Figure 1**). Ultimately, how Rab7 regulates unique subcellular processes on diverse compartments (ranging from early endosomes to autophagosomes) depends on the particular Rab7 effector choices at each endocytic step.

Endocytic trafficking is especially critical and challenging in neurons. Neurons are spatially complex, highly branched and exceptionally large with distinct domains (dendrites vs axons). Further, neurons are post-mitotic, terminally differentiated cells and must survive for the lifespan of an organism. Thus, endosomal functions such as Rab7-

Figure 1

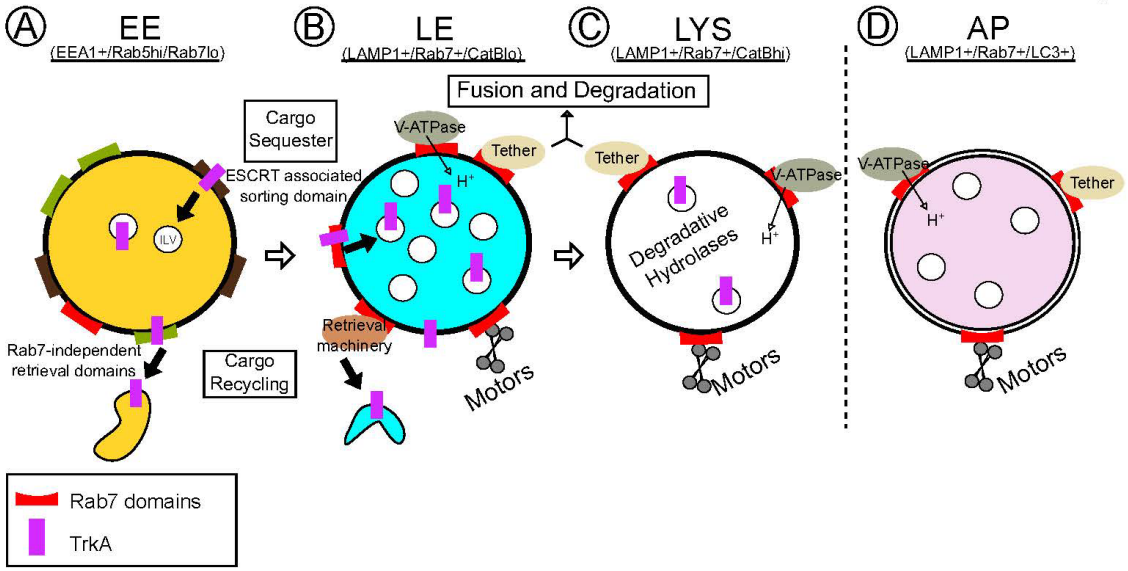

Figure 1 Rab7 executes control over effectors throughout endosomal maturation

Schematic demonstrating endosomal maturation from early endosomes (EE), to late endosomes (LE), lysosomes (LYS), and autophagosomes (AP), each with respective Rab7 levels and domains (red domains). **(A)** EE are low in Rab7 and have domains specialized in cargo sequestration into intraluminal vesicles (brown domains) and cargo recycling (olive domains), each of which are Rab7 independent. TrkA is displayed as a prototypical cargo (magenta rectangle). The transition from low levels of Rab7 on EE to high levels on LE mark a key endosomal maturation step. **(B)** On LE, Rab7 domains contribute to many functions, including Rab7-dependent TrkA sequestration and recycling (brown oval), acidification via proton pumps (green oval), motility via motors (gray helix), and fusion via tethers (beige oval), all of which contribute to the balance between continued TrkA signaling versus TrkA degradation. **(C)** LYS and **(D)** AP Rab7 functions mirror those on LE that facilitate cargo degradation.

mediated degradation, must be maintained with high fidelity in complex space for extremely long times. It is therefore not surprising that genetic mutations in genes related to intracellular trafficking, such as Rab7, are causative for inherited neurologic disease. In fact, both inherited and sporadic neurologic and neurodegenerative disease can often be linked to dysfunction in the endocytic pathway (Winckler et al., 2018). Rab7 is ubiquitously expressed, and Rab7 knockout mice are early embryonic lethal (Kawamura et al., 2020). CMT2B mutations in Rab7 are compatible with life and have minimal effects on mouse body weight and survival (Gu et al., 2022). Instead, they preferentially impact peripheral neurons versus other neuronal or non-neuronal cell types and are thus thought to be mild hypo- or hypermorphs. Notably the mildly dysfunctional CMT2B Rab7 alleles cause pathologies primarily in long axons, consistent

with the notions that endocytic traffic in neurons is highly complex and that alterations in long-distance axonal traffic likely contributes to CMT2B disease phenotypes. Neurons might therefore have less tolerance even for mild Rab7 dysfunction compared to other cell types. As intracellular trafficking mechanisms, and specifically Rab7 activity, contribute to control of tyrosine-receptor kinase signaling and degradation, the prevailing hypothesis to explain Rab7-driven CMT2B disease has been an imbalance in trophic signaling, like that of NGF-TrkA (Liu and Wu, 2017). Within this review, we will discuss the molecular behavior and physiologic roles of neuronal Rab7. We will highlight key effector proteins by following the endocytic journey of the TrkA receptor as a prototypical Rab7- and CMT2B-relevant cargo. Finally, we will discuss how mutant Rab7 alters key effector functions throughout neuronal endosomal trafficking and how this may impact neurotrophic signaling within the context of ordered Rab7 effector cascades in space.

2.2 Molecular Basis of Rab7 Function and Disruption in Disease

In order to appreciate how neuronal Rab7 interacts with effector proteins and controls cargo degradation, it is important to first gain appreciation for its behavior and regulation at the molecular level. Like all Rabs, Rab7 activity is controlled by cycling between an active GTP-bound state and an inactive GDP-bound state. In the active GTP-bound state, Rab7 associates with membranes and binds effector proteins that confer regulatory properties to the membranous compartments it is associated with. GTP/GDP cycling of Rabs is controlled by a balance of guanine exchange factor (GEF) and GTPase activating protein (GAP) activity. The only currently described Rab7 GEF is the Mon1-Ccz1 complex, which facilitates the exchange of GDP for GTP on Rab7, in conjunction with inactivation of Rab5 (Kinchen and Ravichandran, 2010; Nordmann et al., 2010; Stroupe, 2018). This facilitates the Rab5 to Rab7 conversion required for early to late endosome maturation (Poteryaev et al., 2010; Rink et al., 2005). Conversely, a multitude of Rab7 GAPs to drive GTP to GDP conversion, particularly of the TBC family of proteins, have been described (Stroupe, 2018).

The six CMT2B-linked missense mutations in Rab7 (K126R, L129F, K157N, N161T, N161I, V162M) all show autosomal dominant inheritance. They all map to conserved regions of Rab7 which are essential for nucleotide binding (Cogli et al., 2009; Saveri et al., 2020). A crystal structure of the Rab7L129F CMT2B mutant protein bound to a non-hydrolyzable GTP analog revealed that the mutation drives protein conformational changes limited to the nucleotide binding pocket, whereas the switch regions responsible for effector binding mirror that of wild-type (McCray et al., 2010). In silico modeling also found that residues mutated in CMT2B alleles reside within the GTP-binding pocket and alter hydrogen bond capabilities of amino acid side chains with the nucleotide's ribose oxygen (Saveri et al., 2020; Spinosa et al., 2008). Mutant Rab7 alleles have an increased nucleotide exchange rate that occurs independently of Mon1-Ccz1 GEF activity (McCray et al., 2010). Consequently, Rab7 GTP:GDP binding ratios are increased in mutants, as there is more GTP than GDP in the cell (De Luca et al., 2008; McCray et al., 2010; Spinosa et al., 2008). As such, CMT2B Rab7 mutants can collectively be thought of as GEF-independent, 'rapid cycling' mutants, which are disproportionately GTP-bound leading to increased membrane association. Together these findings suggest that downstream effects of CMT2B mutants are a result of increased nucleotide cycling leading to relative independence from regulated GEF and GAP activities. One common notion thus is that CMT2B alleles are gain-of-function and bind all Rab7 effectors in a manner that is dysregulated in time and space (Bucci and De Luca, 2012; Cogli et al., 2009) . A previous review has discussed the evidence for and against CMT2B alleles being gain-of-function as opposed to being haploinsufficient (Liu and Wu, 2017).

Beyond nucleotide binding, Rab7 activity is also modulated by a number of post-translational modifications, notably phosphorylation, ubiquitination and palmitoylation, which is nicely reviewed in (Modica and Lefrancois, 2020). The extent to which these other modifications interplay with Rab7 nucleotide state to control effector binding and activity is an area of active investigation. For instance, phosphomimetic Rab7 mutants (at position S72) are predominantly GDP-bound, while phospho-dead mutants are GTP-bound, suggesting that phosphorylation at S72 might negatively regulate GTP binding (Shinde and Maddika, 2016). How this is achieved molecularly is unknown. Additionally,

two recent reports demonstrate that Parkin-mediated ubiquitination of Rab7 contributes to increased GTP-Rab7 levels and drives Rab7 more stably onto membranes. This leads to increased colocalization with the lysosomal protein LAMP1 (Peng et al., 2023; Song et al., 2016). It is wholly unknown how post-translational modifications may be impacted in CMT2B mutants. It would be interesting to explore whether rapid nucleotide cycling (as found in the CMT2B alleles) impacts the ability of Rab7-modulating kinases or ubiquitin ligases to carry out their function, or conversely, if post-translational modifications can modulate nucleotide or effector binding despite rapid cycling.

2.3 Physiologic control of Rab7 on neuronal trafficking and trophic signaling

Rab7 is important for late endosomal, lysosomal, and autophagosomal function in all cell types. Early studies in non-neuronal cells demonstrated that Rab7 controls multiple steps along the endo/lysosomal pathway. The earliest Rab7-regulated step is to facilitate the transition from early to late endosome identity. Subsequently, Rab7 controls late endosomal maturation, including trafficking of internalized receptor complexes, motility or positioning of organelles, and fusion with lysosomes (Borchers et al., 2021; Bucci et al., 2000; Ceresa and Bahr, 2006; Guerra and Bucci, 2016; Langemeyer et al., 2018; Vanlandingham and Ceresa, 2009; Vitelli et al., 1997). These functions are achieved through interactions of active GTP-Rab7 with an extensive number of effector proteins (**Figure 2**), some of which we will discuss more in depth in the context of CMT2B in subsequent sections.

In neurons, the somatic compartment is functionally similar to non-neuronal cells and Rab7 likely plays similar roles. However, neurons have long axons and highly arborized dendrites, which complicate trafficking processes and demand on Rab7 function. In dendrites, distinct endosomal compartments are found in characteristic spatial distributions, with late endosomes sparser distally and lysosomes overwhelmingly proximal (Boecker et al., 2020; Wang et al., 2023a; Yap et al., 2022a).

Figure 2

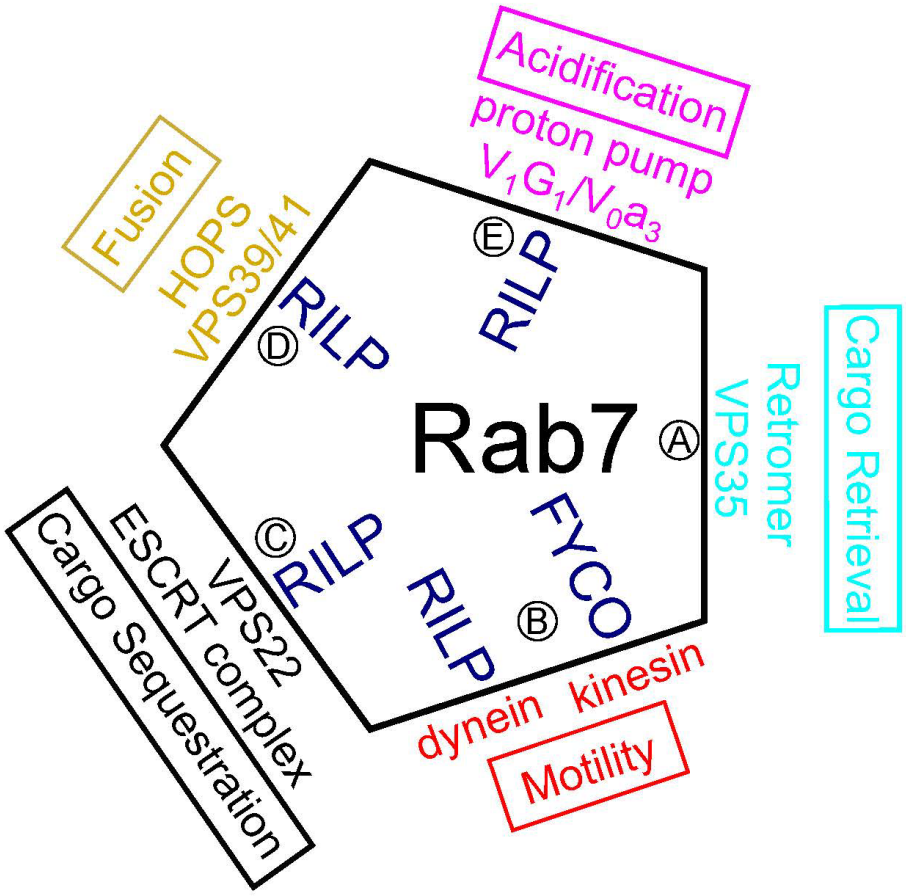

Figure 2 Specific Rab7 effector proteins confer particular properties to endosomes

Schematic demonstrating the breadth and interrelationship of Rab7 effectors and their functions. **(A)** Active Rab7 (black pentagon) facilitates retrieval of cargo like TrkA through interactions with Vps35 and the retromer complex (cyan), preserving active TrkA signals. **(B)** Rab7 interacts with the kinesin motor adaptor protein FYVE and coiled-coil [CC] domain containing 1 (FYCO1) (navy) to confer plus-end directed endosome motility, which in axons is directed toward the distal axon (red). Rab-interacting lysosomal protein (RILP) is the Rab7-interacting dynein motor adaptor, conferring minus-end (toward the soma) directed motility (red). RILP is also an essential interacting partner for other active Rab7 effector complexes vital for TrkA degradation including **(C)** VPS22 (ESCRT) mediated cargo sequestration into intraluminal vesicles (black), **(D)** VPS39/VPS41 (HOPS) mediated late endosome homo- and hetero-typic fusion with lysosomes (gold), and **(E)** V1G1/V0a3 (H+-V-ATPase) mediated regulation of endosomal acidification (magenta). Together, Rab7-dependent motility, acidification, fusion, and proper cargo localization (retrieval vs. sequestration) contribute to TrkA signal duration and degradation in neurons.

Rab7 populates late endosomal/lysosomal compartments that are more degradative as they localize more proximally in the dendrite and the soma (Yap and Winckler, 2022; Yap et al., 2018; Yap et al., 2022a). Rab7 activity and the dynein-associated motility of Rab7-positive compartments promote the retrograde trafficking of late endosomes and are essential for degradation of dendritic membrane receptors (Yap et al., 2018; Yap et al., 2022b). In axons, Rab7 also localizes to late endosomes and autophagic vesicles which progressively increase degradative capacity as they localize more proximally (Cheng et al., 2015; Khobrekar et al., 2020; Lee et al., 2011; Lie et al., 2021), though retrograde Rab7 late endosome and autophagosome maturation progresses independently of one another (Kulkarni et al., 2022). Many studies in numerous model systems have characterized the trafficking dynamics of axonal Rab7-positive endosomes and demonstrated that they undergo long range trafficking within axons, often with retrograde bias, which coincides with their endosomal and autophagosomal maturation (Boecker et al., 2020; Castle et al., 2014; Krzystek et al., 2023; Lie et al., 2021; Lund et al., 2021; Nassal et al., 2022; Zhang et al., 2013). Notably, Rab7-mediated retrograde traffic is also seen within sensory neurons where Rab7 co-trafficks with distally internalized axonal neurotrophin receptors (Deinhardt et al., 2006). These are the neurons primarily affected in CMT2B patients.

Neurotrophin receptors, like TrkA with its ligand NGF, promote neuronal survival and proper circuit formation (da Silva and Wang, 2011; Deppmann and Ginty, 2006; Scott-Solomon and Kuruvilla, 2018). Target organ-secreted neurotrophins are recognized by Trk receptors on distal axons, which together are internalized into an endosome, termed a signaling endosome, and transported retrogradely through axons over exceptionally long distances to potentiate somatic signaling (Howe and Mobley, 2005). There is evidence to support that long distance, retrograde signaling endosomes are Rab7-positive late endosomes (Deinhardt et al., 2006; Ye et al., 2018; Zhang et al., 2013). However, Rab5-positive early endosomes were also demonstrated to traffic TrkA (Delcroix et al., 2003), and a small subset of TrkA is found in Rab11-positive recycling endosomes (Barford et al., 2018). The exact molecular makeup of signaling endosomes could indeed direct their fate since they recruit different downstream effectors that influence their longevity and location, and thus the strength, duration and locale of TrkA-

mediated signaling cascades (Barford et al., 2017). Thus, the signaling endosome comes in several “flavors” which determine the path that Trk receptors take, but ultimately duration and termination of the signal is dependent on Rab7 function upstream of lysosomes (Ye et al., 2018). For instance, in NGF-stimulated rat pheochromocytoma (PC12) cells, TrkA increasingly colocalizes with Rab7 and overexpression of a dominant-negative, GDP-bound Rab7 (Rab7DN) interferes with degradation of TrkA, prolongs signaling, and promotes subsequent neurite outgrowth (Saxena et al., 2005). Similarly, knockdown of Rab7 leads to retention of TrkA in enlarged Rab5-positive endosomes in PC12 cells (Zhang et al., 2013). Rab7 knockout abrogates arrival of TrkA endosomes in the soma of sympathetic neurons grown in cell body and axon compartmentalized cultures (Ye et al., 2018), and thus leads to loss of survival signaling in the soma. Local signaling from early endosomes in the distal axon might still occur normally or even be prolonged in this experimental paradigm.

2.4 Receptor tyrosine kinase signaling in Charcot-Marie Tooth 2B Models

Since Rab7 critically regulates the trafficking of signaling receptors, it is reasonable to ask if CMT2B patient mutations alter Rab7-mediated neuronal tyrosine receptor kinase trafficking and signaling. Perhaps surprisingly, the answer to this question has not been so clear-cut, as studies investigating the impact of CMT2B mutations on tyrosine kinase receptor signaling are often contradictory. Most work has focused on two tyrosine kinase receptors: EGFR in non-neuronal models and TrkA in peripheral neuron models of CMT2B. Early studies in HeLa cells overexpressing CMT2B mutant Rab7 proteins (L129F, K157N, N161T, V162M) found that EGF/EGFR degradation is similar to that of wild-type cells (De Luca et al., 2008; Spinosa et al., 2008). In further support of this, knockdown of Rab7 with siRNA led to slowed EGF/EGFR degradation but could be completely rescued by subsequent overexpression of the CMT2B Rab7 mutants (De Luca et al., 2008; Spinosa et al., 2008). An additional study using similar experimental approaches in HeLa cells found that there was an initial delay in EGFR degradation and failure of loaded EGF to traffic

out of EEA1-positive early endosomes when Rab7 was downregulated (BasuRay et al., 2013). Interestingly, downstream signaling molecules like pERK levels were retained at high levels for longer and failed to translocate from the cytosol to the nucleus. In this study, Rab7N161T was insufficient to rescue EGFR degradation delays caused by siRNA-mediated Rab7 knockdown, though other mutants were not tested (BasuRay et al., 2013). Differences between these two studies might be due to the different time points measured—by assessing the latest time point used by each of these groups, one might come to the same conclusion that overall EGFR degradation is not impacted in CMT2B overexpression or re-expression models, but the kinetics are slowed.

The interpretation of these initial studies is complicated by the fact that they had to rely on overexpression or on knockdown coupled to re-expression of Rab7 mutants, which might not recapitulate the levels of Rab7 found in patient cells. However, in line with the conclusions of Basuray et al. 2013, a later study assayed whole cell lysates from dermal fibroblasts and a sural nerve biopsy of a Rab7K126R patient and revealed higher steady state levels of EGFR plus increased colocalization of loaded EGF with EEA1-positive late endosomes, suggesting that Rab7K126R did not support normal EGF/EGFR degradation (Saveri et al., 2020). Confusingly, similar studies using Rab7V162M patient fibroblasts demonstrated the opposite: that EGFR degradation was increased and EGF increasingly colocalized with LAMP1-positive lysosomes, leading to decreased levels of signaling molecules like pERK1/2 (Romano et al., 2021). These more recent physiologic model systems (i.e., patient tissue) are an important step in avoiding the overexpression complications from early studies. Surprisingly though, different patient alleles from patient-derived cells have shown differences in EGF/EGFR fates. These studies are thus beginning to demonstrate that there are functional differences between different CMT2B Rab7 alleles with respect to alterations in receptor trafficking. It is surprising that several CMT2B-associated Rab7 mutants affect EGFR trafficking in opposite directions since they are thought to share the common underlying deficits in nucleotide binding. Notably, several Rab7 CMT2B alleles (L129F, K157N, V162M), but not N161T, show slowed fluorescence recovery after photobleaching, indicative of hyperstabilization on endosomes (BasuRay et al., 2010; McCray et al.,

2010). It is clear that our understanding of the molecular defects shared or distinct among the different CMT2B Rab7 alleles is still incomplete.

The data investigating CMT2B mutant Rab7 impacts on NGF-TrkA signaling are more relevant to peripheral nervous system disease but equally conflicting. Importantly, Rab7 can be co-immunoprecipitated with TrkA, and this is not impacted by CMT2B mutants (BasuRay et al., 2010). Studies, for the most part, have found that TrkA-dependent neurite outgrowth is deficient in CMT2B overexpression mutant PC12 [L129F, K157N, N161T, V162M], mouse neuro-2a (N2A) [K126R, L129F, K157N, N161T, V162M], N1E-115 [L129F, K157N, N161T, V162M], patient derived iPSCs [V162M], and cultured dorsal root ganglia (DRGs) [L129F, K157N, N161T, V162M] (Cogli et al., 2010; Markworth et al., 2021; Romano et al., 2021; Saveri et al., 2020; Yamauchi et al., 2010; Zhang et al., 2013). This is perplexing given nervous system development in patients appears to proceed normally (i.e., disease onset is in the second or third decade of life). Consequently, it has been widely suggested that defective neurite outgrowth in CMT2B is primarily relevant in axonal regeneration following injury. One study in Zebrafish did demonstrate both central and peripheral axon branching deficits at later stages of development. However, initial stages of axon branching and outgrowth were intact, again suggesting that neurotrophin-dependent maintenance of healthy axons is a predominant issue (Cioni et al., 2019; Ponomareva et al., 2016). How exactly TrkA signaling is dysregulated leading to defective neurite growth or maintenance, is not exactly clear. For example, in one study CMT2B mutant (L129F, K157N, N161T, V162M) overexpression in PC12 cells had higher pTrkA and pERK levels following NGF stimulation and retention of pERK1/2 in the cytosol (BasuRay et al., 2010). In contrast, other studies demonstrated that overexpression in PC12 (L129F, K157N, N161T, V162M) (Zhang et al., 2013) and primary iPSC derived Rab7V162M mutant sensory neurons (Romano et al., 2021) had decreased pERK1/2 levels following NGF stimulation.

Figure 3

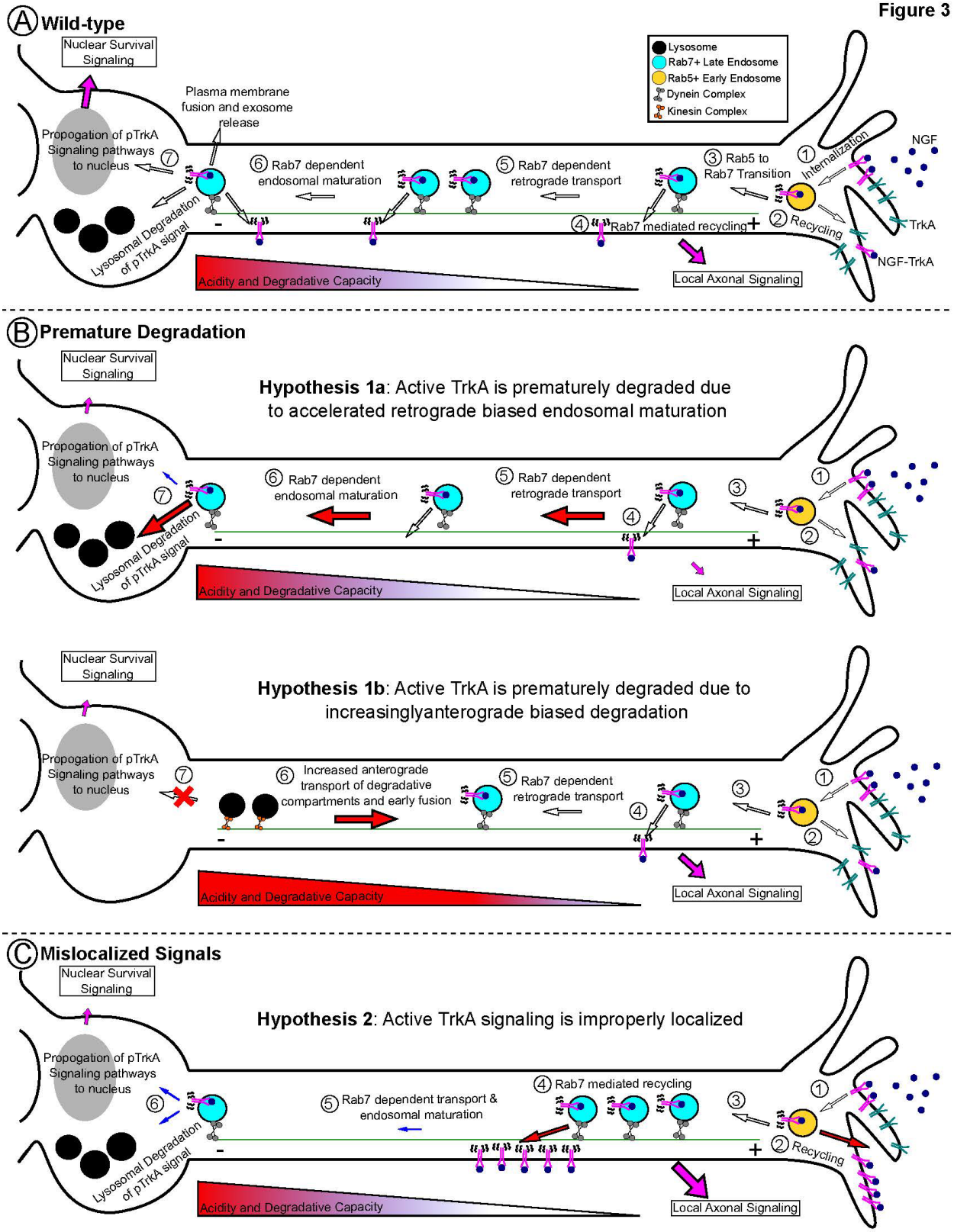
A Wild-type
Nuclear Survival Signaling
Plasma membrane fusion and exosome release
Propogation of pTrkA Signaling pathways to nucleus
⑦
Lysosomal Degradation of pTrkA signal
⑥ Rab7 dependent endosomal maturation
⑤ Rab7 dependent retrograde transport
③ Rab5 to Rab7 Transition
① Internalization
② Recycling
④ Rab7 mediated recycling
Lysosome
Rab7+ Late Endosome
Rab5+ Early Endosome
Dynein Complex
Kinesin Complex
NGF
TrkA
NGF-TrkA
Acidity and Degradative Capacity
Local Axonal Signaling
B Premature Degradation
Hypothesis 1a: Active TrkA is prematurely degraded due to accelerated retrograde biased endosomal maturation
Hypothesis 1b: Active TrkA is prematurely degraded due to increasinglyanterograde biased degradation
⑥ Increased anterograde transport of degradative compartments and early fusion
C Mislocalized Signals
Hypothesis 2: Active TrkA signaling is improperly localized
⑤ Rab7 dependent transport & endosomal maturation

Figure 3 The prevailing hypotheses for how Rab7CMT2B causes disease involve dysregulation of TrkA signaling

(A) Schematic of TrkA signaling in a healthy, wild-type neuron. *(1)* In the distal axon, surface TrkA binds to its ligand NGF secreted by the target organ. Active NGF-TrkA complexes are internalized via endocytosis and arrive at Rab5+ early endosomes (yellow). Active TrkA in an endosome is termed a signaling endosome. *(2)* TrkA, either unbound or active, that arrives in the early endosome can be recycled to recycling endosomes or back to the plasma membrane, which contributes to sustained local TrkA signaling. *(3)* Early endosomes mature into late endosomes via Rab conversion from Rab5 to Rab7. *(4)* Distal Rab7-positive late/signaling endosomes can further recycle TrkA to recycling compartments or the plasma membrane, contributing further to local axonal signaling. *(5)* Rab7 effector functions, such as RILP-dynein mediated motility move signaling endosomes retrograde toward the soma. Further recycling of TrkA might occur as transport proceeds. *(6)* As signaling endosomes move proximally, Rab7 further contributes to endosomal maturation of signaling endosomes, including increasing degradative capacity and acidification, making them more amenable to TrkA degradation. *(7)* Fully mature, somatic Rab7-positive signaling endosomes can be degraded in the lysosome (signal termination), propagate signaling cascades to nucleus (survival signaling), or fuse with the plasma membrane and release contents as exosomes. Together, distal local signaling and somatic nuclear signaling contribute to neuronal health. **(B)** Schematic demonstrating the hypotheses that TrkA is prematurely degraded in CMT2B. Top: Accelerated retrograde transport by RILP-dynein and increased fusion with lysosomes depletes both distal and nuclear TrkA signaling leading to neuronal dysfunction. Bottom: Accelerated anterograde transport of degradative lysosomes prematurely degrades TrkA signals within the axon, leading to decreased nuclear signaling but sustained distal signaling. **(C)** Schematic demonstrating the hypothesis that TrkA is mislocalized in CMT2B. Excessive Rab7-dependent TrkA retrieval or failed retrograde transport and endosomal maturation lead to excess local signaling in the absence of nuclear survival signaling.

In the end despite discrepancies, both EGFR and TrkA data in CMT2B models suggest that there is dysregulation of the trafficking and/or degradation of these receptors. The most coherent explanation of all the data is that Rab7 mutations within peripheral neurons lead to premature degradation of TrkA and thus premature termination of pTrkA signals (**Figure 3 A, B**) and/or that prolonged TrkA signaling in the wrong location leads to defective neurite behavior (**Figure 3 A,C**). Ultimately, it is currently not yet clear how all the existing data can be reconciled into a definitive explanation (see also (Bucci and De Luca, 2012; Cogli et al., 2009; Liu and Wu, 2017)). More broadly, these data speak for the necessity for all signaling molecules to be present at the right levels (i.e., not degraded) but also in the correct location (i.e., TrkA can not be stuck in the axon or dendrites; TrkA must be on the surface of endosomes, not on intraluminal vesicles; pERK must reach the nucleus) in order for normal

downstream functions, like neurite outgrowth and nuclear transcription driven survival, to take place.

2.5 Rab7 effectors and physiologic TrkA trafficking and degradation

In order to achieve appropriate NGF signaling, the cell must properly generate and traffic signaling endosomes to the right locations and then degrade TrkA in the right time frame. Rab7-positive TrkA-containing endosomes must rely on Rab7-effector functions to accomplish a number of tasks which have to occur sequentially. Rab7 effectors bind to Rab7-GTP to control : (1) proper motility and positioning of late endosomes, signaling endosomes, and lysosomes (accomplished by the dynein adaptor Rab-interacting lysosomal protein (RILP), and cholesterol sensitive protein ORP1L) (2) the correct pH (through action of the endosomal vacuolar-ATPase) to activate lysosomal hydrolases, (3) trafficking of newly synthesized lysosomal hydrolases to lysosomes (mediated by mannose-6-phosphate receptors and recycling complexes like retromer), and (4) fusion of late endosomes (through the multimeric HOPS complex) (**Figure 2**). In this section, we review the key physiologic findings pertaining to these Rab7 effector interactions that are necessary to degrade prototypical cargo, including neurotrophin receptors.

a) Rab-interacting lysosomal protein (RILP) and oxysterol related binding protein 1 L (ORP1L): control over Rab7 motility and positioning

Rab7 endosomes move along microtubule tracks via the activity of kinesin and dynein motors. Rab7 interacts with motors through adaptor proteins. The cytosolic adaptor protein RILP links Rab7 with dynein motors (Cantalupo et al., 2001; Jordens et al., 2001). In axons, in which microtubule polarity is uniformly plus end out, this means that the predominant retrograde motility observed for Rab7 late endosomes and autophagic vesicles towards the more degradative soma could be accomplished through the Rab7-RILP-dynein complex. In neurons, RILP was suggested to be

necessary for this function (Khobrekar et al., 2020; Ye et al., 2018). Recently, however, the two RILP-targeted shRNAs used in these earlier studies appear to have a neuronal specific off target phenotype that resulted in depletion of Golgi staining, in addition to potential on-target effects (Yap et al., 2023). Further, knockdown of RILP using a siRNA only minimally affected retrograde motility in the proximal axon, and had no effect on medial or distal axonal traffic (Cason et al., 2021). Thus, the exact role of RILP in axonal retrograde transport is still under investigation.

The motility of Rab7 late endosomes via RILP is also regulated by additional features of late endosomes, namely the lipid composition, which affects the recruitment of additional Rab7 effectors. Interestingly, it appears that these interactions are initiated at and regulated by endoplasmic reticulum (ER)-endosome contact sites. ER-organelle contact sites are gaining increasing attention in cell biology and are critical for normal organelle function (Wenzel et al., 2022). The oxysterol binding protein (OSBP) family binds and mediates transfer of lipids, like cholesterol, between ER and other intracellular compartments (Nakatsu and Kawasaki, 2021). Oxysterol binding protein (OSBP) related protein 1 L (ORP1L) was identified as a Rab7 interacting protein (Johansson et al., 2005). It was found that in addition to RILP, proper activation of dynein and subsequent positioning of late endosomes requires a tripartite complex with ORP1L in a cholesterol-dependent manner (Johansson et al., 2005; Johansson et al., 2007; Rocha et al., 2009). The tripartite complex mediates late endosome contact sites with the ER, which ultimately influences endosomal positioning (Ma et al., 2018; Rocha et al., 2009). This is dependent on ORP1L responses to cholesterol availability. As evidence of this, excess cholesterol, such as in diseases like Niemann Pick type C (Mukherjee and Maxfield, 2004), drives late endosomal positioning to perinuclear regions, whereas cholesterol depletion leads to late endosomal accumulation at microtubule plus ends (Sugii et al., 2006). ORP1L is also required for the resolution of phagosomes, suggesting degradation of internalized cargo is in part dependent on its function (Levin-Konigsberg et al., 2019). How ORP1L contributes to control of late endosomes within the complexity of neuronal space, however, has not been elucidated. However, alterations in Rab7-ORP1L interactions and cholesterol metabolism have the

potential to disrupt dynein activation via RILP and ultimately endosome positioning, which could negatively impact TrkA trafficking or degradation.

b) V-ATPase

As endosomes mature from early to late endosomes, then to lysosomes, the intraluminal pH becomes increasingly more acidic. Endo/lysosomal pH is in large part established through the activity of the endosome-localized vacuolar H+-ATPase (V-ATPase), which is regulated by the assembly of a cytosolic ATPase containing V1 complex with a membrane embedded proton translocating V0 domain (Collins and Forgac, 2020). Correct endosomal/lysosomal pH is critical for functions such as cargo degradation and ligand receptor dissociation (Chadwick et al., 2021; Freeman et al., 2023). Rab7 has been implicated in V-ATPase function and endosomal acidification through direct interaction with the V0a3 subunit in secretory lysosome trafficking (Nakanishi-Matsui and Matsumoto, 2022) and by forming a ternary complex with RILP and the cytosolic V1G1 subunit of the V1 complex to regulate V1G1 availability (De Luca et al., 2014). The data from this study suggest that RILP is responsible for the correct endosomal-lysosomal localization of V1G1 and thus involved in regulating acidification (De Luca et al., 2014). Fitting this notion, acidification was positively correlated with the level of Rab7 on endosomes, and depletion of RILP by siRNA led to global increases in endosomal/lysosomal pH (Chadwick et al., 2021; Johnson et al., 2016). Acidification is also important for neurotrophin signaling, as treatment with the V-ATPase inhibitor Bafilomycin-A1 (BafA1) results in failed recycling of TrkA to the plasma membrane and accumulation within intracellular compartments (Diering et al., 2013). Following NGF stimulation, BafA1-treated cells have lower levels of pAkt and pERK, suggestive of deficient TrkA signaling (Diering et al., 2013). Conversely, hyper-acidification of endosomes leads to less neurotrophin signaling (Ouyang et al., 2013). Thus, degradation of Trk receptors and NGF-TrkA dissociation events are in part dependent on both Rab7 function and V-ATPase mediated endosomal acidification. Furthermore, acidification might also impact endosomal localization along axons since

in fibroblasts, less acidified endosomes/lysosomes localize more peripherally (Johnson et al., 2016).

c) Vps35: Connections to both TrkA sorting and degradation

Degradation of any cargo like TrkA requires functional lysosomes, which depend on proper trafficking of degradative hydrolases, such as cathepsins. Cathepsins are trafficked via specialized pathway(s) that involve binding of a mannose-6-phosphate moiety in the trans-Golgi network (TGN) by the mannose-6-phosphate receptor (M6PR) and trafficking to late endosomes where M6PR dissociates from its cargo and recycles to the TGN (Ghosh et al., 2003). This retrieval pathway is in part dependent on the activity of retromer (Arighi et al., 2004; Seaman, 2004; Seaman, 2018). If retrieval is defective, M6PR gets stuck in endosomes and fails to continue to deliver cathepsins to the late endosome/lysosome. To what degree M6PR trafficking and lysosomal biogenesis in particular cell types depend on the activity of retromer is actively debated (McNally and Cullen, 2018; Seaman, 2018).

Retromer is composed of a trimeric core complex involved in cargo sorting (Vps26/29/35) and heterodimeric SNX-BAR family proteins which facilitates membrane tubulation. The core retromer complex subunit Vps35 is a Rab7 effector protein (Priya et al., 2015; Rojas et al., 2008; Seaman et al., 2009). Vps35 interacts directly with active GTP-bound Rab7 (Rojas et al., 2008). Increased GTP-Rab7 levels following depletion of the Rab7 GAP TBC1D5 increases membrane recruitment of retromer, whereas overexpression of the GAP inhibits membrane localization (Jimenez-Orgaz et al., 2018; Seaman et al., 2009; Seaman et al., 2018). Rab7 knockdown or disruption of Rab7-Vps35 interaction leads to subsequent loss of Vps26 membrane localization, suggesting the Vps35-Rab7 is a key component of retromer assembly (Priya et al., 2015; Seaman et al., 2009). Knockout of Vps35 leads to clear changes in lysosomal morphology and degradative capability (Arighi et al., 2004; Cui et al., 2019; Maruzs et al., 2015). Vps35 is likely especially critical in neurons, as it is a genetic locus for familial Parkinson's disease, which has been discussed extensively elsewhere (Muraleedharan and Vanderperre, 2023; Rahman and Morrison, 2019; Sassone et al., 2021). Recent omics

data validate this importance, as Vps35 knockout neuroglioma cells exhibit a wide breadth of proteomic and transcriptomic changes pertaining to endosomal function (Daly et al., 2023). However, what role Vps35 plays in neurotrophin trafficking is not fully understood. At a minimum, it has been demonstrated that a subset of Rab7+TrkA+ signaling endosomes are positive for Vps35 (Ye et al., 2018).

d) Homotypic Fusion and Protein Sorting (HOPS) Complex for Tethering and Fusion

The multimeric HOPS complex was identified as the Rab7 effector machinery that facilitates membrane tethering and fusion between late endosomes and the vacuole in yeast (Seals et al., 2000; Spang, 2016; Wurmser et al., 2000). HOPS subunits Vps39 and Vps41 can bind Rab7 in pulldown experiments in vitro (Plemel et al., 2011; Wurmser et al., 2000) In liposome assays, fusion required Rab7 on both opposing membranes and the presence of HOPS (Ho and Stroupe, 2015). Even though HOPS subunits are able to bind Rab7, evidence that HOPS is a direct Rab7 effector protein in mammalian cells is lacking (Stroupe, 2018). Instead, there is evidence that other small GTPases, such as Arl8b or Rab2, mediate recruitment of HOPS for fusion in mammalian systems (Khatter et al., 2015; Schleinitz et al., 2023). Furthermore, Rab2 and/or Arl8b may instead facilitate the inactivation of Rab7 in a HOPS-dependent manner (Jongsma et al., 2020). HOPS complex can simultaneously bind Rab7 and RILP and form Rab7-HOPS-RILP complexes, which are likely necessary for lysosomal fusion events in mammalian cells (Jiang et al., 2014; Lin et al., 2014; Takáts et al., 2014; van der Kant et al., 2013). It is thus possible that RILP-Rab7 recruits HOPS machinery onto late endosomal/lysosomal membranes where they are handed off to Rab2 or Arl8b, and then Rab7 is inactivated prior to actual fusion. The details of these cascades are still not fully elucidated nor are the specific implications for HOPS in neurotrophin trafficking and degradation.

2.6 A novel notion of effector balance and ordering: is this disrupted in disease?

To this point, we have discussed the changes to TrkA signaling cascades in CMT2B and physiologic interactions of Rab7 with various effectors. In the following sections, we will build on the notion that CMT2B is a product of dysregulation of TrkA signaling due to degradative impairments and/or signaling in the wrong location (**Figure 3**) and ask how disease-related changes in specific Rab7 effector interactions may drive either of these outcomes.

Notably, however, the experiments conducted up to this point elucidate changes in Rab7 CMT2B mutant behavior with regard to a single effector. This is clearly an important first step to provide foundational evidence of changes in Rab7 function in CMT2B disease. It is however a great simplification of the cytosolic milieu of multiple effectors that GTP-bound Rab7 may encounter. At any given moment, which effector does active Rab7 choose to bind? In our minds, this minimally depends on the affinity of Rab7 for a particular effector and the absolute abundance of any given effector versus another. In a hypothetical situation of active Rab7 with equal affinity for two different effectors, but one at high concentration and one at low concentration, we would expect the effector present in excess to be bound by more GTP-Rab7, simply as a consequence of mass action. These are all important notions as it has long been proposed that CMT2B is a disease of quantitative, rather than qualitative Rab7 effector changes (McCray et al., 2010). In addition, the spatiotemporal ordering of Rab7-effector cascades along lengthy axons might be changed in CMT2B Rab7 alleles, altering where and when active TrkA is signaling, and thus needs to be considered. Therefore, in addition to reviewing known data regarding how Rab7 effectors are changed in CMT2B and what this means for TrkA, our discussion will bear differential Rab7 affinity, effector abundance, and neuronal spatial complexity in mind.

a) RILP in CMT2B: A case for effector abundance?

Overexpression of CMT2B mutant Rab7 proteins in HeLa cells did not alter RILP expression (Spinosa et al., 2008), and co-immunoprecipitations of overexpressed Rab7 mutants and RILP demonstrated equal and preserved interactions as compared to wild-type (McCray et al., 2010).

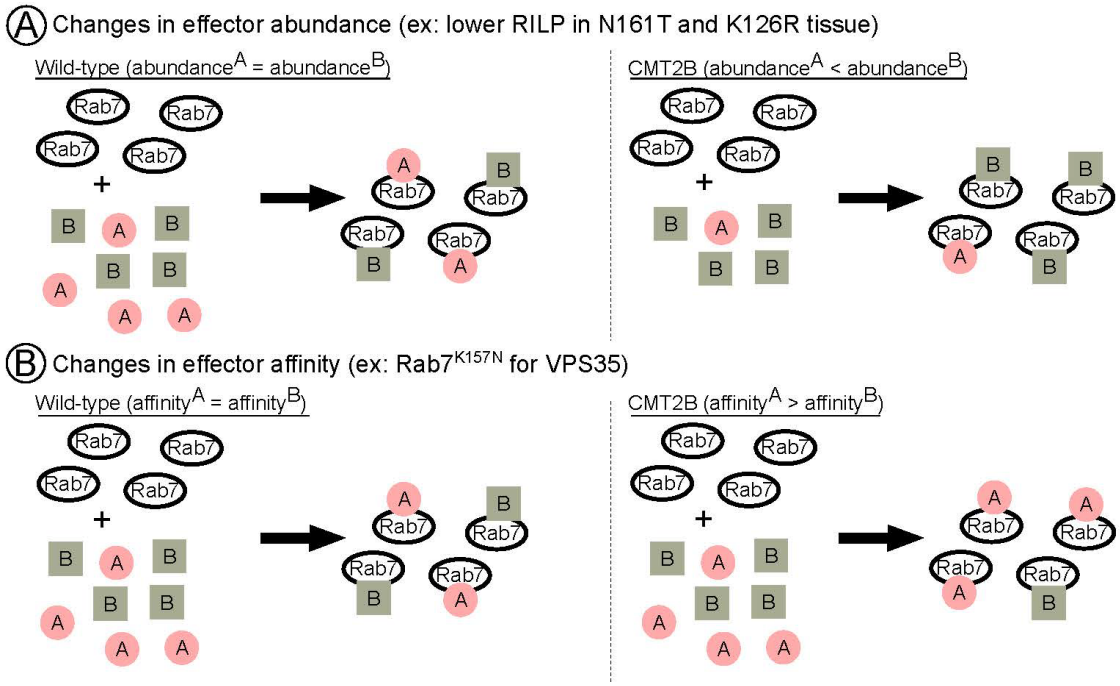

Figure 4 Effector abundance and affinity affect Rab7 functional balance

(A) Changes in absolute abundance of an effector protein can alter Rab7 function balance. Left: In control scenarios where effectors A and B are in equal abundances, under the assumption that affinities are also equivalent, Rab7 will bind A and B in equal proportions. Right: In CMT2B, where effector abundance is altered (e.g., lower RILP (represented by A) in N161T and K126R patient tissue), but affinities are assumed to remain equivalent, Rab7 will bind effector B in greater proportion to effector A (RILP). **(B)** Changes in Rab7 affinity for particular effectors can alter Rab7 function balance. Left: In control scenarios where Rab7 has equal affinity for equally abundant effectors A and B, Rab7 will bind A and B in equal proportions. Right: In CMT2B, where Rab7 has altered affinity for particular effectors (e.g., decreased affinity for VPS35 (represented by B) in K157N), under the assumption of equal abundance, Rab7 will bind effector B (VPS35) in lesser proportion to effector A.

However, sural nerve biopsies from the Rab7N161T mutant proband stained for RILP demonstrated loss of RILP protein levels compared to healthy controls (Houlden et al., 2004). Similarly, whole cell lysates from sural nerve biopsies of the Rab7K126R proband also showed reduced RILP levels (Saveri et al., 2020). Thus, in patient peripheral nervous system tissues, RILP expression appears to be decreased but most likely the affinity of CMT2B Rab7 alleles for RILP is not changed (**Figure 4A**). It is not known why levels of Rab7 effectors (such as RILP) would be decreased in CMT2B. It is also not known if all CMT2B alleles equally affect expression levels of RILP nor if other (or all) Rab7 effectors also change levels in CMT2B. Regardless, lower levels of RILP

could have profound impacts on dynein-mediated retrograde trafficking of TrkA containing endosomes by having less RILP available to hook endosomes to motors. Considering that RILP is also a part of tripartite Rab7 effector complexes (like the V-ATPase and HOPS; **Figure 2**), the lower levels of RILP also could affect the function of these complexes. This also raises the question of whether certain complexes (such as Vps35/retromer) would now become favored in a low RILP environment, and in what proportion. Changed Rab7 effector complex distribution due to low RILP may dysregulate TrkA endosome behavior because both Rab7-RILP function is lost and Rab7 complexes with another effector are increased.

What is the experimental evidence for alterations in RILP behavior and what are its effects on intracellular trafficking of Rab7 and TrkA in CMT2B? There is data to support both the TrkA degradation (**Figure 3B**) and TrkA mislocalization hypotheses (**Figure 3C**). Multiple studies across model systems have concluded that CMT2B mutations result in increased speed and processivity of Rab7-positive endosomes in the axon, though they disagree on the impacts on movement directionality (anterograde or retrograde) (Cioni et al., 2019; Janssens et al., 2014; Zhang et al., 2013). Faster retrograde motility could prematurely deplete signaling endosomes from distal axons and shorten local signaling cascades required for axon growth. In addition, faster retrograde motility of Rab7 endosomes could lead to premature degradation of TrkA cargo within the soma and shorten somatic signaling cascades or alternatively an excess of somatically arriving signaling endosomes which signal for longer (**Figure 3B**). Which of these outcomes is observed might depend on the individual CMT2B allele and its particular effector binding affinity and particular changes in effector abundance.

Similarly, faster anterograde motility of degradative lysosomes and fusion with TrkA carriers could also prematurely degrade the signal within the axon, preventing the signal from reaching the soma (**Figure 3B**). Zhang et al. 2013 found increased anterograde motility of Rab7N161T, though they did not assess other mutants. Notably, this is also one of the mutants in which we have patient data on RILP levels. It is reasonable that the decreased abundance of RILP in this mutant leads to a shift in the

bias of anterograde to retrograde transport given the requirement of RILP for retrograde motility.

In contrast to the above cited studies, in a Zebrafish transgenic model with in vivo live imaging more closely mirroring physiologic protein levels, Rab7L129F and Rab7K157N endosomes had decreased velocities, and Rab7N161T and Rab7V162M endosomes exhibited a stationary bias (Ponomareva et al., 2016). These data are consistent with the known patient data of reduced abundance of RILP, which predicts that motility is negatively impacted. These findings are consistent with the pathological loss of RILP observed in patient samples and supports the notion that decreased abundance of RILP impacts Rab7 effector function. These data also support the hypothesis that active TrkA reaches the soma and encounters degradative compartments more slowly in CMT2B neurons, possibly resulting in extended signaling in the axon and decreased signaling in the soma (**Figure 3C**).

Nevertheless, the impacts on Rab7 endosome motility in CMT2B are debated. With the advent of newly developed transgenic models (Gu et al., 2022), advances in in vivo imaging, and increasing availability of patient derived iPSCs, better studies can be carried out to more definitively elucidate impacts on Rab7 and TrkA motility in relevant heterozygote models and relevant cell types. Side by side comparisons of all mutants in these most physiologic models, particularly in microfluidic devices to separate distal axon and somatic signaling effects, will help clear the discrepancies between previous overexpressed in vitro studies and in vivo studies, and determine the impact and differences between mutants for axonal traffic.

b) VPS35 in CMT2B: A case for effector affinity?

Multiple studies have determined that some CMT2B Rab7 mutants have altered interactions with Vps35. Overexpressed Rab7K157N immunoprecipitated significantly less Vps35 than Rab7WT overexpression cells (Seaman et al., 2009). Rab7L129F and Rab7N161T mutants were also tested and though they had mild decreases in interaction with Vps35, they were not significantly changed (Seaman et al., 2009). Rab7K157N also could not rescue retromer component membrane localization to the

same degree as Rab7WT/L129F/N161T (Seaman et al., 2009). Further, in liposome sedimentation assays, a combination of SNX3 and Rab7WT was shown to be sufficient to drive retromer association with membranes, versus either SNX3 or Rab7WT alone. However, Rab7K157N could not drive the same recruitment, even in the presence of SNX3 (Harrison et al., 2014). The lack of Vps35 immunoprecipitation by Rab7K157N as compared to other mutants in an identical experimental paradigm where Rab7 and Vps35 levels were controlled is evidence of change in affinity for Vps35 by this particular mutation (**Figure 4B**). Whether or not this holds true in vivo where abundances, both global and locally, can vary remains to be seen. The consequences of deficient Rab7K157N-Vps35 interactions on TrkA or lysosomal enzyme trafficking, however, have also not been elucidated. One would speculate that reduced Rab7K157N-Vps35 interactions would result in failed recycling of TrkA receptors, resulting in degradation rather than prolonging the duration of an active TrkA receptor. In contrast, data from Rab7V162M patient fibroblasts and iPSC-derived sensory neurons show alterations in retromer-dependent processes as they contain increased levels of M6PR and mature cathepsins (Romano et al., 2021). Similarly, Rab7K126R patient fibroblasts [131] had more mature cathepsin and degradation of the sensor DQ-BSA, suggesting increased degradation. However, we do not currently know the true impact of these particular mutations on Vps35-Rab7 interactions (Seaman et al., 2009), nor the impact of Rab7 mutations on local or somatic signaling.

In addition to Vps35 core retromer complex sorting activities, retromer associated SNX-BAR proteins promote membrane tubulation. In Markworth et al. 2021 (Markworth et al., 2021), the authors investigate the relationship between Rab7+ tubule formation and active TrkA. Stimulation of DRGs and mouse embryonic fibroblasts (MEFs) with NGF results in active TrkA-containing Rab7 tubules. In MEFs overexpressing Rab7K157N and Rab7V162M, there was no increase in tubulation following NGF stimulation and subsequently lower levels of active TrkA. In Rab7L129F and Rab7N161T, tubulation was increased at baseline and could not be further increased by NGF addition, resulting in persistently high active TrkA levels. The exact dependence on Vps35 or SNX family proteins was not established in this study, but it is evident that TrkA incorporation into tubules is key to controlling signaling fates and that mutations

impact this process differently. Together, similar to EGFR degradation and Rab7 motility studies, it is clearly evident that different CMT2B alleles show clear differences in retromer-related enzyme trafficking and tubulation phenotypes that may be tied to changes in affinity. Since all CMT2B alleles appear to be fast-cycling in biochemical assays, the definitive structural basis for these differences is not clear.

Figure 5

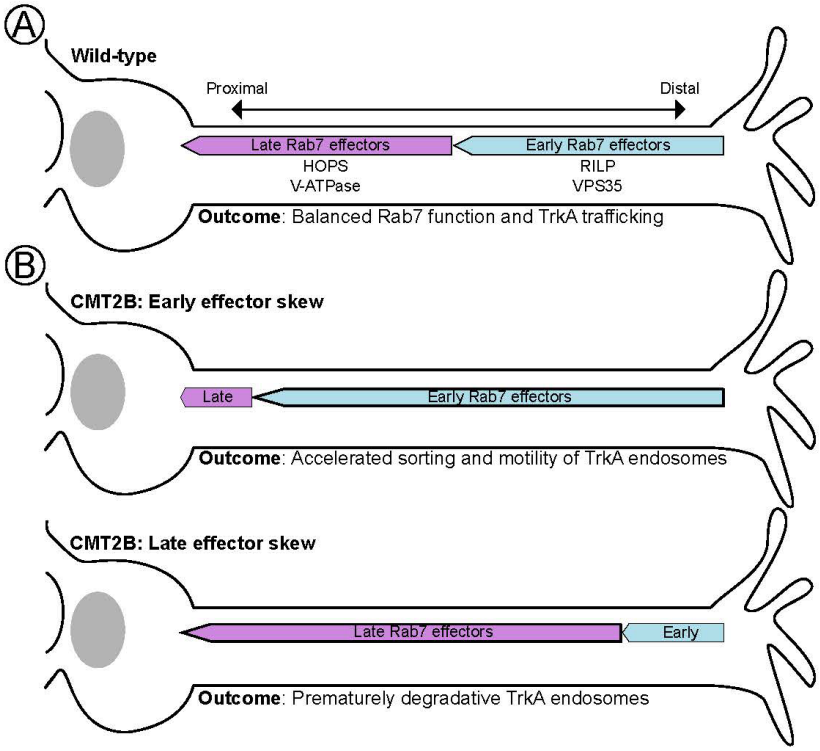

Figure 5 Changes in Rab7 effector binding within neuronal space impact TrkA signaling

(A) Under wild-type conditions, Rab7 effector functions are grouped into early, distal effectors (RILP, VPS35) which position active TrkA in the correct location, and late, somatic effectors (HOPS, V-ATPase) which prime endosomes for TrkA degradation and signal termination. Balanced distal versus somatic effector binding and functions ensure proper TrkA trafficking and both local and nuclear signaling. **(B)** Possible early effector skew in CMT2B leads to more RILP and/or VPS35 function across greater neuronal space. As a result, excess motility and/or sorting of TrkA receptors contributes to either premature degradation or improper localization of TrkA signals. These scenarios would have negative impacts on the sustainment of proper nuclear and local signaling. **(C)** Possible late effector skew in CMT2B leads to more HOPS and/or V-ATPase function across greater neuronal space, contributing to degradative endosomes or lysosomes further down the axon and leading to early termination of TrkA signaling. Early termination of TrkA signals within the axon would lead to a loss of necessary nuclear survival signaling.

c) Spatial ordering of Rab7 effectors along the TrkA trafficking route

Consider again an active, internalized TrkA receptor which must travel from the distal axon to the soma and undergo multiple endosomal maturation steps to potentiate signaling or be degraded. As we have discussed, these steps, including motility, sorting, acidification and fusion, are Rab7-dependent. They also exist along a distal to proximal gradient within neuronal processes. TrkA signaling must also exist in a gradient in order to support local effects at distal axons like axonal growth and maintenance and somatic global effects like survival. This then raises the questions: which effectors are needed first, and is there particular ordering to Rab7 effector cascades in space that impacts TrkA signaling? We speculate that the Rab7 effector functions can be grouped into early and late effectors (**Figure 5**). Early effectors, like RILP and Vps35, can potentiate long range movement and recycling of receptors, and thus contribute to correct distributions of TrkA receptor complexes. Late effectors, like HOPS and the V-ATPase, which mediate lysosomal fusion and acidification respectively, would advance TrkA and other cargos towards degradation. Thus, within the large space of the axon, early effector functions would occur more distally, allowing distal signaling to occur as well as promoting retrograde transport towards the soma, whereas late effector functions would occur more proximally in the axon and in the soma to promote fusion with somatic lysosomes. There is a body of evidence just beginning to support this notion. For instance, a recent study found that there is an ordering to Rab effector cascades. Specifically, Rab7 is found with RILP first on earlier endosomal compartments and only later engages with HOPS on more mature compartments to mediate lysosomal fusion (Schleinitz et al., 2023). Furthermore, pH-neutralized distal TrkA carriers are still able to retrogradely traffic from the distal axon in compartmentalized chambers all the way to the soma (Harrington et al., 2011), suggesting that acidification is not a prerequisite for motility and Rab7-RILP-dynein complexes likely precede that of V-ATPase complexes. This is further supported by the long-standing notion that acidification progresses as a compartment moves retrograde, and that the most acidic compartments are somatically localized (Overly and Hollenbeck, 1996).

What are the implications for a distal-to-proximal axon Rab7 effector cascades with respect to CMT2B Rab7 alleles that may change effector choice? Progressing from

most distal to most proximal, excessive engagement of an early effector like Vps35 would result in excessive active TrkA distally. With the consideration that local TrkA signaling may potentiate axonal growth, while somatic signaling would support survival, excessive TrkA sorting distally would diminish neuronal survival. A similar outcome could be achieved in settings of low RILP driven motility (as in N161T and K126R mutants) (Houlden et al., 2004; Saveri et al., 2020), where TrkA carriers become stalled distally (**Figure 3 B,C** and **Figure 5B**). Conversely, high engagement with RILP or loss of interaction with Vps35 (as in K157N (Harrison et al., 2014; Seaman et al., 2009)) would deplete local axonal growth signals and could support either excessive somatic degradation or somatic survival signaling of active TrkA.

Alternatively, excessive or premature engagement of a late effector like HOPS or the V-ATPase on retrograde Rab7+TrkA+ carriers and an acidified compartment, for example, might result in early degradation of the signal within the axon, in line with the model proposed in Zhang 2013 (**Figure 3B** and **Figure 5B**). Multiple studies report that a small number of acidified and degradative LAMP1+ compartments, i.e. lysosomes, move anterogradely and are present in axons (Farfel-Becker et al., 2019), which could potentiate such degradation. However, most LAMP1+ compartments in axons are not highly acidic or degradative (Cheng et al., 2018) or are Golgi carriers (Lie et al., 2021), and premature fusion of anterograde degradative compartments with retrograde TrkA carriers has not been directly observed. Disruption of HOPS-mediated fusion or V-ATPase-mediated acidification would support too much signaling both somatically and distally. As evidence of this, treatment with the V-ATPase inhibitor Bafilomycin-A1 (BafA1) treatment results in accumulation of TrkA within intracellular compartments, which may be signaling-competent (Diering et al., 2013). Further, NGF- and BafA1- or NH_4Cl-treated distal axons still traffic FLAG-tagged TrkA to the cell body following NGF stimulation, but the spatial gradient of NGF-TrkA signaling output is shifted from predominantly in the cell body to equivalent between the axon and cell body (Harrington et al., 2011).

Together, effector affinity, abundance, and ordering likely all contribute to normal Rab7 function and ultimately endosomal maturation and TrkA signaling gradients within

neuronal space. However, we know remarkably little about these processes for wild-type Rab7, and even less so for CMT2B mutants. It is unclear what the balance between affinity and abundance changes exist in CMT2B disease, and ultimately how this affects the effector ordering within the axon. However, it is clear that the balance of all of these factors is necessary for faithful trafficking and degradation of TrkA, and without such distal local signaling, somatic signaling, and degradation becomes disrupted.

2.7 Other Rab7 hypotheses: it's not all about TrkA

Even though we have discussed Rab7 within the hypothesis that TrkA signaling is dysregulated in CMT2B, this is not the only current possible contributing mechanism underlying CMT2B. Other data support defects in additional processes. For instance, CMT2B mutants display dysregulation in autophagy and lipophagy progression, leading to failure of autophagic clearance and lipid droplet accumulation (Colecchia et al., 2018; Giudetti et al., 2020; Romano et al., 2022). These defects might also lead to the observed axonopathies observed in CMT2B. Rab7 has known roles in autophagy progression (Kuchitsu and Fukuda, 2018), which requires orderly Rab7 effector progression as we have discussed. These data also provide an interesting future avenue of investigation for a lipid-centric ypothesis of CMT2B, given CMT2B mutant Rab7 increasingly binds both ORP1L and the lipid transfer protein Vps13C (Hancock-Cerutti et al., 2022; McCray et al., 2010), though it is unclear whether this is due to changes in abundance or affinity. Mutant cells also have excessive lipid droplets and broad changes in their lipidome (Giudetti et al., 2020; Romano et al., 2022). Increased Rab7-ORP1L interactions could have profound impacts on endosome motility, given their involvement in a tripartite complex with RILP, though this remains to be explored in the setting of disease. The literature also supports a role for cholesterol-sensitive ER-endosome contact sites in mediating neurite health and outgrowth, as the loss of other Rab7-interacting ER resident proteins like protrudin negatively affect axonal growth and

entry of anterograde traffic into the axon (Gao et al., 2022; Kuijpers et al., 2023; Özkan et al., 2021). In Rab7V162M patient fibroblasts, the proportion of neutral lipids made up by cholesterol is decreased (Giudetti et al., 2020). In settings of low cholesterol, ER-late endosome contact sites are increasingly formed, ORP1L is not engaged with RILP-dynein complexes and instead engages with autophagosomes, which is inhibitory to Rab7-mediated minus-end directed transport (Rocha et al., 2009; Wijdeven et al., 2016). This would result in distal stalling of TrkA endosomes and thus possible signaling in the wrong location. Thus, altered ER-endosome contacts via ORP1L could be impactful for axonal maintenance. Ultimately, the increased ORP1L/Vps13C interactions with Rab7 mutants with concomitant decreases in cholesterol will need to be simultaneously validated within patient tissues and novel knock-in model systems to better understand the contribution of changes in lipid metabolism in CMT2B disease.

Further, given the specificity of impact of Rab7 mutations on the peripheral nervous system (PNS), it has long been speculated that there may be a unique PNS Rab7 effector that mediates disease (Bucci and De Luca, 2012). To this end, it was found that the intermediate filament peripherin, specific to the PNS, more highly interacts with all of the Rab7 CMT2B mutants versus wild-type Rab7 (Cogli et al., 2013; Saveri et al., 2020). Higher levels of peripherin were also found within Rab7K126R patient dermal punch biopsies (Saveri et al., 2020). It is thought that Rab7 mutants may impact the balance of soluble to insoluble peripherin, affecting filament formation. Since the roles of neuronal intermediate filaments with regards to endosomal trafficking and long term health of neurons are poorly understood, it is not at all clear how changes of Rab7-peripherin interactions in CMT2B might contribute to pathologies (Cogli et al., 2013). Finally, recent studies have begun to emphasize the impacts of Rab7 on mitochondrial health and how this may become changed in disease, resulting in altered neuronal metabolism. Multiple studies have described both increased retrograde biased motility and morphology of mitochondria in settings of CMT2B Rab7 mutants (Cioni et al., 2019; Gu et al., 2022). Within a new heterozygous Rab7V162M knock-in model, mitochondrial trafficking deficits were specifically found within the primary peripheral sensory neurons, and not in primary hippocampal or cortical neurons (Gu et al., 2022). Whether this relates to peripherin expression is not known. Local translation of key

mitochondrial proteins is also diminished in mutants (Cioni et al., 2019). Given that some of the regulation of Rab7 activity takes place at mitochondria (Jimenez-Orgaz et al., 2018; Wong et al., 2018; Wong et al., 2019a), GEF-independent cycling of Rab7 may reciprocally disrupt typical mitochondrial dynamics. In support of this, Rab7V162M mutants displayed prolonged lysosomal-mitochondrial contacts which ultimately altered inter-mitochondrial tethering dynamics (Wong et al., 2019b).

2.8 Concluding remarks

In conclusion, the peripheral neuropathy Charcot Marie Tooth 2B can largely be attributed to alterations in Rab7 interactions with its many important effectors, summarized in **Table 1**. The prevailing hypothesis, among others, has been that dysfunctional Rab7 nucleotide cycling and subsequent alterations in effector interactions disrupt intracellular trafficking and lead to deficits in neuronal survival signals via the NGF-TrkA neurotrophin receptor complex. Since different CMT2B alleles show distinct alterations in Rab7 effector binding, we postulate that currently unexplored changes in differential effector affinities and levels as consequence of mutations may alter the spatial ordering of Rab7 effector interactions along an axon, leading to either premature degradation of TrkA signaling or mislocalization of the signal. With recent advances in better physiologic models, as well as increased access to patient tissues, the field is making significant progress in accurately understanding underlying causes of the CMT2B which were previously complicated by non-neuronal overexpression systems. We are also closer to answering some of these more complicated questions regarding Rab7 effector balance and cargo trafficking, and how this is altered in disease.

Table 1. Summary of Rab7 effector changes in CMT2B

Effector	Function	$Rab7^{CMT2B}$ Interaction vs $Rab7^{WT}$	Abundance	Observed outcomes for CMT2B alleles attributable to effector

RILP	Dynein motor adaptor protein; late endosomal positioning and motility	Equal, in overexpression followed by immunoprecipitation experiments (McCray et al., 2010)(Spinosa et al., 2008)	Decreased in N161T and K126R patient tissues (Houlden et al., 2004; Saveri et al., 2020)	-Increased anterograde motility (Zhang et al., 2013) -Increased retrograde motility (Cioni et al., 2019) -Decreased stationary and pausing time (Cioni et al., 2019; Janssens et al., 2014; Ponomareva et al., 2016) -Increased endosome speeds (Cioni et al., 2019; Zhang et al., 2013) -Decreased endosome speeds (Ponomareva et al., 2016)
ORP1L	Late endosome positioning and motility (w/ RILP); lipid exchange and ER contacts	Increased by IP-MS [L129F, V162M] (McCray et al., 2010)	Undetermined	-Positioning and motility same as RILP -ER contact sites undetermined
VPS13C	Lipid exchange and ER contact sites	Increased by IP-MS [L129F, V162M] (McCray et al., 2010)	Undetermined	-Increased lipid droplet abundance (Colecchia et al., 2018; Romano et al., 2022) -Increased cholesterol ester:cholesterol ratios, increased monounsaturated fatty acids, free fatty acids, and total neutral lipids (Giudetti et al., 2020)
VPS35	Core retromer complex component; sorting and recycling of membrane receptors	-Preserved [L129F, N161T] -Decreased [K157N] -Undetermined [V162M, K126R] (McNally and Cullen, 2018)	Undetermined	-Increased M6PR levels [V162M] (Romano et al., 2021) -Increased mature cathepsins [V162M/K126R] (Romano et al., 2021; Romano et al., 2022)

				-Increased TrkA tubule behavior [L129F/N161T]; no change in TrkA tubule behavior [K157N/V162M] (Markworth et al., 2021)
V-ATPase Subunits	Endosomal and lysosomal acidification (w/RILP)	Undetermined	Undetermined	Undetermined
HOPS Subunits	Endosomal tethering and fusion (w/RILP)	Undetermined (possibly decreased (Liu and Wu, 2017))	Undetermined	Undetermined
Peripherin	Peripheral nervous system specific intermediate filament	Increased (Cogli et al., 2013; Saveri et al., 2020)	Increased (Saveri et al., 2020)	-Increased soluble: insoluble peripherin (Cogli et al., 2013) -Undetermined impact on endosome behavior

Chapter III. Collapse of late endosomal pH elicits a rapid Rab7 response via V-ATPase and RILP

This chapter is published as “Collapse of late endosomal pH elicits a rapid Rab7 response via V-ATPase and RILP.” Mulligan RJ, Magaj MM, Digilio L, Redemann S, Yap CC, Winckler B. Collapse of late endosomal pH elicits a rapid Rab7 response via V-ATPase and RILP. J Cell Sci. 2024 Apr 5:jcs.261765. doi: 10.1242/jcs.261765. Epub ahead of print. PMID: 38578235.All experiments and analysis were carried out by Ryan J Mulligan. Electron microscopy sample preparation and imaging was performed by Magdalena Magaj and Stefanie Redemann. Laura Digilio aided in preparation of primary mouse fibroblasts.

3.A Abstract

Endosomal-lysosomal trafficking is accompanied by the acidification of endosomal compartments by the H^+-V-ATPase to reach low lysosomal pH. Disruption of proper pH impairs lysosomal function and the balance of protein synthesis and degradation (proteostasis). We used the small dipeptide LLOMe, which is known to permeabilize lysosomal membranes, and find that LLOMe also impacts late endosomes (LEs) by neutralizing their pH without causing membrane permeabilization. We show that LLOMe leads to hyper-activation of Rab7 and disruption of tubulation and mannose-6-phosphate receptor (CI-M6PR) recycling on pH-neutralized LEs. Either pH neutralization (NH_4Cl) or Rab7 hyper-active mutants alone can phenocopy the alterations in tubulation and CI-M6PR trafficking. Mechanistically, pH neutralization increases the assembly of the V_1G_1 subunit of the V-ATPase on endosomal membranes, which stabilizes GTP-bound Rab7 via RILP, a known interactor of Rab7 and V_1G_1. We propose a novel pathway by which V-ATPase and RILP modulate LE pH and Rab7 activation in concert. This pathway might broadly contribute to pH control during physiologic endosomal maturation or starvation and during pathologic pH neutralization, which occurs via lysosomotropic compounds or in disease states.

3.1 Introduction

Lysosomes are the principal membrane-bound proteolytic compartment within cells and are the endpoints of degradative endocytic trafficking, phagocytosis, and autophagy. Progression of trafficking pathways to lysosomes is essential for maintaining proteostasis. Numerous pathologies are associated with impaired proteostasis, including disruption of lysosomal membranes leading to lysosomal membrane permeabilization (LMP). LMP is any perturbation that compromises integrity of the lysosomal limiting membrane, leading to leakage of luminal content into the cytosol (Wang et al., 2018), including protons (causing luminal pH neutralization), calcium and often cathepsins (Lakpa et al., 2021). LMP occurs in diseases including lysosomal storage disorders (Kirkegaard et al., 2010) and those with neurotoxic aggregates (Freeman et al., 2013; Dilsizoglu Senol et al., 2021; Flavin et al., 2017; Polanco and Götz, 2022). Still other genetic and neurodegenerative conditions impact maintenance of proper endosomal and lysosomal function, like pH, in the absence of LMP (Colacurcio and Nixon, 2016; Pescosolido et al., 2021). It is thus important to study how cells mechanistically respond to endosomal dysfunction, including repairing LMP or correcting pH disruption. Our understanding of cellular LMP responses has been greatly advanced by using the lysosomotropic dipeptide L-leucyl L-leucine-O-methyl-ester (LLOMe), which damages lysosomal membranes. Studies using LLOMe have uncovered rapid membrane repair mechanisms (within minutes), such as via ESCRT or PI4P/ATG2 (Bohannon and Hanson, 2020; Jia et al., 2020a; Niekamp et al., 2022; Radulovic et al., 2018; Radulovic et al., 2022; Skowyra et al., 2018; Tan and Finkel, 2022; Yim et al., 2022), as well as delayed lysosome-specific autophagy pathways (within hours) via galectins (Gal-3/8/9) and autophagy adaptors (Jia et al., 2020b; Papadopoulos et al., 2020; Zoncu and Perera, 2022; Yang and Tan, 2023). How pH disruptions play into such stress responses, however, is not fully elucidated.

Before reaching lysosomes, endocytosed cargo traffics through a series of endosomal compartments, including early (sorting) endosomes (EE), late endosomes (LE) and ultimately lysosomes (LYS). Maturation of LEs ensures endocytosed cargos

encounter activated lysosomal hydrolases in increasingly acidified compartments before fusing with maximally degradative lysosomes. LE maturation is triggered by switching of Rab family proteins (i.e., Rab5 to Rab7). Active GTP-bound Rab7a (herein, Rab7) now engages Rab7 effector proteins (Huotari and Helenius, 2011), including the core retromer complex (Vps26/29/35) and RILP (Cantalupo et al., 2001; Progida et al., 2007). Rab7-Retromer has been implicated in retrieval of trafficking receptors like mannose-6-phosphate receptors (M6PRs) from LEs back to the trans-Golgi network (TGN), and for tubule generation necessary for recycling (Priya et al., 2015; Rojas et al., 2008; Seaman et al., 2009; Seaman et al., 2018). RILP links LEs to dynein motors for motility, but RILP/Rab7 complexes may also be involved in tubule formation from lysosomes (Mrakovic et al., 2012). These tubules likely require proper Rab7 GDP/GTP cycling for their formation (Markworth et al., 2021). Even though high-fidelity membrane trafficking through EEs/LEs is necessary for lysosomal function, studies regarding the impact of lysosomal disruption on endosomal trafficking or tubulation, and on regulation of Rab7 are lacking.

Maturation of LEs is further accompanied by decreasing intra-endosomal pH to that of the highly acidic lysosome (pH≈4.5). Cells establish and maintain endo/lysosomal pH through the endosome/lysosome-localized vacuolar H^+-ATPase (V-ATPase), which is activated by the assembly of the cytosolic V_1 complex with the membrane-embedded V_0 domain (Collins and Forgac, 2020). Rab7 has been implicated in V-ATPase function and endosomal acidification by forming a ternary complex with its effector RILP and the V_1G_1 subunit of the V_1-ATPase complex (De Luca et al., 2014) and by direct interaction with the V_0a_3 subunit in secretory lysosome trafficking in osteoclasts (Nakanishi-Matsui and Matsumoto, 2022). However, the precise connections between Rab7 activity, V_0-V_1 assembly and endosomal acidification are not well elucidated. Thus, it is unknown if luminal pH can coordinate cytoplasmic effector cascades like those of Rab7.

In this study, we sought to address the gaps in knowledge regarding how endosomal compartments critical for membrane trafficking (i.e., LEs) behave in the context of LMP. We report here that a pH-driven mechanism in otherwise undamaged

LEs leads to V-ATPase- and RILP-mediated hyperactivation of the small GTPase Rab7, disrupting normal Rab7 tubulation and biosynthetic receptor trafficking. These findings suggest a Rab7-RILP-V-ATPase axis involved in pH modulation and pH-driven LE stress responses. We thus describe a novel LE stress response, likely relevant in LMP and pathologic pH neutralization.

3.2 Materials and Methods

Immortalized cell line culture and transfection

Normal rat kidney (NRK) cells (ATCC CRL6509) and COS-7 cells (UVA Tissue Culture Facility) were maintained in DMEM with glucose and GlutaMAX (Gibco 10566-016) plus 10% fetal bovine serum (FBS) without antibiotics, and tested upon acquisition. All cells were incubated at 37°C and maintained at 5% CO_2. For fixed imaging, cells were plated on coverslips coated with 10 µg/mL fibronectin (Sigma) for 1 hour at 37°C. For live imaging, cells were plated on 35mm dishes with 14mm glass bottom inserts (MatTek) coated with 10µg/mL fibronectin for 1 hour at 37°C. Transfections into NRK and COS-7 cells for fixed or live imaging experiments and for GST-RILP Rab7 activity pulldowns were performed using Lipofectamine 2000 (Invitrogen) per manufacturer's instructions. Downstream applications were conducted 24 hours post-transfection unless otherwise stated. For establishment of stable Emerald-Rab7-WT and Em-Rab7-L8A NRK cell lines, Em-Rab7^{WT} or Em-Rab7^{L8A} were transfected into NRK cells. 24 hours post transfection, cells were maintained on 100µg/mL geneticin (Gibco) in complete DMEM. After 5 days of selection, individual cell colonies were selected and expanded in geneticin-containing medium. Purity of clones was screened for homogenous Em-Rab7 expression by fluorescence microscopy. Pure clones were expanded, frozen, and maintained in geneticin-containing DMEM for downstream applications.

Primary mouse embryonic fibroblast isolation and nucleofection

All experiments were performed in accordance with the University of Virginia Institutional Animal Care and Use Committee guidelines and regulations (ACUC protocol #3422). Primary mouse embryonic fibroblasts (MEFs) for all experiments were isolated from E13.5 Rab7$^{fl/fl}$ mice (Kawamura et al., 2012) (Riken BioResource Research Center #RBRC05600), maintained on C57BL/6 background, from 3 independent litters. Embryos were sterilely isolated from fluid sacs and torsos were isolated by removal of the head, limbs and tail. Internal organs and spinal cord were then removed by forceps. Remaining tissue was triturated in 0.05% trypsin-EDTA then incubated at 37°C for 10 minutes. An equivalent volume of 20% FBS in MEF medium [DMEM with glucose and L-glutamine (Gibco 11965-092)] was then added and the tissue was re-triturated. Cells were then spun, re-suspended, and plated in MEF medium containing 10% FBS for expansion, freezing, or downstream applications. Sex of embryos was not determined, and tissue derived from multiple embryos was mixed prior to plating, therefore, all cells were randomized between control and experimental groups. No animals were excluded. Experimental manipulation and outcome measures were all conducted *in vitro* and are discussed below. Data analysis and statistics were conducted on *in vitro* experiments as described in figure legends and below.

Upon use, MEFs were maintained in MEF medium containing 10% FBS without antibiotics. For single or double plasmid expression experiments (e.g., Em-Rab7 overexpression or Cre-recombinase knockouts), MEFs were nucleofected using Ingenio Solution electroporation reagent (Mirus Bio) and Lonza AMAXA Nucleofector II. Briefly, 1.5 million MEFs and 5µg total DNA were diluted in 100µL of Ingenio Solution in a 0.2cm cuvette (Mirus). MEFs were nucleofected using AMAXA program A-023 (MEF). Cells were immediately recovered in 900µL of pre-warmed complete MEF medium and then diluted and plated on 10µg/mL fibronectin coated coverslips. For Rab7 knockout experiments, downstream analyses were conducted three days post pCAG-Cre-GFP nucleofection. For live imaging use, MEFs were plated on 35mm dishes with 14mm glass bottom inserts (MatTek) coated with 10µg/mL fibronectin for 1 hour at 37°C.

Plasmids

The plasmids used in this study are as follows:

Emerald-Rab7^{WT} (Addgene #54244, Davidson Lab), GFP-Rab7^{WT} (Addgene #12605, Pagano Lab), GFP-Rab7^{Q67L} (gift from Dr. James Casanova, University of Virginia), GFP-Rab7^{T22N} (Addgene #12660, Pagano Lab), pCAG-Cre-GFP (Addgene #13776, Cepko Lab), pCDNA3-2xHA-V1G1 (gift from Dr. Cecilia Bucci, University of Salento), pET-His-GST-tev-LIC (Addgene #29655, Gradia Lab), pGEX-4T-3-mR7BD (Addgene #79149, Edinger Lab), mCherry (Clontech), pmRFP-LC3 (Addgene #21075, Yoshimori Lab). To generate Emerald-Rab7^{L8A}, Rab7a with a point mutation at residue 8 from leucine to alanine (L8A) was cloned into pEmerald-C1 (Addgene#54734, Davidson Lab) at XhoI-BamHI sites by Genscript, using gene synthesis.

Primary Antibodies

The list of primary antibodies used in this study are as follows: Anti-Rab7 (rabbit monoclonal; 1:100 IF; abcam 137029; RRID:AB_2629474), Anti-Rab7 (rabbit polyclonal; 1:1000 WB; proteintech 55469-1-AP; RRID:AB_11182831), Anti-Cathepsin B (goat polyclonal; 1:200 IF; R&D Systems AF965; RRID: AB_2086949), Anti-Cathepsin D (goat polyclonal; 1:200 IF; R&D Systems AF1029; RRID: AB_2087094), anti-LAMP1 (mouse monoclonal; 1:1000 IF; Enzo Life Sciences ADI-VAM-EN001; RRID:AB_2038958), anti-GM130 (mouse monoclonal; 1:500 IF; BD Biosciences 610822 RRID: AB_398141), anti-TGN38 (mouse monoclonal; 1:200 IF; BD Biosciences 610898, RRID:AB_398215), anti-Vps35 (goat polyclonal; 1:600 IF, 1:2000 WB; abcam 10099; RRID:AB_296841), anti-EEA1 (mouse monoclonal; 1:100 IF; BD Biosciences 610456; RRID: AB_399409), anti-CI-M6PR (rabbit monoclonal; 1:200 IF; abcam 124767; RRID:AB_10974087), anti-ALIX (mouse monoclonal; 1:100 IF; Santa Cruz sc-53540; RRID: AB_673819), anti-Galectin-3 (mouse monoclonal; 1:100 IF; Santa Cruz sc-25279; RRID: AB_627656), anti-Galectin-3

(rat monoclonal; 1:100 IF; Santa Cruz sc-23938; RRID: AB_627658), anti-GFP (rabbit polyclonal; 1:2000 WB; proteintech 50430-2-AP; RRID: AB_11042881), anti-GST (mouse; 1:1000 WB; Santa Cruz sc-138; RRID: AB_627677); anti-HA (mouse monoclonal; 1:100 IF, 1:1000 WB; Santa Cruz sc-7392; RRID: AB_627809); anti-HA (rabbit; 1:100 IF, 1:1000 WB; Santa Cruz sc-805; RRID: AB_631618). The antibodies used in this study are extensively used in the field by us and others (Cui et al., 2020; Miranda et al., 2018; Mulligan et al., 2023; Yap et al., 2018; Yap et al., 2023).

Secondary Antibodies

For immunocytochemistry, the following Alexa Fluor–coupled antibodies from Invitrogen were used: Alexa405-Phalloidin (A30104), Alexa488 donkey anti-mouse (A21202; RRID: AB_2535792), Alexa488 donkey anti-rabbit (A21206; RRID: AB_ 2534102), Alexa488 donkey anti-goat (A11055; RRID: AB_2534013), , Alexa568 donkey anti-mouse (A10037; RRID: AB_2534017), Alexa568 donkey anti-rabbit (A10042, RRID: AB_2534104), Alexa568 donkey anti-goat (A11057; RRID: AB_162546), Alexa647 donkey anti-mouse (A31571; RRID: AB_2536183), Alexa647 donkey anti-rabbit (A31573; RRID: AB_2535864), Alexa647 donkey anti-goat (A21447; RRID: AB_2340373). The following antibodies from Jackson ImmunoResearch Laboratories, Inc. were used: Alexa488 donkey anti-rat (712-545-153; RRID: AB_2340684), Alexa568 donkey anti-rat (712-585-153; RRID: AB_2340689), Alexa647 donkey anti-rat (712-605-153; RRID: AB_2340694), DyLight405 donkey anti-goat (705-475-147; RRID: AB_2340427), DyLight405 donkey anti-rat (712-475-153; RRID: AB_2340681). For western blotting, the following Jackson ImmunoResearch Laboratories, Inc. antibodies were utilized: donkey anti-mouse Alexa680 (715–625-151; RRID: AB_2340869), donkey anti-mouse Alexa800 (715-655-151; RRID: AB_2340871), donkey anti-rabbit Alexa680 (711-625-152; RRID: AB_2340627), donkey anti-rabbit Alexa790 (111-655-144; RRID: AB_2338086).

Immunocytochemistry and image acquisition

Immunocytochemistry was conducted as described (Mulligan et al., 2023). Briefly, cells were fixed in 4% paraformaldehyde/3% sucrose in PBS at room temperature for 15 minutes. Cells were then blocked and permeabilized using PBS/5% normal donkey serum/0.2% TritonX-100 or 0.1% saponin for 20 minutes at room temperature. Saponin permeabilization was used when staining for lysosomal membrane proteins (e.g., LAMP1, LAMP2); TritonX-100 was used for all others. Primary and secondary antibodies were diluted in 1% bovine serum albumin (BSA)/PBS and incubated for 1 hour and 30 minutes, respectively, at room temperature. 0.1% saponin was included in BSA antibody dilutions when staining for lysosomal membrane proteins. Coverslips were mounted in ProLong Gold antifade mounting medium (Invitrogen).

For widefield imaging, mounted coverslips were viewed using a Zeiss Z1-Observer with a 40x objective (enhanced chemiluminescence Plan-Neofluor 40x/0.9 Pol working distance = 0.41). Apotome structured illumination was used for all images. Images were captured with the Axiocam 503 camera using Zen software (2012 Blue edition, Zeiss) and identically processed in FIJI software. On average, 10 representative fields per condition per experiment were captured, for 3 independent experiments.

For live-cell spinning disk confocal microscopy, medium in live cell imaging dishes was replaced with phenol-red free DMEM (Gibco 31053-028) plus 10% FBS and 1X GlutaMAX (Gibco 35050-061) prior to imaging. Cells were viewed using a temperature-controlled (37°C) Nikon TE 2000 microscope using a 60X/NA1.45 oil objective, equipped with Yokogawa CSU 10 spinning disc and images were captured with a 512X512 Hamamatsu 9100c-13 EM-BT camera. On average, multicolor images were collected at a rate of 1 image/3 seconds for indicated times, with perfect focus on, up to 30 minutes (600 frames) and compiled using FIJI software. Vehicle (DMSO) or LLOMe (final concentration 1mM) were added in a pre-warmed bolus at 2 minutes (frame 40) live on the stage for all live-imaging experiments. On average, 10-15 movies per condition were collected from 3 independent experiments.

For traditional confocal microscopy, cells plated in live imaging dishes with phenol-red free DMEM (Gibco 31053-028) plus 10% FBS and 1X GlutaMAX (Gibco 35050-061)

or mounted coverslips were viewed using a Nikon Ti2-E inverted microscope with AX-R confocal microscopy system and 25 mm FOV resonant scanner/25 mm FOV galvano scanner, with an NSPARC detector unit. The system was controlled and images captured using photomultipliers and the Nikon NIS Elements C software. Cells were viewed using a 60X/NA1.40 oil objective and maintained in a temperature-controlled system at 37°C with perfect focus during live image acquisition. Captured images and movies were identically processed using Elements Denoise.ai followed by compiling in FIJI software. On average, 20-30 movies (FRAP), and 45-60 images (tubulation) per condition were collected from 3 independent experiments.

For Airyscan imaging, mounted coverslips were viewed using the Zeiss 980 NLO system using an inverted Axio Observer microscope with a 63X/NA1.40 oil objective and an 8Y-airyscan detector. Images were collected using Zeiss Zen Blue software on Super-Resolution-4Y mode with 0.13µm z-sections, and z-stacks were identically processed using Zen Airyscan 3-D Processing. On average, 3 representative fields per condition were captured, for 3 independent experiments (approximately 30 total cells per condition).

Lysosomal perturbation treatments

For induction of lysosomal damage, all cells were incubated in complete DMEM or MEF medium with 10% FBS, supplemented with DMSO (vehicle, 0.33%v/v, Millipore Sigma) or L-leucyl-L-leucine dimethyl ester (LLOMe, Sigma) at 1mM (unless otherwise noted) for times indicated. DMSO and LLOMe were equilibrated in fresh, pre-warmed (37°C) complete DMEM with 10% FBS prior to addition to cells.

All other treatments were carried out in complete DMEM or MEF medium with 10% FBS. Bafilomycin-A1 (Sigma) was dissolved in DMSO used at a final concentration of 200nM for 2 hours. Ammonium chloride (Fisher) was dissolved in sterile water and used at a final concentration of 20mM for 1 hour. ML-SA1 (Tocris) was dissolved in DMSO and used at a final concentration of 20µM for 5-30 minutes. For calcium chelation

experiments, cells were pre-treated with 10μM BAPTA-AM (Tocris) for 30 minutes. Then, cells were treated with fresh medium containing either DMSO or LLOMe in the presence of an additional 10μM BAPTA-AM for indicated times.

Electron Microscopy

NRK cells or MEFs were grown on 1% fibronectin (in PBS), and 0.1 mg/mL poly-L-lysine (in ddH2O) coated 6mm sapphire disks (Technotrade International) in complete DMEM, or complete MEF medium, at 37°C and treated with 45 minutes of DMSO, 1mM LLOMe, 20mM NH_4Cl, or 2 hours of 200nM BafA1 before immediate cryo-fixation by high pressure freezing (Leica EM ICE High Pressure Freezer), with 20% BSA in DMEM as a cryoprotectant. Samples were freeze substituted for three days in acetone containing 0.2g/mL methylene green (Spectrum Chemical MFG. GRP.), 0.1% uranyl acetate (Polysciences Inc) and 1% osmium tetroxide (Electron Microscopy Sciences) using Leica EM Automatic Freeze Substitution machine (Leica AFS2). Freeze substituted samples were then infiltrated with increasing Epon/Araldite (Electron Microscopy Sciences) in acetone until they were infiltrated with pure Epon/Araldite, over the course of one day. Epon infiltrated samples were embedded in resin and allowed to set for two days at 60°C followed by mounting on dummy resin blocks. Samples were then sectioned at 70nm using an ultramicrotome (Reichert Ultracuts, Leica) and collected onto 0.7% Pioloform (Ted Pella Inc) coated copper slot grids 2mm x 1mm Ø 3.05mm (Electron Microscopy Sciences). Post staining of samples on grids was performed with 2% uranyl acetate in 70% methanol followed by 0.4% lead citrate in ddH2O. Transmission electron micrographs were collected using a Tecnai F20 Transmission Microscope operated at 200kV and captured using a 4K x 4K UltraScan CCD camera.

Live Imaging Assays

Lysosomal pH Collapse Readouts

NRK, COS-7, or MEF cells were loaded with 100μg/mL10kDa fluorescein (FITC) dextran plus 100μg/mL 70kDa tetramethylrhodamine (TMR) dextran (Invitrogen) in complete DMEM at 37°C for 16 hours. After washing with 1X DPBS, dextrans were chased to lysosomes for an additional 4 hours at 37°C in phenol red-free complete DMEM. Live time lapse images were captured via spinning disk microscopy with LLOMe added on the stage after 2 minutes (Figure S1) or still images were collected following 2-hour treatment courses (Figure S7). Change in cellular FITC fluorescence over time was plotted relative to initial cellular FITC intensity, relative to TMR (Figure S1) or ratio of FITC:TMR dextran was reported within TMR ROIs (Figure S7).

Em-Rab7 Live Imaging of Late Endosomes versus Lysosomes

Stable Em-Rab7^{WT} NRK cells were loaded with 5μg/mL DQ-BSA (Invitrogen) in complete DMEM at 37°C for 16 hours. The following morning, cells were washed with 1X DPBS and chased for 4 hours in complete DMEM at 37°C. DQ-loaded Em-Rab7^{WT} were then imaged at 37°C with spinning disk confocal microscopy, with DMSO or 1mM LLOMe added live on the stage.

pH Collapse of Late Endosomes versus Lysosomes

NRK cells were loaded with 5μg/mL DQ-BSA (Invitrogen) in complete DMEM at 37°C for 16 hours. The following morning, cells were washed with 1X DPBS and then loaded with 100μg/mL10kDa Oregon Green dextran (OGdex) for 2 hours. Following 2-hour OGdex loading, cells were washed with 1X DPBS and replaced with complete

phenol-red free DMEM and imaged with spinning disk confocal microscopy. DMSO or 1mM LLOMe was added live on the stage during movie acquisition.

Dextran tubulation

For Figure 3 F,J and Figure 6 J, MEFs nucleofected with Em-Rab7^{WT} or Em-Rab7^{Q67L} were loaded with 100µg/mL10kDa tetramethylrhodamine (TMR) dextran for 2 hours. After washing with sterile 1X DPBS, the medium was replaced with phenol red-free complete DMEM supplemented with DMSO or 1mM LLOMe for 30 minutes, 20mM NH_4Cl for 20mins, or 200nM BafA1 for 1 hour at 37°C. Still images of dynamic tubules were then captured by live confocal microscopy (Nikon Ti2-E with AX-R) immediately following recovery.

For Figure 3 I, MEFs were loaded with 5µg/mL DQ-BSA in complete DMEM at 37°C for 16 hours. The following day, after washing with sterile 1X DPBS, DQ-BSA were chased for 2 hours in phenol red-free complete DMEM at 37°C. Following chase, cells were then loaded with 100µg/mL10kDa fluorescein (FITC) dextran for 30 minutes. FITC dextran was not chased and imaged immediately after washing and replacement with fresh pre-warmed phenol-red free complete DMEM. Live time lapse images were captured via spinning disk microscopy as described with LLOMe added on the stage after 2 minutes.

Magic Red-Cathepsin B

For use of Magic Red Cathepsin-B (MR-B) (ImmunoChemistry Technologies), MR-B stock was prepared as described in manufacturer's protocol and diluted 1:1000 in complete DMEM. Cells were incubated with dilute MR-B for 20 minutes at 37°C. Cells were then sufficiently washed three times with 1X DPBS and replaced with fresh complete phenol red-free DMEM. MR-B loaded cells were equilibrated by incubation at 37°C for 5

minutes prior to spinning disk confocal microscopy. Change in cellular MR-B fluorescence over time was plotted relative to initial intensity.

Western blotting

Samples containing 1.2X Sample Buffer (Genscript) were separated via SDS-PAGE using 4-12% Bis-Tris (Genscript) in 1X MES Running Buffer (Genscript) according to manufacturer's instructions. Protein was transferred to nitrocellulose membranes (Bio-Rad) using the high molecular weight program of the Trans-Blot Turbo Transfer system (Bio-Rad) according to manufacturer's instructions. Blocking was performed for 1 hour at room temperature with 100% LI-COR Odyssey Blocking Buffer. Primary antibody incubation (4°C, 16 hours) and secondary antibody incubations (22°C, 1 hour) were performed in 50% Odyssey Blocking Buffer/50% TBS + 0.1% Tween-20. Washes were conducted following primary and secondary incubations, 3 times 10 minutes, with excess TBS + 0.1% Tween-20. Blots were visualized and captured using the LI-COR Odyssey CL-X imaging system with LI-COR ImageStudio software. Densitometry analyses were performed using ImageStudio software.

Rab7 activity assays

Preparation of bead conjugated GST-fusion proteins and GST-RILP based pulldown assays were performed as described in (Romero Rosales et al., 2009). GST fusion proteins (GST-stop and GST-RILP) were transformed and isolated from BL21 *E.coli* and conjugated to Pierce Superflow GST agarose (Thermo Scientific). To probe for Rab7-GTP, COS-7 cells expressing Em-Rab7^{WT} were treated with DMSO or 1mM LLOMe for 1 hour. Cells were collected by scraping in 1mL PBS containing Complete EDTA-free Protease Inhibitor (Roche) and pelleted. Cell pellets were resuspended in 200µL of GST Pulldown Buffer [20mM HEPES pH 7.4, 100mM NaCl, 5mM $MgCl_2$, 1% TX-100, Roche

Complete Protease Inhibitors] and incubated on ice for 15 minutes. Samples were then spun at 14,000rpm for 15 minutes at 4°C. Supernatant was collected in a clean tube and quantitated using Micro-BCA Protein Assay Kit. Excess GST-stop and GST-RILP bound beads (150µg per reaction) were pre-equilibrated in GST Pulldown Buffer. 50µg of input lysates were added to pre-equilibrated beads and rotated for 16 hours at 4°C. Beads were then washed four times with GST Pulldown Buffer and re-suspended in 35µL of 1.2X Sample Buffer before visualization by SDS-PAGE and Western blotting for GFP and GST. 5% inputs were loaded in parallel. GST-RILP pulldowns of Em-Rab7^{WT} were normalized to input levels of Em-Rab7^{WT}.

Em-Rab7 Fluorescence Recovery After Photobleaching (FRAP)

Stable Em-Rab7^{WT} or Em-Rab7^{L8A} NRK cells were imaged live at 37°C in complete phenol red-free DMEM using the Nikon Ti2-E inverted microscope with AX-R confocal microscopy system and Nikon elements software. To generate FRAP movies, images were collected for one minute prior to bleaching at 1 frame per 10 seconds using the AX-R resonant scanner. To bleach Em-Rab7+ endosomes/lysosomes, a 33.0625µm^2 area was bleached for 10 seconds using the 488-laser line (laser power = 15) and the AX-R galvano scanner. Images were then collected post-bleach for 4 minutes, at 1 frame per 10 seconds, using the AX-R resonant scanner. All movies were processed identically following collection using Nikon Elements Denoising.ai and subsequent histogram matching bleach correction in FIJI.

siRNA Knockdown of Rab7

NRK or stable EmRab7^{L8A} expressing NRK cells were lipofected using Lipofectamine 2000 with empty mCherry plasmid and siRNA targeting either a non-targeted sequence (5′-UGGUUUACAUGUCGACUAA, Dharmacon #D-001810-01-05) or

rat Rab7 (5′-GACCAAGAACACACACGUA, Dharmacon #J-089334-10-0010). After 1 hour of exposure to complexes, medium containing complexes was exchanged for complete DMEM medium. Knockdown was allowed to progress for 4 days prior to either fixation or FRAP analyses. To quantify degree of knockdown, equivalent numbers of mCherry- and mCherry+ cells were selected from each field and measured for fluorescence intensity in FIJI. Raw intensity values were divided by the cell area to provide fluorescence/unit area values, which were then normalized to the mean of the mCherry- group.

Starvation Experiments

For starvation experiments, COS-7 cells plated on coverslips were transfected with either pmRFP-LC3 or HA-V_1G_1. 24h post-transfection, cells were washed 1X with sterile 1X-DPBS then replaced with either complete DMEM medium or EBSS (Sigma #E2888). 20 hours post medium replacement, wells designated in the Torin-1 treatment arm were replaced with fresh complete medium containing 1μM Torin-1 (Sigma #475991), and treated for 4 hours. Following 4-hour treatment, all wells were fixed and the HA-V_1G_1 transfected cells were immunostained for endogenous Rab7. 24-hour EBSS and 4-hour Torin-1 treatments were selected due to their ability to produce expected responses in pmRFP-LC3.

Image and Statistical Analyses

All statistical analyses were performed using either R Studio or Prism 9 software. All assumptions were deemed to be met before a selection of a statistical test. Normality of residuals was tested using the Shapiro-Wilk test. Specific tests used are denoted in figure legends and statistical significance was defined as a p value < 0.05. All t-tests conducted were unpaired and two-tailed unless otherwise stated. All image analysis was

conducted with either Bitplane Imaris 9.3.1 or FIJI (NIH). There were no exclusion criteria. Any specific randomization and blinding is reported below.

Quantification of Rab7 compartment volume and area: Due to a mix of puncta and apparent cytosolic distributions of Rab7, the surface generation tool in Bitplane Imaris 9.3.1 were utilized to define Rab7 compartments. Rab7 surfaces >0μm^2 and <30μm^2 or >0μm^3 and <5μm^3 were filtered for 2-D area calculations and 3-D volumetric analyses, respectively, which eliminated the cytosolic pool and heavily clustered compartments. We confirmed that area and volume bounds filtered the same population of compartments. The number of compartments per cell, average surface size, and average surface fluorescence intensity per unit area for the entire field were reported.

Quantification of Airyscan endosomal marker colocalization: Two marker colocalization was determined using the colocalization function in Bitplane Imaris 9.3.1. Images were equivalently thresholded before determining Pearson's and Mander's correlation coefficients.

Quantification of time-lapse changes in Em-Rab7 area: Em-Rab7 objects and DQ-BSA objects were defined across all timepoints using the region-growing object generation tool in Imaris 9.3.1. Equivalent thresholds were used for creation of DQ*hi* and DQ*lo* objects across movies and conditions, within each replicate, based on an average intensity of a sample of DQ objects. Em-Rab7 objects were then filtered into DQ*lo* and DQ*hi* compartments based on colocalization with created DQ-BSA objects. The average Em-Rab7 object area per field of view was then extracted for each time point and fitted using R-studio. N= 10 (DMSO) and 9 (LLOMe) fields of view from 3 independent experiments.

Quantification of fluorescent dextran de-quenching: De-quenching of total cellular Fluorescein (FITC) following LLOMe treatment (as in Figure S1A-C) was determined using Imaris. Whole cell regions of interest were denoted and cropped. FITC dextran objects were then created using the region-growing object generation tool. The average FITC object fluorescence intensity at each time point for each cell was then extracted and normalized to the first frame. Cumulative averages of all movies for each condition were then plotted over time using Prism. De-quenching of Oregon Green dextran (OGdex) fluorescence (as in Figure 5) was determined using FIJI. Images were first processed using a median filter with a radius of 2 pixels. A binary mask of Oregon Green compartments was created and added to the ROI manager partitioned as individual objects for single frames 2 minutes prior and 3 minutes following DMSO or LLOMe addition. Fluorescence intensities of Oregon Green and DQ-BSA were measured within each ROI at each time point. ROIs were then filtered into DQ*lo* and DQ*hi* compartments (threshold= 10,000 a.u., determined by random sampling of apparent DQ*lo/negative* compartments by eye) and Oregon Green fluorescence was compared within each DQ filtered group using a paired t-test between pre- and post-treatment time points.

Quantification of ALIX+ LEs and LYS: Total ALIX puncta and colocalization of ALIX puncta with Rab7 and CatB was determined using the region-growing object generation tool in Imaris 9.3.1. Individual objects were created for each ALIX, Rab7 and CatB compartment. MatLab dual and triple object colocalization Imaris plugins were utilized to determine colocalized objects with overlapping radius= 1μm. Colocalization is expressed as the percentage of total Rab7 only, CatB only, or Rab7/CatB dual positive objects that colocalize with an ALIX object.

Quantification of ALIX responsiveness in BAPTA-AM: ALIX puncta and intensity in the presence or absence of Ca^{2+} chelation was quantitated using FIJI. Images were first processed using a median filter with a radius of 2 pixels. A binary mask of ALIX space was created in FIJI and applied to the original image as ROIs. The number of ROIs and average measured intensity of the ROIs were then extracted and reported.

Quantification of HA-V_1G_1 compartments: HA-V_1G_1 puncta number, intensity, and area was calculated using FIJI. All images were first processed using a median filter with a radius of 2 pixels. To determine HA-V_1G_1 intensity on endogenous Rab7 space (Figure 7B, Figure S8E-F), a binary mask of Rab7 area was first created. The mask was refined by then eliminating the nucleus and highly clustered Rab7 perinuclear regions which are non-permissive to distinguishing individual compartments. The refined binary mask was applied to the original image as individual ROIs and the fluorescence intensity of HA-V_1G_1 was then measured. Measured HA-V_1G_1 intensity was then normalized to the Rab7 ROI area and reported. To determine the HA-V_1G_1 puncta number and area (as in Figure 7E-F, Figure S7D-E, Figure S8C-D), a binary mask of HA-V_1G_1 was created and similarly refined by eliminating the nuclear and highly clustered perinuclear regions. The mask was then applied to the original image as individual ROIs and the total number and area of individual ROIs was determined. The number and average area of all HA-V_1G_1 ROIs was then reported. In starvation experiments specifically, we only selected cells with responsive V1G1 cells to analyze for Rab7 changes, as the starvation response was not homogenous (~50% of transfected cells).

FRAP Quantification: FRAP movies were equivalently processed using Nikon Elements Denoising.ai followed by Histogram Matching bleach corrections in FIJI. Using FIJI, the fluorescence intensity over time within the bleached area and an equivalently sized ROI control area was measured. Measurements within the bleached area were affinely scaled by subtracting the minimum intensity within the bleached area intensity from the bleached and control area intensity. Average intensity values at each time point were then plotted. FRAP recovery curves, starting at t= 70s, were fitted using least squares fit, with a one-phase exponential association equation in Prism. $t_{1/2}$ and plateau values of fitted lines only were reported. Y_{max} values were calculated as the intensity of the bleached area at t = 300s, and compared across conditions using an ordinary One-Way ANOVA.

Rab7 Tubulation Quantification: Em-Rab7 tubulation in MEFs was quantified manually in FIJI. Images across conditions were randomized and blinded. Tubules were manually traced using the line tool in FIJI using the Rab7 channel, and confirmed to contain dextran prior to addition to the ROI manager. Tubules were explicitly defined as lighter linear membrane extensions emanating from a darker source endosome. Homogenous streaks were not counted due to the possibility of these being highly motile compartments. Total tubule ROIs from each cell were then measured for their length. The number and average length per cell was then reported.

Quantification of CI-M6PR Puncta and Distribution: CI-M6PR puncta number and Rab7 intensity were quantified in FIJI. The CI-M6PR channel for all images was first processed using a median filter with a radius of 2 pixels, then masked. To determine the number of CI-M6PR compartments, the mask was refined to eliminate the nuclear and highly clustered perinuclear regions which are non-permissive to distinguishing individual compartments. The number of remaining individual CI-M6PR ROIs was then counted and reported. To determine the intensity of Rab7 on CI-M6PR space, the unrefined CI-M6PR mask was applied to the un-processed Rab7 channel and the fluorescence intensity of Rab7 was measured. The average Rab7 intensity across ROIs was then calculated for each cell, and subsequently divided by the total CI-M6PR area to provide a value of Average Rab7 intensity per unit CI-M6PR area.

To determine peripheralization of CI-M6PR in WT- or Q67L- COS-7 cells (Figure 3N) or EEA1 (Figure S2 E-F), we utilized an ImageJ plugin to measure the distance to the nucleus, and intensity of CI-M6PR compartments. Distances were binned into the perinuclear area (closest 33%) and peripheral area (distal 66%). In brief, equivalently transfected cells were selected, the nucleus and outer edge of the cell was manually annotated based on phalloidin staining, and a Euclidian distance map was created from the nucleus to the outer edge. Then, using a duplicate of the CI-M6PR or EEA1 channel, compartments were defined via thresholding and added to the region of interest manager, before being added back to the source CI-M6PR or EEA1 channel and the Euclidian distance map to measure intensity and distance values for each object, respectively.

Using R, objects were then binned according to distance and the total intensity of objects within each bin was determined.

3.3 Results

LLOMe disrupts lysosomes in NRK cells leading to expected LMP responses

In order to ask if and how endosomal organelles upstream of lysosomes were impacted in LMP, we treated normal rat kidney cells (NRK) and primary mouse embryonic fibroblasts (MEFs) with LLOMe. We first determined if these cells responded to LLOMe as previously described for other cell lines. We focused on key LMP responses including pH neutralization, direct membrane repair processes (i.e., ESCRT), and lysophagy (i.e., Gal3). We found each of these to occur in our cell lines, as pH-sensitive dextrans were de-quenched (pH neutralization, **Figure S1A-C**), ALIX was recruited following short LLOMe exposures (direct membrane repair, **Figure S1D-E**, performed in MEFs due to antibody), and Gal-3 was recruited following long exposures (**Figure S1 F-G**). To further observe the kinetics of minimal LMP events, we loaded cells with Magic-Red Cathepsin B substrate (MR-B), a small peptide that fluoresces when cleaved by cathepsin B in degradative lysosomes. Unlike the larger dextrans, the fluorescent product of MR-B proteolysis is lost from degradative compartments in LLOMe indicating the presence of minimal LMP (**Figure S2A-D**, NRKs).

Having established that LLOMe drives LMP as expected in NRK and MEF cells, we used a multi-marker immunostaining approach to ask whether LMP affected biosynthetic organelles [cis-Golgi and trans-Golgi Network (TGN), early (EE) and late (LE) endosomes] upstream of lysosomes (LYS). LLOMe treatment did not disrupt Golgi stacks, as markers for both the cis-Golgi (GM130) and trans-Golgi network (TGN38) were not altered (**Figure 1A-B**). The appearance of EEs, marked by EEA1, was mildly, though not significantly ($p= 0.0779$), peripheralized in LLOMe (**Figure 1C**, **FigureS2 E-**

F). In contrast, we observed marked changes in Rab7 staining, a canonical LE protein, after 1 hour of LLOMe treatment (**Figure 1D**), as compared to DMSO controls.

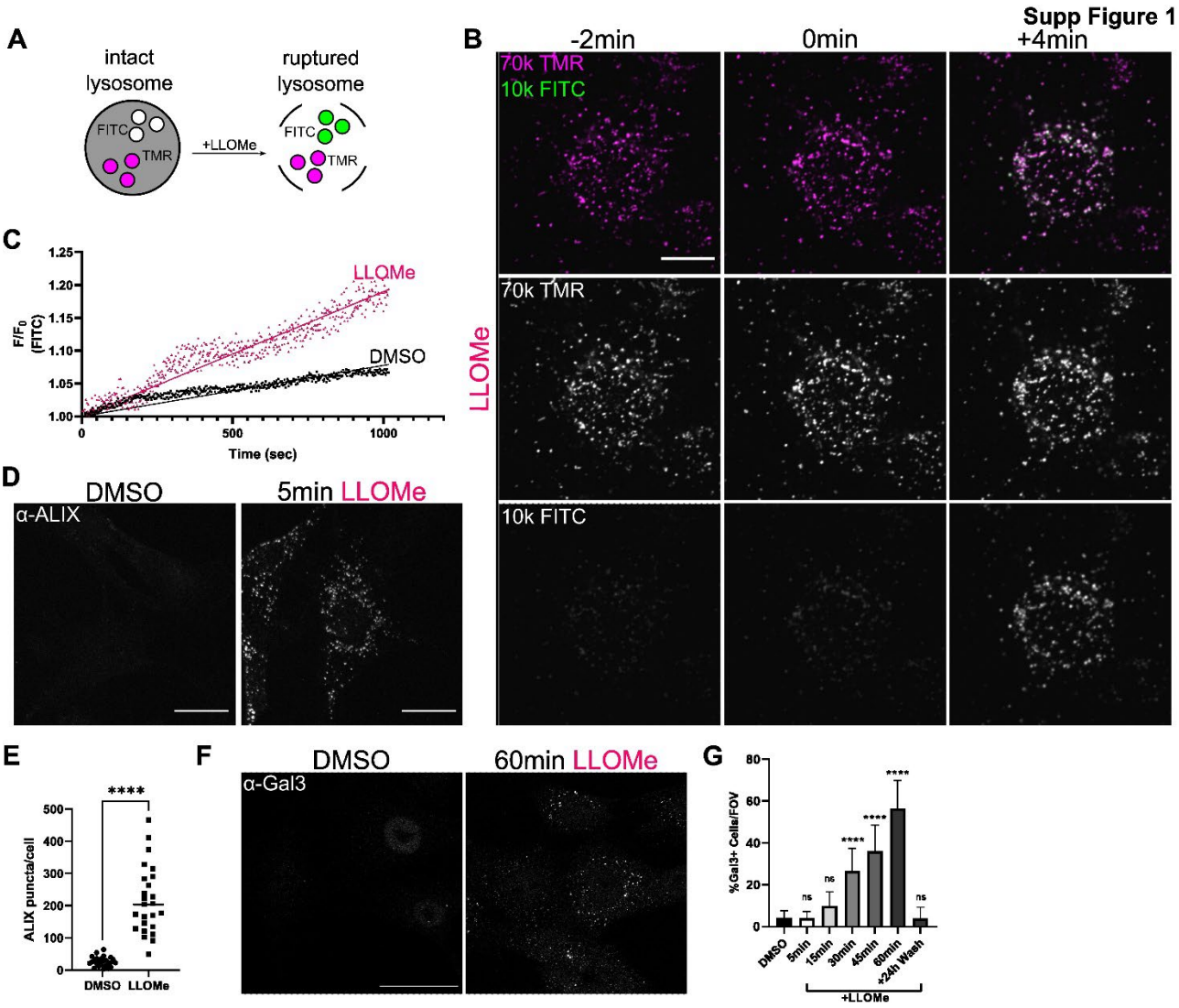

Supplementary Figure 1 LLOMe disrupts organelles leading to pH collapse, membrane repair, and lysophagy in NRK and MEF cells

(A) Schematic of pH dextran experiment: lysosomes were dually loaded with 100µg/mL pH-sensitive 10kDa FITC-dextran and pH-insensitive 70kDa TMR-dextran. Lysosomal disruption with LLOMe de-quenches FITC fluorescence. **(B)** Representative time-lapse images of NRK cells loaded with dual dextrans and exposed to 1mM LLOMe at t=0 min (scale=10µm). **(C)** Change in FITC fluorescence of the experiment in (B) quantified over time and fitted linearly (n=9 movies per condition from 3 independent experiments, see Video 1)**. (D)** Primary mouse embryonic fibroblasts (MEFs) treated with vehicle (DMSO) or 1mM LLOMe for 5 minutes were immunostained for ESCRT-associated protein ALIX (scale=25µm). **(E)** Number of ALIX puncta per cell were quantified and compared using Welch's t-test (n= 24 field of view (FOV) from 3 independent experiments, line = median, ****p<0.0001). **(F)** NRK cells were treated with vehicle (DMSO) or 1mM LLOMe for one hour and immunostained for galectin-3 (Gal3) (scale= 25µm). **(G)** The percentage of Gal3+ cells per field of view were quantified over time. A washout condition was included to show that cells will clear damaged lysosomes in NRK cells, similar to what is reported for other cell lines. LLOMe-treated time points were compared to vehicle (DMSO) using One-Way ANOVA (n= 30 FOV per condition from 3 independent experiments, n.s. = not significant, *p<0.05, **p<0.01, ***p<0.001, ****p<0.0001. Error bars indicate Mean± SEM).

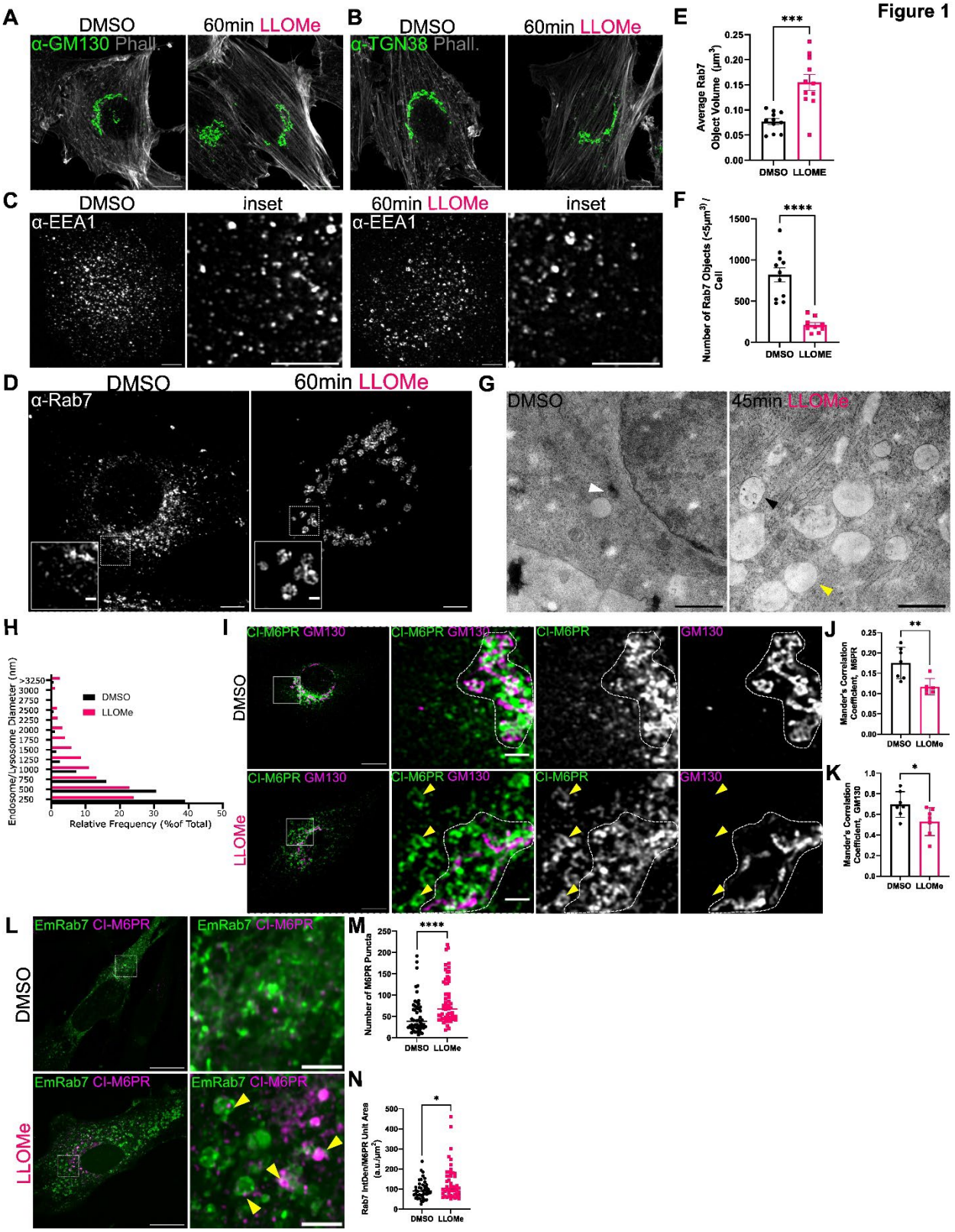
A
DMSO
60min LLOMe
α-GM130 Phall.
B
DMSO
60min LLOMe
α-TGN38 Phall.
E
***
Average Rab7 Object Volume (μm³)
DMSO LLOME
C
DMSO
inset
60min LLOMe
inset
α-EEA1
F
****
Number of Rab7 Objects (<5μm³) / Cell
DMSO LLOME
D
DMSO
60min LLOMe
α-Rab7
G
DMSO
45min LLOMe
H
Endosome/Lysosome Diameter (nm)
DMSO
LLOMe
Relative Frequency (%of Total)
I
Cl-M6PR GM130
Cl-M6PR
GM130
DMSO
LLOMe
J
**
Mander's Correlation Coefficient, M6PR
K
*
Mander's Correlation Coefficient, GM130
L
EmRab7 Cl-M6PR
DMSO
LLOMe
M
****
Number of M6PR Puncta
N
*
Rab7 IntDen/M6PR Unit Area (a.u./μm²)

Figure 1

Figure 1 LLOMe treatments perturbs upstream Rab7-positive endosomes and M6PR-trafficking

(A-C) Normal rat kidney cells (NRK) were treated with DMSO or LLOMe (1mM, 1h)_and immunostained for (A) GM130 (cis-Golgi), (B) TGN38 (trans-Golgi network), and (C) early endosome antigen 1 (EEA1) (early endosomes) and imaged by Airyscan microscopy (scale= 5μm). Phalloidin staining is in white in A and B. **(D)** NRK were immunostained for Rab7 following DMSO or LLOMe (1mM, 1h) treatment (scale= 5μm, inset = 1μm) and imaged by Airyscan microscopy. Average Rab7 object volume **(E)** and number **(F)** per cell were determined and compared using Mann-Whitney-U (n= 55 cells, 3 independent experiments, ***p<0.001, ****p<0.0001, error bars= mean±SEM) **(G)** Representative transmission electron micrographs (TEM) of DMSO- and LLOMe-treated NRK cells (70nm sections, scale=2μm, n= 2 experiments). Highly electron-dense vesicle (lysosome), indicated with white arrowhead in DMSO (*left*). Single membraned, enlarged, lucent structures with (black) and without (yellow) luminal contents indicated in LLOMe (*right*). Additional examples in FigureS3. **(H)** Relative frequency distribution of TEM diameters in DMSO and LLOMe, binned by 250nm (n=275(DMSO)/546(LLOMe) endosomes/lysosomes from 2 independent experiments) **(I)** NRK cells were immunostained for endogenous CI-M6PR (green) and GM130 (magenta) following DMSO or LLOMe (1mM, 1h) treatment (scale= 5μm, inset = 1μm), and imaged with Airyscan microscopy. GM130-positive Golgi area (dotted outline), peripherally mis-localized CI-M6PR (yellow arrowheads). **(J)** Mander's correlation coefficients (MCC) for CI-M6PR intensity on GM130 space, and **(K)** GM130 intensity on CI-M6PR space compared using student's t-test (n= 10 field of view (FOV), 3 independent experiments, *p<0.05, **p<0.01, error bars= mean±SD). **(L)** Confocal micrographs of primary MEFs transfected with Em-Rab7^{WT} and treated with either DMSO or LLOMe (1mM, 1hr) were fixed and stained for endogenous CI-M6PR (scale= 20μm, inset = 3μm). **(M)** Quantification of the total number of CI-M6PR puncta in (L). **(N)** Quantification of the intensity of Em-Rab7^{WT} signal on masked CI-M6PR area in (L). For M-N, conditions were compared using Mann-Whitney-U (n= 40 transfected cells per condition, 3 independent experiments) (*p<0.05, ****p<0.0001, lines = medians).

The apparent volume of individual Rab7 compartments was increased whereas the total number of compartments was decreased in LLOMe (**Figure 1E-F**). Staining was often punctate but seemed to decorate the edge of an enlarged compartment. Due to this discontinuous appearance, we wondered whether these were single compartments or clustering of smaller vesicles. Therefore, we performed ultrastructural analysis using transmission electron microscopy (TEM). TEM revealed the presence of numerous single-membraned vacuolar-like structures in LLOMe, rather than clusters of small vesicles (**Figure 1G**), confirming our interpretation of singular enlarged Rab7-positive compartments. Further, measurements of the diameter of endosomes and lysosomes in electron micrographs revealed a shift toward larger structures in LLOMe (**Figure 1H, Figure S3A**). Whereas in DMSO conditions, the presence of enlarged endosomes was rare (**Figure S3B**), in LLOMe conditions there were frequent examples of structures that are highly lucent (**Figure 1G**, *yellow*, **Figure S3C,F**) and those with

dense, observable material within the lumen (**Figure 1G**, *black*, **Figure S3D**), suggesting that not all of the enlarged compartments are lysosomes. In keeping with this, we also observed double-membraned structures likely to be autophagosomes (**Figure S3E**).

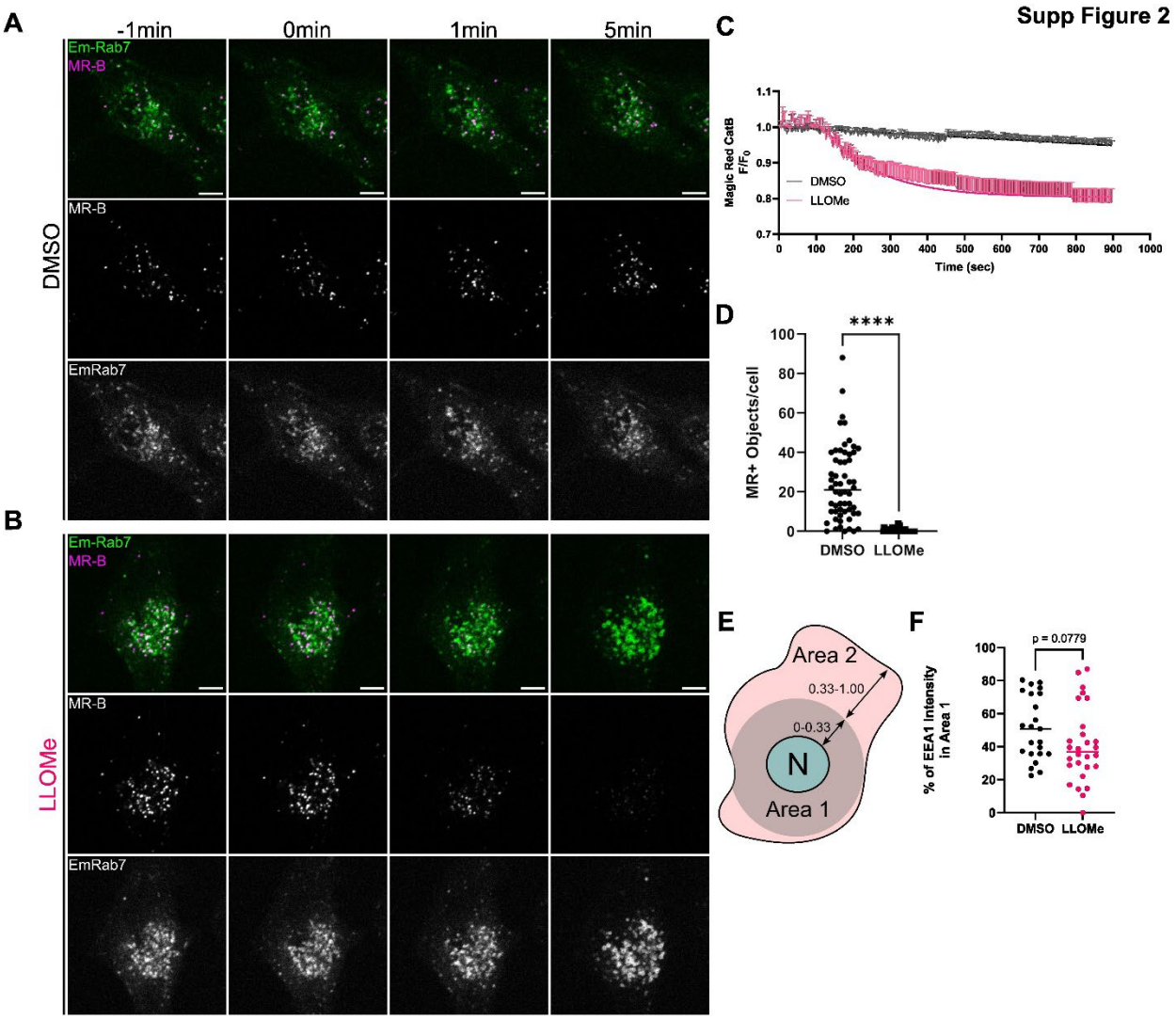

Supplemental Figure 2 Degradative Rab7+ lysosomes leak luminal peptides in LLOMe

Live imaging of EmRab7^{WT}-transfected NRK cells loaded with the cathepsin-B substrate MR-B for 20 minutes and treated with vehicle (DMSO) **(A)** or 1mM LLOMe **(B)** (scale= 5μm). The small dipeptide leaks out of degradative Em-Rab7+ lysosomes, which is quantified over time via non-linear one phase decay equation in **(C)** (n= 9 movies per condition from 3 independent experiments). **(D)** MR-B puncta number in EmRab7^{WT}-transfected NRK cells collected as still images prior to and following 5-minute LLOMe treatment (1mM), quantified in FIJI, and compared using Welch's t-test (*p<0.0001) (n=58 (DMSO) and 59 (LLOMe) cells captured live from 2 independent experiments, line = median). **(E)** Schematic of EEA1 objects binned into the perinuclear Area 1 (first 33% of cell area) and peripheral Area 2 (outer 66% of cell area), and measured for intensity of EEA1 in Area 1 **(F)** Percentage of total cellular EEA1 intensity in Area 1 was compared using unpaired two-tailed student's t-test (p =0.0779) (n=23 (DMSO) and 29 (LLOMe 1mM, 1h) cells from 9 Airyscan micrographs per condition, line = median).

Supp Figure 3

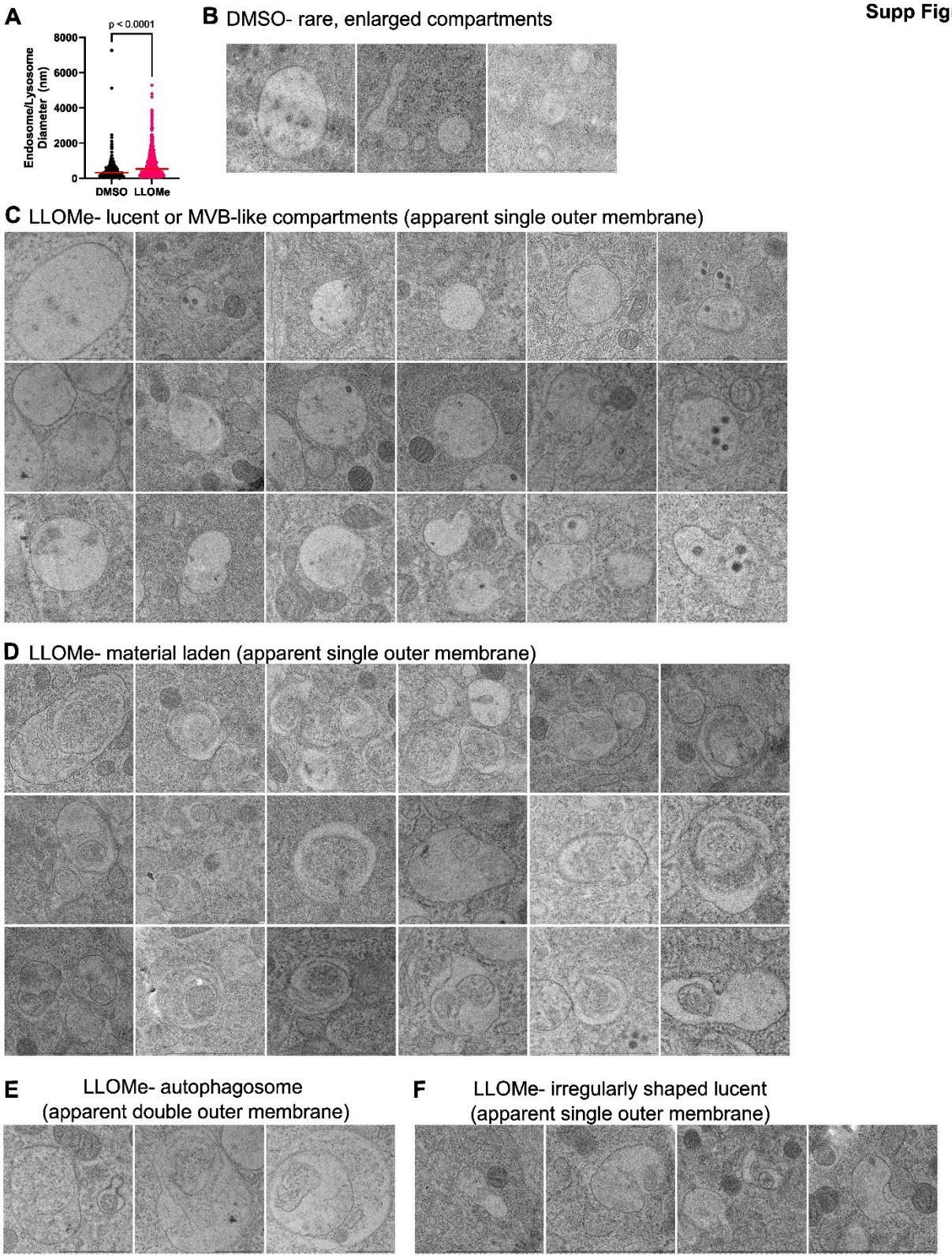

Supplemental Figure 3 Electron microscopy demonstrates a variety of altered endo-lysosomal compartments in LLOMe

(A) Endosomal/lysosomal diameters in NRK cells treated with DMSO or 1mM LLOMe for 45min, measured manually on electron micrographs and compared using Mann-Whitney U test (n =275 (DMSO)/546(LLOMe) endosome/lysosomes from 2 independent experiments, ****p<0.0001, line = median). **(B)** Rare examples of enlarged compartments observed in DMSO conditions. **(C)** Numerous examples of frequently observed single membraned, lucent compartments in LLOMe, containing intraluminal vesicles (see also Fig.1G, yellow arrow). **(D)** Numerous examples of frequently observed single membraned, material laden compartments, containing apparent organelles, membranes and dense material (scale bars = 1 μm). **(E)** Examples of occasionally observed double membraned compartments, most likely to be autophagosomes (scale bars = 1 μm). **(F)** Examples of occasional irregularly shaped, single membraned, and lucent compartments (scale bars = 1 μm).

Since Rab7 compartments were enlarged in LLOMe, we wondered if the localization of cation-independent mannose-6-phosophate receptor (CI-M6PR), which traffics lysosomal cathepsins from the Golgi to endosomes but then recycles back from LEs to the TGN, was also disturbed. In control cells, we observed strong perinuclear colocalization between CI-M6PR and GM130, as expected. In contrast, CI-M6PR mis-localized in enlarged, more peripheral compartments in LLOMe (**Figure 1I**) and co-localized less with GM130 (**Figure 1J,K**). To test if these compartments were Rab7-positive, we expressed Emerald-Rab7^{WT} (Em-Rab7^{WT}) in primary MEFs and immunostained for endogenous CI-M6PR. The peripheralized compartments containing mis-localized CI-M6PR were largely Rab7-positive (**Figure 1L**; *yellow arrowheads*). Furthermore, peripheral CI-M6PR compartments were more abundant (**Figure 1M**) and had more Rab7 on them, as compared to controls (**Figure 1N**). Together, these results show that LLOMe-induced perturbation leads to rapid responses in Rab7+ compartments that retain CI-M6PR.

Late endosomes rapidly respond to LLOMe.

Given that Rab7 is present on multiple endosomal compartments, including transitioning EEs, LEs, and LYS, we investigated the identity of the LLOMe-responsive Rab7 compartments. We have previously distinguished EEs, LEs and LYS on the basis of multi-marker immunostaining and degradative capacity (Yap et al., 2018). We distinguish EEs from LEs based on the presence of EEA1, and LEs from LYS on the basis of degradative capacity, where LEs are degradatively (CatB or DQ-BSA) low and

LYS are degradatively high (**Figure 2A**). As compared to controls, transitioning EE-LEs (EEA1+Rab7+) in LLOMe-treated cells were not disrupted (**Figure S4A-C**), despite the mild alterations in EE distribution (**Figure 1C**, **Figure S2E-F**). Interestingly, however, both LEs (Rab7+CatB*lo*: white arrowhead) and LYS (Rab7+CatB*hi:* yellow arrowhead) were enlarged following LLOMe treatment (**Figure 2B**), consistent with our previous ultrastructural observations (**Figure 1G**, **Figure S3**). The co-localization of CatB with Rab7 was not changed (**Figure 2C**) whereas LAMP1 staining was mildly enriched on Rab7 compartments following LLOMe treatment (**Figure 2D**). LLOMe thus leads to phenotypic alterations in both LEs and LYS but not in transitioning EE-LEs. In order to determine the kinetics of Rab7+ responses to LLOMe, we carried out live imaging of NRK cells stably expressing Em-Rab7^{WT}. We used DQ-BSA to distinguish degradative Rab7+ LYS from lowly degradative Rab7+ LEs. The apparent area of both LEs (Rab7+DQ*lo)* and LYS (Rab7+DQ*hi)* rapidly increased following LLOMe exposure (**Figure 2E-I**, **Figure S4D**). These compartments continued to increase in size over the course of thirty minutes, but a significant size increase was apparent in less than ten (**Figure 2G,I**). Interestingly, the Em-Rab7 signal expanded on both LEs and LYS with LLOMe, but the DQ-BSA within degradative LYS appeared contained within a subdomain of the enlarging LYS and did not fill the whole lumen. Similarly, endogenous CatB staining also often occupied only a subdomain within enlarged Rab7+ lysosomes (**Figure 2B**). These data show that Rab7+ LEs are novel upstream responders to LLOMe.

Figure 2 (*next page*) Rab7-positive late endosomes rapidly respond to LLOMe.

(A) Definitions of late endosomes (LE) versus lysosomes (LYS). Both are positive for Rab7 (cyan) and lysosomal associated membrane protein 1 (LAMP1) (yellow) but differ on degradative ability (CatB*lo*/DQ-BSA*lo* versus CatB*hi*/DQ-BSA*hi*, magenta). **(B)** NRK cells were immunostained for Rab7, LAMP1, and lysosomal hydrolase cathepsin B (CatB) following DMSO or LLOMe (1mM, 1h) treatment (scale= 5µm, inset = 2µm) and imaged by Airyscan microscopy. Representative LE (white arrowhead) and LYS (yellow arrowhead) are indicated. MCC for CatB on Rab7 space ($p = 0.1708$) **(C),** and LAMP1 on Rab7 space ($p = 0.0251$) **(D)** were determined and compared using student's t-test (n= 10 FOV per condition, 3 independent experiments, error bars= mean±SD). **(E)** EmRab7^{WT}-transfected NRK cells loaded with 5µg/mL DQ-BSA overnight, were imaged live in the presence of 1 mM LLOMe for 15mins. Still frames are shown. LEs (Rab7+DQ*lo*, white) and LYS (Rab7+DQ*hi*, yellow) are indicated. Single channel insets of a representative LE **(F)** and LYS **(H)** are shown. Mean area of DQ*lo* LEs **(G)** and DQ*hi* LYS **(I)** per cell were quantified over time (n= 10 (DMSO) and 9 (LLOMe) movies, from 3 independent experiments).

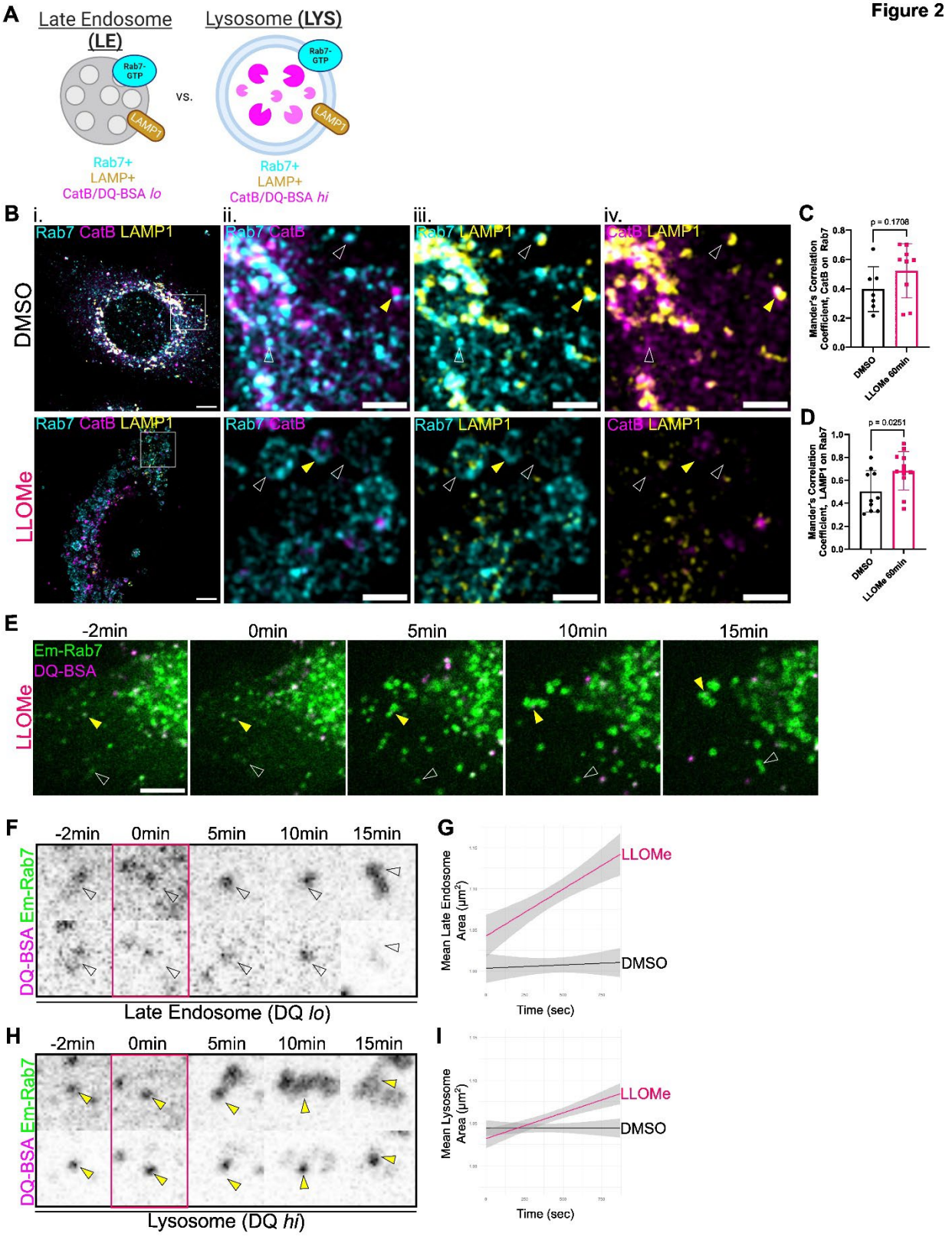
A
Late Endosome (LE)
Lysosome (LYS)
Rab7-GTP
LAMP1
vs.
Rab7+ LAMP+ CatB/DQ-BSA lo
Rab7+ LAMP+ CatB/DQ-BSA hi
B
i.
ii.
iii.
iv.
DMSO
LLOMe
Rab7 CatB LAMP1
Rab7 CatB
Rab7 LAMP1
CatB LAMP1
C
p = 0.1708
Mander's Correlation Coefficient, CatB on Rab7
DMSO
LLOMe 60min
D
p = 0.0251
Mander's Correlation Coefficient, LAMP1 on Rab7
E
-2min
0min
5min
10min
15min
Em-Rab7
DQ-BSA
F
DQ-BSA Em-Rab7
Late Endosome (DQ lo)
G
Mean Late Endosome Area (µm²)
Time (sec)
H
Lysosome (DQ hi)
I
Mean Lysosome Area (µm²)

Supp Figure 4

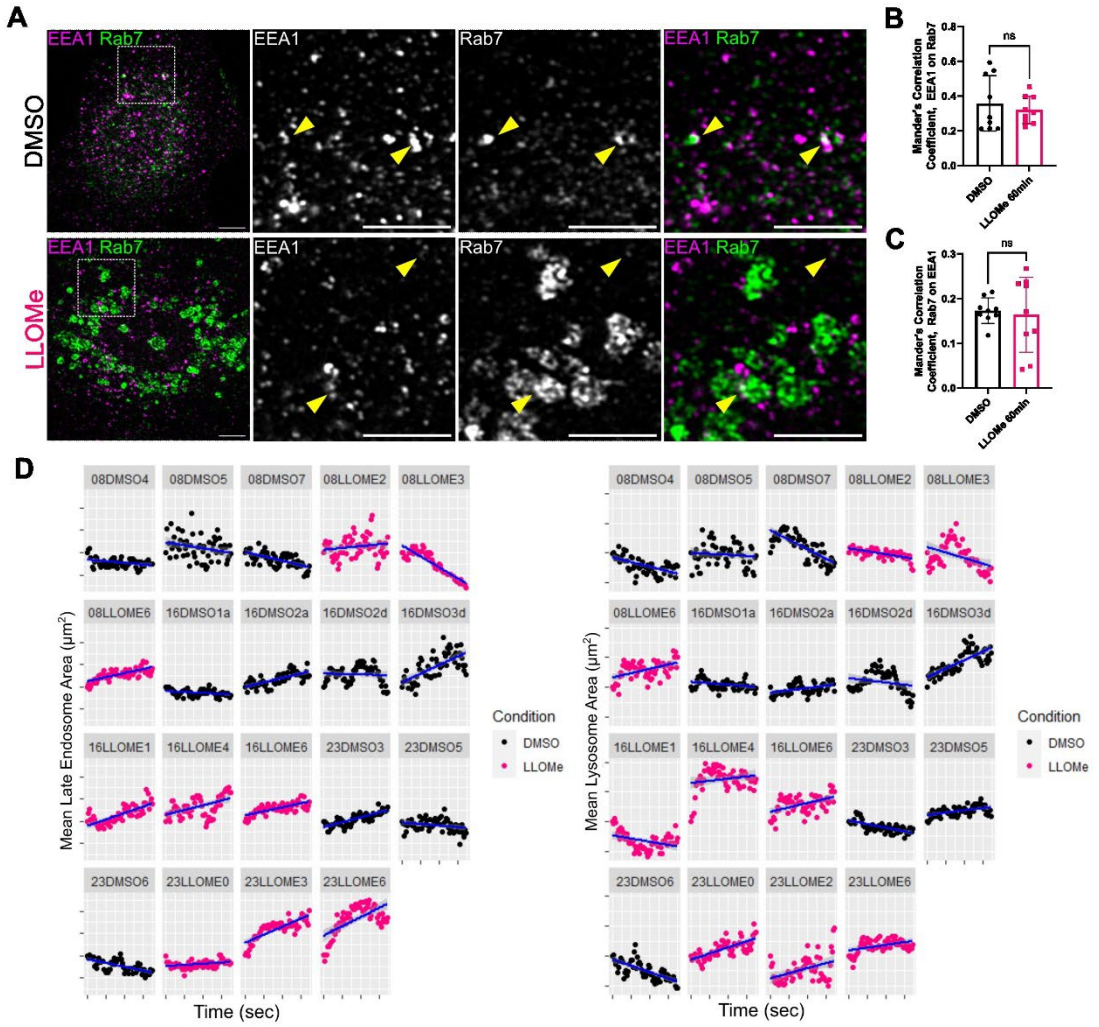

Supplemental Figure 4 Early endosomes are preserved in LLOMe

(A) Airyscan micrographs of NRK cells treated with vehicle (DMSO) or LLOMe (1mM, 1h), immunostained for Rab7 (green) and EEA1(early endosomes; magenta) and imaged by Airyscan microscopy (scale= 5µm, inset= 1µm). Yellow arrowheads point at EEA1+ Rab7+ transitioning EE/LEs which are not enlarged. Mander's correlation coefficients for **(B)** EEA1 intensity on Rab7 space (p = 0.7712) and **(C)** Rab7 intensity on EEA1 space (p= 0.5310) were calculated using Imaris and compared using unpaired two-tailed student's t-test (n= 9 FOV per condition from 3 independent experiments, Error bars = mean ± SD). **(D)** Individual live imaging traces of average cellular EmRab7^{WT} object volumes over time (blue = DMSO 10 cells; pink = LLOMe 9 cells, from 3 independent experiments). These traces were combined for statistical analysis in Fig. 2 G and I.

Rab7 is hyper-activated following LLOMe treatment

We next sought to elucidate what could lead to the changes observed in Rab7+ compartments. LLOMe-mediated Rab7+ endosome enlargement (**Figure 1**) is

reminiscent of the accumulation of constitutively active (CA) Rab7^{Q67L} on enlarged endosomes (Bucci et al., 2000). CA-Rab7 is GTP-bound, which binds strongly to effectors. Thus, we sought to test whether LLOMe alters Rab7 nucleotide binding via interaction with an immobilized effector. To do so, we expressed GFP-tagged Rab7^{WT} or GFP-CA-Rab7^{Q67L} in COS-7 cells, treated with DMSO or LLOMe, and immunoprecipitated lysates with a GST-fusion protein containing the Rab7-binding domain of RILP, to specifically capture active Rab7-GTP. GFP-CA-Rab7^{Q67L} was used as a positive control to provide the maximum possible effector binding. Lysates from LLOMe-treated cells revealed a moderate but consistent increase (20%) in bound GFP-Rab7, as compared to DMSO-treated controls (**Figure 3A-B**).

To further validate that Rab7 was hyperactivated following LLOMe, we performed fluorescence recovery after photobleaching (FRAP) experiments to observe Rab7 membrane dynamics. Active Rab7-GTP is strongly associated with endosomal membranes compared to GDP-Rab7 and previous work reported slowed exchange of CA-Rab7^{Q67L} on endosomes via FRAP (McCray et al., 2010). We carried out FRAP on Rab7+ compartments in NRK cells stably expressing Em-Rab7^{WT} following treatment with either DMSO or LLOMe for 10 minutes (**Figure 3C**). Control FRAP experiments led to 50% recovery of Rab7 fluorescence within one minute and complete recovery to pre-bleach intensity within four minutes (**Figure 3C-D**, *black line*). LLOMe treatment led to slower (**Figure 3C-D**, *pink line*) and incomplete fluorescence recovery, which was significantly different than that of controls (**Figure 3E**, *pink*). Together, these data suggest that LLOMe leads to increased GTP-bound and hyper-stabilized Rab7 on enlarged endosome/lysosomes.

A recent report demonstrated that Rab7 needs to be inactivated for some tubulation events to take place (Bhattacharya et al., 2023). Since we observe hyperactivated Rab7 after LLOMe treatment, we investigated whether tubulation of Rab7+ compartments was impacted. We loaded primary MEFs transfected with Em-Rab7^{WT} continuously with tetramethyl-rhodamine dextran (TMRdex) for 2 hours to populate all endosomal compartments and then treated with either DMSO or 1mM LLOMe for 45 minutes. Live imaging of Em-Rab7^{WT}+/TMRdex+ compartments in DMSO

revealed many tubules emanating from Rab7+ compartments (**Figure 3F**). Interestingly, the exposure to LLOMe led to a significant reduction in the number of Em-Rab7^{WT}+/TMRdex+ tubules per cell (**Figure 3F-G**). The small number of tubules still forming in LLOMe-treated conditions were shorter and had a reduced range of sizes (**Figure 3H**). To characterize acute tubule dynamics in relation to pH neutralization following LLOMe, we performed live imaging of cells loaded with DQ-BSA and FITC-dextran. DQ-BSA containing tubules collapsed within 2 minutes of LLOMe exposure, which was temporally linked to de-quenching of FITC dextran (i.e., increased luminal pH) (**Figure 3I**). These data suggest that Rab7+ tubules that contain luminal cargoes are reduced in the presence of LLOMe. Thus, these observations might explain both the CI-M6PR mis-localization and the increased Rab7 compartment size.

We next asked whether Rab7 hyper-activation alone was sufficient to lead to the observed deficits in CI-M6PR trafficking and Rab7+ endosome tubulation. To do so, we overexpressed CA-Rab7^{Q67L} and assessed endosomal tubulation in primary MEFs, and endogenous CI-M6PR distributions in COS-7 cells, respectively. Rab7^{Q67L} overexpression alone was sufficient to significantly reduce the number and length of Rab7+/TMRdex+ tubules as compared to Rab7^{WT} (**Figure 3J-L**). Similarly, Rab7^{Q67L} overexpression led to CI-M6PR mis-localization akin to LLOMe treated Rab7^{WT} cells, as CI-M6PR staining was significantly increased in the peripheral two thirds of cell areas, as compared to control (**Figure 3M-N**). Together, these data suggest that hyper-activation and hyper-stability of Rab7 on endosomes following LLOMe is sufficient to drive endosomal tubulation deficits and receptor mis-trafficking.

Figure 3

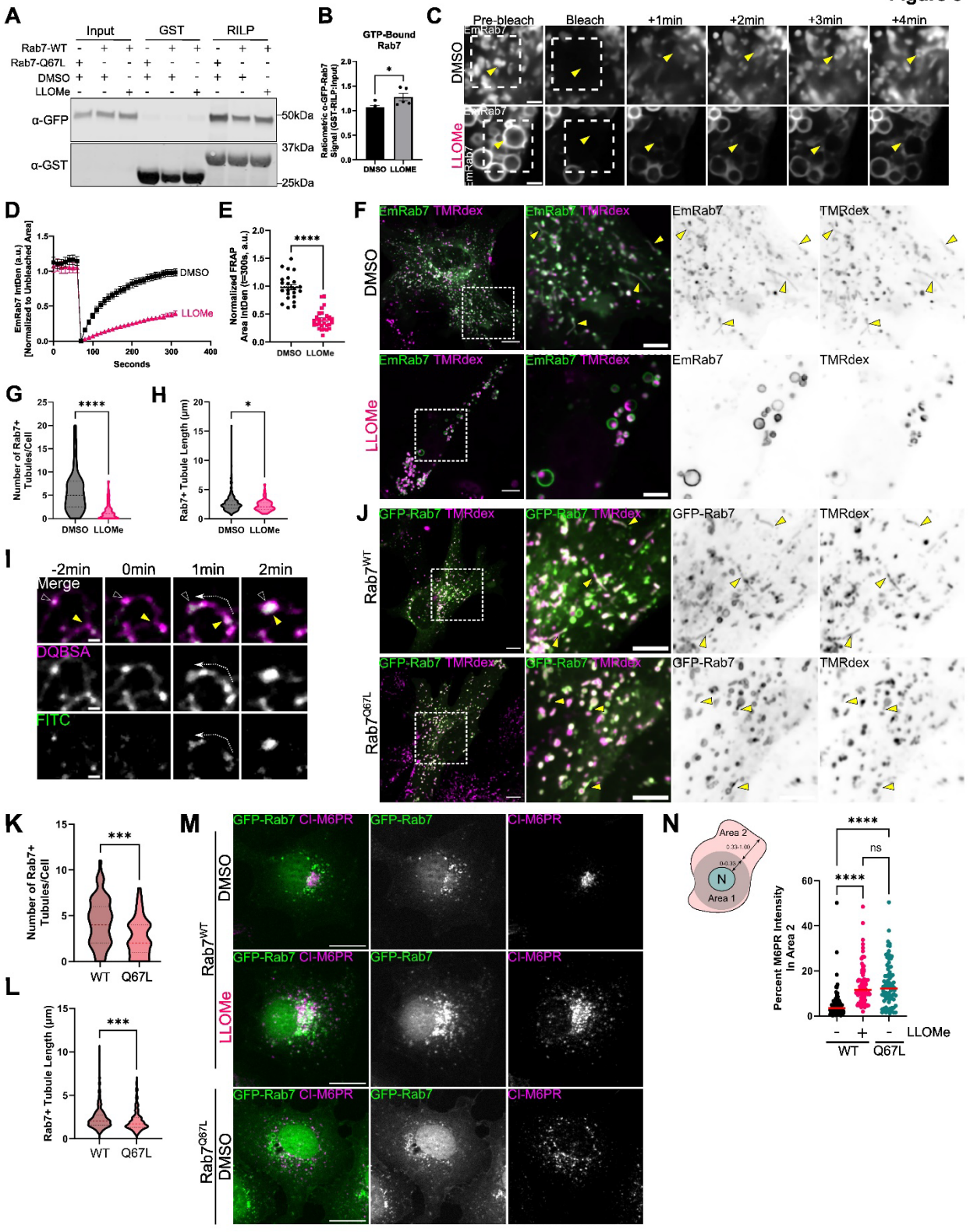
A
Input
GST
RILP
Rab7-WT
Rab7-Q67L
DMSO
LLOMe
α-GFP
α-GST
50kDa
37kDa
25kDa
B
GTP-Bound Rab7
Ratiometric c-GFP-Rab7 Signal (GST-RILP:Input)
DMSO
LLOME
C
Pre-bleach
Bleach
+1min
+2min
+3min
+4min
EmRab7
DMSO
LLOMe
D
EmRab7 IntDen (a.u.) [Normalized to Unbleached Area]
DMSO
LLOMe
Seconds
E
Normalized FRAP Area IntDen (t=300s, a.u.)
DMSO
LLOMe
F
EmRab7 TMRdex
EmRab7
TMRdex
DMSO
LLOMe
G
Number of Rab7+ Tubules/Cell
DMSO
LLOMe
H
Rab7+ Tubule Length (μm)
DMSO
LLOMe
I
-2min
0min
1min
2min
Merge
DQBSA
FITC
J
GFP-Rab7 TMRdex
GFP-Rab7
TMRdex
Rab7WT
Rab7Q67L
K
Number of Rab7+ Tubules/Cell
WT
Q67L
L
Rab7+ Tubule Length (μm)
WT
Q67L
M
GFP-Rab7 CI-M6PR
GFP-Rab7
CI-M6PR
Rab7WT
Rab7Q67L
DMSO
LLOMe
N
Area 2
Area 1
N
Percent M6PR Intensity In Area 2
ns
LLOMe
WT
Q67L

Figure 3 LLOMe-driven hyper-activation of Rab7 is sufficient to disrupt endosomal tubulation and CI-M6PR trafficking

(A) Representative immunoblot of GST or GST-RILP immunocaptured lysates from GFP-Rab7 transfected COS-7 cells treated with either DMSO or LLOMe (1mM, 1hr). GFP-Rab7^{Q67L} was used as a positive control for maximum GTP binding. **(B)** Quantified RILP-bound GFP-Rab7 in DMSO- and LLOMe- conditions by densitometry using student's t-test (n= 5 independent lysates and Western blots, p = 0.0433, error bar = mean±SEM). **(C)** Representative stills from confocal fluorescence recovery after photobleaching (FRAP) live imaging of Em-Rab7^{WT} expressing cells under DMSO (10mins, n=23 cells) and 1mM LLOMe (10mins, n=27 cells) conditions. Bleach area indicated by white box (33.0625μm^2) with representative Rab7+ endosomes indicated by yellow arrowhead (scale = 2μm). **(D)** Normalized FRAP recovery curves were plotted over time. **(E)** Mean FRAP area intensity at t=300sec (Y_{max}) was compared using student's t-test (n= as in (C) from 3 independent experiments). **(F)** Confocal micrographs of Em-Rab7^{WT} transfected primary MEFs loaded with 100μg/mL tetramethyl-rhodamine dextran (TMRdex; magenta) for 2hr, prior to treatment with DMSO or 1 mM LLOMe for 45min. Em-Rab7^{WT} tubules (green) = yellow arrowheads (scale= 10μm, inset= 5μm). **(G)** Quantification of the number of Em-Rab7^{WT}+TMRdex+ tubules in (F), compared using Mann-Whitney-U (n=57 (DMSO) and 50 (LLOMe) cells, 3 independent experiments). **(H)** Quantification of the length of Em-Rab7^{WT}+TMRdex+ tubules from conditions in (F), compared using Mann-Whitney-U test (n=331 (DMSO) and 64 (LLOMe) tubules, 3 independent experiments). **(I)** Representative stills from live imaging of LLOMe-treated MEFs loaded with 5μg/mL DQ-BSA overnight and 100μg/mL FITC-dextran for 30min prior to imaging. Yellow arrowhead=terminal end of a tubule collapsing into its source endosome (white arrowhead). **(J)** Confocal micrographs of GFP-Rab7$^{WT/Q67L}$ transfected primary MEFs loaded with 100μg/mL TMRdex for 2hr (scale= 10μm, inset= 5μm). **(K)** Quantification of the number of GFP-Rab7$^{WT/Q67L}$TMRdex+ tubules compared using student's t-test (n=62 (WT), 59 (Q67L) cells, 2 independent experiments). **(L)** Length quantification of GFP-Rab7$^{WT/Q67L}$TMRDex+ tubules, compared using Mann-Whitney-U (n=266 (WT) and 159 (Q67L) tubules, 2 independent experiments). **(M)** Widefield micrographs of GFP-Rab7^{WT} (DMSO or LLOMe 1 mM, 1h) and GFP-Rab7^{Q67L} (DMSO) transfected COS-7 cells, immunostained for endogenous CI-M6PR (scale = 20μm). **(N)** Binned CI-M6PR objects and measured for intensity of CI-M6PR in Area 2 compared using Kruskal-Wallis test (n=83 (WT-DMSO), 88 (WT-LLOMe), and 78 (Q67L-DMSO) cells, 3 independent experiments) (n.s. = non-significant, *p<0.05, ***p<0.001, ****p<0.0001).

LLOMe does not rupture Rab7-positive late endosomes but does neutralize their pH

We next sought to uncover the signal following LLOMe-induced perturbation that could drive changes in Rab7. Given the lysosomotropic weak base properties of LLOMe, more LLOMe will concentrate in more acidic, mature compartments compared to earlier more neutral compartments (Thiele and Lipsky, 1990; Uchimoto et al., 1999).

Since LEs are relatively acidic (~pH=5.5), Rab7+ LEs could concentrate enough LLOMe to damage membranes, explaining common phenotypes of LE and LYS. Alternatively, it is possible that LLOMe only damages membranes of highly acidified LYS but not of less acidified LEs. In this case, two alternative hypotheses are that Rab7+ LE changes result from signaling cascades via leaking LYS content (e.g., Ca^{2+}) or that Rab7+ LEs are undergoing a direct LLOMe-mediated stress response in the absence of LMP.

Figure 4

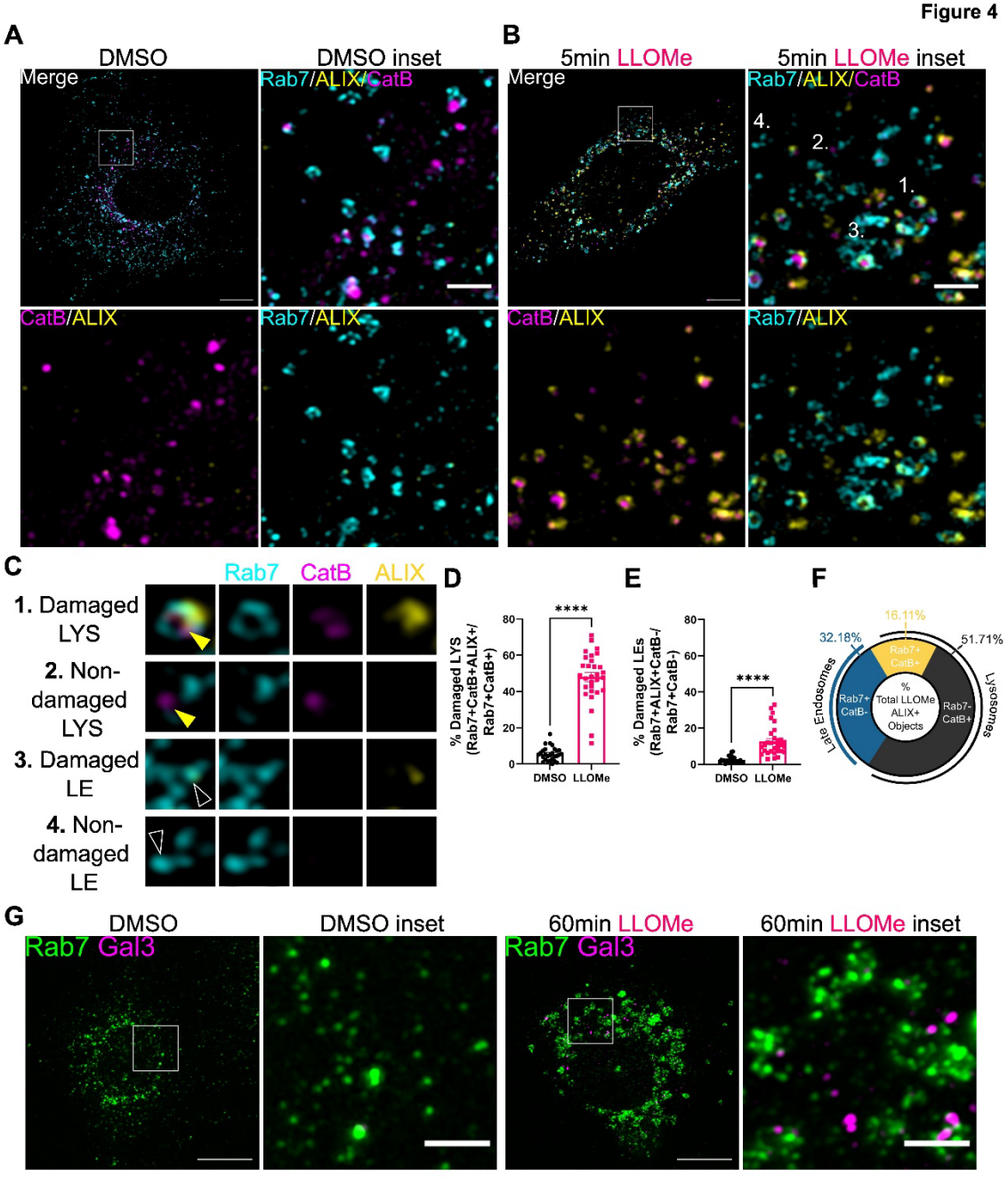

Figure 4 Most Rab7-positive late endosomes do not sustain membrane rupture after LLOMe

Airyscan micrographs of primary MEFs immunostained for endogenous Rab7 (cyan), ALIX (yellow), and CatB (magenta) following **(A)** DMSO or **(B)** 5-minute LLOMe treatment (scale= 10μm, inset = 2μm). Representative damaged LYS (1; CatB+ALIX+), non-damaged LYS (2; CatB+ALIX-), damaged LE (3; CatB-ALIX+), non-damaged LE (4; CatB-ALIX-) in **(C)**. The percentage of total ALIX+ LYS **(D)** and LE **(E)** objects were quantified and compared using Welch's t-test (n= 30 FOV, 3 independent experiments, ****p<0.0001. Error bars=mean±SEM.). **(F)** The proportion of ALIX+ objects in LLOMe that are LE vs LYS. **(G)** Airyscan micrographs of NRK cells treated with DMSO or LLOMe (1mM, 1h) and immunostained for endogenous Rab7 and Gal3 (scale= 10μm, inset = 2μm). Rab7 intensity levels were artificially matched for viewing.

To evaluate these possibilities, we first determined if LLOMe causes membrane permeabilization of LEs. We stained for endogenous ALIX (as in **Figure S1**) combined with Rab7 and partitioned LEs from LYS by presence of CatB. Following 5 minutes of 1mM LLOMe exposure, ALIX was markedly recruited to organelles as compared to controls (**Figure 4A-B**; *yellow*). We are able to observe both damaged (ALIX+) and undamaged (ALIX-) LYS (Rab7+CatB*hi*) and LEs (Rab7+CatB*lo*) (**Figure 4C**). Quantification of damaged species revealed >50% of LYS recruited ALIX within the first 5 minutes of LLOMe exposure (**Figure 4D**) while only 15% of LEs did (**Figure 4E**). Of the total LLOMe-induced ALIX+ compartments, 67.82% were LYS while only 32.18% are LEs (**Figure 4F**). Thus, these data suggest that LYS are the predominant species with membrane damage following LLOMe, while LE membranes are largely preserved. To see if Rab7+ endosomes would progress to stages of extensive LMP involving lysophagy, we co-immunostained treated NRK cells for Rab7 and Gal3. We observed minimal overlap of Rab7 compartments with Gal3, indicating the majority of LEs do not develop extensive damage (**Figure 4G**). These data suggest that phenotypic changes in Rab7 are not dependent on endosomal membranes being physically damaged.

We next investigated the alternative hypothesis that luminal content from damaged LYS might cause phenotypic changes in size and number of Rab7 compartments in response to LMP. In particular, local Ca^{2+} release from LYS after LLOMe is required for both ESCRT-dependent and -independent repair mechanisms (Niekamp et al., 2022; Radulovic et al., 2022; Skowyra et al., 2018; Tan and Finkel, 2022; Yim et al., 2022). Cytosolic Ca^{2+} release can also elicit signaling through adaptor

proteins (Clapham, 2007) that have profound impacts on membrane trafficking (Chadwick et al., 2021), and thus might drive downstream changes in Rab7+ LE size and number. However, local Ca^{2+} chelation with BAPTA-AM in LLOMe, or stimulation of Ca^{2+} release with TRPML1 agonism were not sufficient to drive Rab7 phenotypic changes (**Figure S5A-E**). Together, these data suggest that Ca^{2+} release, the most likely ionic signaling molecule for LYS to LE communication, is not responsible for observable changes in Rab7+ LEs.

Supp Figure 5

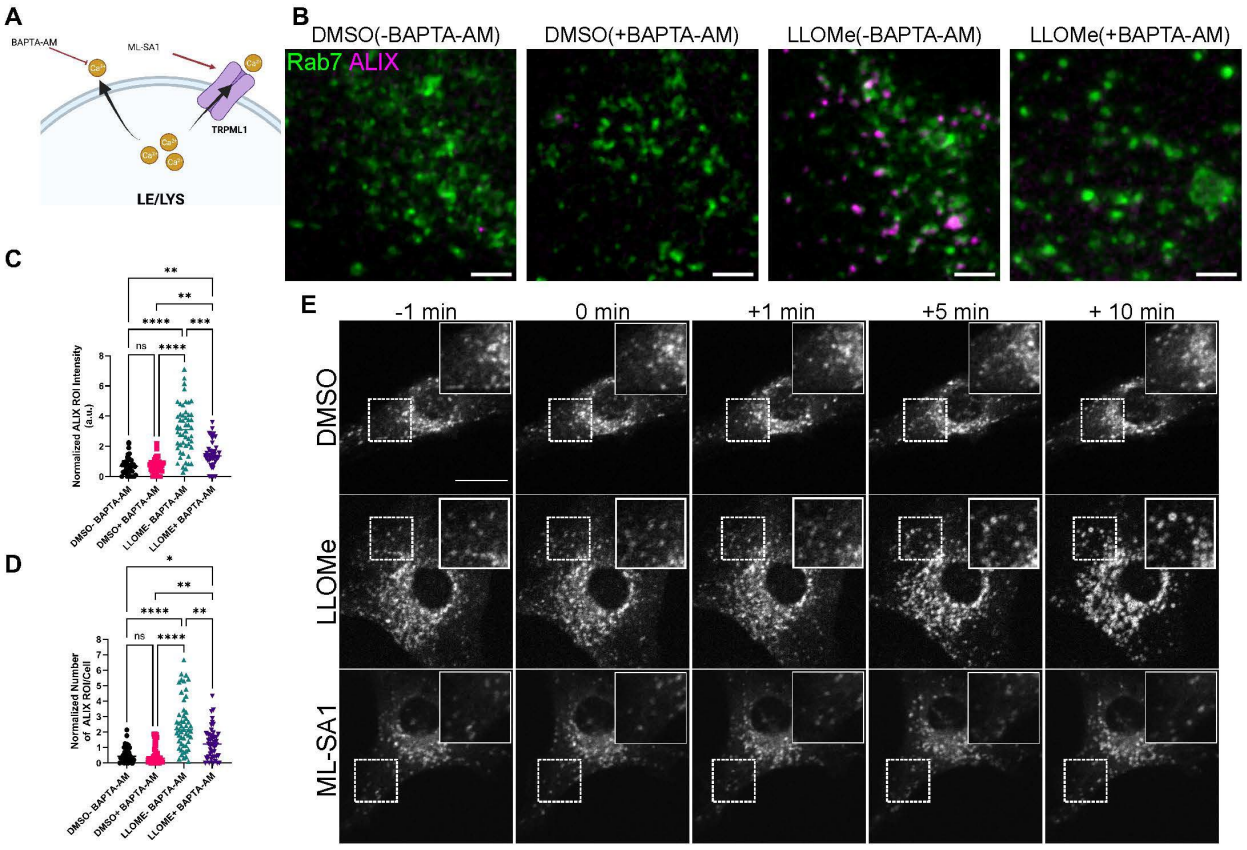

Supplemental Figure 5 Ca^{2+} release from ruptured lysosomes is not responsible for alterations in Rab7 in LLOMe

(A) Schematic for LE/LYS Ca^{2+} manipulation including cytosolic Ca^{2+} chelation with cell permeable BAPTA-AM and stimulated Ca^{2+} release using the TRPML1 agonist ML-SA1.

(B) Representative micrographs of primary MEFs pre-treated (or not) with 10μM BAPTA-AM for 30 minutes and then treated for 5 min with DMSO or 1mM LLOMe. Cells were then fixed and immunostained for endogenous Rab7 (green) and ALIX (magenta) (scale = 5μm). Rab7 intensity and size still increased in +BAPTA-AM even though ALIX recruitment was abolished. Rab7 intensity levels were artificially matched for viewing. **(C)** Quantification of ALIX puncta intensity and **(D)** number per cell following LLOMe and BAPTA-AM treatments and compared using Kruskal-Wallis test (n = 40 cells per condition from 2 independent experiments, line = median, n.s. = not significant, *p<0.05, **p<0.01, ***p<0.001, ****p<0.0001). Similarly, to published results, chelation of cytosolic calcium with BAPTA-AM

after LLOMe diminishes ALIX recruitment. **(E)** Representative stills from spinning disk microscopy (see Video 5) of Emerald-Rab7^{WT} expressing NRK cells exposed to vehicle, 1mM LLOMe or 20μM ML-SA1 for 10 minutes (scale = 10μm). Activation of lysosomal calcium efflux by ML-SA1 does not lead to changes in Rab7+ endosomes. These data argue that lysosomal calcium does not drive Rab7 changes observed in LLOMe.

Finally, we investigated the hypothesis that Rab7+ compartments were undergoing a direct LLOMe-mediated stress response independent of membrane damage. Given the weak base properties of LLOMe, we posited that LLOMe treatment might lead to direct pH neutralization of LEs without membrane damage and ALIX recruitment. To test this, we loaded cells with DQ-BSA overnight and then acutely loaded pH-sensitive Oregon Green-dextran (OGdex) for 1hr (to populate all endocytic compartments) before live imaging of cells exposed to DMSO or LLOMe (**Figure 5A**). As expected, LLOMe treatment led to rapid de-quenching of OGdex in LYS (DQ*hi)*, indicative of pH neutralization (**Figure 5B-C,E**, *yellow arrowhead*). Similarly, OGdex was also de-quenched in other endocytic compartments (DQ*lo)* following LLOMe treatment (**Figure 5B,D,F**, *empty arrowhead*). Overall, these data suggest that while LLOMe does not extensively damage LEs as compared to LYS, it accumulates enough to neutralize their pH.

Figure 5

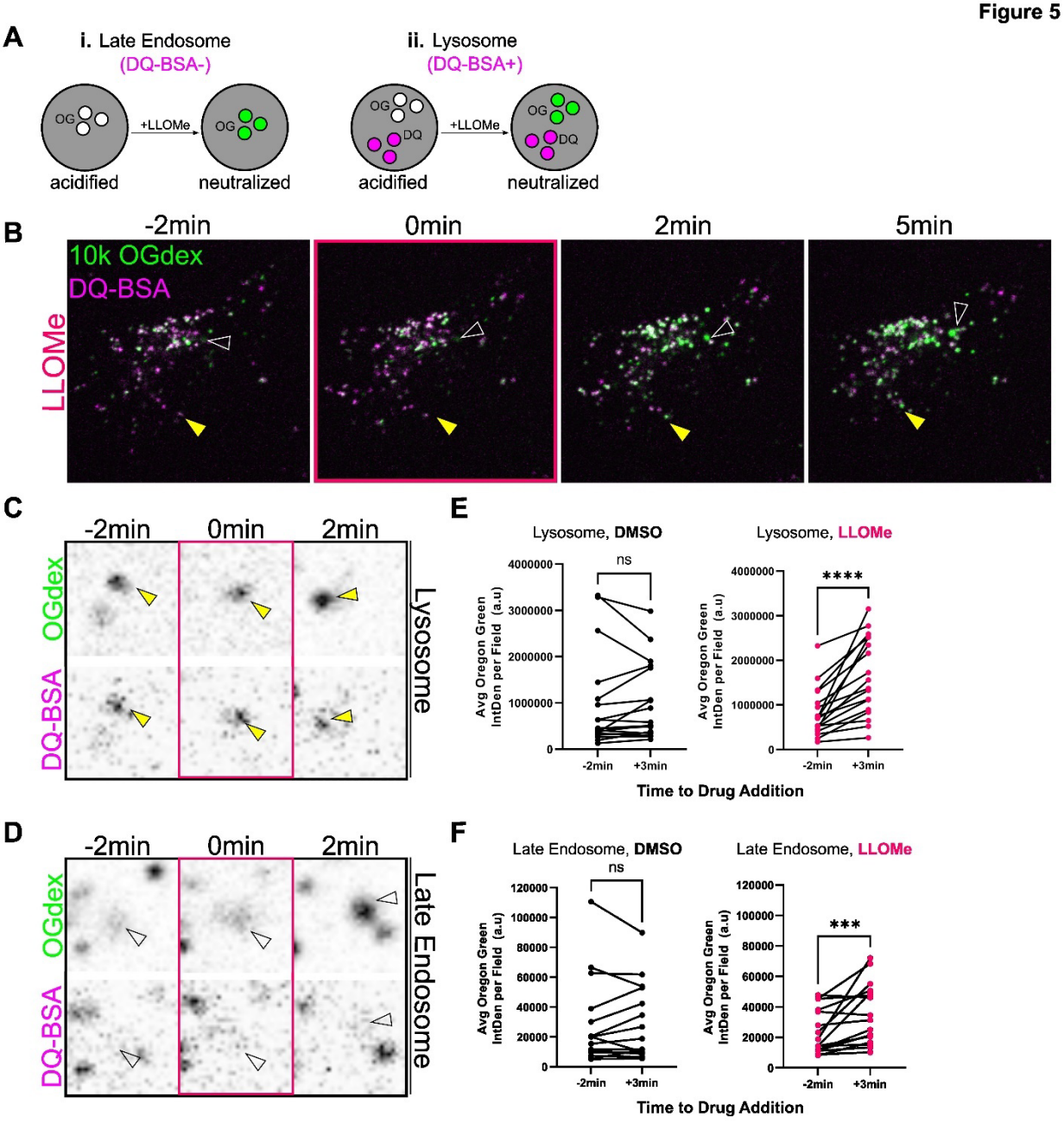

Figure 5 LLOMe leads to pH collapse of Rab7-positive late endosomes and lysosomes. (A) pH disruption de-quenches OGdex fluorescence in DQ*lo* LEs and DQ*hi* LYS. **(B)** Frames from live spinning disk microscopy of NRK cells preloaded with 5µg/mL DQ-BSA and then loaded with 100µg/mL OGdex for 1hr, followed by live LLOMe treatment. LEs (white arrowhead), LYS (yellow arrowhead). Representative stills of de-quenching of OG fluorescence in a DQ*hi* LYS **(C)** or DQ*lo* LE **(D).** OG fluorescence in **(E)** DQ*hi* LYS and **(F)** was quantified at t=-2 min and t=3 min after DMSO (black dots) or LLOMe (pink dots) and compared using paired Wilcoxon-Test. (n=15 movies per condition, 3 independent experiments, n.s. = non-significant, ***p<0.001, ****p<0.0001).

pH gradient collapse is sufficient to phenocopy many LLOMe-driven Rab7 phenotypes

Since LLOMe neutralizes the luminal pH of both LE and LYS (**Figure S1A-C**, **Figure 5**), we next wondered whether pH collapse alone is sufficient to lead to the observed phenotypic changes in Rab7. To do so, we perturbed endosomal/lysosomal pH pharmacologically (**Figure 6A**) and performed Rab7 immunostaining. We first used the weak base ammonium chloride (NH_4Cl) to neutralize luminal pH (**Figure 6B**). Treatment with NH_4Cl resulted in Rab7 compartments that were enlarged, reduced in number, and greater in Rab7 intensity (**Figure 6B-E**). We also directly inhibited the endosomal V-ATPase using Bafilomycin-A1 (BafA1). BafA1 blocks key interactions within the V-ATPase V_0 domain preventing proton translocation (Wang et al., 2021). Importantly, we used treatment parameters of BafA1 previously shown to have primary effects on endosomal/lysosomal acidification but not secondary effects on endo-lysosome fusion (Klionsky et al., 2008). Rab7+ compartments in cells treated with BafA1 also increased in size, reduced in number, and increased in Rab7 intensity (**Figure 6F-I**). To determine if these pH-disruptive treatments caused LMP, we screened for ALIX and Gal3 recruitment in NH_4Cl- and BafA1-treated cells by fixed immunostaining. Importantly, only LLOMe treatment led to accumulation of these markers (**Figure S6A**). Ultrastructural analysis by TEM revealed the appearance of enlarged compartments after LLOMe, NH_4Cl and BafA1 treatment (**Figure S6B-F**), including both lucent and dense enlarged compartments in all three conditions, as previously seen in LLOMe-treated NRK cells (**Figure 1G**). Together these data suggest that pH neutralization alone is sufficient to alter Rab7+ compartment intensity, area, and number, but not sufficient to trigger membrane damage.

Figure 6

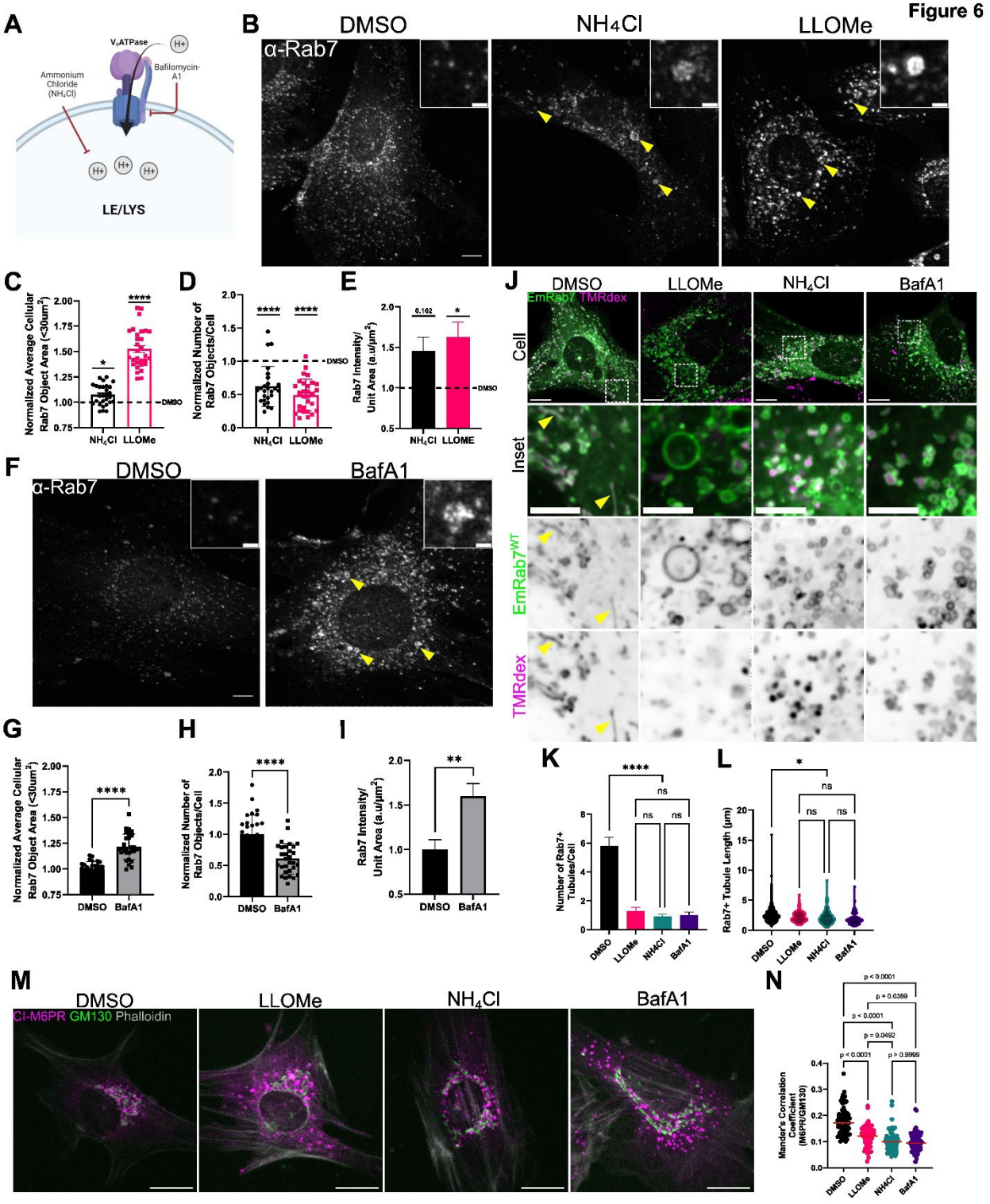
A
V0ATPase
H+
Bafilomycin-A1
Ammonium Chloride (NH4Cl)
LE/LYS
B
DMSO
NH4Cl
LLOMe
α-Rab7
C
Normalized Average Cellular Rab7 Object Area (<30um2)
NH4Cl
LLOMe
DMSO
D
Normalized Number of Rab7 Objects/Cell
E
Rab7 Intensity/ Unit Area (a.u/μm2)
0.162
J
DMSO
LLOMe
NH4Cl
BafA1
EmRab7 TMRdex
Cell
Inset
EmRab7WT
TMRdex
F
α-Rab7
G
H
I
K
Number of Rab7+ Tubules/Cell
ns
L
Rab7+ Tubule Length (μm)
M
CI-M6PR GM130 Phalloidin
N
Mander's Correlation Coefficient (M6PR/GM130)
p < 0.0001
p = 0.0389
p = 0.0492
p > 0.9999

Figure 6 pH gradient collapse is sufficient to phenocopy select LLOMe-driven Rab7 phenotypes

(A) LE/LYS pH manipulation with neutralizing base NH_4Cl and V-ATPase inhibitor Bafilomycin-A1 (BafA1). **(B)** Widefield micrographs of primary MEFs treated with DMSO (1hr), NH_4Cl (20mM, 1hr), and LLOMe (1mM, 1hr) and immunostained for endogenous Rab7 (scale = 10μm, inset= 2μm). **(C-E)** Using Imaris, Rab7 surfaces were created and filtered for those <30μm^2 in area. Cumulative cellular surface properties were analyzed for average area of Rab7 surfaces (mean±SEM) **(C)**, number of Rab7 surfaces (mean±SD) **(D)**, and Rab7 intensity per unit area of created surfaces (mean±SEM) **(E)**, per cell. (C-E) were compared using One-Way ANOVA, Welch's ANOVA, and Kruskal-Wallis, respectively (n=30 FOV, 3 independent experiments) **(F)** Widefield micrographs of primary MEFs treated with DMSO (1hr) and BafA1 (200nM, 2hr) and immunostained for endogenous Rab7 (scale = 10μm, inset= 2μm). **(G-I)** Quantification and comparisons were performed in parallel to those in (C-E). **(J)** Confocal micrographs of Em-$Rab7^{WT}$ transfected primary MEFs loaded with 100μg/mL TMRdex (magenta) for 2hr, prior to DMSO, 1mM LLOMe or 20mM NH_4Cl for 45mins, or 200nM BafA1 for 1hr. Em-$Rab7^{WT}$ tubules (green) = yellow arrowheads (scale= 10μm, inset= 5μm). **(K)** Quantification of the number of Em-$Rab7^{WT}$+TMRdex+ tubules in (J), compared using Kruskal-Wallis (n=57 (DMSO), 50 (LLOMe), 57 (NH4Cl) and 60 (BafA1) cells, shown mean±SEM, 3 independent experiments). DMSO and LLOMe conditions are the same as Figure3 F-H. **(L)** Length quantification of Em-$Rab7^{WT}$+TMRdex+ tubules in (F), compared using Kruskal-Wallis (n=331 (DMSO), 64 (LLOMe), 53 (NH4Cl), and 61 (BafA1) tubules, 3 independent experiments). **(M)** Widefield micrographs of primary MEFs treated with pH drugs as in (B) and (F) and immunostained for endogenous CI-M6PR (magenta) and GM130 (green) (scale =20μm) **(N)** Manders correlation coefficients for M6PR on GM130 space were determined using Imaris and compared using Kruskal-Wallis (n=74 (DMSO), 57 (LLOMe), 69 (NH4Cl), and 63 (BafA1) cells from 2 independent experiments, line = median) (n.s. = not significant, *p<0.05, **p<0.01, ***p<0.001, ****p<0.0001).

We next asked whether direct pH collapse is sufficient to cause endosomal tubulation deficits and CI-M6PR mis-trafficking akin to LLOMe-mediated stress. Assessment of tubulation activity in Em-$Rab7^{WT}$ expressing MEFs loaded with TMR-dextran and treated with NH_4Cl or BafA1 reduces tubule number and length, as compared to DMSO (**Figure 6J-L**). Similarly, endogenous CI-M6PR was mis-localized away from the cis-Golgi marker GM130 in NH_4Cl- and BafA1-treated COS-7 cells (**Figure 6M-N**). Together, these data suggest that pH neutralization is sufficient to disrupt Rab7+ endosome tubulation dynamics and to cause mis-localization of CI-M6PR.

Supp Figure 6

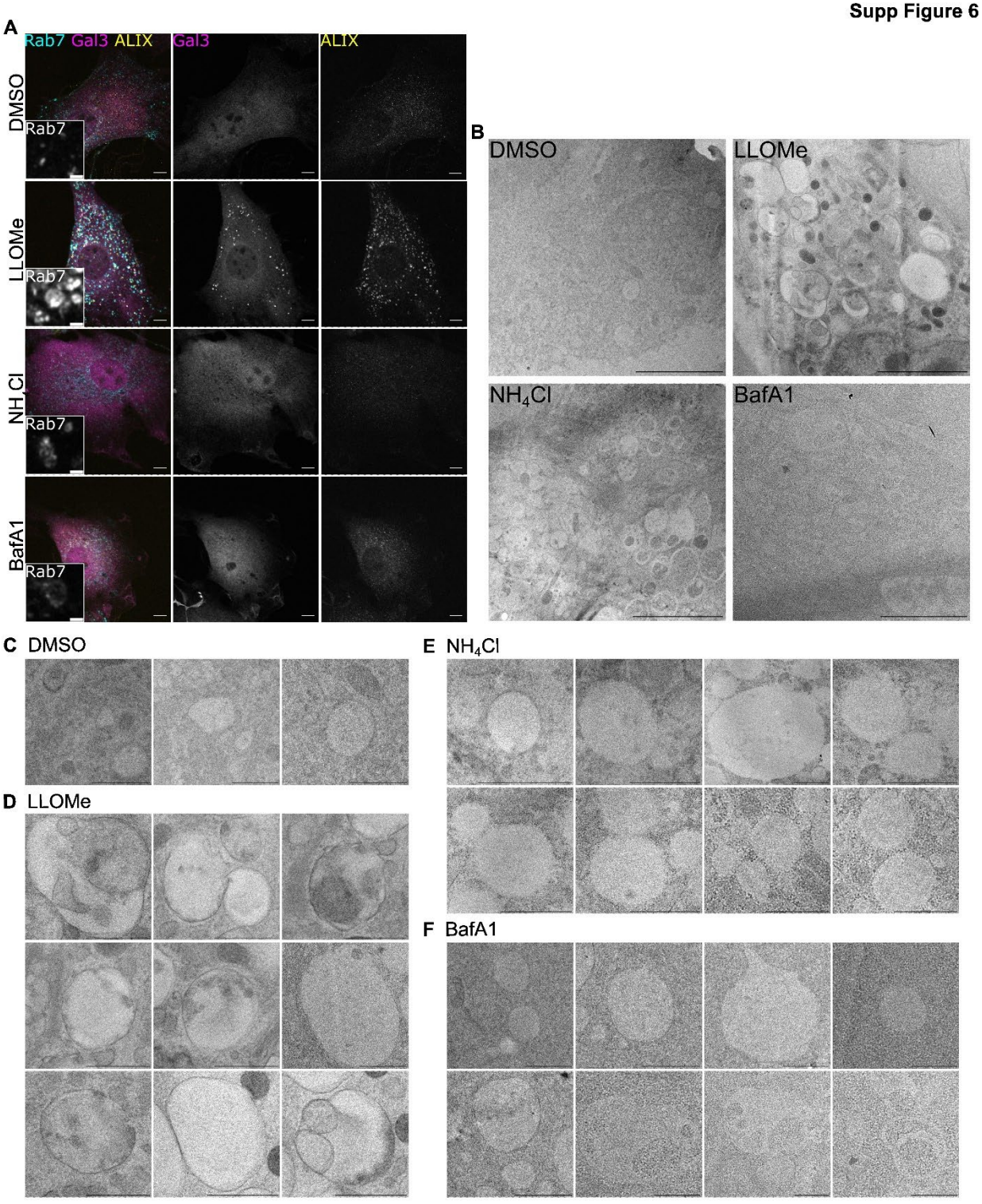

Supplemental Figure 6 Membrane rupture is only observed in LLOMe but not NH_4Cl or BAF-A1.

(A) Widefield micrographs of primary MEFs treated with vehicle (DMSO, 1 hour), LLOMe (1mM, 1 hour), NH_4Cl (20mM, 1 hour), and BafA1 (200nM, 2 hour) and immunostained for endogenous Rab7 (cyan), ALIX (yellow), and Gal3 (magenta) (scale = 10μm, inset= 2μm). ALIX recruitment occurs with minimal membrane permeabilization whereas Gal3 requires larger membrane disruption. Neither occurs with NH_4Cl or BafA1. **(B)** Under same conditions as (A), MEFs were high-pressure frozen and processed for transmission electron microscopy. Representative transmission electron micrographs for each condition are shown. Scale bar = 5μm, n = 1 independent experiment. **(C-F)** Representative examples of single compartments from control and pH perturbation treatments in MEFs demonstrate similarities between frequently appearing endosome/lysosome compartments in LLOMe (D), NH_4Cl (E), and BafA1 (F) treatments (scale = 1μm). Control (DMSO) is shown in C.

LLOMe-mediated pH collapse recruits V-ATPase V_1 subunits to late endosomes and lysosomes independently of Rab7

We have shown that LLOMe-mediated luminal pH neutralization and Rab7 hyper-activation are both sufficient to lead to changes in Rab7+ endosome/lysosomes (including defects in CI-M6PR trafficking and tubulation dynamics). We next sought to address how luminal pH changes, such as from LLOMe treatment, might be connected to the altered activity of cytosolic Rab7. V_0 subunits of the endosomal V-ATPase are responsive to luminal pH changes (Hurtado-Lorenzo et al., 2006; Marshansky, 2007), making the V-ATPase itself a likely candidate to transmit pH information across the endosomal membrane. In yeast and HEK293T cells, vacuolar and lysosomal pH neutralization increases pump assembly (Shao and Forgac, 2004; Stransky and Forgac, 2015). We thus hypothesized that LLOMe would lead to increased V-ATPase assembly (and thus activity) on endosomes in an attempt to re-establish low luminal pH. To test this, we overexpressed an HA-tagged version of V_1G_1 in COS-7 cells and co-immunostained for endogenous Rab7 and the HA-tag. 30 minutes of 1mM LLOMe treatment led to increased V_1G_1 on Rab7 endosomes as compared to controls, consistent with increased V-ATPase assembly (**Figure 7A-B**). To then test whether V_1G_1 recruitment occurred on LEs or LYS, we loaded HA-V_1G_1 transfected COS-7 cells with DQ-BSA to mark LYS. After LLOMe treatment, we observed increased recruitment of HA-V_1G_1 to both LEs (Dq*lo*; white arrowhead*)* and LYS (Dq*hi*; yellow arrowhead*)* Rab7+

compartments (**Figure 7C**). These data suggest that LLOMe increased pump assembly on both LEs and LYS. Given that LEs themselves are not extensively damaged (**Figure 4**), these data also suggest that membrane damage is not a pre-requisite for V-ATPase assembly in LLOMe.

Rab7 indirectly associates with the V-ATPase via a ternary Rab7-RILP-V_1G_1 complex (De Luca et al., 2014). Since both Rab7 and V_1G_1 levels are increased on endo-lysosomes following LLOMe, we hypothesized that Rab7 activity might control V_1G_1 localization and thus V-ATPase activity following LLOMe. To investigate this hypothesis, we overexpressed either GFP-Rab7^{WT}, GFP-CA-Rab7^{Q67L}, or dominant negative (GFP-DN-Rab7^{T22N}) with HA-V_1G_1 in COS-7 cells and then treated with LLOMe (**Figure S7A-C**). If hyperactivated Rab7 is responsible for HA-V_1G_1 assembly on endosomal membranes, we expect GFP-CA-Rab7^{Q67L} to drive HA-V_1G_1 assembly regardless of LLOMe treatment, and GFP-DN-Rab7^{T22N} to prevent HA-V_1G_1 assembly in LLOMe. Surprisingly, HA-V_1G_1 assembly was not increased with GFP-CA-Rab7^{Q67L} expression alone, even though Rab7 is highly recruited and endosomes were enlarged (**Figure S7B,D-E**). Similarly, HA-V_1G_1 assembly in LLOMe was not inhibited by GFP-DN-Rab7^{T22N} (**Figure S7C-E**). Interestingly, GFP-DN-Rab7^{T22N} was mildly recruited to HA-V_1G_1 compartments in LLOMe, raising the possibility of a nucleotide-independent mechanism for the initial Rab7 recruitment under these conditions. To test whether Rab7 was required for HA-V_1G_1 localization at all, we transiently transfected Cre-GFP and HA-V_1G_1 into primary MEFs from Rab7$^{fl/fl}$ mice. Despite the lack of Rab7 in Cre-GFP+ cells, HA-V_1G_1 localized normally to endosomes under untreated conditions (**Figure S7F**). Together, these data suggest that LLOMe pH neutralization leads to proton pump assembly (V_1G_1 recruitment) on both LEs and LYS independently of Rab7.

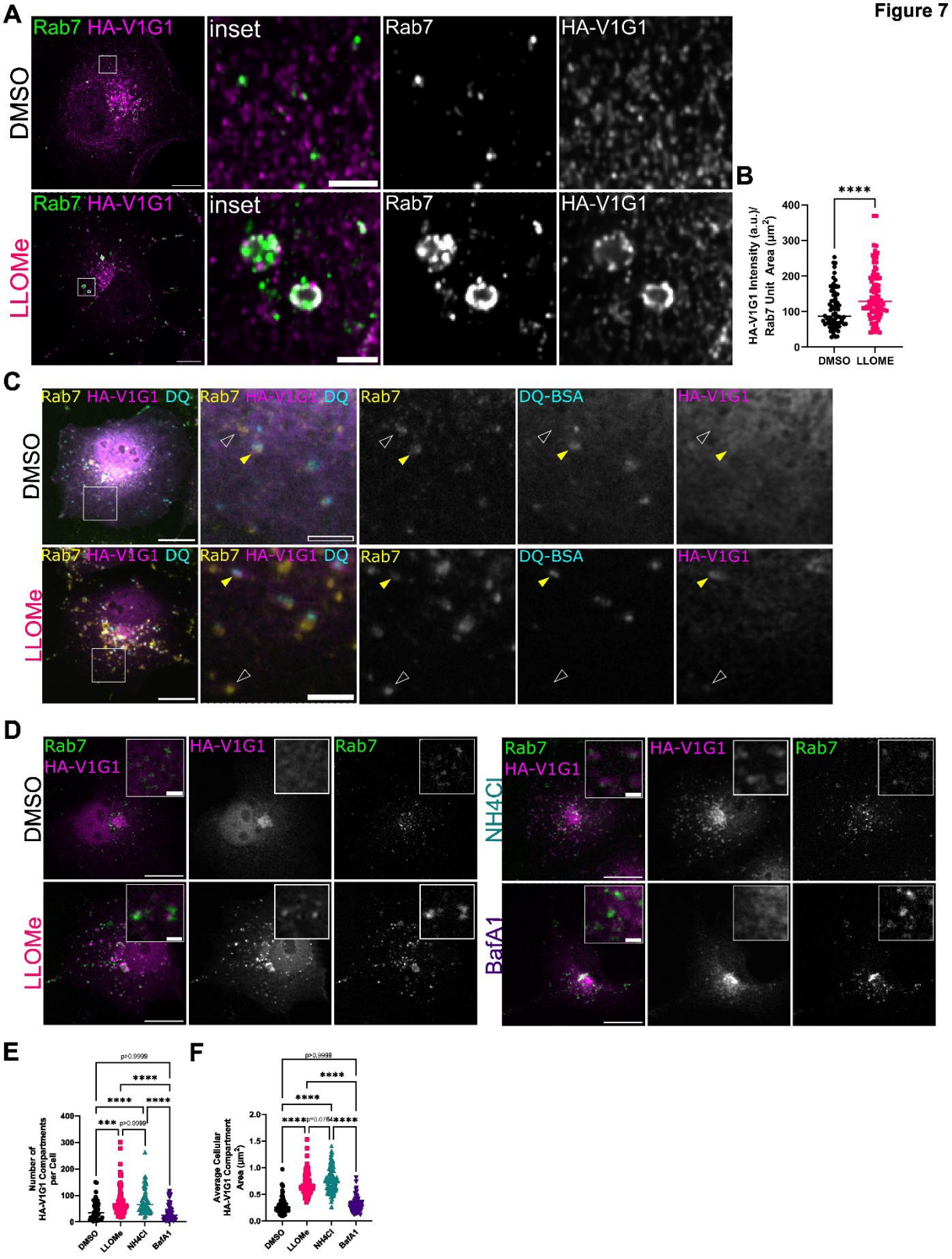
A
Rab7 HA-V1G1
inset
Rab7
HA-V1G1
DMSO
LLOMe
B
****
HA-V1G1 Intensity (a.u.)/ Rab7 Unit Area (μm²)
400
300
200
100
0
DMSO
LLOME
C
Rab7 HA-V1G1 DQ
Rab7
DQ-BSA
HA-V1G1
DMSO
LLOMe
D
Rab7
HA-V1G1
DMSO
LLOMe
NH4Cl
BafA1
E
p>0.9999
****
***
Number of HA-V1G1 Compartments per Cell
DMSO
LLOMe
NH4Cl
BafA1
F
p>0.9999
****
p=0.0764
Average Cellular HA-V1G1 Compartment Area (μm²)
2.0
1.5
1.0
0.5
0.0

Figure 7 LLOMe-mediated pH collapse recruits the V_1G_1 subunit of the V-ATPase to late endosomes and lysosomes

(A) Confocal micrographs of HA-V_1G_1 transfected COS-7 treated with DMSO or LLOMe (1mM, 30mins), then immunostained for endogenous Rab7 and HA-epitope (scale= 10μm, inset = 2μm). **(B)** Quantification of (A) compared using Mann-Whitney-U (n=76 (DMSO) and 85 (LLOMe) cells, 3 independent experiments, line = median). **(C)** Widefield micrographs of HA-V_1G_1 transfected COS-7 loaded with 5μg/mL DQ-BSA (cyan) overnight and treated with DMSO or LLOMe (1mM, 30mins), fixed, and immunostained for endogenous Rab7 (yellow) and HA-epitope (magenta) (scale= 20μm, inset= 5μm). LEs (white arrowhead), LYS (yellow arrowhead) **(D)** Widefield micrographs of HA-V_1G_1 transfected COS-7 treated with pH drugs as in Figure6B,F, immunostained for endogenous Rab7 (green) and the HA-epitope (magenta) (scale= 20μm inset= 2μm). The **(E)** number and **(F)** area of HA-V_1G_1 compartments were quantified and compared using Kruskal-Wallis [n=47 (DMSO), 63 (LLOMe), 56 (NH_4Cl), 51 (BafA1) HA-V_1G_1 transfected cells, 3 independent experiments, line = median] (n.s. = not significant, *p<0.05, **p<0.01, ***p<0.001, ****p<0.0001).

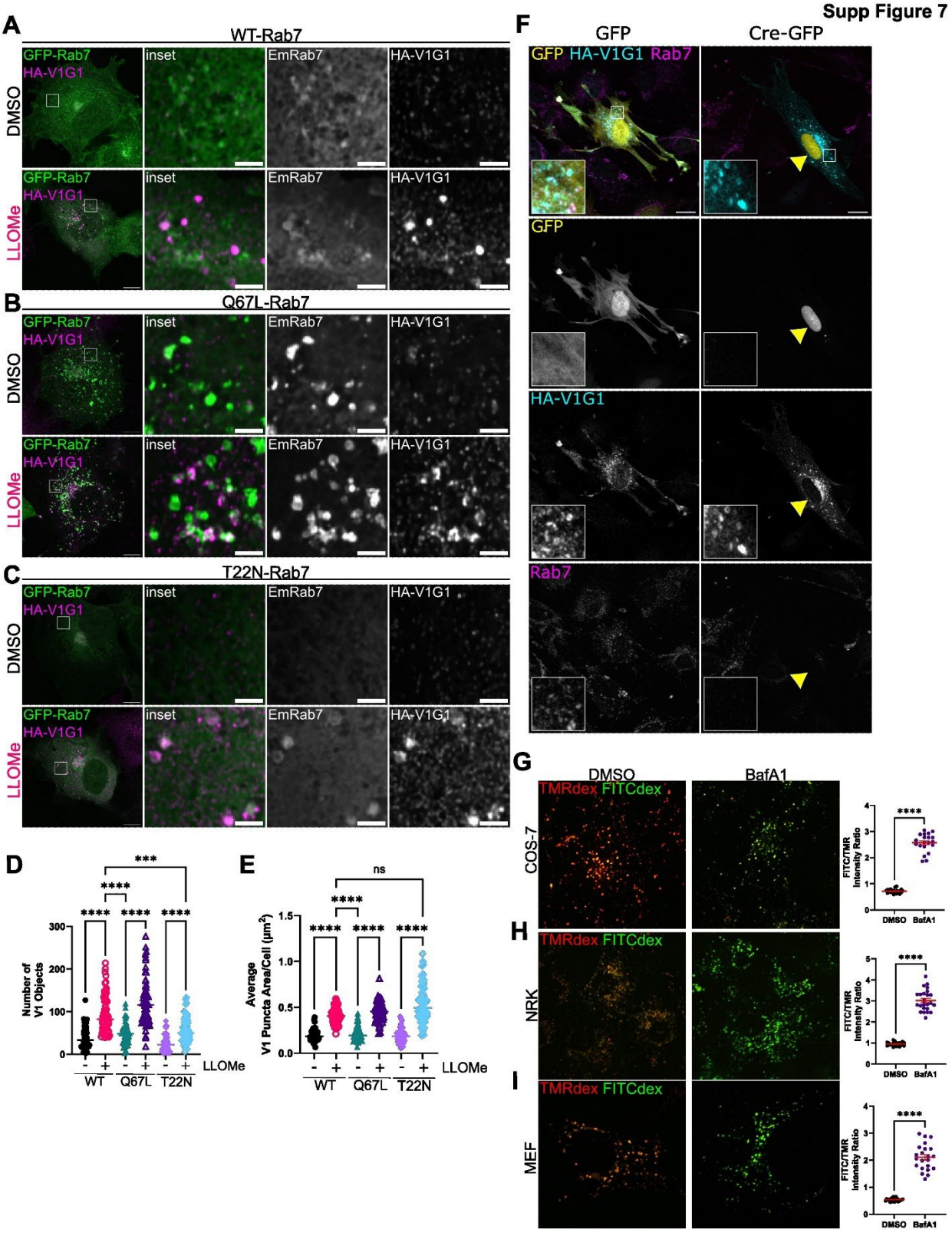
A
WT-Rab7
GFP-Rab7
HA-V1G1
inset
EmRab7
HA-V1G1
DMSO
LLOMe
B
Q67L-Rab7
C
T22N-Rab7
D
Number of V1 Objects
WT
Q67L
T22N
LLOMe
E
Average V1 Puncta Area/Cell (μm²)
ns
F
GFP
Cre-GFP
GFP HA-V1G1 Rab7
HA-V1G1
Rab7
G
DMSO
BafA1
TMRdex FITCdex
COS-7
FITC/TMR Intensity Ratio
H
NRK
I
MEF

Supplemental Figure 7 Rab7 is not essential for V_1G_1 recruitment to endosomes

(A-E) Rab7 activation state does not impact HA-V_1G_1 recruitment. (A) Confocal micrographs of COS-7 cells transfected with GFP-$Rab7^{WT}$ and HA-V_1G_1 treated with vehicle (DMSO) or 1mM LLOMe for 30 minutes (scale= 10μm, inset= 5μm). (B) Confocal micrographs of COS-7 cells transfected with constitutively active (CA) GFP-$Rab7^{Q67L}$ and HA-V_1G_1 treated with vehicle (DMSO) or 1mM LLOMe for 30 minutes (scale= 10μm, inset= 5μm). (C) Confocal micrographs of COS-7 cells transfected with dominant negative (DN) GFP-$Rab7^{T22N}$ and HA-V_1G_1 treated with vehicle (DMSO) or 1mM LLOMe for 30 minutes (scale= 10μm, inset= 5μm). Quantification of the number (D) and average area (E) of peripheral V_1G_1 objects from (A-D) compared using Kruskal Wallis test (n= 51 (WT-DMSO), 62 (WT-LLOMe), 59 (Q67L-DMSO), 60 (Q67L-LLOMe), 52 (T22N-DMSO), 65 (T22N-LLOMe) equivalent dual transfected cells from 3 independent experiments, n.s. = not significant, ***p<0.001, ****p<0.0001). **(F)** Rab7 is not required for HA-V_1G_1 recruitment. Widefield micrographs of untreated primary $Rab7^{fl/fl}$ MEFs transfected with HA-V_1G_1 and GFP or pCAG-GFP-Cre (yellow) for 3 days, and immunostained for endogenous Rab7 (cyan) and HA-tag (magenta). (scale = 20μm). **(G-I)** BafA1 causes endosome/lysosome pH collapse across cell types. Cells were loaded with 10kDa FITC dextran (green) and 70kDa TMR dextran (magenta) overnight, then chased for 4 hours prior to treatment with either vehicle (DMSO) or BafA1 (200nM, 2hr) followed by spinning disk confocal microscopy. All endosome/lysosomes were thresholded as ROI using the TMR channel in the entire fields of (G) COS-7 [DMSO-20, BafA1-22 FOV], (H) NRK [DMSO-20, BafA1-24 FOV], and (I) MEF [DMSO-22, BafA1-22 FOV] cells, and then analyzed for the ratio of FITC:TMR within ROIs. Compared using either unpaired, two tailed student's t-test (NRK) or Mann-Whitney U test (COS-7 and MEF) (****p<0.0001, from 1 independent experiment, scale bar = 20μm).

V-ATPase assembly contributes to Rab7 membrane stabilization

Since Rab7 was not required for V_1G_1 recruitment, we wondered if V-ATPase assembly instead stabilized Rab7, which would constitute a "lumen-to-cytosol"-driven Rab7 regulation mechanism. To begin to support this possibility, we first tested whether Rab7 localized to endosomes/lysosomes in conditions were V_1 is known to be highly recruited for active acidification, such as starvation, in the absence of pH neutralization. HA-V_1G_1 transfected COS-7 cells were exposed to either 24-hour nutrient deprivation in EBSS or 4-hour treatments with Torin-1. These treatments were capable of inducing formation of RFP-LC3 puncta (**Figure S8A**) and led to significant changes in V_1G_1 compartment number and area (**Figure S8B-C**). Notably, endogenous Rab7 that localized to V_1G_1 space was also significantly increased (**Figure S8D**). Conversely, only Torin-1 led to significant changes in Rab7 puncta number and area (**Figure S8E**), and showed V_1G_1 enrichment on Rab7 space (**Figure S8F**). Together, these data support that active V_1 recruitment to endosomes is correlated with increased endosomal Rab7, irrespective of the pH at the time of recruitment.

We then determined whether pH neutralization alone was sufficient to recruit HA-V_1G_1 to endosomes. Whereas LLOMe and NH_4Cl treatment led to high degrees of recruitment of HA-V_1G_1 to endosomal compartments, BafA1 did not (**Figure 7D-F**), despite BafA1 causing pH collapse in COS-7 cells and all other cell types (**Figure S7G-I**), consistent with previous literature (Hooper et al., 2022). Therefore, LLOMe and NH_4Cl lead to pH neutralization with pump assembly (i.e., V_1G_1 recruitment) whereas BafA1 leads to pH neutralization without significant pump assembly.

Leveraging differential proton pump assembly in pH-neutralizing conditions, we next asked if Rab7 membrane stability was changed as a result of assembly, speaking to V-ATPase mediated changes to Rab7. We carried out FRAP on Rab7+ endosome/lysosomes in stable Em-Rab7^{WT} NRK cells under various pH-neutralizing conditions and compared them to previously established DMSO and LLOMe conditions (**Figure 3C-E**; **Figure 8A**). Em-Rab7 recovery in NH_4Cl-treated cells was significantly slower than controls (**Figure 8A-C**, *teal*), indicating increased Rab7 stability on endosomes in both LLOMe and NH_4Cl. Interestingly, while BafA1-treated Em-Rab7 endosome/lysosomes also recovered significantly slower than controls, they recovered significantly faster and to a greater extent compared to LLOMe (**Figure 8A-C**, *purple*), indicating lower degrees of Rab7 membrane stabilization. Importantly, the randomly selected cells used for bleaching were similar in normalized fluorescence intensity of Em-Rab7^{WT} across conditions (**Figure 8D**). Single exponential phase fitting of FRAP curves (**Figure 8I**) confirmed these findings and revealed altered half-times ($t_{1/2}$) of recovery following pH neutralizing conditions. Specifically, while the half time in control cells was quick ($t_{1/2}$= 54.87s), LLOMe greatly extended this ($t_{1/2}$= 188.2s), whereas BafA1 was only partially impacted ($t_{1/2}$= 66.1s). Putting these data together, pH neutralization conditions that enhanced V-ATPase assembly (i.e., LLOMe and NH_4Cl) stabilized Rab7 association with LE/LYS membranes, whereas conditions without V-ATPase assembly (i.e., BafA1) did so to a significantly lesser degree (**Figure 8J**).

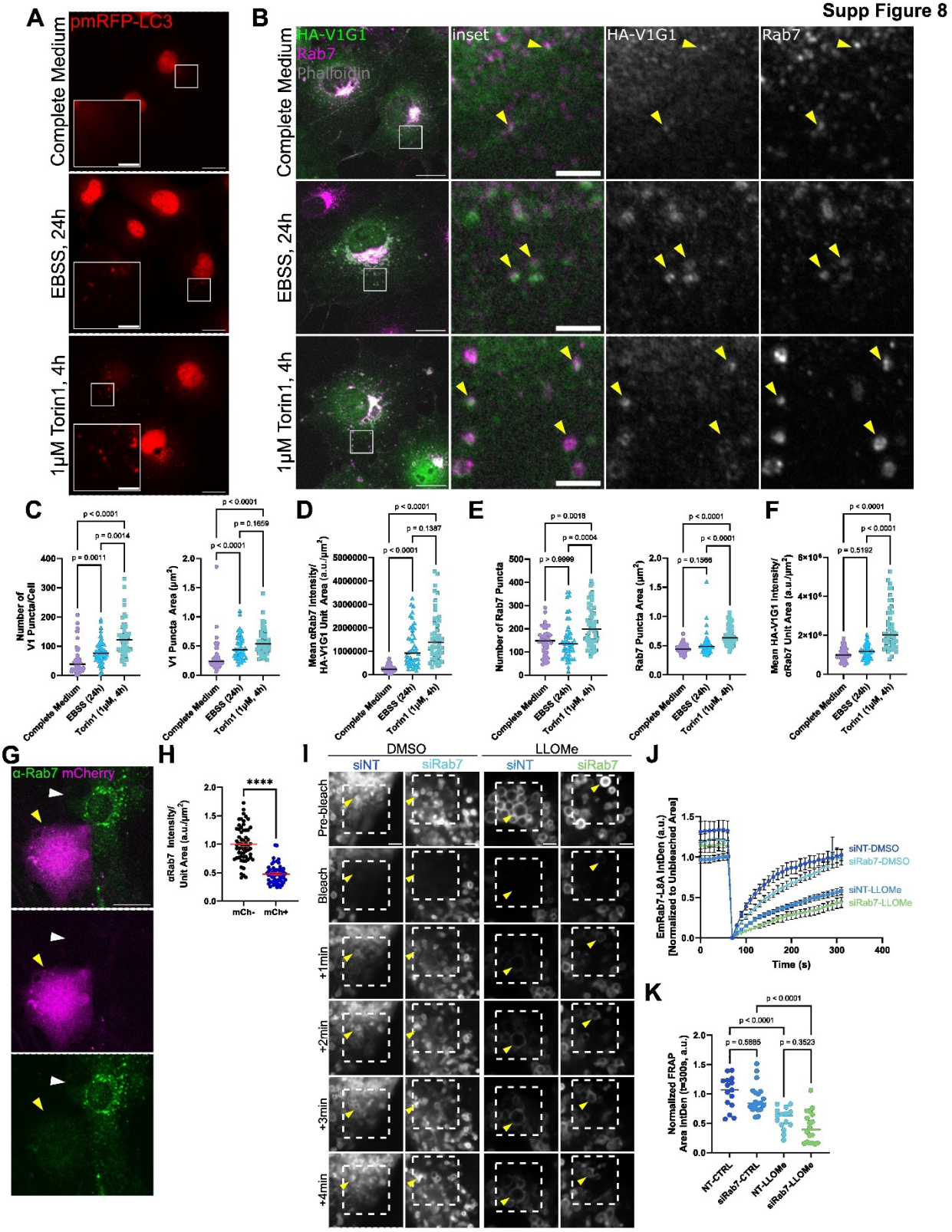
A
pmRFP-LC3
Complete Medium
EBSS, 24h
1μM Torin1, 4h
B
HA-V1G1
Rab7
Phalloidin
inset
HA-V1G1
Rab7
C
Number of V1 Puncta/Cell
V1 Puncta Area (μm²)
D
Mean αRab7 Intensity/ HA-V1G1 Unit Area (a.u./μm²)
E
Number of Rab7 Puncta
Rab7 Puncta Area (μm²)
F
Mean HA-V1G1 Intensity/ αRab7 Unit Area (a.u./μm²)
Complete Medium
EBSS (24h)
Torin1 (1μM, 4h)
G
α-Rab7 mCherry
H
αRab7 Intensity/ Unit Area (a.u./μm²)
****
mCh-
mCh+
I
DMSO
LLOMe
siNT
siRab7
Pre-bleach
Bleach
+1min
+2min
+3min
+4min
J
EmRab7-L8A IntDen (a.u.) [Normalized to Unbleached Area]
Time (s)
siNT-DMSO
siRab7-DMSO
siNT-LLOMe
siRab7-LLOMe
K
Normalized FRAP Area IntDen (t=300s, a.u.)
NT-CTRL
siRab7-CTRL
NT-LLOMe
siRab7-LLOMe

Supplemental Figure 8 Cellular starvation leads to Rab7 accumulation on V_1G_1-positive compartments

(A) Widefield micrographs of COS-7 cells transfected with pmRFP-LC3 and treated with either complete medium, EBSS (24hr), or Torin-1 (1μM, 4hr) demonstrating expected LC3 responses in this cell type at the times and concentrations of starvation conditions used (scale = 20 μm, inset = 5 μm). **(B)** Widefield micrographs of COS-7 cells transfected with HA-V_1G_1, treated with either complete medium, EBSS (24hr), or Torin-1 (1μM, 4hr), and immunostained for endogenous Rab7 and HA-tag. Only V_1-responsive cells are shown and analyzed (~50% total transfected cell population) (scale = 20μm, inset = 5μm, yellow arrowhead = representative V_1G_1 compartments). **(C)** Quantification of the number (*left*) and area (*right*) of V_1 puncta in (B). **(D)** Quantification of the mean intensity of endogenous Rab7 on V_1 space, per cell in (B). **(E)** Quantification of the number (*left*) and area (*right*) of Rab7 puncta in (B). **(F)** Quantification of the mean intensity of HA-V1G1 on Rab7 space, per cell in (B). (C-F) compared using Kruskal Wallis Test (n= 48 (Complete), 48 (EBSS), and 51 (Torin) equivalently transfected cells per condition, line = median, from 2 independent experiments). **(G)** Widefield micrographs of NRK cells lipofected with a mixture of mCherry plasmid and anti-Rab7 siRNA (magenta) for 4 days, and immunostained for endogenous Rab7 (green). Representative mCherry/siRab7+ cell (yellow arrowhead) and mCherry- (white arrowhead) are shown (scale = 20μm). **(H)** Endogenous Rab7 intensity per cell was quantified for mCherry- and mCherry+ NRK cells and compared using Mann-Whitney U test (n= 61 (mCherry-) and 54 (mCherry+) cells, ****p<0.0001, line = median, from 1 experiment). **(I)** Representative stills from confocal FRAP live imaging of mCherry+/EmRab7^{L8A} NRK cells lipofected with mCherry and either non-targeting siRNA (siNT) or siRab7 under DMSO (10mins) or LLOMe (1mM, 10mins) conditions (n= siNT/DMSO (15 cells), siRab7/DMSO (15 cells), siNT/LLOMe (21 cells), siRab7/LLOMe (18 cells), from 2 independent experiments). Only EmRab7^{L8A} fluorescence is shown for clarity. Bleached area indicated by white box (33.0625μm^2) with representative Rab7+ endosomes= yellow arrowhead (scale = 2μm). **(J)** FRAP recovery curves were plotted over time for siNT versus siRab7 under DMSO and LLOMe conditions. **(K)** Mean FRAP area intensity values were determined at t= 300sec (Y_{max}) and compared using One-Way ANOVA (n= as listed in (I), 2 independent experiments, line = median).

Rab7 indirectly associates with the V-ATPase via a ternary Rab7-RILP-V_1G_1 complex. We thus investigated if Rab7 stabilization on membranes in response to LLOMe required this complex be intact. Since knockdown of RILP is prone to off-target effects (Yap et al., 2023), we used a point mutant in Rab7 (Em-Rab7^{L8A}) which cannot bind RILP (Wu et al., 2005) and thus lacks V_1G_1 binding. We created a stable NRK line overexpressing mutant Em-Rab7^{L8A}. Normalized fluorescence intensity of Em-Rab7 signal in WT and L8A groups was similar in selected cells (**Figure 8H**). Given Rab7 is non-essential for HA-V_1G_1 responses to LLOMe (**Figure S7**), V-ATPase assembly is intact under these conditions. We then subjected these cells to FRAP experiments. In DMSO, Em-Rab7^{L8A} recovered similarly to Em-Rab7^{WT} following photobleaching (**Figure 8E-G,** *light purple*). However, in LLOMe, recovery of Em-Rab7^{L8A} was significantly faster than that of Em-Rab7^{WT} (**Figure 8E-G**, *blue*). Further, plateau values of LLOMe-treated Em-Rab7^{L8A} recovered to a significantly greater degree than LLOMe-treated Em-Rab7^{WT} cells (**Figure 8G**). Single exponential fitting of FRAP curves (**Figure 8I**) revealed the half time in LLOMe treated Em-Rab7^{L8A} was much shorter than the equivalent treatment in Em-Rab7^{WT} cells ($t_{1/2}$= 90.84s vs. 188.2s). Interestingly, the

fitted recovery of Em-Rab7^{L8A} in LLOMe closely resembled that of BafA1 treatment (**Figure 8I**). Since Rab7 can dimerize, we next tested whether depletion of endogenous Rab7^{WT} would lead to even greater FRAP recovery of Em-Rab7^{L8A}. We depleted endogenous Rab7 in NRK using an siRNA that we previously validated (Yap et al., 2022b). We found a 50% decrease in endogenous Rab7 levels after 4 days of knockdown, in concordance with our previous validation (**Figure S8G-H**). This 50% depletion in stable EmRab7^{L8A} mutant NRK cells did not significantly impact FRAP recovery in either DMSO or LLOMe conditions, as compared to a non-targeting control, suggesting the endogenous Rab7 pool is not a significant player in determining recovery of Em-Rab7^{L8A} (**Figure S8I-K**). These data together suggest that Rab7 is less stabilized on membranes following LLOMe in the absence of RILP binding (**Figure 8J**). Notably, Em-Rab7^{L8A} compartments were still vacuolar and partially stabilized Rab7 in LLOMe, suggesting that other mechanisms exist beyond RILP-mediated stabilization. Since both BafA1 and Em-Rab7^{L8A} conditions independently led to partial rescue of Em-Rab7 recovery relative to LLOMe, we suggest that together V-ATPase assembly and RILP contribute to Rab7 membrane stabilization in pH-neutralizing conditions.

Figure 8 (*next page*) LLOMe drives membrane stabilization and hyperactivation of Rab7 through influence from V-ATPase assembly and RILP

(A) Representative stills from confocal FRAP live imaging of Em-Rab7^{WT} NRK cells under DMSO (10mins, n=23), LLOMe (1mM, 10mins, n=27), NH_4Cl (20mM, 10mins, n=26), or BafA1 (200nM, 1hr, n=21) conditions. Bleached area indicated by white box (33.0625μm^2) with representative Rab7+ endosomes= yellow arrowhead (scale = 2μm). **(B)** FRAP recovery over time from (A). **(C)** Mean FRAP area intensity values at t= 300sec (Y_{max}) and compared using One-Way ANOVA (n= as in (A), 3 independent experiments, line = median, ***p<0.001, ****p<0.0001). DMSO and LLOMe conditions are from Figure 3 C-E. **(D)** Mean normalized Em-Rab7 intensity of FRAP cells prior to bleaching. Red bar= median, compared using Kruskal-Wallis (n= as in (A)). **(E)** Representative stills from confocal FRAP live imaging of Em-Rab7^{L8A} NRK cells under DMSO (10mins, n=28) or LLOMe (10mins, n=30). 33.0625μm^2 bleached area indicated by white box. Representative Rab7+ endosomes = yellow arrowhead. (scale = 2μm). **(F)** FRAP recovery over time in (E). **(G)** Mean FRAP area intensity values at t= 300sec (Y_{max}) and compared using One-Way ANOVA (n= as listed in (E), 3 independent experiments, line = median, ***p<0.001, ****p<0.0001). Wild-type data in (E-H) are identical to that of (A-D); mutant data has been separated for clarity. **(H)** Mean normalized Em-Rab7 intensity of L8A FRAP cells, prior to bleaching. Red bar= median, compared using Kruskal-Wallis (n= as in (E)). **(I)** ***Left:*** One-way exponential phase association fitted curves for all conditions following bleach. ***Right:*** Parameters from fitted curves indicating the plateau values and half-time for each condition. **(J)** FRAP summary table for all conditions

based on V-ATPase assembly and RILP binding. **(K)** Our model for pH regulation on Rab7-positive late endosomes proposes that upon pH neutralization there is increased V-ATPase assembly (1.), via a RILP-V-ATPase axis, stabilizing Rab7 in a hyperactive form (2.) which contributes to the loss of endosomal tubulation (3.) and proper CI-M6PR trafficking (4.).

Figure 8

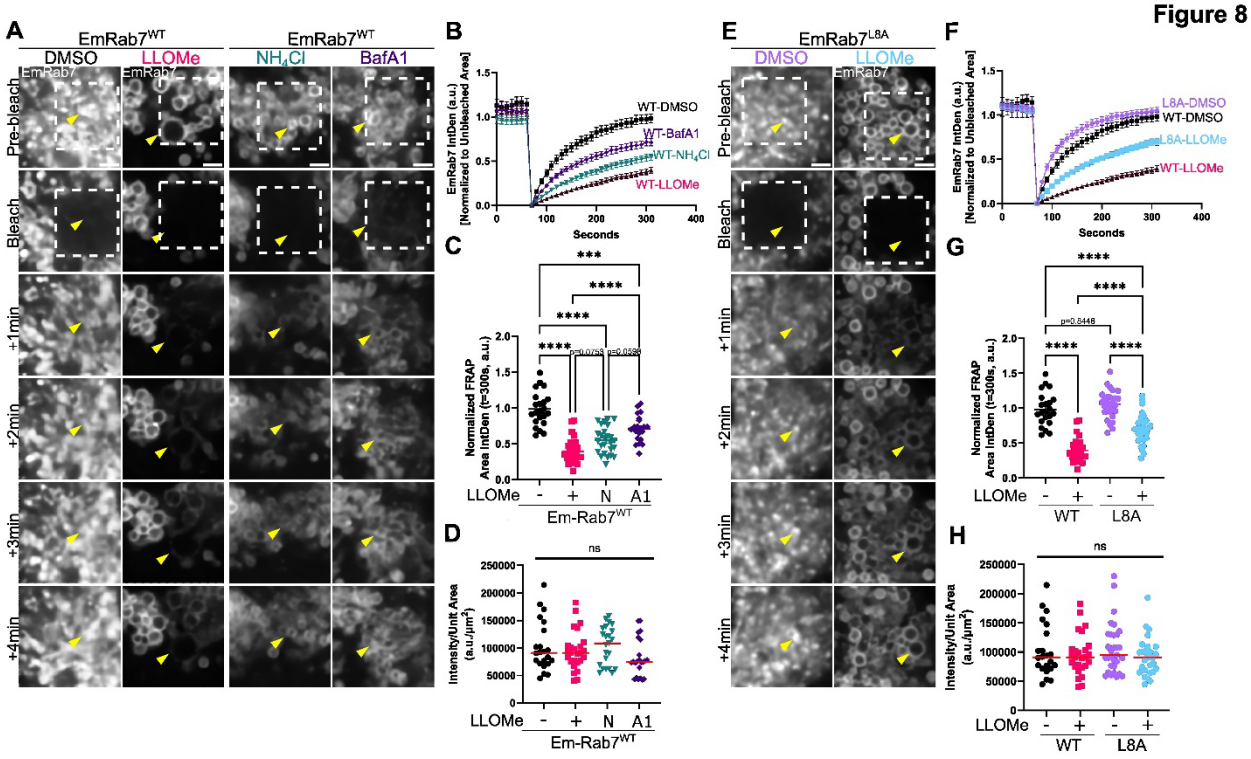

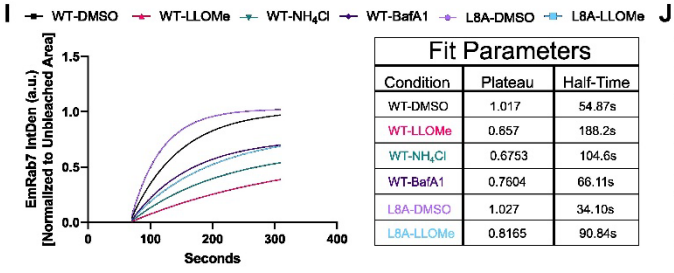

J

Fit Parameters		
Condition	Plateau	Half-Time
WT-DMSO	1.017	54.87s
WT-LLOMe	0.657	188.2s
WT-NH4Cl	0.6753	104.6s
WT-BafA1	0.7604	66.11s
L8A-DMSO	1.027	34.10s
L8A-LLOMe	0.8165	90.84s

FRAP Summary			
Condition	V-ATPase Assembly	RILP binding	Rab7 stabilization
WT-DMSO	LOW	Present	---
WT-LLOMe	HIGH	Present	↑↑↑
WT-NH4Cl	HIGH	Present	↑↑↑
WT-BafA1	LOW	Present	↑
L8A-DMSO	LOW	Absent	—
L8A-LLOMe	HIGH	Absent	↑

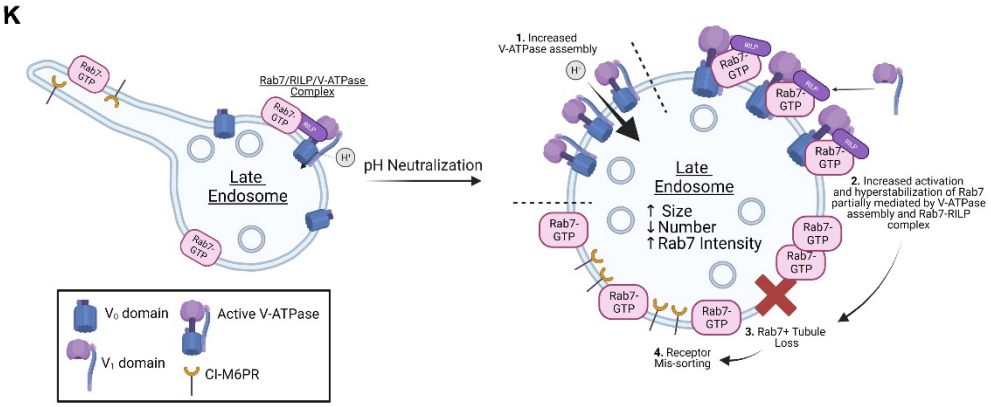

3.4 Discussion

In summary, the present study finds that the behavior of Rab7+ late endosomes upstream of damaged lysosomes is profoundly altered by pH neutralization: increased V-ATPase assembly (Step 1, **Figure 8K**) promotes activation and membrane stabilization of Rab7 (Step 2, **Figure 8K**), leading to decreased membrane tubulation of endosomes (Step 3, **Figure 8K**) and faulty trafficking of CI-M6PR (Step 4, **Figure 8K**). In a previous report, chloroquine- or sirasamine-driven LMP damaged 30% of Rab7+ compartments. This population includes LYS and LEs/EEs since they were not distinguished from each other (Du Rietz et al., 2020). Notably, our work carefully defined compartmental markers and confirmed that the majority of Rab7+ compartments with membrane permeabilization were LYS, whereas Rab7+ LEs rapidly respond to LLOMe with pH neutralization but do not exhibit LMP. The acute LE response is characterized by rapid enlargement from pH neutralization, which led to increased V-ATPase assembly on both undamaged LEs and damaged LYS. Whereas pH neutralization due to vacuolar damage in *Salmonella* infection (Xu et al., 2019) or LLOMe treatment (Cross et al., 2023a) assembles V-ATPase for autophagy conjugation, our data reveal the novel notion that V-ATPase assembly in sterile (non-infection) pH-neutralized late endosomes leads to increased activation and membrane stability of Rab7, which we found to be further influenced by the ability of Rab7 to bind its effector RILP.

The relationship between V-ATPase, Rab7 and endosomal pH

The current assumption is that active Rab7 contributes to acidification of endosomes as they mature into functional lysosomes based on a correlation between lower pH and increased Rab7 on endosomes, and early data suggesting DN-Rab7^{T22N} affects lysosomal pH (Bucci et al., 2000). This notion is supported by data including RILP controlling V_1G_1 stability, increased pH after RILP depletion, and the correlation of lower levels of Rab7 on less acidic peripheral lysosomes (De Luca et al., 2014; Johnson et al.,

2016). However, definitive data demonstrating the ability of active Rab7 to recruit pump subunits or tune luminal pH is lacking. More recent Lysotracker data in Rab7-DN expressing *Drosophila* oocytes, Rab7-KO MEFs, and Rab7-KO MDCK cells demonstrate Rab7 is dispensable for maintenance of endosomal pH (Kuchitsu et al., 2018; Liang et al., 2023; Yu et al., 2024). Now, we further demonstrate that Rab7 is dispensable for the assembly of V_1G_1 on endosomes, given complete knockout of Rab7 could not deplete endosomal association of V_1G_1. Collectively, these data point to the importance of RILP in acidification and stabilization of Rab7.

Whereas initial work suggested that Rab7 was upstream of V-ATPase and regulated acidification via V_1G_1 (De Luca et al., 2014), newer work suggested instead that Rab7 membrane recruitment and stabilization may be downstream of the V-ATPase subunit V_0a_3. Knockout of V_0a_3 eliminates Rab7 association with lysosomes and anterograde trafficking (Matsumoto et al., 2018). BafA1 also decreases anterograde lysosomal trafficking and depletes constitutively active Rab7 in complex with pump subunits (Matsumoto and Nakanishi-Matsui, 2019). Whereas these data identify the V_0a_3 subunit, our data more generally implicate an assembled V-ATPase in contributing to the control of Rab7 activation state. In scenarios with pH neutralization and extensive pump assembly (i.e., LLOMe or NH_4Cl), we observed high degrees of membrane stabilization of Rab7 by FRAP. On the contrary, low pump assembly conditions (i.e., BafA1) had significantly destabilized Rab7 on endosomal membranes.

In our interpretation, these data provide evidence that Rab7 activity is subject to regulation by luminal pH-driven V-ATPase assembly when pH is too alkaline. This might include, for example, the maturational transition from more alkaline EE to acidic LEs. Our Rab7-mutant and knockout data suggest that physiologic acidification is Rab7-independent, and rather V-ATPase reciprocally increases the presence of active Rab7 on more mature compartments. In support of the notion, we demonstrate that physiologic starvation conditions, such as in EBSS or direct mTOR inhibition, increased Rab7 on V_1G_1 membranes, when acidification occurs without neutralization (Collins and Forgac, 2020; McGuire and Forgac, 2018; Ratto et al., 2022; Stransky and Forgac, 2015). Our data and others also support a role for pump-mediated initiation of Rab7 activation. Previous data

suggests V-ATPase may contribute to recruitment of inactive Rab7 and its cognate GEF to the membrane (Matsumoto et al., 2022). Our data further support this possibility, as DN-Rab7^{T22N} is modestly recruited to V_1G_1 positive membranes following LLOMe.

Together, it appears that fine tuning endosomal pH involves extensive communication between the V-ATPase and Rab7. Our new data and others are consistent with the idea that V-ATPase is a main driver of Rab7 activation and stabilization on membranes, which is akin to similarly described V-ATPase driven recruitment of the ARF-GEF ARNO for Arf6 activation (Maranda et al., 2001). Our results are further relevant to all instances of endosomal/lysosomal neutralization, including the use of lysosomotropic pH-neutralizing therapeutics, such as selective-serotonin reuptake inhibitors (SSRIs) or atypical antipsychotic therapeutics (Kuzu et al., 2017; Kuwahara et al., 2020; Lakpa et al., 2021), which may similarly cause pH neutralization in LEs and disruption of membrane trafficking in the absence of LMP.

Endosomal membrane stabilization of active Rab7 is influenced by V-ATPase assembly and RILP binding: an effector balance?

Modest changes in Rab7 activation as a result of pump assembly, downstream of pH sensing, could have profound effects on effector binding important for control of endosomal transitions and cellular membrane trafficking. As evidence of this, the extreme cases of pH neutralization we explore in this paper disrupt normal Rab7-positive tubulation and CI-M6PR trafficking events. These tubulation events are thought to be dependent on dynein-RILP effector complexes (Mrakovic et al., 2012). In our FRAP data, we demonstrate that the increased membrane stabilization of Rab7 is partially due to Rab7 interactions with RILP, as Rab7^{L8A} mutants recover quicker than Rab7^{WT}. This is consistent with previous data from both our lab and others that demonstrate overexpressed RILP massively stabilized Rab7 on membranes (Jordens et al., 2001; Yap et al., 2022b). Collectively, these data begin to suggest a complex balance of Rab7 effectors on late endosomes that depend on RILP as a limiting factor. We speculate that

increased V_1-RILP-Rab7 interactions in pH neutralization responses sequesters active Rab7 away from other effectors which rely on RILP interactions. CI-M6PR mis-sorting and tubulation deficits might thus be a consequence of a disrupted Rab7 effector balance. Rab7 effector balance is an exciting avenue of future exploration, as it may play key roles in long range trafficking and degradation of important trophic molecules relevant to disease (Mulligan and Winckler, 2023).

Rab7 tubulation and lysophagy

Our data demonstrate a drastic change in the tubulation activity of Rab7+ compartments after LLOMe. In contrast to the appearance of LAMP1-negative tubules on LAMP1-positive LYS after extensive damage (>1h LLOMe) (Bonet-Ponce et al. 2020) or tubules formed during LMP recovery (Bhattacharya et al. 2023), we observe an acute loss of Rab7+ tubulation in a short temporal window following LLOMe exposure. Recovery of lysosomal tubules from LLOMe requires Rab7 inactivation by the GAP TBC1D15 (Bhattacharya et al., 2023). We speculate that LLOMe initially disrupts normal Rab7-positive tubulation via hyperactivation, which affects the retrieval of membrane cargos that should not enter lysosomes (e.g. CI-M6PR), whereas Rab7-negative tubulation events with separate functions may still occur at later stages of LMP (Bonet-Ponce et al. 2020; Bhattacharya et al. 2023). We further suggest that the rapid loss of tubulation in LLOMe partially contributes to the Rab7 compartment phenotypes (e.g., size) observed in LLOMe. Other factors such as excessive fusion events or lipid exchange mechanisms might play additional roles (Radulovic et al., 2022; Tan and Finkel, 2022).

Finally, V-ATPase assembly-driven Rab7 activation may serve as an accelerant of the endo-lysosomal system. As V-ATPase assembly and acidification were recently linked to increased degradation in previously quiescent compartments (Ratto et al., 2022), it is possible that this mechanism serves to activate a pool of initially weakly-degradative LEs to generate functional lysosomes in order to maintain proteostasis or progress to lysophagy. Given that in other contexts Rab7 activation provides control over the selective

autophagy of organelles (Jimenez-Orgaz et al., 2018), future studies are needed to elucidate the definitive downstream role of undamaged, actively acidifying LEs following lysosomal disruption for lysophagic resolution.

Collectively, our data further raise new questions about Rab7 effector selection and its connection to luminal pH, with considerations for lysophagy progression. This mechanistic link likely underlies dynamic changes in homeostatic endosomal behavior in health and might be disrupted in several genetic disorders, including neurodegenerative diseases (Colacurcio and Nixon, 2016; Pescosolido et al., 2021). This study therefore broadens our understanding of physiologic pH regulation, control of Rab7 activity and effector binding, and ultimately cellular responses to LE/LYS disruptions.

Chapter IV. Rab7 compartments in neuronal soma and dendrites respond differentially to endo-lysosomal stress

Contributions by others: Laura Digilio assisted with primary neuron isolation and culture. Chan Choo Yap provided valuable expertise and guidance.

4.A Abstract

Disruptions of lysosomal membranes occur frequently within the nervous system, such as after stroke, as a result of neurotoxic aggregate accumulation, or in genetic lysosomal storage disorders. The resulting perturbation of lysosomal function often leads to neuronal death in the long term. Previous studies have elucidated mechanistic pathways to repair or clear damaged lysosomes in non-neuronal cells, but the impact of lysosomal perturbation in neurons needs to be evaluated keeping in mind that the large distances of neuronal processes as well as heterogeneity in endosomal-lysosomal trafficking and degradative compartments in soma and dendrites create spatial complexities not present in non-neuronal cells. Here, we investigate somatic versus dendritic trafficking of endosomal and lysosomal compartments in response to lysosomal damage states, using fixed and live imaging approaches of primary neuronal culture and the lysosomal disrupting dipeptide LLOMe. We particularly focus on the impacts on events upstream of lysosomes which are driven by the small GTPase Rab7, given its necessity for dendritic traffic and degradation. Akin to non-neuronal cells (Chapter 3), we find an accumulation of enlarged Rab7-positive late endosomal and lysosomal compartments in the soma. Surprisingly, these enlarged compartments did not accumulate lysosomal fated cargos which were enriched in non-enlarged compartments instead, seemingly not fusing with the enlarged late endosomal and lysosomal compartments. In dendrites, we noted an increase of cathepsin-positive Rab7 carriers in the medial dendrite, which correlated with increased anterograde motility of a subset of Emerald-Rab7 compartments from the proximal dendrite by live imaging. We found additional upstream trafficking disruption in dendrites, as the neuronal specific trafficking receptor Nsg2/p19 accumulated in early endosomes following LLOMe treatment. Together, these data suggest a stalling of retrograde dendritic traffic in the presence of lysosomal disruption, which may be compensated for by increased anterograde delivery of degradative enzymes. These findings broadly relevant to our understandings of bidirectional dendritic trafficking in the context of Rab7 dysregulation with implications for neurologic pathology.

4.1 Introduction

Neurons have unique challenges in balancing protein synthesis and degradation (i.e., maintaining proteostasis) (Winckler et al., 2018). For one, they are extensive and spatially complex, with some peripheral nerves in humans spanning greater than one meter in length. Proteins fated for degradation must therefore be trafficked via endosomes or autophagosomes and degraded by fusion with lysosomes in a coordinated manner over such long distances. Neurons are also post-mitotic, meaning they must survive for the lifetime of an organism. As such, endosomal/lysosomal-mediated protein degradation must proceed faithfully for up to a century.

Cells must also ensure the integrity of lysosomes themselves. An extensive body of work has shown that lysosomal membranes can be physically damaged, causing lysosomal membrane permeabilization (LMP), i.e. holes. LMP is defined by the leaking of luminal lysosomal contents (like ions), degradative proteins or reactive oxygen species (ROS), into the cytosol (Serrano-Puebla and Boya, 2016). LMP thus impairs lysosomal functions as well as releasing damaging molecules into the cytosol, often leading to cell death. Lysosomal dysfunction is of particular concern in the central nervous system, given the size and longevity of neurons and the growing evidence that disruptions in lysosomal homeostasis is linked to neurodegenerative disease (Malik et al., 2019). Indeed, pathologic processes that impact neurons can cause LMP and further precipitate neuronal death. This includes damage with reperfusion after ischemic injury (Lipton, 2013; Windelborn and Lipton, 2008), neurotoxic aggregates which accumulate in neurodegenerative diseases such as tau or synuclein fibrils (as in AD or PD, respectively) (Flavin et al., 2017; Polanco et al., 2021), or lysosomal storage disorders like Niemann-Pick type A or Gaucher's disease (Kirkegaard et al., 2010). Endosome or lysosome rupture may also contribute to the pathologic spread and seeding of neurotoxic proteins in neighboring cells(Polanco and Götz, 2022; Polanco et al., 2021). In addition, commonly used neuropsychiatric drugs, including tricylic antidepressants (TCAs), antipsychotics and selective serotonin reuptake inhibitors (SSRIs) can accumulate in lysosomes and cause lysosomal dysfunction (Berg et al., 2022; Kuwahara et al., 2020; Lakpa et al., 2021). Therefore, elucidating the mechanisms by which neurons respond to LMP can aid in better understanding and

prevention of cell death pathways. In non-neuronal cells, detailed molecular cascades involving direct membrane repair processes (such as via ESCRTs and PI4P) (Radulovic et al., 2018; Skowyra et al., 2018; Tan and Finkel, 2022) and lysosomal specific autophagy cascades (via galectins and E3 ubiquitin ligases) (Papadopoulos et al., 2020; Yang and Tan, 2023) have been discovered to explain how cells maintain lysosomal homeostasis in light of LMP. However, these studies fail to glean how LMP impacts upstream endosomal trafficking, perhaps most importantly in neurons, which are heavily reliant on long-range trafficking.

We have previously described how lysosomal degradation and endosomal flux in neurons is spatially regulated. In neuronal dendrites, degradative lysosomes are restricted to the soma and proximal 25μm of dendrites, with minimal degradative capacity in medial or distal dendrites (Yap et al., 2018). Thus, bulk degradation of somato-dendritic membrane proteins, such as the neuronal specific proteins NEEP21/Nsg1 and p19/Nsg2, cannot take place locally in the dendrite but must be transported to the soma for degradation. Nsg1/2 have short half-lives (~1.5 hours) and thus make great tools to assess neuronal degradation and endocytic flux (Yap et al., 2017). We have further described how neuronal degradation is dependent on the small, late endosomal GTPase Rab7a (herein Rab7) and its effectors. Knockdown of endogenous Rab7 (Yap et al., 2022b) or overexpression of a dominant negative form of Rab7 (Yap et al., 2018) leads to accumulation of Nsg1/2 within dendrites. Similarly, disruption of the interaction between Rab7-positive (Rab7+) late endosomes and the minus-end directed microtubule motor dynein also leads to Nsg1/2 accumulation and defective endosomal flux (Yap et al., 2022b). Recently, we described how Rab7 is hyperactivated and membrane stabilized following lysosomal disruption in non-neuronal cells, leading to the cessation of tubulation and retention of trafficking receptors upstream of lysosomes, likely due to an imbalance between Rab7 effectors including dynein (Chapter 3). Ultimately what role Rab7 plays in controlling upstream dendritic endosomal traffic and the degradation of neuronal membrane proteins like Nsg1/2 following lysosomal damage is an open question.

Here, we utilize the lysosomal damaging dipeptide L-leucyl-L-leucine-O-methyl ester (LLOMe) to elucidate the impact of lysosomal damage on Rab7-mediated dendritic endosomal flux and protein degradation. Notably, we find distinct pools of Rab7+ compartments in the soma and dendrites. In the soma, akin to non-neuronal cells, both Rab7+ late endosomes and lysosomes accumulate. In the proximal dendrite, Rab7+ compartments exhibit mild anterograde motility bias following LLOMe, which correlates with an increased presence of Rab7+ compartments immuno-positive for the hydrolase cathepsin-B (CatB) in the medial dendrite. Nsg2 accumulated both in the soma and dendrites and was less colocalized with Rab7. Instead, it was retained in enlarged, dendritic early endosomes. These findings not only definitively demonstrate that lysosomal damage disrupts neuronal protein degradation, but also suggest Rab7 mediated early to late endosomal transitions in the dendrite are impacted, with potential compensatory anterograde trafficking of degradative enzymes.

4.2 Materials and Methods

Primary Neuronal Culture and Transfection

All experiments were performed in accordance with the Institutional Animal Care and Use committee guidelines and regulations as the University of Viriginia (ACUC protocol #3422). Primary neuronal cultures were prepared from E18 rat cortex. Cortices from all pups in one litter were combined and thus contained mixed male and female animals. For fixed experiments, cells were plated on poly-L-lysine coated coverslips and incubated with plating medium containing DMEM with 10% horse serum. 1.5 million cells were plater per 60mm dish containing 10-11 coated coverslips, or a coated 60mm dish for western blotting. For live imaging use, cells were plated on similarly coated 35mm glass bottom dishes (MatTek). 250,000 cells were plated per 35mm glass bottom dish. After 4 hours, plating medium was removed and replaced with serum-free neurobasal medium supplemented with B27 (ThermoFisher). For live imaging dishes, B27-supplemented phenol-red free neurobasal medium was used. Transfections were performed via lipofection using Lipofectamine 2000 (Invitrogen). Neurons at day-in-vitro

13 (DIV13) were singly or dually transfected with Emerald-Rab7^{WT} (Addgene #54244, Davidson Lab) and Neep21(Nsg1)-mCherry (generated in Yap et al. 2017) and expressed for 24 hours before use in downstream applications on DIV14.

Immunocytochemistry and image acquisition

Immunocytochemistry was conducted as described (Mulligan et al., 2023). Briefly, cells were fixed in 4% paraformaldehyde/3% sucrose in PBS at room temperature for 15 minutes. Cells were then blocked and permeabilized using PBS/5% normal donkey serum/0.2% TritonX-100 or 0.1% saponin for 20 minutes at room temperature. Saponin permeabilization was used when staining for LAMP1. TritonX-100 was used for all others. Primary and secondary antibodies were diluted in 1% bovine serum albumin (BSA)/PBS and incubated for 1 hour and 30 minutes, respectively, at room temperature. 0.1% saponin was included in BSA antibody dilutions when staining for LAMP1. Coverslips were mounted in ProLong Gold antifade mounting medium (Invitrogen). When co-immunostaining with LAMP1, fixation through secondary antibody staining was performed first for LAMP1 in saponin, then again for other markers using Triton-X.

For widefield imaging, mounted coverslips were viewed using a Zeiss Z1-Observer with a 40x objective (enhanced chemiluminescence Plan-Neofluor 40x/0.9 Pol working distance = 0.41). Apotome structured illumination was used for all images. Images were captured with the Axiocam 503 camera using Zen software (2012 Blue edition, Zeiss) and identically processed in FIJI software.

For live-cell spinning disk confocal microscopy, neurons plated in phenol-red free medium in live cell imaging dishes were viewed using a temperature-controlled (37°C) Nikon TE 2000 microscope using a 60X/NA1.45 oil objective, equipped with Yokogawa CSU 10 spinning disk. Images were captured with a 512X512 Hamamatsu 9100c-13 EM-BT camera. On average, multicolor images were collected at a rate of 1 image/3 seconds for indicated times, with perfect focus on, up to 30 minutes (600 frames) and compiled using FIJI software. Vehicle (DMSO) or LLOMe (final concentration 1mM) were added in

a pre-warmed bolus at 2 minutes (frame 40) live on the stage for all live-imaging experiments.

For Airyscan imaging, mounted coverslips were viewed using the Zeiss 980 NLO system using an inverted Axio Observer microscope with a 63X/NA1.40 oil objective and an 8Y-airyscan detector. Images were collected using Zeiss Zen Blue software on Super-Resolution-4Y mode with 0.13µm z-sections, and z-stacks were identically processed using Zen Airyscan 3-D Processing.

Primary Antibodies

The list of primary antibodies used in this study are as follows: Anti-Rab7 (rabbit monoclonal; 1:100 IF; abcam 137029; RRID:AB_2629474), Anti-Cathepsin B (goat polyclonal; 1:200 IF; R&D Systems AF965; RRID: AB_2086949), anti-LAMP1 (mouse monoclonal; 1:1000 IF; Enzo Life Sciences ADI-VAM-EN001; RRID:AB_2038958), anti-EEA1 (mouse monoclonal; 1:100 IF; BD Biosciences 610456; RRID: AB_399409), anti-MAP2 (chicken polyclonal; 1:2,000 IF; CPCA-MAP2; RRID:AB_2138173; EnCor Biotechnology), anti-Nsg2 (goat polyclonal; 1:400 IF, 1:2000 WB; EB12967; Everest Biotech), and anti–βIII tubulin (chicken polyclonal; 1:7,500 WB; TUJ; Aves Lab).

Secondary Antibodies

For immunocytochemistry, the following Alexa Fluor–coupled antibodies from Invitrogen were used: Alexa488 donkey anti-mouse (A21202; RRID: AB_2535792), Alexa488 donkey anti-rabbit (A21206; RRID: AB_ 2534102), Alexa488 donkey anti-goat (A11055; RRID: AB_2534013), Alexa568 donkey anti-mouse (A10037; RRID: AB_2534017), Alexa568 donkey anti-rabbit (A10042, RRID: AB_2534104), Alexa568 donkey anti-goat (A11057; RRID: AB_162546), Alexa647 donkey anti-mouse (A31571; RRID: AB_2536183), Alexa647 donkey anti-rabbit (A31573; RRID: AB_2535864), Alexa647 donkey anti-goat (A21447; RRID: AB_2340373). The following from Jackson ImmunoResearch Laboratories Inc. was used: aminomethylcoumarin donkey anti–

chicken (Jackson cat#703-155-155, RRID: AB_2340361). For Western blotting, the following LI-COR secondary antibodies were used: donkey anti-chicken-680 (926-68075, RRID: AB_10974977), donkey anti-goat-800 (926-32214; RRID: AB_621846).

Lysosomal perturbation treatments

For induction of lysosomal damage, all neurons were incubated in complete conditioned medium, supplemented with DMSO (vehicle, 0.33%v/v, Millipore Sigma) or L-leucyl-L-leucine dimethyl ester (LLOMe, Sigma) at 1mM (unless otherwise noted) for 1 hour, unless otherwise indicated. DMSO and LLOMe were equilibrated in a small volume of conditioned neuronal medium from the dish fresh at 37° prior to addition to cells.

Cycloheximide (CHX) Chase Experiments and Western Blotting

DIV14 primary cortical neurons plated on poly-L-lysine coated coverslips or 60mm treated tissue culture dishes were treated with the following: *(1)* 4 hours of untreated, complete conditioned medium, *(2)* 2 hours of untreated, complete conditioned medium + 2 hours of the translational inhibitor (CHX, 20µg/mL), *(3)* 1 hour of 1mM LLOMe + 2 hours 1mM LLOMe and 20µg/mL CHX, *(4)* 2 hours of pan-cathepsin inhibitor E64-d (200µM) + 2 hours 200µM E64-d and 20µg/mL CHX. 2 hours of CHX or 2 hours CHX with lysosomal disrupting drugs were started and collected at the same time. Coated coverslips were collected by fixation with 4% PFA/3% sucrose in PBS at room temperature for 15 minutes. 60mM dishes for western blotting were collected by scraping with 1mL sterile 1X DPBS into 1.5mL microcentrifuge tube. Cell pellets were collected by a 10-minute spin at 1000x*g* at 4°C. Cell pellets were directly resuspended in pre-warmed 5X Sample Buffer (Genescript) diluted to 1.2X in water.

Samples containing 1.2X Sample Buffer (Genscript) were separated via SDS-PAGE using 4-12% Bis-Tris (Genscript) in 1X MES Running Buffer (Genscript) according to manufacturer's instructions. Protein was transferred to nitrocellulose membranes (Bio-Rad) using the high molecular weight program of the Trans-Blot Turbo Transfer system

(Bio-Rad) according to manufacturer's instructions. Blocking was performed for 1 hour at room temperature with 100% LI-COR Odyssey Blocking Buffer. Primary antibody incubation (4°C, 16 hours) and secondary antibody incubations (22°C, 1 hour) were performed in 50% Odyssey Blocking Buffer/50% TBS + 0.1% Tween-20. Washes were conducted following primary and secondary incubations, 3 times 10 minutes, with excess TBS + 0.1% Tween-20. Blots were visualized and captured using the LI-COR Odyssey CL-X imaging system with LI-COR ImageStudio software. Densitometry analyses were performed using ImageStudio software.

Kymograph Generation and Analysis

Live imaging of Emerald-Rab7 and/or Neep21-mCherry were analyzed for dendritic motility using kymographs. Using ImageJ, movies were corrected for drift using Manual Registration functions, using a reference static object in the field. Visible dendrites were traced using the segmented line function from the point of intersection with the soma (i.e., proximal dendrites) to the furthest visible point of the process. The multi-kymograph function (line width = 5 pixels) was used to generated kymographs. Kymographs were cropped to remove the first 40 frames (pre-drug addition) so that only post-drug addition motility was considered. For Em-Rab7/Np21-mCherry dual channel imaging, kymographs of dual tracks were generated using KymoMerge (ref Digilio bioprotocols) in addition to single channel kymographs. All kymographs for a given experiment were then submitted to Kymobutler (ref Jakobs 2019) for analysis (submission parameters: threshold = 0.2, minimum object size = 5px, minimum consecutive frames = 3, pixel size = 0.108μm, frame rate = 3 sec). Output summary files from Kymobutler were then analyzed using an R script (*KymobutlerAnalysis_final.Rmd*) to elucidate track displacement, velocity, event directionality, stop time, pause time, and track reversal data, organized by either cell or dendrite.

Statistical Analysis and Image Quantification

All statistical analyses were performed using Graphpad Prism 10 software. All assumptions were deemed to be met before a selection of a statistical test. Normality of residuals was tested using the Shapiro-Wilk test. Specific tests used are denoted in figure legends and statistical significance was defined as a p value < 0.05. All tests were two-tailed and unpaired unless otherwise explicitly stated. All image analysis was conducted with either Bitplane Imaris 9.3.1 or FIJI (NIH). There were no exclusion criteria.

CHX Chase Quantification

Prior to analysis, all images were equivalently batch adjusted for brightness and contrast using the untreated condition as reference. Using ImageJ, composite files were split into individual channels and the MAP2 channel was used to designated dendrites. Dendrites were traced (line width = 15 pixels) using the segmented line tool starting 20μm from the intersection point with the soma and traced for as long as possible away from the soma until intersection with other structures (i.e., medial dendrite segments). The area, raw integrated density, and length of lines were measured from dendrite segments on the Nsg2/p19 channel. An equivalent line was measured in background space. Similarly, using the MAP2 channel, a region of interest was designated around the soma and an equivalent area in the background and measured for area, and raw integrated density on the Nsg2/p19 channel. Soma or dendrite intensity of p19 per unit area was adjusted for background and normalized to the mean of the untreated group on the respective day, before comparison.

Endogenous marker colocalization analyses

All colocalization analyses were conducted using Bitplane Imaris 9.3.1 software. To measure correlation coefficients in the soma, Imaris surfaces were manually created around designated somas. The soma surfaces were masked on the MAP2 channel (outside surface = 0, inside surface= 50,000). Using the colocalization tab, two channels

of interest within MAP2 masked somas were thresholded and coefficients generated using the generate colocalization channel function.

To measure object colocalization in dendrites, dendrites were first straightened and saved as 32-bit composite files in ImageJ, before loading into Imaris. Using the spots function, objects were created for all three channels of multi-channel micrographs [use region-growing function (spots of different sizes, with local contrast) and object size = 0.5 µm]. Designated spot creation parameters were saved for each marker and used across all images and groups for a given experimental replicate. Colocalization of three markers (spots) was computed using the TripleColocalizeSpot (MatLab) function. The total number, mean area, and mean intensity of spots for each channel were manually recorded. The number of dual or triple colocalized spots for each channel with each other channel was also recorded. The percentage of dual or triple colocalized spots out of total number of spots for a given channel was manually computed before comparison in Prism 10 software.

4.3 Results

Somatic late endosomes and lysosomes accumulate in LLOMe

In order to assess the impacts of lysosomal damage on endosomal trafficking and degradation in the central nervous system, we utilized cultured primary rat cortical neurons isolated from embryonic day 18 rat embryos (E18) and cultured *in vitro* for two weeks (DIV14), treated with the lysosomal damaging agent LLOMe. Building upon our observations of Rab7-positive (Rab7+) endosomes in other cell types, we first wanted to test whether lysosomes and late endosomes similarly behaved under lysosomal perturbation conditions in neurons. To do so, we treated DIV14 rat cortical neurons with either vehicle (DMSO) or 1mM LLOMe for one hour, and immunostained for endogenous lysosomal associated protein 1 (LAMP1), Rab7, and the lysosomal acid hydrolase cathepsin-B (CatB). We used microtubule associated protein 2 (MAP2) to visualize neuronal somatic and dendritic domains. For the purposes of this work, we differentially define late endosomes (LEs) and lysosomes (LYS) as follows: LE =

LAMP1+Rab7+CatB*lo*; LYS = LAMP1+Rab7+CatB*hi*.

Figure 1

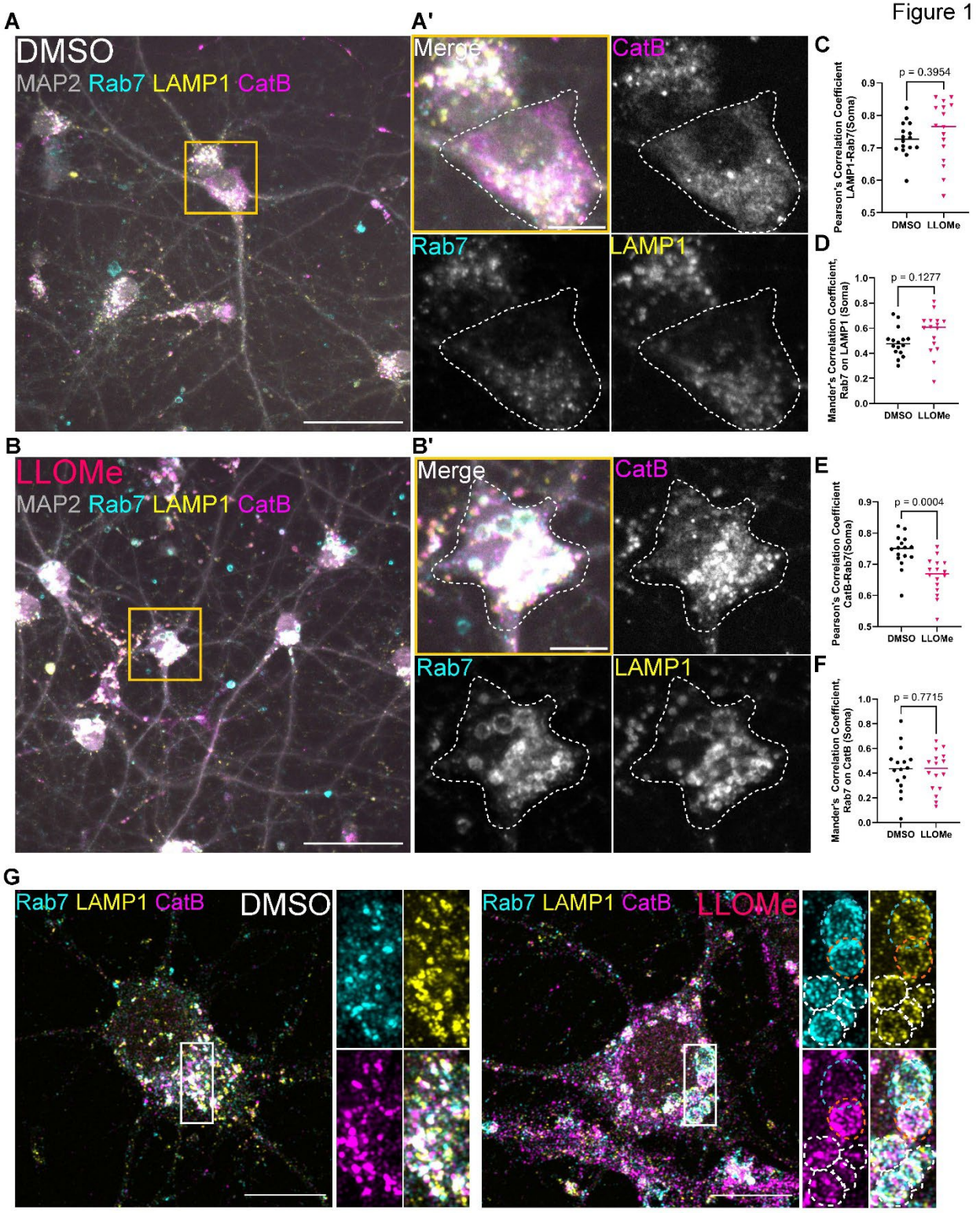

Figure 1 Somatic lysosomes and late endosomes accumulate following LLOMe treatment

Representative widefield micrograph of day-in-vitro 14 (DIV) primary rat cortical neurons treated with either **(A)** vehicle (DMSO) or **(B)** 1mM LLOMe for 1 hour, and immunostained for endogenous somatodendritic microtubule associated protein-2 (MAP2, gray), lysosomal associated membrane protein 1 (LAMP1, yellow), Rab7 (cyan) and lysosomal hydrolase cathepsin-B (CatB, magenta) (scale = 50μm). The soma is boxed in yellow. Soma insets are shown and outlined in white dashes for **(A')** DMSO and **(B')** 1mM LLOMe, demonstrating enlarged Rab7-positive endosomes and lysosomes following LLOMe treatment (scale = 10μm). **(C)** Pearson's Correlation Coeffiecient (PCC) for LAMP1 and Rab7 was calculated for soma regions and compared using unpaired student's t-test (n= 16 somas per group). **(D)** Mander's Correlation Coefficient (MCC) was calculated for the overlap of Rab7 on LAMP1 in the soma and compared using unpaired student's t-test (n= 16 somas per group). **(E)** PCC for CatB and Rab7 was calculated for soma regions and compared using unpaired student's t-test (n= 16 somas per group). **(F)** MCC was calculated for the overlap of Rab7 on CatB in the soma and compared using unpaired Mann-Whitney-U test (n= 16 somas per group). **(G)** Representative Airyscan super resolution micrograph of DMSO (*left*) or 1mM LLOMe treated (*right*) DIV14 primary rat cortical neurons immunostained with MAP2 (gray), LAMP1 (yellow), Rab7 (cyan) and CatB (magenta). Enlarged single and merged insets (white box) are shown to the right of each image. Enlarged endo-lysosomes in LLOMe are outlined with white dashes. An example Rab7+CatB*lo* late endosome (blue dashes) and example Rab7+CatB*hi* lysosome (orange dashes) are specifically noted.

As compared to DMSO controls (**Figure 1A-A'**), we observe stark changes to membrane bound compartments in neuronal somata as a result of LLOMe treatment (**Figure 1B-B'**). Specifically, in DMSO controls there are numerous small Rab7 and LAMP1 compartments, with few bright CatB compartments with a more extensive hazy appearance (**Figure 1A'**). However, in LLOMe treated soma, Rab7 and LAMP1 compartments both expand in parallel, and CatB puncta appear much brighter and larger (**Figure 1B'**). To better understand these changes, and to detect if there were specific enrichments of either LE or LYS among enlarged compartments following damage, we performed coefficient based colocalization analyses between Rab7 and either LAMP1 and CatB. When compared using both Pearson's correlation coefficient (PCC, **Figure 1C**) or the Mander's Correlation Coefficient (MCC, for Rab7 on LAMP1 space, **Figure 1D**), Rab7 and LAMP1 relationships were not significantly changed. This suggests that Rab7 and LAMP1 increasingly occupy the same space as result of LLOMe treatment, which could be LE or LYS enlargement. Comparison of Rab7 and CatB by PCC (**Figure 1 E**) revealed a statistically significant decrease in their colocalization, while the MCC of Rab7 on CatB space was unchanged (**Figure 1 F**). We reconcile the differences in directionality

in Rab7-CatB analyses due to the expansion of Rab7 area, which will differentially impact PCC and MCC calculations. The greater Rab7 occupied space without similar changes in CatB occupied area means Rab7 and CatB will be less correlated in individual pixels within newly occupied Rab7 area, decreasing the PCC. However, the proportion of Rab7 intensity that is with CatB (MCC, Rab7 on CatB) could remain the same despite area expansion. Overall, these data begin to suggest that both Rab7+LAMP1+ late endosomes and lysosomes are disrupted in somata following LLOMe.

To better visualize and distinguish LE from LYS in the crowded soma, we performed Airyscan super-resolution microscopy of quadruple immunostained neurons. We found that DMSO controls had strong, punctate localization of Rab7, LAMP1 and CatB (**Figure 1 G**, *left*). Similar to widefield micrographs, we observe multiple enlarged compartments in LLOMe treated somas (**Figure 1 G**, *right*). At this resolution, we can specifically observe enlarged late endosomes (CatB*lo, blue dashed outline*) and lysosomes (CatB*hi*, orange dashed lysosomes), akin to what we had previously seen in non-neuronal cells. Together, these data suggest that within the soma, lysosomal damage leads to the accumulation of both Rab7+ LE and LYS, and behavior is likely akin to our non-neuronal findings.

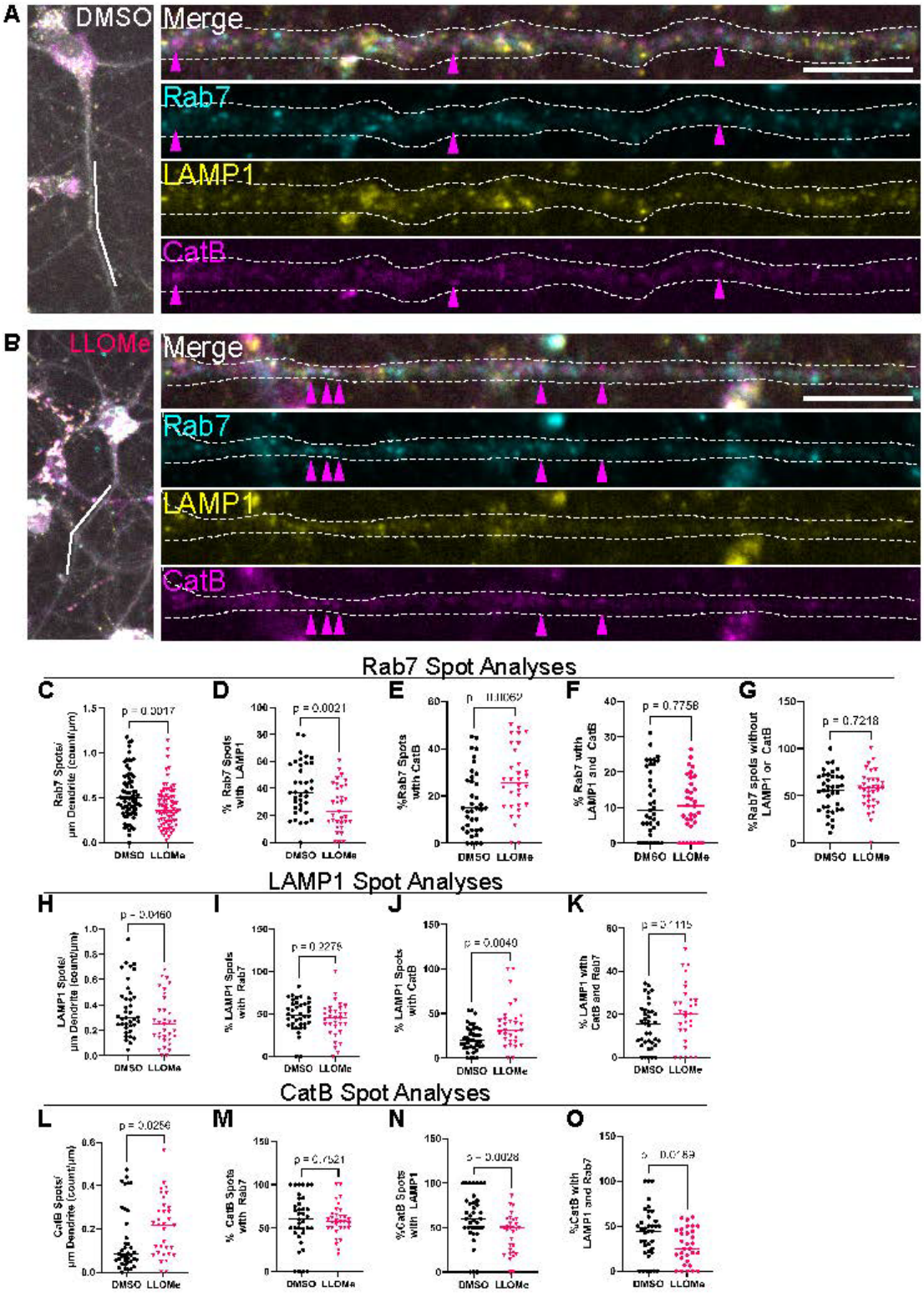
A
DMSO
Merge
Rab7
LAMP1
CatB
B
LLOMe
Merge
Rab7
LAMP1
CatB
Rab7 Spot Analyses
C
p = 0.0017
Rab7 Spots/ µm Dendrite (count/µm)
DMSO LLOMe
D
p = 0.0021
% Rab7 Spots with LAMP1
DMSO LLOMe
E
p = 0.0062
%Rab7 Spots with CatB
DMSO LLOMe
F
p = 0.7758
% Rab7 with LAMP1 and CatB
DMSO LLOMe
G
p = 0.7218
%Rab7 spots without LAMP1 or CatB
DMSO LLOMe
LAMP1 Spot Analyses
H
p = 0.0160
LAMP1 Spots/ µm Dendrite (count/µm)
DMSO LLOMe
I
p = 0.2276
% LAMP1 Spots with Rab7
DMSO LLOMe
J
p = 0.0040
% LAMP1 Spots with CatB
DMSO LLOMe
K
% LAMP1 with CatB and Rab7
DMSO LLOMe
CatB Spot Analyses
L
p = 0.0256
CatB Spots/ µm Dendrite (count/µm)
DMSO LLOMe
M
% CatB Spots with Rab7
DMSO LLOMe
N
p = 0.0028
%CatB Spots with LAMP1
DMSO LLOMe
O
%CatB with LAMP1 and Rab7
DMSO LLOMe

Figure 2 Cathepsin-B positive Rab7 carriers are present in the medial dendrite after LLOMe

Representative widefield micrographs (*left*) and traced, straightened dendrites (*left*, white bar) of **(A)** DMSO or **(B)** 1mM LLOMe treated DIV14 primary rat cortical neurons immunostained with MAP2 (gray), LAMP1 (yellow), Rab7 (cyan) and CatB (magenta), as in Figure 1. Merged and individual channels of straightened dendrites are shown (scale = 10μm). Pink arrowheads indicate cathepsin-B compartments in the dendrite, above threshold, which are increased in LLOMe. **(C-G)** Properties and colocalization of Rab7 compartments in straightened dendrites were analyzed and compared between DMSO and LLOMe treatment groups for (C) the number of Rab7 compartments per μm of dendrite (Mann Whitney U test, n = 71 (DMSO) and 72 (LLOMe) dendrites), (D) the percentage of Rab7 objects that colocalized with LAMP1 objects (two-unpaired student's t-test, n = 37 (DMSO) and 33 (LLOMe) dendrites) (E) the percentage of Rab7 objects that colocalized with CatB objects (Mann Whitney U test, n = 37 (DMSO) and 32 (LLOMe) dendrites), (F) the percentage of Rab7 objects that simultaneously colocalized with both LAMP1 and CatB objects (Mann Whitney U test, n = 37 (DMSO) and 33 (LLOMe) dendrites) and (G) the percentage of Rab7 objects that colocalized with neither LAMP1 nor CatB objects (unpaired student's t-test, n = 37 (DMSO) and 33 (LLOMe) dendrites). **(H-K)** Properties and colocalization of LAMP1 compartments in straightened dendrites were analyzed and compared between DMSO and LLOMe treatment groups for (H) the number of LAMP1 compartments per μm of dendrite (Mann Whitney U test, n = 38 (DMSO) and 33 (LLOMe) dendrites), (I) the percentage of LAMP1 objects that colocalized with Rab7 objects (two-unpaired student's t-test, n = 38 (DMSO) and 31 (LLOMe) dendrites), (J) the percentage of LAMP1 objects that colocalized with CatB objects (Mann Whitney U test, n = 38 (DMSO) and 31 (LLOMe) dendrites), and (K) the percentage of LAMP1 objects that simultaneously colocalized with Rab7 and CatB objects (Mann Whitney U test, n = 38 (DMSO) and 30 (LLOMe) dendrites). **(L-O)** Properties and colocalization of CatB compartments in straightened dendrites were analyzed and compared between DMSO and LLOMe treatment groups for (L) the number of CatB compartments per μm of dendrite (Mann Whitney U test, n = 38 (DMSO) and 33 (LLOMe) dendrites), (M) the percentage of CatB objects that colocalized with Rab7 objects (Mann Whitney U test, n = 37 (DMSO) and 31 (LLOMe) dendrites), (J) the percentage of CatB objects that colocalized with LAMP1 objects (unpaired student's t-test, n = 37 (DMSO) and 31 (LLOMe) dendrites), and (K) the percentage of CatB objects that simultaneously colocalized with Rab7 and LAMP1 (unpaired student's t-test, n = 37 (DMSO) and 31 (LLOMe) dendrites).

LLOMe treated dendrites have increased CatB compartments

To explore the key differences in LMP responses that may arise in neurons due to their size and spatial complexity, we separately explored the impact of LLOMe on dendrites. Using DIV14 cortical neurons immunostained for LAMP1, Rab7, CatB, and MAP2 and treated with DMSO or LLOMe (as in **Figure 1**), we compared colocalization of different markers using an object-based approach on straightened medial dendrite segments (>20μm from the soma), where each punctate structure is an object. In DMSO treated neurons, medial dendrites contained ample Rab7 and LAMP1 compartments and

few CatB^{hi} compartments (**Figure 2 A**). However, in LLOMe treatments, dendrites were depleted of Rab7 and LAMP1 compartments, and were enriched with an increasing number of CatB compartments above background (**Figure 2 B**, *magenta arrowheads*). Quantification confirmed these observations as both Rab7 and LAMP1 density in dendrites were decreased (**Figure 2 C and H**), whereas CatB density was increased (**Figure 2 L**). Object-based analyses demonstrated that dendritic Rab7 compartments are mildly decreased in intensity and increased in area (**Figure S1 A-B**) following LLOMe. A decreasing percentage of them were LAMP1+ (**Figure 2 D and I**, **Figure S1 C**), and an increasing percentage of them were CatB+ (**Figure 2 E**). There was no change to the percentage of Rab7 compartments that were triply immune-positive (**Figure 2 F**) or contained Rab7 alone (**Figure 2 G**). These data suggest that an increased proportion of Rab7 compartments in dendrites contain CatB following LLOMe, without impacting the proportion of bona fide LYS (CatB+Rab7+LAMP1+).

From a LAMP1 perspective, fewer LAMP1 compartments colocalized with Rab7 (**Figure 2 I**) and more colocalized with CatB following LLOMe (**Figure 2 J**). However, LAMP1 did not have increased colocalization with both CatB and Rab7 in LYS following LLOMe (**Figure 2 K**). Given that the total density of LAMP1 is decreased in dendrites (**Figure 2 H**), these data seem to suggest that the limited number of LYS (LAMP1+Rab7+CatB+) in dendrites at baseline is unaffected by LLOMe, while the LAMP1 carrier pool (either LAMP1 alone or LAMP1+Rab7+) is preferentially depleted. The size and area of LAMP1 objects were not changed (**Figure S1 D-E**).

Surprisingly, CatB compartment density, area, and intensity were increased in the medial dendrite following LLOMe (**Figure 2 L**, **Figure S1 F-G**). CatB either existed on its own or with Rab7 (**Figure 2 M**), as colocalization with LAMP1 containing lysosomal compartments was decreased (**Figure 2 N-O**). Thus, most importantly, these data suggest that Rab7+CatB+ carrier vesicles are increased in dendrites following lysosomal insult.

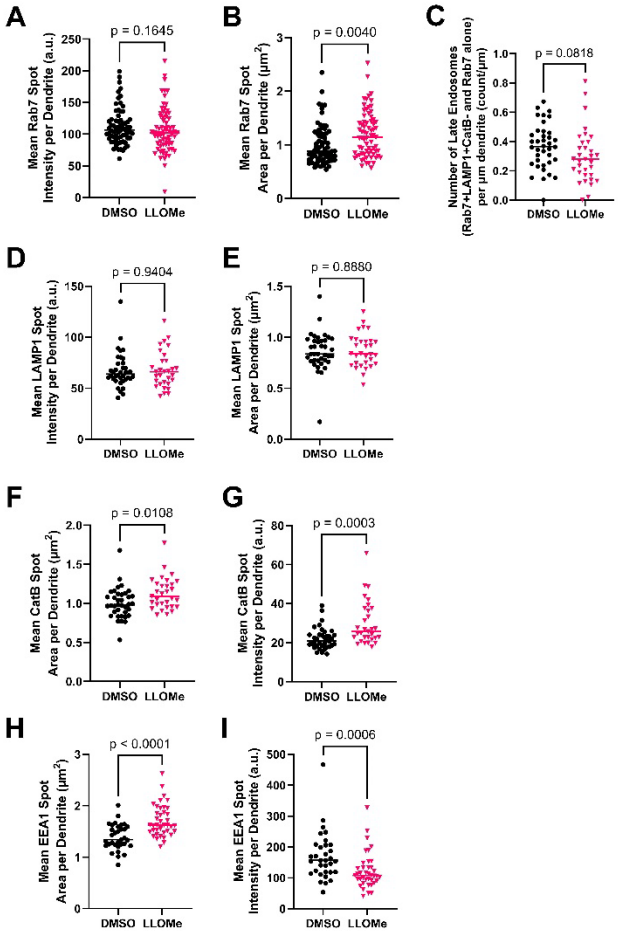

Supplemental Figure 1 Endosomal markers in the medial dendrite have altered sizes and intensities as a result of LLOMe

(A-C) With *Figure 2 C-G*, properties of Rab7 compartments in straightened dendrites were analyzed and compared between DMSO and LLOMe treatment groups for (A) the mean intensity of thresholded Rab7 spots (Mann Whitney U test, n = 68 (DMSO) and 72 (LLOMe) dendrites) (B) the mean area of thresholded Rab7 spots (Mann Whitney U test, n = 69 (DMSO) and 71 (LLOMe) dendrites) and (C) the density of late endosomes (defined as either Rab7+LAMP1+CatB- or Rab7+LAMP1-CatB-) per µm of dendrite (unpaired student's t-test, n = 38 (DMSO) and 33 (LLOMe) dendrites). **(D-E)** With *Figure 2 H-K,* properties of LAMP1 in straightened dendrites were analyzed and compared between DMSO and LLOMe treatment groups for (D) the mean intensity of thresholded LAMP1 spots (Mann Whitney U test, n = 38 (DMSO) and 31 (LLOMe) dendrites) (E) the mean area of thresholded LAMP1 spots (Mann Whitney U test, n = 38 (DMSO) and 31 (LLOMe) dendrites). **(F-G)** With *Figure 2 L-O*, properties of CatB in straightened dendrites were analyzed and compared between DMSO and LLOMe treatment groups for (D) the mean intensity of thresholded CatB spots (Mann Whitney U test, n = 37 (DMSO) and 31 (LLOMe) dendrites) (E) the mean area of thresholded CatB spots (Mann Whitney U test, n = 37 (DMSO) and 31 (LLOMe) dendrites). **(H-I)** With *Figure 3 G-L*, properties of EEA1 in straightened dendrites were analyzed and compared between DMSO and LLOMe treatment groups for (H) the mean intensity of thresholded EEA1 spots (Mann Whitney U test, n = 33 (DMSO) and 39 (LLOMe)

dendrites) (I) the mean area of thresholded EEA1 spots (Mann Whitney U test, n = 33 (DMSO) and 39 (LLOMe) dendrites).

Proximal dendrite Emerald-Rab7 compartments move anterogradely in response to LLOMe

To better understand the dynamics and temporal nature of Rab7+ LE and LYS responses within neuronal somas and dendrites following lysosomal damage, we performed live imaging of DIV14 rat cortical neurons overexpressing fluorescent Emerald-Rab7^{WT} (EmRab7) in the presence of either DMSO or 1mM LLOMe (**Figure 3**). We recorded movies at a rate of one frame per every three seconds, for a total of 600 frames (or 30 minutes) post DMSO or LLOMe addition. Somatic EmRab7 compartments in DMSO appeared static without apparently changing size, though quantification over many movies showed the selected population actually had a smaller diameter by 30 minutes (**Figure 3 A-B**, *top*). In contrast, somatic EmRab7 compartments in LLOMe treated neurons noticeably increased in size in as little as 10 minutes and were statistically larger at 30 minutes when compared to t = 0 minutes, consistent with our fixed imaging observations (**Figure 3 A-B**, *bottom*). We similarly compared the diameter of dendritic EmRab7 compartments. In contrast to somata and our fixed object-based analyses, there was no observable difference between DMSO and LLOMe-treated dendrites (**Figure 3 C-D**), likely due to time points at collection (30mins vs. 1 hr), the quantification method, and our limitations in resolution and ability to perceive small, faint compartments in live imaging. Together, these data suggest that while somatic EmRab7 compartments are highly responsive to LLOMe (in terms of volumetric increase), dendritic compartments are unresponsive in this regard, which begins to establish spatial differences in Rab7 in response to LLOMe.

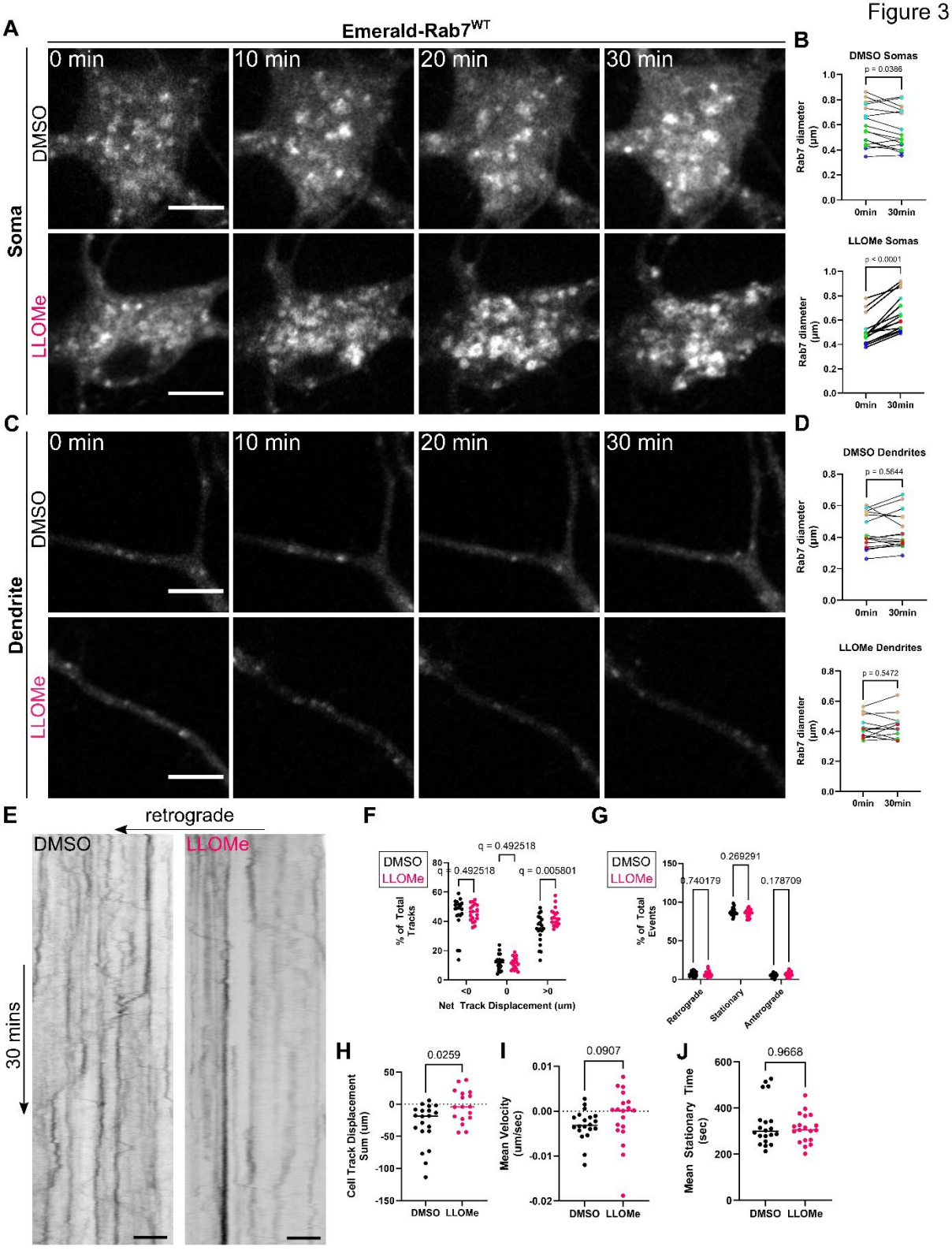
A
Emerald-Rab7WT
0 min
10 min
20 min
30 min
DMSO
LLOMe
Soma
B
DMSO Somas
p = 0.0386
Rab7 diameter (µm)
0min
30min
LLOMe Somas
p < 0.0001
C
Dendrite
D
DMSO Dendrites
p = 0.5644
LLOMe Dendrites
p = 0.5472
E
retrograde
30 mins
F
q = 0.492518
q = 0.492518
q = 0.005801
% of Total Tracks
Net Track Displacement (um)
G
0.269291
0.740179
0.178709
% of Total Events
Retrograde
Stationary
Anterograde
H
0.0259
Cell Track Displacement Sum (um)
I
0.0907
Mean Velocity (um/sec)
J
0.9668
Mean Stationary Time (sec)

Figure 3 Rab7 compartments originating in the proximal dendrite display anterograde bias following LLOMe treatment

(A) Representative stills from time-lapse imaging of DIV14 primary cortical neuron somas expressing Emerald-Rab7^{WT}, and subjected to a 30-minute time course following either DMSO (*top*) or 1mM LLOMe (*bottom*) (frame rate = 3sec/frame for 30 minutes, scale = 5μm). **(B)** The mean diameter of all Rab7 compartments in the somas from (A) DMSO (*top*) and LLOMe (*bottom*) treated cells were measured manually and compared using two-tailed Wilcoxon test (n = 16 somas) and paired two-tailed t-test (n = 15 somas), respectively. Pairs are indicated with connected lines with colors indicating each of 5 independent experiments. **(C)** Representative stills from time-lapse imaging of DIV14 primary cortical neuron dendrite segments expressing Emerald-Rab7^{WT}, and subjected to a 30-minute time course following either DMSO (*top*) or 1mM LLOMe (*bottom*) (frame rate = 3sec/frame for 30 minutes, scale = 5μm). **(D)** The mean diameter of all Rab7 compartments in traced dendrites per cell from (C) DMSO (*top*) and LLOMe (*bottom*) treated cells were measured manually and compared using and paired two-tailed t-test (n = 16 (DMSO) and 15 (LLOMe) cells). Pairs are indicated with connected lines with colors indicating each of 5 independent experiments. **(E)** Representative kymographs of Emerald-Rab7^{WT} compartments in DMSO (*left*) and LLOMe (*right*) treated dendrites over 30-minute time course following drug exposure (scale bar = 10μm, x-axis = distance with most proximal on left, y-axis = time progressing downward). Dendrites traces were started at the soma/dendrite interface and traced anterogradely, such that kymographs represent the most proximal dendrite segments. **(F-J)** All kymographs from DMSO and LLOMe treated DIV14 cortical neurons expressing Em-Rab7 were submitted to Kymobutler AI for analysis and subsequently compared for (F) the percentage of tracks per cell exhibiting anterograde (>0 μm), stationary (0 μm), or retrograde (<0 μm) net displacement (compared using multiple unpaired t-tests with false discovery rate correction), (G) the percentage of events (movements) within tracks classified as anterograde, stationary, or retrograde across all detected tracks, per cell (compared using multiple unpaired t-tests with false discovery rate correction), (H) the sum of all track displacements, per cell (compared using Mann-Whitney U test) (I) the mean stationary time of all tracks, per cell (compared using Mann-Whitney U test), and the mean velocity of all tracks, per cell (compared using Man-Whitney U test) [n = 20 (DMSO) and 19 (LLOMe) Em-Rab7 transfected neurons].

To further investigate the behavior of Rab7 endosomes in dendrites, we performed motility analysis of EmRab7 compartments over 30 minutes of DMSO or LLOMe exposure. We analyzed kymographs that were created by tracing from the soma to the furthest perceptible point of a dendritic branch (**Figure 3 E**). Thus, kymographs overwhelmingly captured motility of proximal dendrite segments. We analyzed all dendrites per cell. In both DMSO and LLOMe treatments, we observed numerous anterograde, retrograde, and stationary EmRab7 tracks (**Figure 3 E**), consistent with previous reports of dendritic Rab7 motility. Kymographs were analyzed in a high-throughput manner using Kymobutler AI (Jakobs et al., 2019). Kymobutler calculates

thresholded *tracks,* which are the individual EmRab7 compartments traced through the time course, and *events*, which are the shorter movements within tracks. We calculated net track displacement of all tracks, which was binned as either anterograde (>0 μm), retrograde (<0 μm), and stationary (=0 μm), and found that the percentage of EmRab7 tracks in LLOMe treated neurons were anterogradely biased (**Figure 3 F**, **Figure S2 A**). Events within these tracks, however, did not show such anterograde bias (p=0.18) (**Figure 3 G**). Other captured parameters including the net sum displacement of all tracks and mean velocity of all tracks also supported an anterograde direction bias following LLOMe (**Figure 3 H-I**; negative numbers refer to retrograde direction). Parameters including mean stationary time of tracks, the number of track reversals, and the mean pause time of tracks were not different between control and LLOMe treated cells (**Figure 3 J**, **Figure S2 B-C**). Together, these data suggest that a subset of EmRab7 compartments in proximal dendrites move anterogradely in response to lysosomal damage.

Supplemental Figure 2

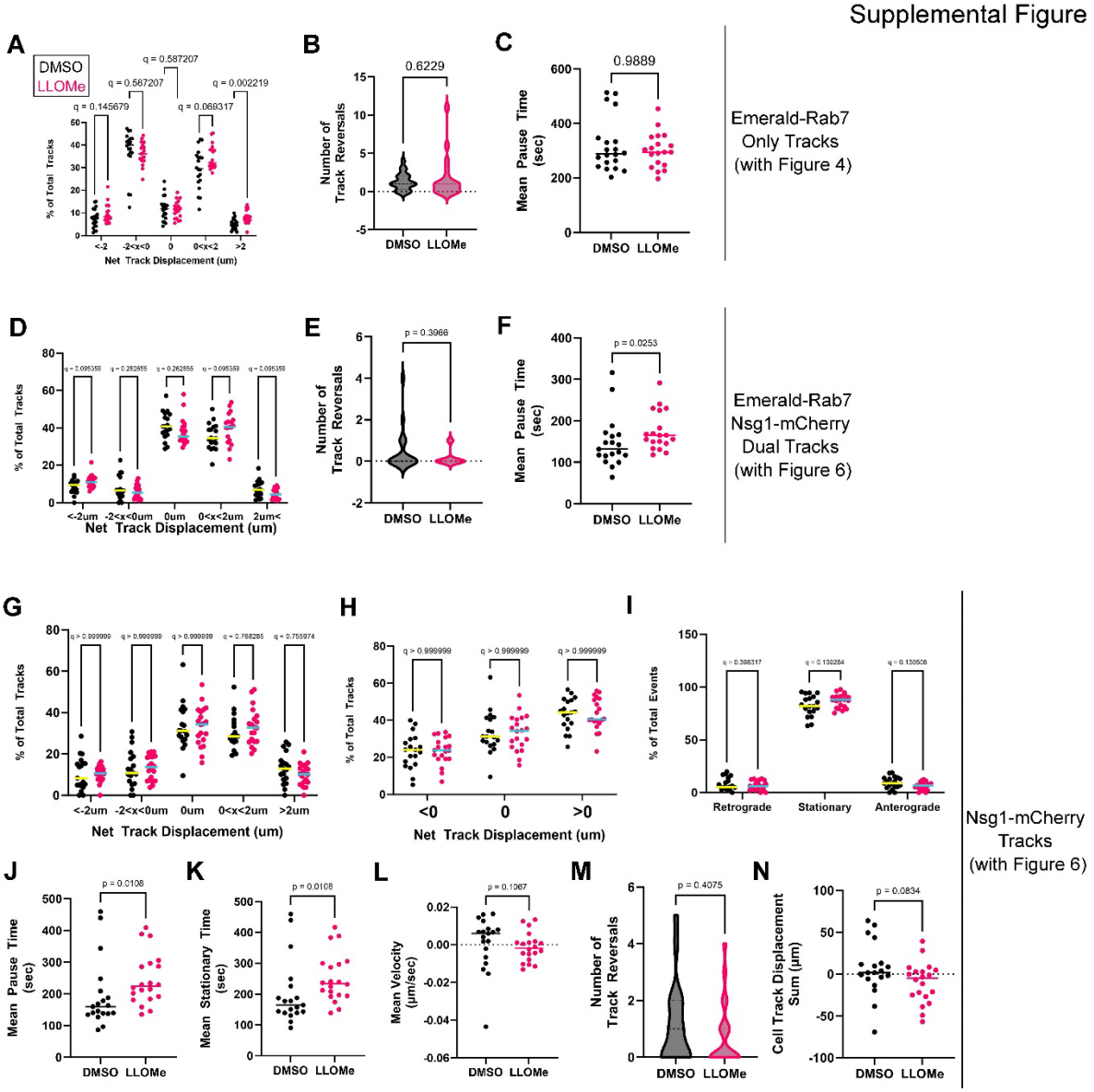

Supplemental Figure 2 LLOMe leaves many aspects of dendritic endosomal motility unchanged

(A-C) With *Figure 3 E-J*, motility in dendrites of Em-Rab7 expressing neurons were analyzed via kymograph generation and Kymobutler submission and subsequently compared for (A) the percentage of tracks per cell exhibiting long anterograde (>2 µm), short anterograde (2 µm>x>0 µm), stationary (0 µm), short retrograde (-2 µm<x<0 µm) or long retrograde (-2µm>) net displacement (compared using multiple unpaired t-tests with false discovery rate correction), (B) the total number of track reversals per cell and (C) the mean pause time of all tracks per cell. B-C compared using Man-Whitney U test. [n= 20 (DMSO) and 19 (LLOMe) Em-Rab7 transfected neurons]. **(D-F)** With *Figure 5 D-H*, motility of dual Em-Rab7 and Np21-mCh tracks in DIV14 cortical neuron dendrites were analyzed via kymograph generation, Kymomerge, and Kymobutler submission and subsequently compared for (D) the percentage of tracks per cell exhibiting long anterograde (>2 µm), short anterograde (2 µm>x>0 µm), stationary (0 µm), short retrograde (-2 µm<x<0

μm) or long retrograde (-2μm>) net displacement (compared using multiple unpaired t-tests with false discovery rate correction), (E) the total number of track reversals per cell and (F) the mean pause time of all tracks per cell. E-F compared using Man-Whitney U test. [n= 19 (DMSO) and 19 (LLOMe) Em-Rab7/Np21-mCh dually transfected neurons]. **(G-N)** With *Figure 5 D-H*, the motility of all Np21-mCh tracks within Em-Rab7/Np21-mCh expressing neurons were analyzed via kymograph generation, Kymobutler submission and subsequently compared for (G) the percentage of tracks per cell exhibiting long anterograde (>2 μm), short anterograde (2 μm>x>0 μm), stationary (0 μm), short retrograde (-2 μm<x<0 μm) or long retrograde (-2μm>) net displacement (compared using multiple unpaired t-tests with false discovery rate correction), (H) the percentage of tracks per cell exhibiting anterograde (>0 μm), stationary (0 μm), or retrograde (<0 μm) net displacement (compared using multiple unpaired t-tests with false discovery rate correction), (I) the percentage of events (movements) within tracks classified as anterograde, stationary, or retrograde across all detected tracks, per cell (compared using multiple unpaired t-tests with false discovery rate correction), (J) mean track pause time per cell, (K) mean track stationary time, per cell, (L) mean track velocity per cell, (M) total number of track reversals per cell, and (N) the summative track displacement per cell. J-M compared using Mann-Whitney U test. [n= 19 (DMSO) and 19 (LLOMe) Em-Rab7/Np21-mCh dually transfected neurons].

LLOMe-mediated lysosomal damage disrupts degradation of neuronal membrane protein p19/Nsg2

To this point, we have observed marked changes to somatic Rab7+ LE and LYS, increased CatB+ endosomes in the medial dendrite, and anterograde motility of a subset of EmRab7 compartments in the proximal dendrite. We have previously shown that Rab7 is essential for neuronal degradation of dendritic membrane proteins. Given the numerous changes to Rab7 across neuronal domains in LLOMe, we thus wanted to assess whether there were impacts on Rab7-mediated neuronal degradation due to lysosomal perturbation. We hypothesized that the disruption of somatic degradative compartments and biases toward anterograde Rab7 motility would impact degradation of dendritic cargos that need to move retrogradely to reach somatic lysosomes. To assess this, we made use of the neuronal specific protein p19/Nsg2, which has a half-life of ~1.5 hours, making it a useful tool to study dendritic degradation. To test p19/Nsg2 degradation, we treated neurons with cycloheximide (CHX) to inhibit new translation for 2 hours, followed by fixation and immunostaining for endogenous p19/Nsg2. As compared to untreated controls, CHX lead to a drastic decrease in the levels of p19/Nsg2, as degradation continued to occur in the absence of new translation (**Figure 4 A-C**, *black and pink*). To then assess what the impacts of LLOMe were on degradation, we pre-treated neurons

with LLOMe for 1 hour, followed by 2 hours of simultaneous CHX/LLOMe treatment. We also utilized a fourth condition as a positive control for degradation inhibition, in which neurons were pretreated for 2 hours with 200 μM of the lysosomal protease inhibitor E64D, followed by 2 hours of simultaneous CHX/E64D treatment. In the presence of LLOMe and CHX, the level of p19/Nsg2 was significantly elevated compared to CHX negative controls in both the soma and dendrites (**Figure 4 A-C**, *teal*), suggesting degradation and retrograde endocytic flux from dendrites is inhibited in LLOMe. However, CHX/LLOMe conditions did not accumulate p19/Nsg2 to the same level as complete protease inhibition with E64D (**Figure 4 A-C**, *purple*).

We then tested the relationship of p19/Nsg2 to somatic Rab7 LE and LYS under CHX chase conditions. Whereas p19/Nsg2 was found inside somatic Rab7 compartments in either untreated or E64D conditions, in LLOMe it was in small puncta outside or on the border of enlarged Rab7 compartments (**Figure 4D**). This was further supported by PCC (**Figure 4 E**) and MCC (**Figure 4 F**) quantifications of the p19/Nsg2 to Rab7 relationship in the soma, in which LLOMe-treated cells had significantly less colocalization as compared to controls. These data suggest 1) that LLOMe impacts transport of p19/Nsg2 into the lumen of somatic Rab7 compartments, and 2) that protease inhibition alone (i.e. E64D) is not sufficient to lead to phenotypic changes in Rab7 or p19/Nsg2 localization in endo-lysosomes.

We confirmed our CHX chase immunofluorescence study by Western blotting against endogenous p19/Nsg2, using the neuronal specific β3-tubulin as a loading control (**Figure 4 G**). Similar to immunofluorescence studies, the levels of p19/Nsg2 were greatly reduced under CHX conditions, but degradation was inhibited in both CHX/LLOMe and CHX/E64D conditions (**Figure 4 G**, *red arrow*). Densitometry analyses confirmed these observations, though in this experiment, we did not observe statistically significant differences between LLOMe and E64D conditions. Altogether, these data suggest that LLOMe inhibits degradation of dendritically delivered cargo, but LLOMe and E64d conditions lead to different spatial accumulation of Nsg2.

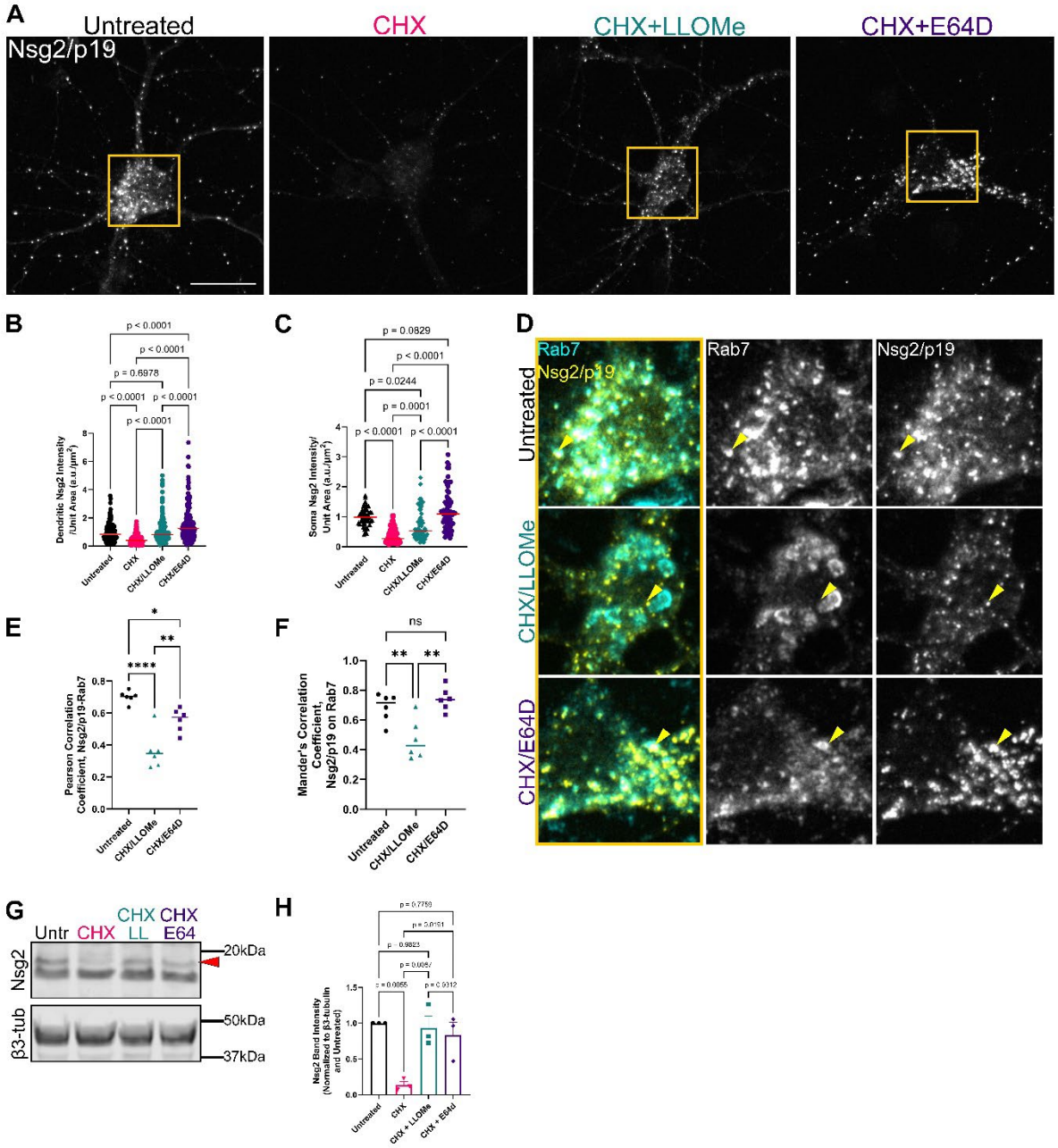

Figure 4 The neuronal specific cargo Nsg2 accumulates in the dendrite and beyond Rab7-positive somatic compartments in lysosomal damage conditions

(A) Representative widefield micrographs of DIV14 primary cortical neurons subjected to cycloheximide (CHX) chase experiment and stained for endogenous Nsg2/p19. CHX chase was conducted over the course of 4 hours as follows: (*1*) 4 hours untreated (*2*) 2 hours untreated, 2 hours 20µg/mL CHX (*3*) 1 hour untreated, 1 hour 1mM LLOMe, 2 hours 20µg/mL CHX + 1mM LLOMe, (*4*) 2 hours 200µM E64D, 2 hours 20µg/mL CHX + 200µM E64D. Nsg2 is rapidly

degraded in the absence of new translation (*CHX)* but is no longer degraded in lysosomal damage (*LLOMe*) or protease inhibition (*E64D*) (scale=20μm) **(B-C)** Nsg2/p19 levels in the (B) dendrites and (C) somas were quantified and compared using Ordinary One-Way ANOVA [n= (B) 48 (Untr), 50 (CHX), 54 (LLOMe), 63 (E64D) somas and (C) 172 (Untr), 207 (CHX), 192 (LLOMe) and 202 (E64D) dendrites from 3 independent experiments] **(D)** Soma insets of (A) showing Nsg2/p19 (yellow) and a Rab7 counterstain (cyan) demonstrating differences in Nsg2/p19 localization relative to Rab7 in LLOMe group. **(E)** PCC of Nsg2-Rab7 and **(F)** MCC of Nsg2 on Rab7 within the soma of Untreated, LLOMe, and E64D treatment groups from (A) compared using Ordinary One-Way ANOVA (n= 6 FOV). **(G)** Representative Western blot of whole cell lystates collected from mass cell culture of DIV14 primary cortical neurons subjected to cycloheximide chase experiments, and immunoblotted for endogenous Nsg2/p19 (*top, red arrow, 19kDa*) and neuron specific loading control β3-tubulin (*bottom, 50kDa*). **(H)** Quantification of immunoblots from (G) analyzed using densitometry analysis and compared using Ordinary One Way ANOVA (n = 3 independent experiments).

Dendritic cargo delivery is stalled in dendrites

Given degradation and the proper flux into somatic compartments of the dendritically delivered cargo p19/Nsg2 was disrupted following LLOMe, we then sought to elucidate whether there were trafficking issues in the dendrites that could explain these findings. To answer this question, we performed live imaging on DIV14 cortical neurons dually transfected with EmRab7 and mCherry-tagged NEEP21/Nsg1 (Nsg1-mCh), a neuronal specific endocytic protein of the same family as p19/Nsg2, with a similar localization and half-life. We therefore studied the somatic and dendritic behavior of compartments carrying degradative cargo (i.e. dual EmRab7+Np21-mCh+ compartments). Consistent with previous reports (Yap et al., 2017), overexpressed Nsg1-mCh strongly colocalized with EmRab7 compartments in the dendrites (**Figure 5 A**, *-2min*) and soma (**Figure 5 B**) at steady state. Following LLOMe exposure, somatic Np21-mCh compartments rapidly enlarged with strong localization of EmRab7 on their limiting membranes (**Figure 5 A-B**). We did not observe such changes in Np21-mCh compartments beyond the proximal dendrite (**Figure 5A**, *white bar*).

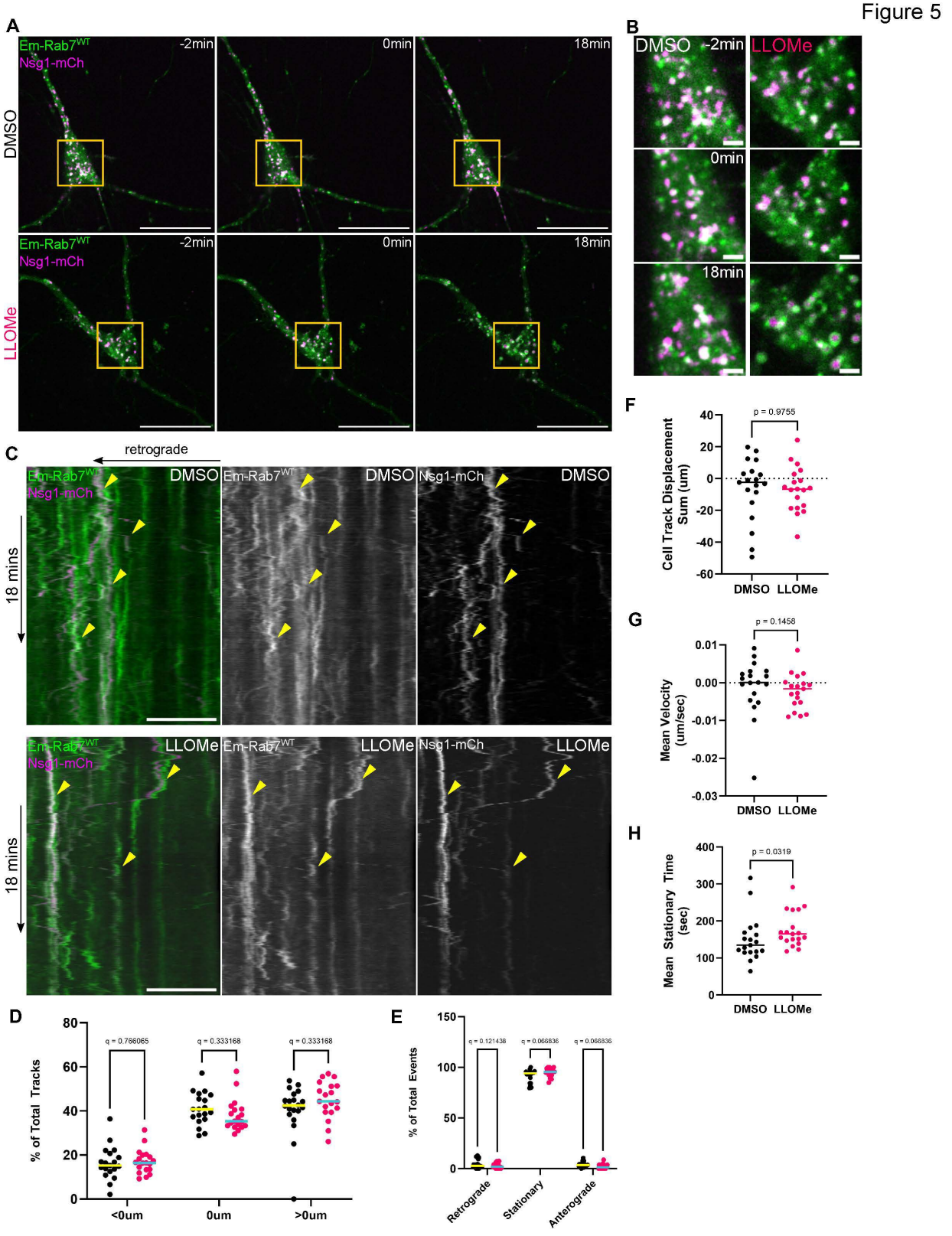
A
Em-Rab7WT
Nsg1-mCh
-2min
0min
18min
DMSO
LLOMe
B
DMSO
LLOMe
-2min
0min
18min
C
retrograde
Em-Rab7WT
Nsg1-mCh
DMSO
LLOMe
18 mins
D
% of Total Tracks
q = 0.766065
q = 0.333168
q = 0.333168
<0um
0um
>0um
E
% of Total Events
q = 0.121438
q = 0.066836
q = 0.066836
Retrograde
Stationary
Anterograde
F
Cell Track Displacement Sum (um)
p = 0.9755
DMSO
LLOMe
G
Mean Velocity (um/sec)
p = 0.1458
H
Mean Stationary Time (sec)
p = 0.0319

Figure 5 Motility of late endosomes in the dendrite following LLOMe is largely unchanged

(A) Representative stills from time-lapse imaging of DIV14 primary cortical neurons expressing Neep21-mCherry [Np21-mCh] (magenta) and Emerald-Rab7^{WT} [EmRab7] (green), and subjected to an 18-minute time course following either DMSO (*top*) or 1mM LLOMe (*bottom*) addition at t = 0min (frame rate = 3sec/frame for 18 minutes, scale = 20μm). Yellow box = representative somas, white bars = representative dendrites. **(B)** Yellow box insets of somas from (A) of EmRab7 (green) and Np21-mCh (magenta) expressing neurons demonstrating enlargement of somatic EmRab7+Np21mCh+ compartments (scale = 2μm). **(C)** Representative kymographs of dendrites (white bar in (A)) EmRab7/Np21mCh expressing neurons demonstrating EmRab7+, Np21-mCh+ and dual EmRab7+Np21mCh+ tracks over time. Example dual positive tracks are indicated by yellow arrowheads. Leftward motility = retrograde, time progresses downward. **(D)** motility of dual Em-Rab7 and Np21-mCh tracks in DIV14 cortical neuron dendrites were analyzed via kymograph generation, Kymomerge, and Kymobutler submission and subsequently compared for (D) the percentage of tracks per cell exhibiting anterograde (>0 μm), stationary (0 μm), or retrograde (<0 μm) net displacement (compared using multiple unpaired t-tests with false discovery rate correction), (E) the percentage of events (movements) within tracks classified as anterograde, stationary, or retrograde across all detected tracks, per cell (compared using multiple unpaired t-tests with false discovery rate correction), (F) the net track displacement of all tracks per cell (compared using unpaired two-tailed t-test), (G) mean stationary time of all tracks per cell, and (H) the mean velocity of all tracks per cell. G-H were compared using Mann-Whitney U test. [n = 19 (DMSO)and 19 (LLOMe) cells].

To better address whether trafficking of Np21-mCh from the dendrite was disrupted in LLOMe, we performed kymograph-based motility analyses (**Figure 5C**), as previously done for EmRab7 expressing cells alone (**Figure 3**). Within both DMSO and LLOMe conditions, we can observe motile and stationary dual EmRab7 and Np21-mCh tracks (**Figure 5 C**, *yellow arrowheads*). In addition to kymographs generated for the individual EmRab7 and Np21-mCh channels, we used an ImageJ macro programmed by our lab (Kymomerge) to create additional kymographs which included only EmRab7/Np21-mCh colocalized tracks. Such dual EmRab7/Np21-mCh compartments are those that we would expect to be delivering Np21-mCh late in the degradative pathway for fusion with lysosomes. Both individual channel kymographs and dual EmRab7/Np21-mCh "Kymomerged" kymographs were then submitted to Kymobutler AI for analysis, as in Figure 3. To our surprise, dual EmRab7/Np21-mCh compartments in LLOMe displayed no statistically significant differences in track displacement (**Figure 5 D**, **Figure S2 D**), the sum of the displacements of all tracks per cell (**Figure 5 F**), the velocity of tracks (**Figure 5 G**), or the number of track reversals (**Figure S2 E**), as compared to DMSO

controls. They only differed in the amount of time spent stationary or paused (**Figure 5 H**, **Figure S2 F**). We performed similar analyses on the isolated Np21-mCh tracks which demonstrated a similar trend across motility parameters (**Figure S2 G-N**). Isolated EmRab7 tracks (data not shown) were similar to the experiments in Figure 3, including an anterograde pool. Therefore, following LLOMe, dendritic Rab7 late endosomes containing cargo stall more in route to the soma within dendrites, but ultimately do not differ in their net displacement, and do not correspond to the anterograde pool we previously observed.

Transitioning early endosomes are disrupted in LLOMe

Surprisingly the behavior of late endosomal Rab7 compartments with cargo was not disrupted following LLOMe in dendrites. To explore alternative hypotheses as to why degradative cargo might accumulate, and to harp back to our original motivation of looking at effects of LLOMe on earlier endosomes in the pathway, we next sought to elucidate whether even more upstream trafficking events from late endosomes were affected by downstream damage. To do this, we counterstained DIV14 cortical neurons with Rab7 and the early endosomal marker early endosome antigen-1 (EEA1) and compared their relationship in the soma and medial dendrites. As the transition from early to late endosomes is determined by a Rab5 to Rab7 switch, and EEA1 is a Rab5 effector protein, we define early endosomes as EEA1+Rab7- and transitioning early to late endosomes (aka “early” late endosomes) as EEA1+Rab7+. Traditional late endosomes are Rab7+ in the absence of EEA1. In DMSO conditions, EEA1 in the soma appeared as many bright dots, that had some but not obvious colocalization with Rab7 (**Figure 6 A**). There were numerous EEA1+ compartments in the dendrites, a number of which colocalized with Rab7 indicative of transitioning early to late endosomes (**Figure 6 B**, *magenta arrowheads)*. In LLOMe conditions, we observed an expansion of the somatic Rab7 compartments but EEA1 compartments did not change in the same manner (**Figure 6 C**). Colocalization coefficient analyses comparing Rab7 and EEA1 in the soma revealed a statistically significant decrease in the PCC, again likely due to the expansion of Rab7 occupied space thus increasing the number of pixels in which Rab7 and EEA1 do not

strongly covary (**Figure 6 D**). Bidirectional MCC calculations revealed there to be no significant difference between DMSO and LLOMe groups (**Figure 6 F-G**). Within medial dendrites in LLOMe, there were noticeably fewer EEA1 compartments (**Figure 6 D,H**) that also tended to be larger and less intense (**Figure S1 H-I**). Interestingly, a lesser percentage of EEA1 objects within dendrites colocalized with Rab7 (**Figure 6 I**). Similarly, the percentage of Rab7 with EEA1 objects also decreased (**Figure 6 J**). These last pieces of data together suggest that transitioning early endosomes (Rab7+EEA1+) are significantly reduced in dendrites following LLOMe, suggesting potential deficits in endosomal maturation as a result of damaged lysosomes.

Figure 6

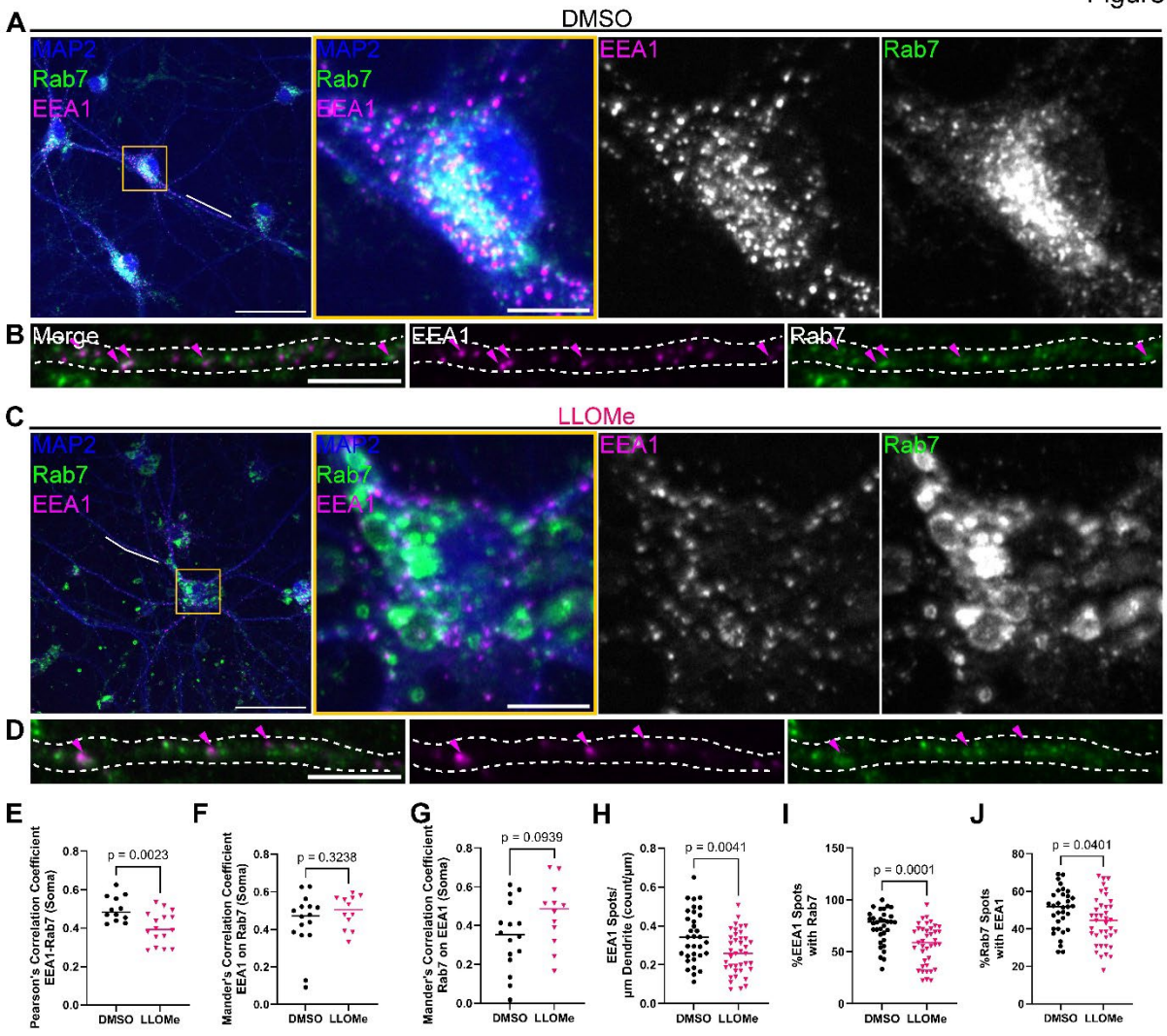

Figure 6 Transitioning early to late endosomes are depleted in LLOMe

(A) Representative widefield micrograph of day-in-vitro 14 (DIV) primary rat cortical neurons treated with DMSO and immunostained for endogenous MAP2 (blue), Rab7 (green) and early endosome antigen 1 (EEA1, magenta). Soma is boxed in yellow and shown as enlarged inset to right, as merged and individual channels. (scale = 50 μm, inset = 10 μm). **(B)** Straightened dendrites (outlined with white dash) from (A) showing merged and individual EEA1 (magenta) and Rab7 (green) channels. Magenta arrowheads mark Rab7+EEA1+ transitioning early to late endosomes. **(C)** Representative widefield micrograph of day-in-vitro 14 (DIV) primary rat cortical neurons treated with LLOMe and immunostained for endogenous MAP2 (blue), Rab7 (green) and EEA1 (magenta). Soma is boxed in yellow and shown as enlarged inset to right, as merged and individual channels. (scale = 50 μm, inset = 10 μm). **(D)** Straightened dendrites (outlined with white dash) from (A) showing merged and individual EEA1 (magenta) and Rab7 (green) channels. Magenta arrowheads mark Rab7+EEA1+ transitioning early to late endosomes. (scale = 10 μm) **(E-G)** Colocalization of EEA1 and Rab7 compartments in the soma (as in A and C) was analyzed and compared between DMSO and LLOMe treatment groups using (E) PCC (unpaired student t-test), (F) MCC of EEA1 on Rab7 (Mann-Whitney U test) and (G) MCC of Rab7 on EEA1 (unpaired student t-test) [n= 12 (DMSO) and 16 (LLOMe) somas]. **(H-J)** Properties and colocalization of EEA1 compartments in the dendrites were quantified and analyzed for (H) the number of EEA1 compartments per μm of dendrite (unpaired student's t-test), (I) the percentage of EEA1 spots colocalized with Rab7 (Man Whitney U test) and (J) the percentage of Rab7 spots colocalized with EEA1 (unpaired student's t-test) [n = 33 (DMSO) and 39 (LLOMe) dendrites.

Lysosomal damage leads to degradative cargo retention in early endosomes

Lastly, we sought to explore what the consequences of having less transitioning early to late endosomes were on trafficking of degradation fated cargos. We again used p19/Nsg2 to probe this question and hypothesized that if early to late transitions were disrupted during lysosomal damage states, p19/Nsg2 would be stuck within early endosomes. To test this hypothesis, we co-immunostained DIV14 cortical neurons treated with either DMSO or LLOMe with Rab7, EEA1, and p19/Nsg2 and evaluated colocalization of p19/Nsg2 within medial dendrites. Within dendrite segments of control cells (**Figure 7 A-B**, *white bar*), p19/Nsg2 could be found alone, in early endosomes (with EEA1 alone, *yellow arrowhead*), in transitioning early to late endosomes (with EEA1 and Rab7, *white arrowhead*) or in late endosomes (with Rab7 alone, *blue arrowheads*). In LLOMe treated cells, the p19/Nsg2 species colocalized with EEA1 became dominant, with much fewer appearing to colocalize with Rab7 and EEA1 together (**Figure 7 C-D**). Consistent with our hypothesis, quantification revealed that the percentage of p19/Nsg2 in early endosomes was significantly increased following LLOMe treatment (**Figure 7 E**), while the percentage in transitioning early late endosomes was significantly reduced

(**Figure 7 F**). Together, these data further support the notion that upstream of damaged lysosomes, the transition from early to late endosomes is disrupted affecting the traffic of degradative cargoes.

Figure 7

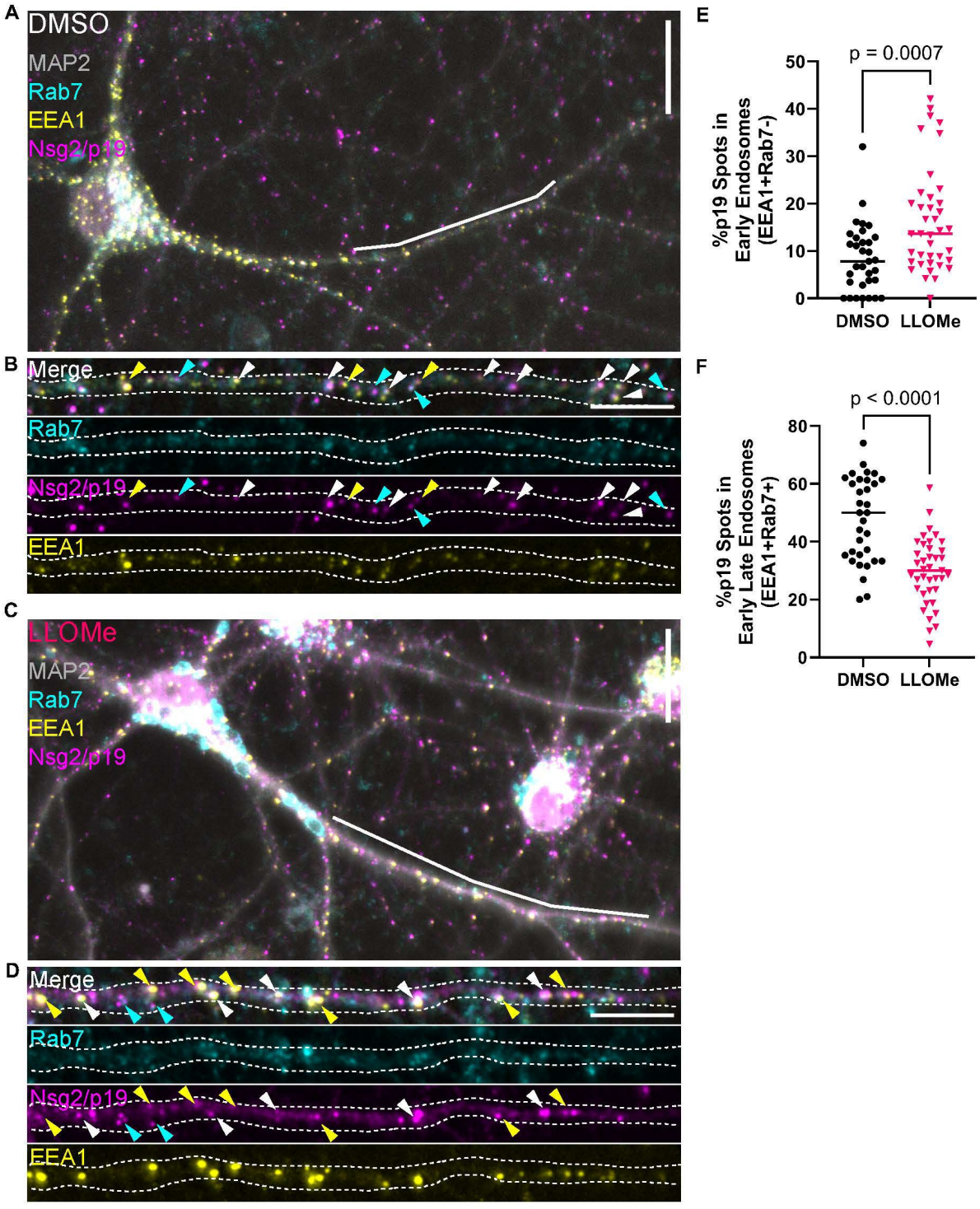

Figure 7 LLOMe disrupts trafficking of Nsg2 out of early endosomes

(A) Representative widefield micrograph of day-in-vitro 14 (DIV) primary rat cortical neurons treated with DMSO and immunostained for endogenous MAP2 (gray), Rab7 (cyan), EEA1 (yellow), and Nsg2/p19 (magenta). Representative dendrite is demarcated by white bar (scale = 50 μm). **(B)** Straightened dendrite (outlined with white dash) from (A) showing merged and individual Rab7 (cyan), Nsg2/p19 (magenta), and EEA1 (yellow) channels . Yellow arrowheads mark Nsg2+EEA1+ early endosomes. Blue arrowheads mark Nsg2+Rab7+ late endosomes. White arrowheads mark Nsg2+EEA1+Rab7+ transitioning endosomes (scale = 10 μm). **(C)** Representative widefield micrograph of day-in-vitro 14 (DIV) primary rat cortical neurons treated with DMSO and immunostained as in (A). Representative dendrite is demarcated by white bar (scale = 50 μm). **(D)** Straightened dendrite (outlined with white dash) from (C) showing merged and individual as in (B). Yellow arrowheads mark Nsg2+EEA1+ early endosomes. Blue arrowheads mark Nsg2+Rab7+ late endosomes. White arrowheads mark Nsg2+EEA1+Rab7+ transitioning endosomes (scale = 10 μm). **(E)** The percentage of Nsg2/p19 that was collocated in early endosomes (EEA1+Rab7-) **(F)** The percentage of Nsg2/p19 that was collocated in transitioning early to late endosomes (EEA1+Rab7+). E-F compared using unpaired two-tailed student's t-test (n= 33 (DMSO) and 39 (LLOMe) dendrites].

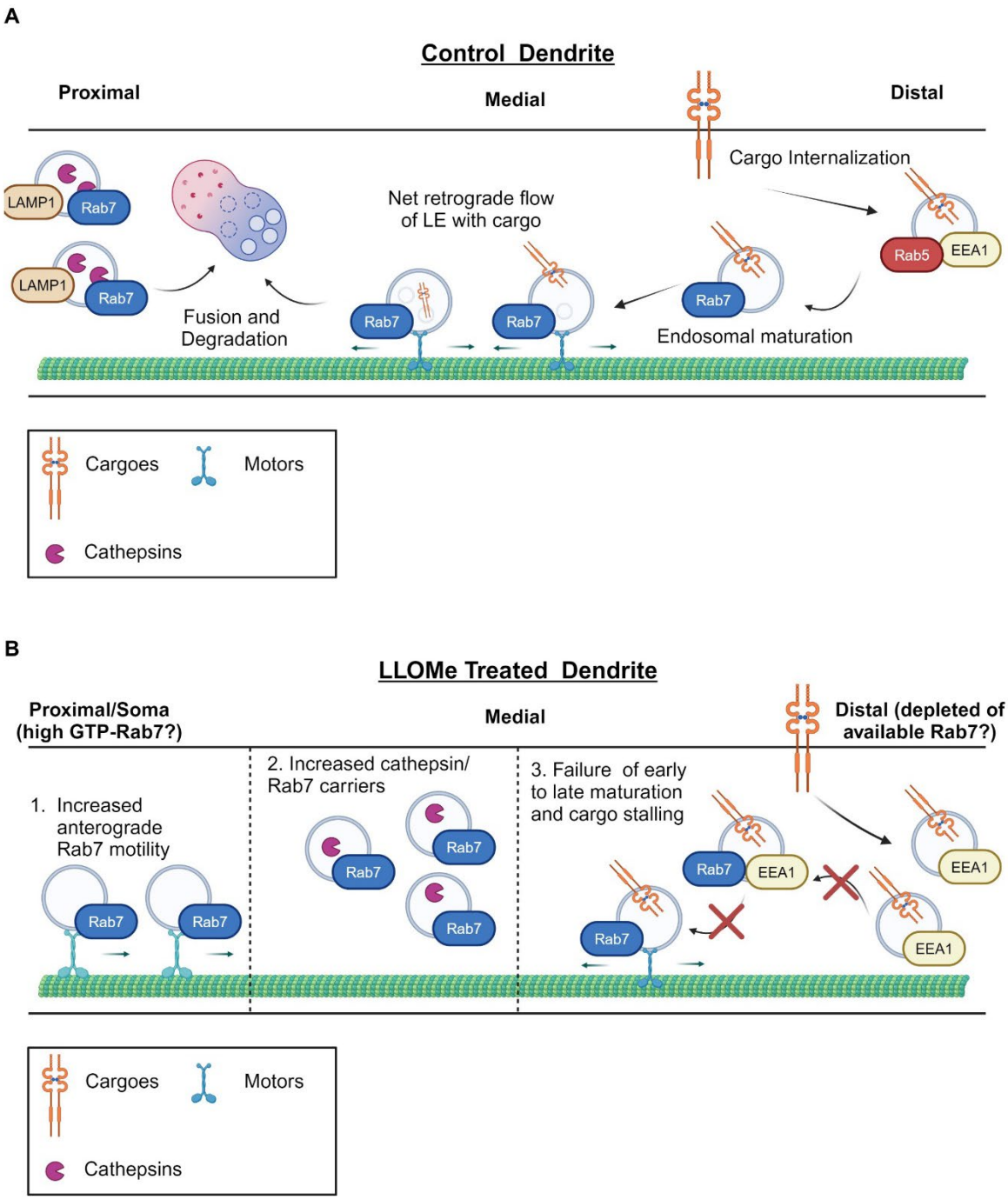

Figure 8 LLOMe alters dendritic membrane trafficking

(A) Schematic demonstrating dendritic membrane trafficking in a healthy dendrite. In the distal dendrite (*right*), membrane receptors are internalized via cargo into Rab5+EEA1+ early endosomes. Through the process of endosomal maturation, early endosomes mature into Rab7+ late endosomes and acquire late endosome properties, like motility, with cargo sorting and fate designation occurring during maturation. Over time, Rab7+ late endosomes

move net retrograde with cargo through the medial dendrite segments to the proximal dendrite. Proximal dendrites contain degradative lysosomes. In the proximal dendrites, dendritically delivered endosomes containing membrane receptors fuse with degradative lysosomes to terminate signals. **(B)** Following LLOMe-mediated endo-lysosomal stress, endosomes in the dendrite display diverse responses. (1) Proximally, a subset of Rab7 compartments exhibit increased anterograde bias, which correlates with an increase in the number of Rab7+ cathepsin-B carriers in the medial dendrite (2). (3) In medial-distal dendrite segments, dendritic membrane receptors like Nsg2 accumulate. This is due to stalling of retrograde motility of dual Rab7+Nsg+ carriers, and through failure of early to late endosomal maturation steps, resulting in retention of Nsg2 in EEA1+ early endosomes.

4.4 Discussion

In summary, this study finds that neuronal Rab7-positive (Rab7+) endosomal compartments are diverse in their responses to lysosomal membrane permeabilization, in a manner dependent on their spatial localization. In the soma, we observe Rab7+ late endosome and lysosome enlargement, as defined by the presence or absence of cathepsin-B (CatB), respectively. These observations are consistent with our previous work in non-neuronal cells, and we posit that the behavior of endosomes within the soma in the context of damage would also be consistent with our previous observations (i.e., V-ATPase mediated Rab7 membrane stabilization, retention of trafficking receptors; see Chapter 3). Definitive evidence of these additional behaviors is a potential route of future experiments. In further support of this, the relationship between Rab7 and EEA1 within the soma is similar to what we had previously observed in non-neuronal cells, in the sense that overt changes to EEA1 compartments and the Rab7-EEA1 relationship were not detected. To our knowledge, this is the first description of the impact of lysosomal damage on non-lysosomes (i.e., early and late endosomes) within the central nervous system, despite the prevalence of LMP in neuronal pathology.

Interestingly, we are better able to parse the relationship between endosomes in lysosomal damage states within the dendrites, given the unique spatial demands of this domain (**Figure 8**). We know from previous work that dendrites display steep spatial maturational and degradative gradients, where the most mature, degradative competent compartments are the most proximal (Yap et al., 2018). Fixed imaging of medial dendrite

segments, beyond the proximal 25 μm, showed the percentage of lysosomal and late endosomes was not changed, while live imaging of EmRab7 demonstrated no change in the phenotypic appearance of endosomes. Further, dual-positive EmRab7/Np21-mCh late endosomes, which we think are late in the degradative pathway and competent for delivery to lysosomes, had normal trafficking behavior except for some additional stalling within the dendrite. Thus, in contrast to the soma, dendritic Rab7+ late endosomal and lysosomal compartments are unperturbed. Instead, we have discovered the novel notion that transitioning early to late endosomes and trafficking of dendritic cargo are affected following lysosomal damage. Hence, key endosomal maturation steps are disrupted.

Novel effects of lysosomal damage on endosomal maturation

How could this deficit in endosomal maturation arise? One possibility, based on our findings in non-neuronal cells, is that neuronal Rab7 is hyperactivated and hyperstabilized with effectors like the V-ATPase on late endosomal compartments following LLOMe treatment (see Chapter 3). This would in theory, deplete the available pool of Rab7 that would normally be required for transition at early endosomal membranes, on a molecular level. A potential alternative molecular explanation is based on the notion that Rab5 to Rab7 transitions require a specific set of Rab7 GEF, Rab5 GAP and phosphoinositides for proper conversion (Stroupe, 2018). In particular, PI3P aids in the recruitment of the Rab7 GEF Mon1-Ccz1 (Poteryaev et al., 2010), and phosphorylation of PI3P to PI(3,5)P2 is characteristic of early to late endosomal conversions (Huotari and Helenius, 2011), which may drive dissociation of Rab5 and Rab7 GEF complexes. There is precedent for LLOMe treatment driving phosphoinositide changes as PI4P is produced on damaged endo-lysosomal membranes to drive lipid exchange and subsequently membrane repair (Radulovic et al., 2022; Tan and Finkel, 2022). How LLOMe impacts PI3P to PI(3,5)P2 conversions, or recruitment of Rab5 GAP and Rab7 GEF to early endosomes remains an open question, however, deficits in any of these behaviors could in theory prevent proper maturation. This hypothesis is complicated by the fact we know very little about the spatial behavior of phosphoinositide conversions and GEF/GAP activity in dendrites.

At an organelle level, there is some evidence in non-neuronal cells that Rab7 may be delivered to Rab5+EEA1+ early endosomes by vesicles, rather than direct association from the cytosol (Podinovskaia et al., 2021). In dendrites, EEA1+ compartments themselves are rather static (Lasiecka et al., 2010), pointing to the need of dendritic Rab7 to “seek out” the early endosome, rather than a serendipitous encounter with Rab7 as the early endosome moves. We have previously observed a deficit in tubulation behavior that would ordinarily generate Rab7 carriers (Chapter 3). Now in neurons, we observed both a depletion of Rab7+ compartments from medial dendrites as a result of LLOMe treatment, and an apparent failure of degradative cargo to fuse with Rab7 compartments in the soma. Thus together, deficient endosomal maturation in the dendrite may be due to the lack of availability and subsequent fusion of competent Rab7 carriers with EEA1+ to facilitate maturation and cargo transport. As Rab7 compartments are mildly retrogradely biased in wild-type neurons, whereas EEA1 compartment motility is minimal, it thus makes sense that p19/Nsg2 would accumulate in dendrites in CHX chase experiments in the absence of endosomal conversion.

Rab7 motility under stress

Interestingly, this study uncovered that in addition to somatic versus dendritic differences in Rab7 responses to lysosomal disruption, there were differences within the motility of Rab7 subsets during the stress response. Notably, a small subset of EmRab7 compartments displayed anterograde motility bias following LLOMe, in both the experiment in which we expressed EmRab7 alone and in co-expression with Np21-mCh. This subset did not, however, correspond to the late endosomal pool containing degradative cargo, whose trafficking was largely unchanged in LLOMe. We similarly noted an increased proportion of Rab7+ cathepsin-B compartments in the medial dendrite by fixed imaging following LLOMe treatment. Given the anterograde pool were not degradative late endosomes, it is tempting to combine these data and speculate that this pool corresponds to a compensatory biosynthetic pool of endosomes delivering hydrolase to the dendrite to ameliorate somatic degradation deficits. Indeed, when comparing dendritic accumulation of p19/Nsg2 in LLOMe and E64D in a CHX chase experiment, the dendrites accumulated significantly less p19/Nsg2 in LLOMe as compared to E64D,

implying that degradative capacity is partially maintained somewhere during LLOMe-mediated damage. It is tempting to further speculate that this subset of Rab7 carriers is the pool typically responsible for fusion with early endosomes to facilitate endosomal transitions, but is not competent for fusion in lysosomal damage states (discussed above).

Another important aspect of the interpretation of LLOMe data is that pH is also perturbed, independent of membrane damage. It is thus possible that LLOMe treatment neutralizes pH across endo-lysosomes, throughout the dendrite. Thus, the change in pH after LLOMe as compared to steady state (ΔpH) is an important factor in determining how different Rab7+ compartments move. For instance, greater ΔpH (neutralization of a Rab7+ lysosome) as compared to a lower ΔpH (neutralization of a transitioning early endosome) likely have different effects on Rab7 stabilization, based on our previous study (Chapter 3), and subsequently motor recruitment. However, we don't currently understand these connections well, and have begun developing tools to more closely observe pH perturbations in dendrites (see *Appendix III*). Current evidence suggests that pH neutralization with can facilitate anterograde movements of compartments to the periphery in non-neuronal systems (Johnson et al., 2016). This, along with our own data, is perplexing given the microtubule orientation in the dendrite is of mixed polarity (~60% plus end out), making directed dendritic transport a complicated process (Maday and Holzbaur, 2016). However, given that a substantial pool of microtubules are in fact minus end out, it is plausible that Rab7 hyperactivation downstream of LLOMe with subsequent stabilization with dynein could facilitate directed anterograde transport into the dendrite of subset of compartments. In contrast, distal axonal compartments can still travel retrogradely to the soma in the presence of pH neutralization (NH4Cl or BafA1) suggesting that in the trafficking of some subsets of Rab7 endosomes, proper pH is not a prerequisite (Harrington et al., 2011). Together, these findings may explain why we observe altered motility only in a subset of Rab7 endosomes following LLOMe.

Many follow up experiments could be performed to better clarify these speculations. Use of inhibitory drugs or could establish motor requirements for Rab7+CatB+ compartment entry into dendrites and the motility of the anterograde Rab7 pool following LLOMe. This would be bolstered through the simultaneous use of tools for

live visualization of either CatB or degradative activity. Unfortunately, we are currently limited by current tools which often depend on pH for localization. Attempts at answering this question using the degradative probe Magic Red-Cathepsin B demonstrated that while most Rab7+MR-B+ compartments are somatic or located in the proximal dendrite, it is impossible to assess their motility or residual degradative capacity in LLOMe because Magic Red-Cathepsin B is no longer trapped in lysosomes if their pH is neutralized (data not shown). The acidification disruption in LLOMe makes MR an unreliable tool for these experiments.

Effects on upstream cargo and signaling

Our study has definitively demonstrated that lysosomal damage results in the disruption of degradation of dendritically delivered cargoes, using the flux sensors NEEP21/Nsg1 and p19/Nsg2. This finding has important considerations for the function of these degradative cargos themselves. NEEP21/Nsg1 contributes to the maintenance of axonal/somato-dendritic polarity (Yap et al., 2008), and may regulate trafficking of synaptic receptors (Alberi et al., 2005; Steiner et al., 2002). Though we are unlikely to see axonal versus somato-dendritic polarization deficits in the short 1-4hr time courses we perform in this study, it is reasonable to speculate that persistent low grade lysosomal disruption and subsequent Nsg1/2 accumulation, such as result of disease or therapeutic treatment, may precipitate polarity deficits and further neuronal dysfunction over time. This idea is also applicable to neuronal trophic signaling, such as through NGF-TrkA or BDNF-TrkB. Internalized and active Trk receptors on Rab7 positive signaling endosomes must properly traffic, either for recycling or degradation, to drive the proper level of trophic signaling (see Chapter 2). Lysosomal disruption, which we now demonstrate disrupts maturation and trafficking of cargos, would lead to improper localization of neurotrophin complexes, likely disrupting downstream survival signaling. Such problem is reminiscent of the Rab7 driven genetic disorder Charcot-Marie Tooth 2B (CMT2B), where improper localization and signaling of NGF-TrkA has been the leading hypothesis as to why neurons die (Cogli et al., 2009; Liu and Wu, 2017) (see also, Chapter 2). Interestingly, both CMT2B and lysosomal damage share the common underlying feature of increased levels of active Rab7, though by different mechanisms. In summary, we have uncovered

that lysosomal damage leads to deficits in endosomal maturation along neuronal dendrites with diverse effects on subsets of Rab7+ endosomes. The conclusions drawn from this study have broad implications for our understand of the relationships between Rab7, motility, pH and cargo degradation within the spatial considerations of neurons.

Chapter V. Characterization of the knockout of Rab7 on endocytic trafficking

Contributions by others: Laura Digilio assisted with primary neuron isolation and culture. Chan Choo Yap provided valuable expertise and guidance.

5.A Abstract

Lysosomes are the principal degradative organelle within cells. Generation and maintenance of lysosomes in part consists of biosynthetic trafficking of luminal proteins, such as acid hydrolases (e.g., cathepsins), to endosomal compartments and retrieval of trafficking receptors (e.g., mannose-6-phosphate receptors (M6PRs)) back to the trans-Golgi network (TGN) for re-use. Failure of faithful lysosome biogenesis results in disrupted proteostasis, which may contribute to cellular death and eventually disease pathology. Rab7 is small endosomal GTPase canonically associated with late endosomes and lysosomes. Rab7 is thought to drive later steps of endosomal biosynthetic trafficking towards highly degradative lysosomes and also regulate fusion events. Though long thought to be an essential gene, the precise steps that require Rab7 within biosynthetic endosomal trafficking have not been comprehensively elucidated and data from different works are not in agreement. Here, using fixed immunostaining and live operational marker approaches of Cre-transfected $Rab7^{fl/fl}$ mouse embryonic fibroblasts, we holistically investigate the necessity for Rab7 across endocytic trafficking steps. We find a consistent increase in the size and decrease in the number of cathepsin-containing compartments, though overall cellular degradative capacity and lysosomal acidification were not impacted. Notably, the mannose-6-phosphate receptor M6PR fails to separate from Cathepsin, suggesting disruption of retrograde retrieval of M6PR. In agreement with this hypothesis, we find that loss of Rab7 drastically impacts the association of the core retromer complex subunit Vps35 with endosomal membranes. Work by others has focused greatly on the roles of Rab7 in late endosome/lysosome fusion and mobility, but these data strengthen the notion that Rab7 is already required for early Vps35-dependent sorting and retrieval events upstream of lysosomes. Loss of Rab7/Vps35 function may ultimately impact downstream degradative compartment composition and morphology. Future work will elucidate the consequences of Rab7-mediated Vps35 depletion and deduce the identity of disrupted cathepsin-containing compartments beyond the simple classification of “dysfunctional lysosomes.”

5.1 Introduction

Lysosomes are principally responsible for maintaining degradation of macromolecules in cells. Establishment of lysosomes and their functional maintenance is dependent on the continuous biosynthetic trafficking of luminal and membranous components of lysosomes via endosomes. The most well studied trafficking of these components includes that of luminal acid hydrolases, such as the cathepsin family of proteins, notably cathepsin-B (CatB), and lysosomal associated membrane proteins (LAMPs and LIMPs). What is the typical route of biosynthetic trafficking to the lysosome? For cathepsins, this begins with biosynthesis in the endoplasmic reticulum and carbohydrate modifications and packaging in the trans-Golgi network (TGN). Cathepsins are recognized and transported from the TGN by mannose-6-phosphate receptors (M6PRs) which deposit cathepsins in more acidic endosomes. M6PRs are then retrieved back to the TGN via retromer (Carosi et al., 2023; Rojas et al., 2008; Seaman, 2004; Seaman, 2018). Retromer, composed of a trimeric (Vps26/29/35) core complex, and sorting nexin dimers (SNX1/2/5/6), sorts out cargo including M6PRs for retrieval, and drives the tubulation and scission of sorted carriers for retrograde retrieval (Carosi et al., 2023). LAMPs are trafficked by alternative routes. Possible hypotheses include constitutive traffic first to the plasma membrane followed by endocytic retrieval and trafficked to lysosomes or direct traffic to lysosomes (Braulke and Bonifacino, 2009; Ecard et al., 2024), possibly in a Vps41-VAMP7 dependent manner (Pols et al., 2013). Despite a largely steady-state localization to lysosomes, LAMPs can thus also be found in trafficking carriers or at the plasma membrane to contribute to the maintenance of lysosomal compartments.

Much of endocytic trafficking regulation is controlled by small, membrane associated GTPases, including Rab proteins. Rab7a (herein Rab7) is canonically associated with late endosomes. What steps in the trafficking of cathepsins and LAMPs are Rab7-dependent? There is evidence from early studies using dominant negative (DN) mutants or siRNA-mediated knockdown of Rab7 that Rab7 is essential for proper maturation of cathepsins from pro- to mature forms (Press et al., 1998; Rojas et al., 2008) and enlarged CatB compartments have also been observed *in vivo* in the pancreas following a conditional Rab7 knockout (Takimoto, 2021). LAMP containing

compartments are also consistently disrupted in Rab7-knockout cells (Hiragi et al., 2022; Homma et al., 2019; Kuchitsu et al., 2018; Takimoto, 2021). Functional properties of lysosomes including acidification (Bucci et al., 2000) and degradation (Bucci et al., 2000; Papini et al., 1997; Vitelli et al., 1997) were demonstrated to be impacted in Rab7 DN mutants. However, the degradative probe MR-B was apparently increased in KO cells in one study, while another degradative probe, DQ-BSA, was decreased in a different study, despite using the same cell line (Hiragi et al., 2022; Kuchitsu et al., 2018). Acidification (Kuchitsu et al., 2018; Liang et al., 2023) and V-ATPase subunit recruitment (Chapter 3) also appears to be intact, if not increased, in the absence of Rab7. Thus, trafficking of cathepsins and LAMPs depend on Rab7 whereas the inherent lysosomal properties (e.g., degradation, acidification) are impacted in some studies but not in others. This thus creates a conundrum since normal degradative capacity requires correct localization of the cathepsins to acidified lysosomes. A mechanistic explanation of their mistrafficking and misprocessing in the absence of Rab7 is lacking since studies usually focus on lysosome function/dysfunction or biosynthetic sorting.

Are earlier endocytic trafficking events also dependent on Rab7? Early endosomes were not impacted in experiments that used DN-Rab7 mutants (Bucci et al., 2000). By contrast, in Rab7 knockout cells, early endosomes are consistently enlarged across studies, suggesting early endosome morphology and behavior may be in part, dependent on Rab7 (Takahashi et al., 2017; Takimoto, 2021). DN or siRNA-mediated knockdown of Rab7 also leads to mis-localization of M6PR (Press et al., 1998; Rojas et al., 2008). Rab7 homologs across multiple organisms (Balderhaar et al., 2010; Nakada-Tsukui et al., 2005; Priya et al., 2015) have been demonstrated to interact with core retromer component Vps35, which contributes to retrograde M6PR trafficking. In line with this, DN or siRNA-mediated knockdown of Rab7 impacts retromer (Vps26 and Vps35) localization (Priya et al., 2015; Rojas et al., 2008; Seaman et al., 2009). However, counter to DN studies, Vps35 signal has been reported to be increased on compartments in Rab7-knockouts (Homma et al., 2019). Furthermore, there is contradictory evidence whether or not M6PR retrieval even depends on retromer in all cell types (Seaman, 2018). Thus, while it has been heavily suggested that Vps35-

mediated M6PR trafficking is Rab7-dependent, our understanding of this process has been muddled by inconsistent data across multiple model systems.

In this study, we have revisited the role of Rab7 in the biosynthetic trafficking of cathepsins and LAMPs. We chose to use an acute knockout of Rab7 for the following reasons: 1) There are many incongruencies between siRNA, dominant negative, and knockout studies, conducted across multiple different cell lines. 2) Previously conducted knockout studies have utilized stable knockout cell lines, which likely upregulate compensatory mechanisms that ensure cell survival. This complicates conclusions as to the primary roles of Rab7. 3) Despite the now many papers that include data with Rab7 disruption, the precise steps and mechanistic connections that connect the gambit of Rab7-dependent phenotypes are lacking. Therefore in this study, I begin to uncover Rab7-regulated steps in biosynthetic trafficking utilizing primary $Rab7^{fl/fl}$ fibroblasts transfected with Cre for only three days. In keeping with other Rab7-KO literature, we find dysfunctional appearing lysosomes, as cathepsin-B and LAMP2 staining is morphologically perturbed. However, functional readouts of lysosomal function in knockout cells, including degradative capacity (via MagicRed-Cathepsin B or DQ-BSA) and acidification (using pH-sensitive dextrans), were not perturbed. Notably, we observe a stark retention of M6PR and CatB together, along with a loss of endosomal recruitment of Vps35, in Rab7KO cells. Overall, these data begin to suggest a more vital role for Rab7 in early steps of lysosomal biosynthesis, with the dependence on Vps35 most critical for control over trafficking, rather than in canonically late functions.

5.2 Materials and Methods

Primary mouse embryonic fibroblast (MEF) isolation and culture

Primary mouse embryonic fibroblasts (MEFs) for all experiments were isolated from E13.5 $Rab7^{fl/fl}$ mice (Kawamura et al., 2012) (Riken BioResource Research Center #RBRC05600). Embryos were sterilely isolated from fluid sacs and torsos were isolated by removal of the head, limbs and tail. Internal organs and spinal cord were then removed

by forceps. Remaining tissue was triturated in 0.05% trypsin-EDTA then incubated at 37°C for 10 minutes. An equivalent volume of 20% FBS in MEF medium [DMEM with glucose and L-glutamine (Gibco 11965-092)] was then added and the tissue was re-triturated. Cells were then spun, re-suspended, and plated in MEF medium containing 10% FBS for expansion, freezing, or downstream applications. Sex of embryos was not determined, and tissue derived from multiple embryos was mixed prior to plating, therefore, all cells were randomized between control and knock-out groups. No animals were excluded. Upon use, MEFs were maintained in MEF medium containing 10% FBS without antibiotics.

Primary mouse embryonic fibroblast (MEF) transfection

For knockout experiments, MEFs were nucleofected using Ingenio Solution electroporation reagent (Mirus Bio) and Lonza AMAXA Nucleofector II with either GFP or pCAG-Cre-GFP. In rescue experiments, MEFs were simultaneously nucleofected with either mCherry or mCherry-Rab7-WT plasmids. Briefly, 1.5 million MEFs and 5µg total DNA were diluted in 100µL of Ingenio Solution in a 0.2cm cuvette (Mirus). MEFs were nucleofected using AMAXA program A-023 (MEF). Cells were immediately recovered in 900µL of pre-warmed complete MEF medium. For fixed applications, cells were then diluted and plated on 10µg/mL fibronectin coated coverslips. For live imaging applications, MEFs were plated on 35mm dishes with 14mm glass bottom inserts (MatTek) coated with 10µg/mL fibronectin for 1 hour at 37°C. Downstream fixation or imaging was conducted three days post pCAG-Cre-GFP nucleofection.

Plasmids

The plasmids used in this study are as follows:

GFP (Clontech), mCherry (Clontech), pCAG-Cre-GFP (Addgene #13776, Cepko Lab), mCherry-Rab7-WT (Addgene #55127, Davidson Lab).

Primary Antibodies

The list of primary antibodies used in this study are as follows: Anti-Rab7 (rabbit monoclonal; 1:100 IF; abcam 137029; RRID:AB_2629474), Anti-Cathepsin B (goat polyclonal; 1:200 IF; R&D Systems AF965; RRID: AB_2086949), Anti-Cathepsin D (goat polyclonal; 1:200 IF; R&D Systems AF1029; RRID: AB_2087094), anti-Vps35 (goat polyclonal; 1:600 IF; abcam 10099; RRID:AB_296841), anti-CI-M6PR (rabbit monoclonal; 1:200 IF; abcam 124767; RRID:AB_10974087), anti-LAMP2 (rat monoclonal, 1:600 IF; DHSB ABL-93, RRID: AB_2134767).

Secondary Antibodies

The following Alexa Fluor–coupled antibodies from Invitrogen were used: Alexa405-Phalloidin (A30104), Alexa488 donkey anti-rabbit (A21206; RRID: AB_ 2534102), Alexa488 donkey anti-goat (A11055; RRID: AB_2534013), Alexa568 donkey anti-rabbit (A10042, RRID: AB_2534104), Alexa568 donkey anti-goat (A11057; RRID: AB_162546), Alexa647 donkey anti-rabbit (A31573; RRID: AB_2535864), Alexa647 donkey anti-goat (A21447; RRID: AB_2340373). The following antibodies from Jackson ImmunoResearch Laboratories, Inc. were used: Alexa488 donkey anti-rat (712-545-153; RRID: AB_2340684), Alexa568 donkey anti-rat (712-585-153; RRID: AB_2340689), Alexa647 donkey anti-rat (712-605-153; RRID: AB_2340694).

Immunocytochemistry and image acquisition

Immunocytochemistry was conducted as described (Mulligan et al., 2023). Briefly, cells were fixed in 4% paraformaldehyde/3% sucrose in PBS at room temperature for 15 minutes. Cells were then blocked and permeabilized using PBS/5% normal donkey serum/0.2% TritonX-100 or 0.1% saponin for 20 minutes at room temperature. Saponin permeabilization was used when staining for LAMP2. TritonX-100 was used for all others. Sequential fixation and permeabilization was used forRab7/LAMP2 co-immunostaining. Primary and secondary antibodies were diluted in 1% bovine serum albumin (BSA)/PBS and incubated for 1 hour and 30 minutes, respectively, at room temperature. 0.1% saponin was included in BSA antibody dilutions when staining for LAMP2. Coverslips were mounted in ProLong Gold antifade mounting medium (Invitrogen).

For fixed imaging, mounted coverslips were viewed using a Zeiss Z1-Observer with a 40x objective (enhanced chemiluminescence Plan-Neofluor 40x/0.9 Pol working distance = 0.41). Apotome structured illumination was used for all images. Images were captured with the Axiocam 503 camera using Zen software (2012 Blue edition, Zeiss) and identically processed in FIJI software. On average, 10 representative fields per condition per experiment were captured, for 3 independent experiments.

For live imaging, media was exchanged in live imaging dishes for phenol-red free DMEM (Gibco 31053-028) plus 10% FBS and 1X GlutaMAX (Gibco 35050-061), prior to start of imaging. Transfected cells were viewed using a Nikon Ti2-E inverted microscope with AX-R confocal microscopy system and 25 mm FOV resonant scanner/25 mm FOV galvano scanner, with an NSPARC detector unit. The system was controlled and images captured using photomultipliers and the Nikon NIS Elements C software. Cells were viewed using a 60X/NA1.40 oil objective and maintained in a temperature-controlled system at 37°C with perfect focus during live image acquisition. Still images of DQ-, MR-, or pHRodo-containing live cells were captured and identically processed using Elements Denoise.ai followed by compiling in FIJI software.

Live Imaging Assays

Magic Red-Cathepsin B

For use of Magic Red Cathepsin-B (MR-B) (ImmunoChemistry Technologies), MR-B stock was prepared as described in manufacturer's protocol and diluted 1:1000 in complete MEF medium. Control and knockout transfected cells were incubated with dilute MR-B for 20 minutes at 37°C. Cells were then sufficiently washed three times with 1X DPBS and replaced with fresh complete phenol red-free DMEM plus 10% FBS and 1X GlutaMAX. MR-B loaded cells were equilibrated by incubation at 37°C for 5 minutes prior to confocal microscopy.

Ratiometric pHRodo pH Readouts

Control and knockout MEFs were loaded with 100µg/mL10kDa pHRodo Red (pHRodo, pH sensitive) dextran plus 100µg/mL 10kDa AF-647 dextran (AF647dex, pH insensitive) (Invitrogen) in complete MEF medium at 37°C overnight for 16 hours. After washing with 1X DPBS, dextrans were chased to lysosomes for an additional 4 hours at 37°C in phenol red-free MEF medium plus 10% FBS and 1X GlutaMAX. Live still images of control and knockout cells were captured via confocal microscopy. To determine relative acidification, the ratio of pHRodo to AF647dex fluorescence was determined within AF647dex demarcated regions of interest.

Ratiometric Degradation (DQ-BSA) Readouts

Control and knockout MEFs were loaded with 5 µg/ml DQ-BSA (DQ-BSA red; D12051; Thermo Fisher Scientific) and 5 µg/ml BSA–Alexa Fluor 647 (BSA–Alexa Fluor 647 conjugate; A34785; Thermo Fisher Scientific) at 37°C overnight for 16 hours. DQ-BSA fluoresces only when proteolytically cleaved, while BSA-647 is fluorescent regardless of degradation and therefore marks all compartments. After washing with 1X DPBS, BSA cargoes were chased to lysosomes for an additional 4 hours at 37°C in phenol red-free MEF medium plus 10% FBS and 1X GlutaMAX. Live still images of control and knockout cells were captured via confocal microscopy. To determine relative degradation, the ratio of DQ-BSA to BSA647 was determined within BSA647 demarcated regions of interest.

Image Analysis and Statistics

All images across conditions from a given day were identically processed post-imaging in Nikon-NIS Elements C software and/or ImageJ (NIH). MR-B and fixed imaging counterstains were analyzed for compartment number, size, intensity, and distribution, along with total cellular fluorescence and area using the following ImageJ macro:
(*EndosomeMarkerDistributionAnalysisManualROI_TotalCellFluorescence_ObejctBased.ijm*).

Briefly, cells selected from a given field were outlined and measured for total fluorescence intensity and area. Then, using the nuclear shadow, a Euclidian distance

map was generated from the nuclear edge to the cellular edge. The desired counterstain was then thresholded and added to the ROI manager as ROIs. ROIs were then measured for area and intensity on the native marker channel, and distance for each ROI to the nucleus was measured using the Euclidian distance map. Number, mean intensity, mean area, and ROI distribution per cell was then analyzed using a generated R script (*EndosomeMarkerAnalysis_all.R*). Total unit intensity per cell area was also determined using a separate R script (*EndosomeMeasurements_TotalCellAreaandInt.Rmd*).

Ratiometric DQ and pHRodo experiments were similarly conducted using an ImageJ macro (*RatioPunctaCountandIntnesityCell.ijm*). Briefly, AF647dex or AF647BSA ROIs were generated. pHRodo/AF647dex and DQBSA/AFBSA647 intensity were then measured within defined ROIs.

Statistical analyses were conducted using Graphpad Prism 10 software. All assumptions were deemed to be met before a selection of a statistical test. Normality of residuals was tested using the Shapiro-Wilk test. Specific tests used are denoted in figure legends and statistical significance was defined as a p value < 0.05.

5.3 Results

To comprehensively assess the role of Rab7 in biosynthetic endocytic trafficking and the effects on lysosomal function, we made use of primary embryonic fibroblasts isolated from $Rab7^{fl/fl}$ mice ($Rab7^{fl/fl}$ MEFs). Given previously described impacts of Rab7 perturbation on cathepsin processing (Press et al., 1998; Rojas et al., 2008) and lysosomal associated membrane protein compartment phenotypes (Bucci et al., 2000; Papini et al., 1997; Vitelli et al., 1997), we first sought to confirm similar perturbations of presumptive lysosomes within our system.

$Rab7^{fl/fl}$ MEFs were nucleofected with either GFP or pCAG-GFP-Cre and cultured for three days before fixation and immunostaining for lysosomal markers. We opted for more acute nucleofection of Cre rather than a stable Rab7-KO cell line to minimize any long-term compensatory mechanisms when Rab7 is not present. In GFP-expressing control cells, there were few cathepsin-B (CatB) positive compartments, which tended to be faint in appearance (two examples shown in **Figure 1 A-A'**). However, in GFP-Cre expressing cells where Rab7 was absent, CatB compartments appeared much larger and brighter (**Figure 1 B-B'**). Quantification of CatB compartments across numerous parameters demonstrated that though there was no significant change in the number of CatB compartments (**Figure 1 D**), they were indeed larger (**Figure 1 E**) and brighter (**Figure 1 F,H**). Importantly, co-expression of mCherry-Rab7-WT to restore Rab7 levels was able to rescue these knockout phenotypes, i.e. CatB compartment area and intensity (**Figure 1 E,F**). This demonstrates that the phenotypes are due to loss of Rab7 and not non-specific side effects of Cre expression. Notably, neither the percentage of peripherally localized CatB compartments (**Figure 1 G**) nor the overall cellular intensity per unit area of CatB (**Figure 1 I**), which takes into account more cytosolic appearing CatB staining, were impacted as a result of Rab7 knockout.

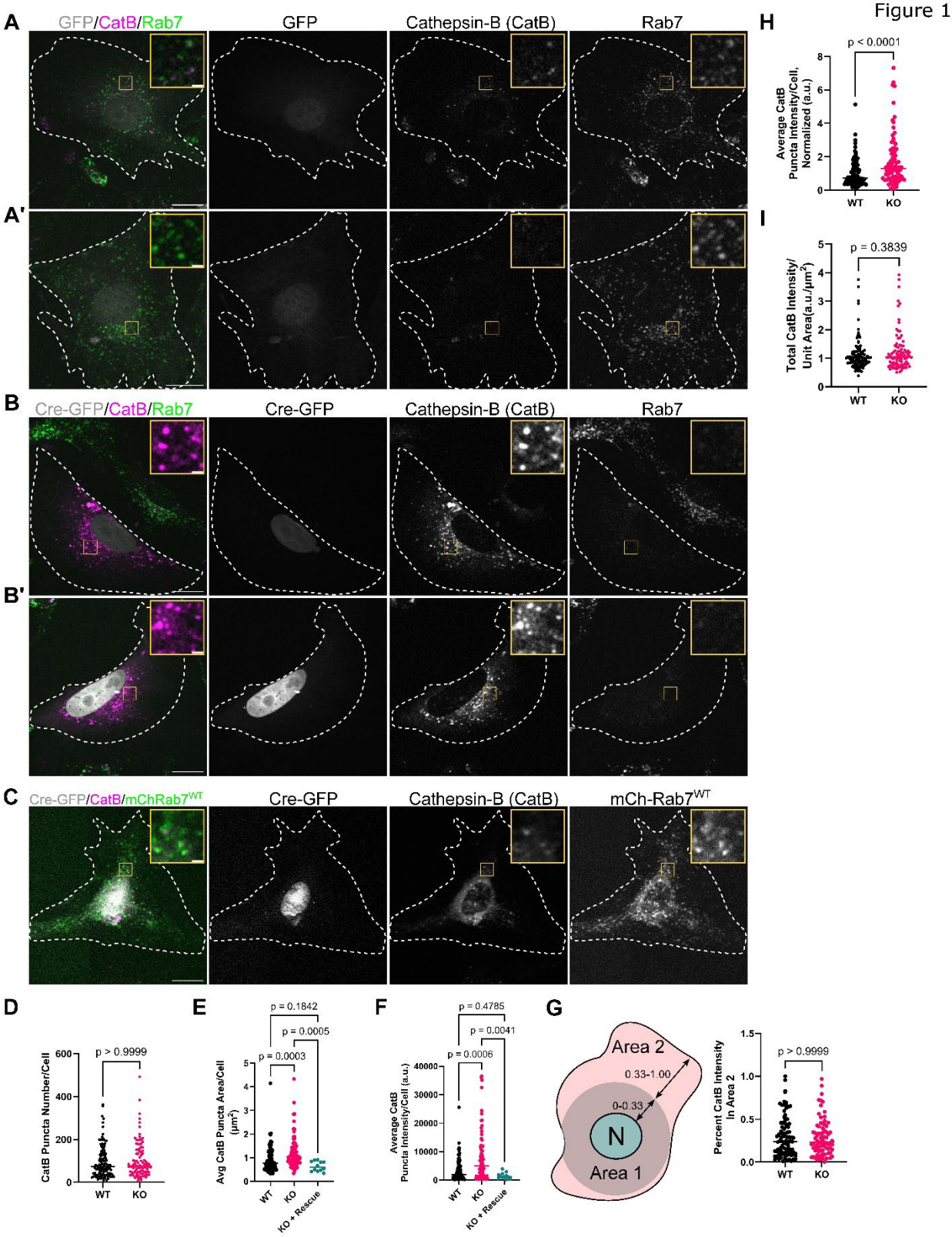
A
GFP/CatB/Rab7
GFP
Cathepsin-B (CatB)
Rab7
A'
B
Cre-GFP/CatB/Rab7
Cre-GFP
Cathepsin-B (CatB)
Rab7
B'
C
Cre-GFP/CatB/mChRab7WT
Cre-GFP
Cathepsin-B (CatB)
mCh-Rab7WT
H
p < 0.0001
Average CatB Puncta Intensity/Cell, Normalized (a.u.)
WT
KO
I
p = 0.3839
Total CatB Intensity/ Unit Area(a.u./μm2)
WT
KO
D
p > 0.9999
CatB Puncta Number/Cell
WT
KO
E
p = 0.1842
p = 0.0005
p = 0.0003
Avg CatB Puncta Area/Cell (μm2)
WT
KO
KO + Rescue
F
p = 0.4785
p = 0.0041
p = 0.0006
Average CatB Puncta Intensity/Cell (a.u.)
WT
KO
KO + Rescue
G
Area 2
0.33-1.00
0-0.33
N
Area 1
p > 0.9999
Percent CatB Intensity in Area 2
WT
KO

Figure 1 Cathepsin-B (CatB) compartments are morphologically perturbed in Rab7 knockout cells

(A-A') Primary mouse embryonic fibroblasts isolated from $Rab7^{fl/fl}$ mice ($Rab7^{fl/fl}$ MEFs) were nucleofected with GFP (gray) and expressed for three days prior to fixation and immunostained for endogenous cathepsin-B (CatB, magenta) and Rab7 (green) (scale = 20μm, inset = 2 μm). Two example widefield micrographs are shown. **(B-B')** $Rab7^{fl/fl}$ MEFs were nucleofected with pCAG-GFP-Cre (gray) and expressed for three days prior to fixation and immunostained for endogenous cathepsin-B (CatB, magenta) and Rab7 (green) (scale = 20μm, inset = 2 μm). Two example widefield micrographs are shown. **(C)** $Rab7^{fl/fl}$ MEFs were nucleofected with pCAG-GFP-Cre (gray) and mCherry-Rab7-WT (green), and expressed for three days prior to fixation and immunostained for endogenous cathepsin-B (CatB, magenta). (scale = 20μm, inset = 2 μm). WT (GFP control), KO (pCAG-Cre-GFP) and KO + Rescue (pCAG-Cre-GFP with mCh-Rab7-WT) cells were analyzed for **(D)** number of CatB puncta per cell (Kruskal-Wallis test, n = 120 (WT), 98 (KO), 12 (Rescue) cells) **(E)** average size of CatB puncta per cell (Kruskal-Wallis test, n = 96 (WT), 80 (KO), 12 (Rescue) cells) **(F)** average CatB puncta intensity per cell (Kruskal-Wallis test, n = 96 (WT), 80 (KO), 12 (Rescue) cells) and **(G)** the percentage of CatB staining in the peripheral two-thirds of cells (*Area 2, left)* (Kruskal-Wallis test, n = 96 (WT), 80 (KO), 12 (Rescue) cells). **(H)** WT and KO CatB puncta intensity (from (F)) was also normalized to the mean each respective day and compared using two-tailed Mann-Whitney-U test (n = 96 (WT) and 80 (KO) cells) **(I)** The total cellular intensity of CatB in WT and KO cells per unit area, normalized to the mean of control on the day collected, was quantified and compared using two-tailed Mann-Whitney-U test (n = 105 (WT) and 92 (KO) cells). Cells counted were from 6 (WT and KO) and 1 (Rescue) independent experiment(s).

Evaluation of cathepsin-D (CatD) compartments by endogenous CatD immunostaining revealed similar results to that of CatB. CatD compartments were generally small and faint under control conditions (**Figure 2 A-A'**) and became larger and brighter following acute Rab7 knockout (**Figure 2 B-B', D-F**). Despite these differences between controls and knockouts, CatD compartment number (**Figure 2 C**), total intensity per unit area (**Figure 2 G**) and peripheral distribution (**Figure 2 H**) were not changed. Lysosome associated membrane protein 2 (LAMP2) compartments in controls were generally small and numerous (**Figure 3 A-A'**) but became brighter and enlarged, to the degree we can appreciate a lumen, in knockout conditions (**Figure 3 B-B'**). Larger compartments tended to appear more perinuclearly as compared to control cells. Despite the presence of these perinuclear large compartments, none of the quantification reached significance (**Figure 3 C-H**). Together, these data suggest that loss of Rab7 perturbs the morphology of cathepsin and LAMP2 containing compartments, typically thought to be lysosomes.

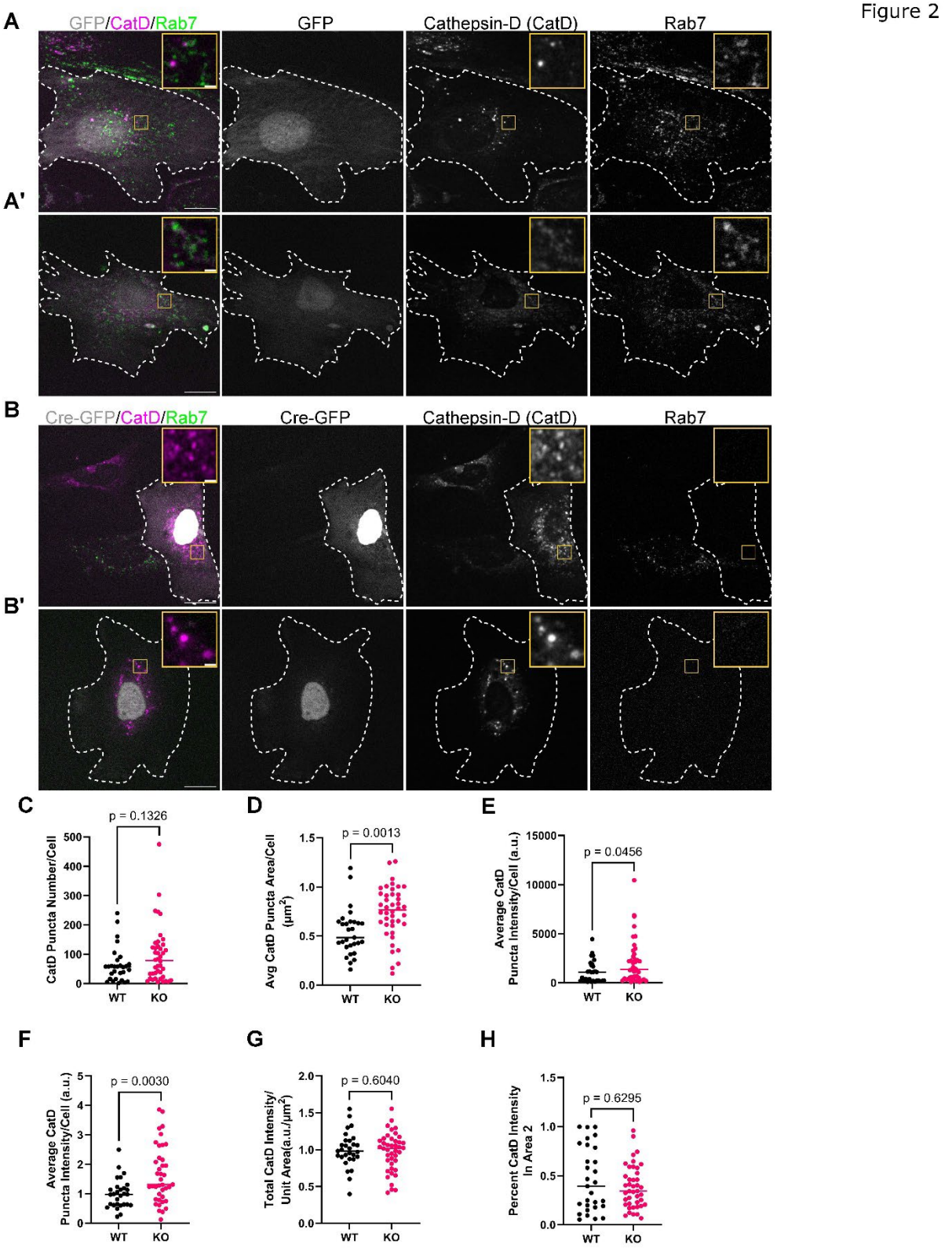
A
GFP/CatD/Rab7
GFP
Cathepsin-D (CatD)
Rab7
A'
B
Cre-GFP/CatD/Rab7
Cre-GFP
Cathepsin-D (CatD)
Rab7
B'
C
p = 0.1326
CatD Puncta Number/Cell
WT
KO
D
p = 0.0013
Avg CatD Puncta Area/Cell (μm²)
E
p = 0.0456
Average CatD Puncta Intensity/Cell (a.u.)
F
p = 0.0030
G
p = 0.6040
Total CatD Intensity/ Unit Area(a.u./μm²)
H
p = 0.6295
Percent CatD Intensity In Area 2

Figure 2 Cathepsin-D (CatD) compartments are morphologically perturbed in Rab7 knockout cells

(A-A') Rab7$^{fl/fl}$ MEFs were nucleofected with GFP (gray) and expressed for three days prior to fixation and immunostained for endogenous cathepsin-D (CatD, magenta) and Rab7 (green) (scale = 20μm, inset = 2 μm). Two example widefield micrographs are shown. **(B-B')** Rab7$^{fl/fl}$ MEFs were nucleofected with pCAG-GFP-Cre (gray) and expressed for three days prior to fixation and immunostained for endogenous cathepsin-D (CatD, magenta) and Rab7 (green) (scale = 20μm, inset = 2 μm). Two example widefield micrographs are shown. WT (GFP control) and KO (pCAG-Cre-GFP) cells were analyzed for **(C)** number of CatD puncta per cell (two-tailed Mann-Whitney U, n = 29 (WT), 42 (KO) cells, from 2 independent experiments) **(D)** average size of CatD puncta per cell (unpaired two-tailed t-test, n = 29 (WT), 42 (KO) cells, from 2 independent experiments) and **(E)** average CatD puncta intensity per cell (two-tailed Mann-Whitney U, n = 29 (WT), 42 (KO) cells, from 2 independent experiments). **(F)** WT and KO CatD puncta intensity (from (E)) was also normalized to the mean each respective day and compared using two-tailed Mann-Whitney U, n = 29 (WT), 42 (KO) cells, from 2 independent experiments. **(G)** The total cellular intensity of CatD in WT and KO cells per unit area, normalized to the mean of control on the day collected, was quantified and compared using two-tailed unpaired t-test (n = 29 (WT), 42 (KO) cells, from 2 independent experiments). **(H)** The percentage of CatD staining in the peripheral two-thirds of cells (*Area 2)* was compared with Mann-Whitney U test (n = 29 (WT), 42 (KO) cells, from 2 independent experiments).

Given our observation that knockout of Rab7 perturbed the morphology of compartments containing typical lysosomal makers, we then wanted to test whether there were any functional consequences of these compartments due to Rab7 loss. As Rab7 functions within the degradative arm of the endocytic pathway, and perturbation of Rab7 function has often been shown to perturb degradation of substrates like EGFR (BasuRay et al., 2013), we sought to test whether acute knockout of Rab7 would impact degradative capacity. To test this, we loaded control and knockout Rab7$^{fl/fl}$ MEFs with various degradative sensors and imaged them live. First, following our observation that cathepsin-containing compartments were morphologically perturbed following Rab7 knockout, we tested whether CatB-mediated degradation specifically was impacted in Rab7 knockout cells. To do this, we loaded cells with the fluorescent substrate Magic Red Cathepsin B (MR-B) which liberates and de-quenches a cresyl violet dye molecule following proteolytic cleavage by CatB. Control cells loaded with MR-B demonstrate numerous, often small, fluorescent compartments (**Figure 4 A-A'**). In Rab7 knockout MEFs (**Figure 4 B-B'**), the number of observed MR-B compartments was comparable to controls (**Figure 4 C**). The compartments themselves appeared similar or occasionally brighter than control counterparts, but there was not a significant difference (**Figure 4 D**). However, consistent

with the CatB and CatD observations, the compartments containing MR-B were larger in size (**Figure 4 E**), further supporting the observation that cathepsin containing compartments are morphologically perturbed. Given the unchanged MR-B staining in Rab7 KO cells, CatB-containing compartments appear to be degradatively normal despite their enlarged size and increased brightness.

Figure 3

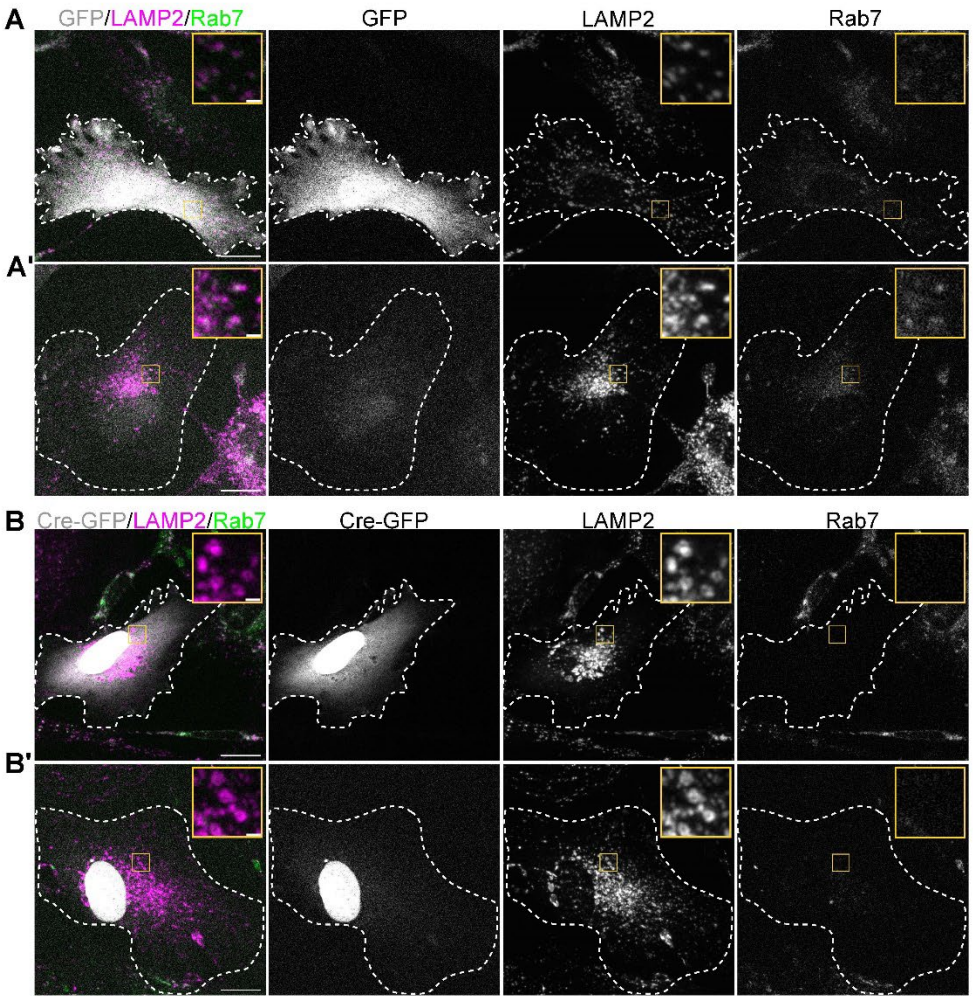

Figure 3 LAMP2 compartments are larger and brighter in the absence of Rab7

(A-A') Rab7$^{fl/fl}$ MEFs were nucleofected with GFP (gray) and expressed for three days prior to fixation and immunostained for endogenous LAMP2 (magenta) and Rab7 (green) (scale = 20μm, inset = 2 μm). Two example widefield micrographs are shown. **(B-B')** Rab7$^{fl/fl}$ MEFs were nucleofected with pCAG-GFP-Cre (gray) and expressed for three days prior to fixation and immunostaining for endogenous LAMP2 (magenta) and Rab7 (green) (scale = 20μm, inset = 2 μm). Two example cells are shown. Consistent with previous reports, LAMP2 compartments appear noticeably larger and brighter than control cells.

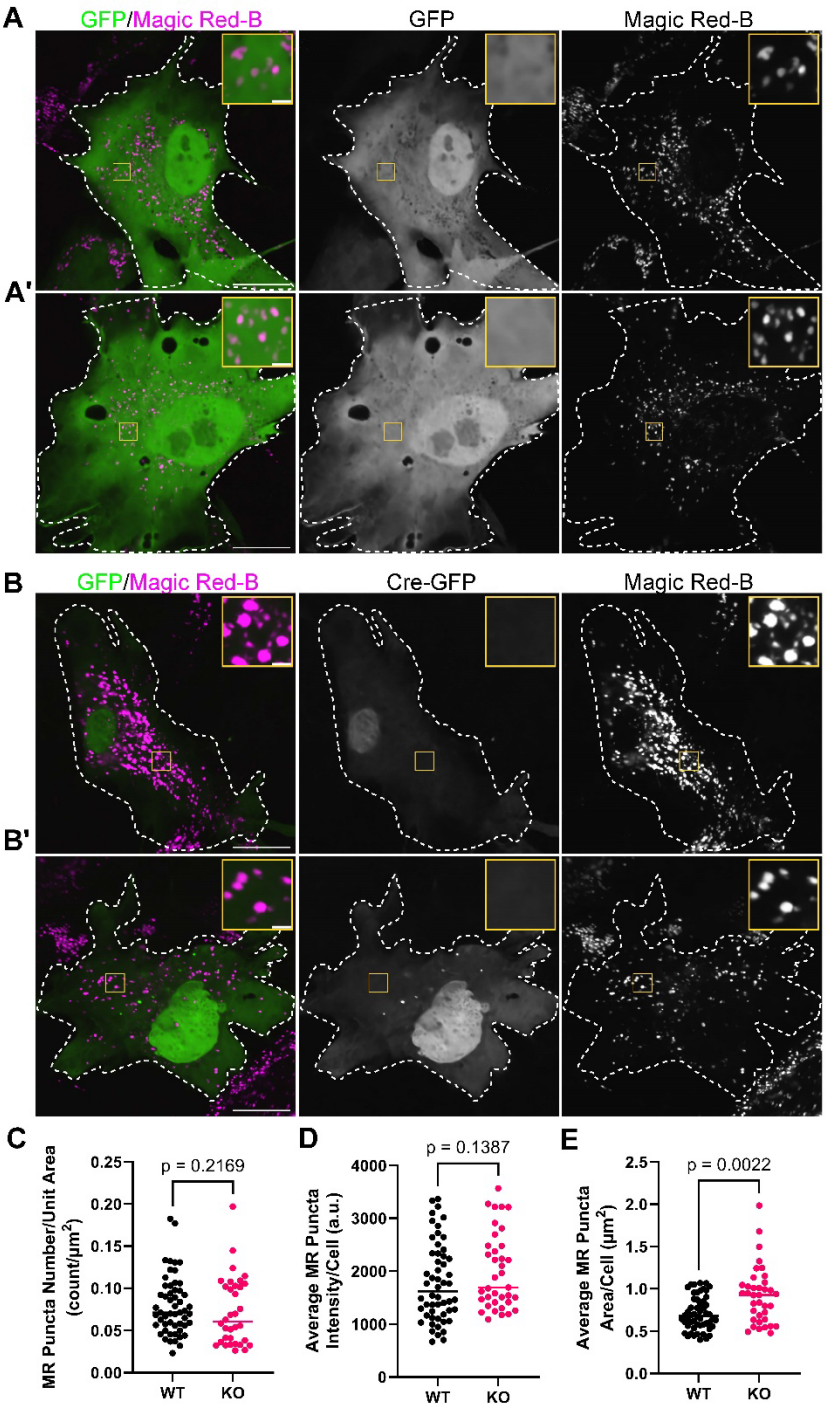

Figure 4 Cathepsin-B proteolysis is unperturbed in Rab7 knockouts

(A-A') Rab7$^{fl/fl}$ MEFs were nucleofected with GFP (green) and expressed for three days prior to loading with cathepsin-B substrate Magic-Red-Cathepsin-B (MR-B, magenta) for 15 minutes. MR-B loaded cells were washed and then

imaged live via confocal microscopy. Two representative still images captured from live cells are shown. MR-B positive compartments indicate sites of CatB mediated proteolysis (scale = 20μm, inset = 2 μm). **(B-B')** Rab7$^{fl/fl}$ MEFs were nucleofected with pCAG-GFP-Cre (green) and expressed for three days prior to MR-B (magenta) proteolysis assay (scale = 20μm, inset = 2 μm). Two representative still images captured from live cells are shown. Control (WT) and knockout (KO) cells were analyzed for the **(C)** number of MR puncta per unit area, per cell, compared using two-tailed Mann-Whitney U test (n = 54 (WT) and 34(KO) cells, from 2 independent experiments) **(D)** mean MR puncta intensity per cell compared using Mann-Whitney U test (n = 54 (WT) and 37 (KO) cells, from 2 independent experiments) and **(E)** the mean MR puncta area per cell, compared using Mann-Whitney U test (n = 54 (WT) and 37 (KO) cells, from 2 independent experiments)

We similarly assessed degradation by using a dye-quenched BSA (DQ-BSA), which is quenched until proteolytically cleaved by hydrolases within lysosomes (i.e., fluoresces only in degradative compartments). In contrast to MR-B, appearance of red fluorescence by DQ-BSA depends on normal endocytosis and subsequent transport to lysosomes as well as degradative capacity in lysosomes. We loaded cells overnight followed by a chase to lysosomes with DQ-BSA and AlexaFluor-647-coupled BSA to ratiometrically assess both endocytosis capability (both Alexa647 and DQ are changed) and degradative capacity (Alexa647 is changed but DQ is not). In control cells, we observe numerous dually positive DQ-BSA/BSA-647 containing compartments (**Figure 5 A-A').** In knockout cells, the number of compartments containing DQ-BSA and BSA-647 was noticeably fewer (**Figure 5 B-B', C**) even though we observed no decrease in CatB- or CatD-positive compartments. However, evaluation of both the ratio of DQ-BSA to BSA-647 (**Figure 5 D**) and the total cellular DQ-BSA intensity per unit area (**Figure 5 E**) revealed there to be no difference between control and knockout cells. Interestingly, there was a significant decrease in the intensity of the BSA-647 fill per cell area (**Figure 5 F**), suggesting the endocytic uptake of DQ-BSA and BSA-647 conjugates is likely impacted in the absence of Rab7. Together, these data suggest that while degradative compartments are morphologically altered, they are still degradatively competent to the level of control cells in the absence of Rab7.

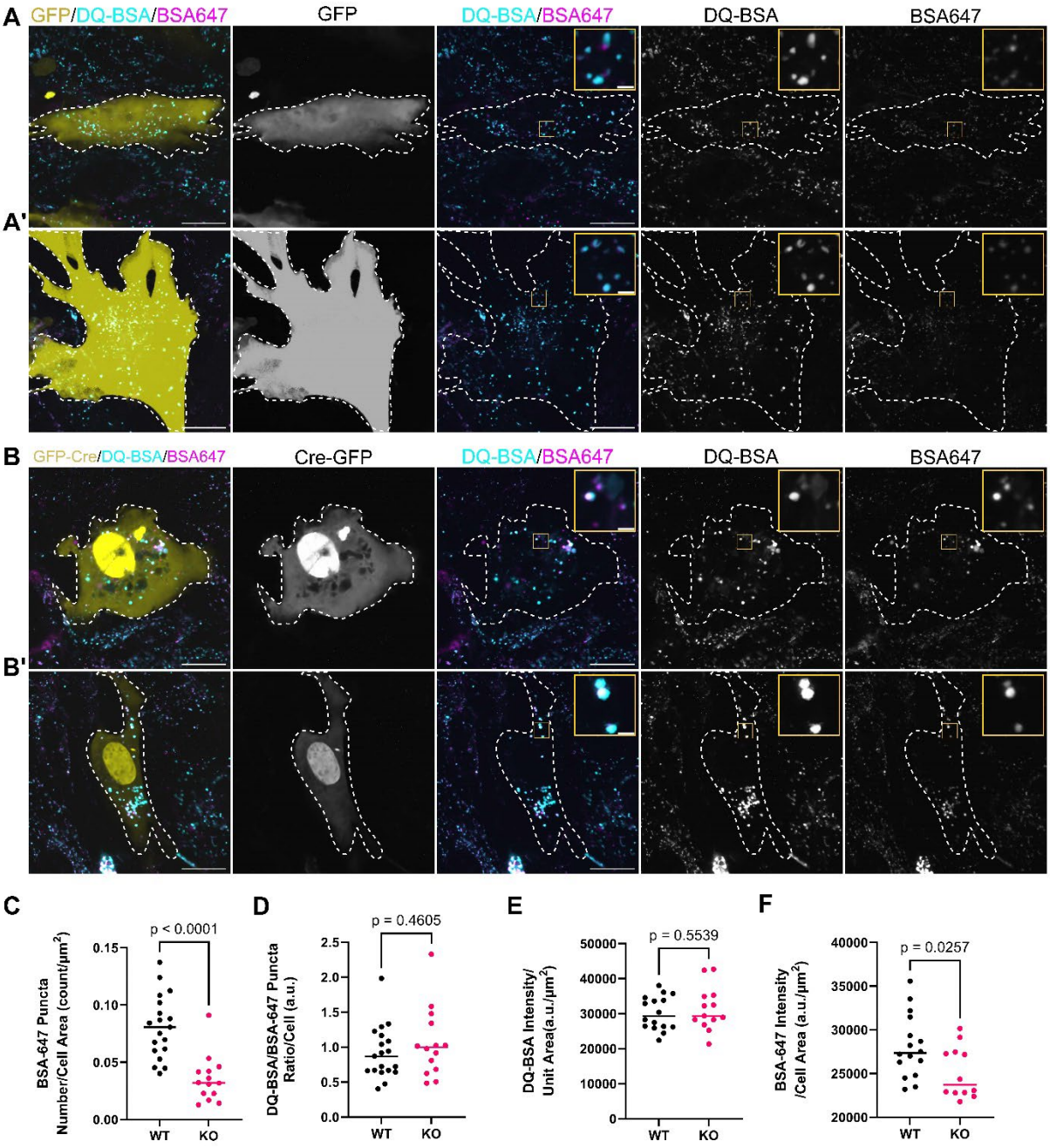

Figure 5 Cellular degradative capacity is unchanged in the absence of Rab7, though endocytosis is affected

(A-A') Rab7$^{fl/fl}$ MEFs were nucleofected with GFP (yellow) and expressed for two days prior to simultaneous loading with dye-quenched BSA (DQ-BSA, cyan) substrate and Alexa-Fluor 647 coupled BSA (BSA647, magenta) overnight for 16 hours. After overnight load, BSA was chased to terminal compartments for 4 hours before live confocal imaging. DQ-BSA is fluorescent only when cleaved by lysosomal hydrolases while BSA647 serves as an endocytic fill. Two representative still images captured from live cells are shown. (scale = 20μm, inset = 2 μm). **(B-B')** Rab7$^{fl/fl}$ MEFs were

nucleofected with pCAG-GFP-Cre (yellow) and expressed for two days prior to DQ-BSA (cyan)/ BSA647 (magenta) proteolysis assay (scale = 20μm, inset = 2 μm). Two representative still images captured from live cells are shown. Control (WT) and knockout (KO) cells were analyzed for the **(C)** number of BSA647 puncta per unit area, per cell, compared using unpaired two-tailed t-test (n = 19 (WT) and 14 (KO) cells, from 1 independent experiment) **(D)** mean ratio of DQ-BSA:BSA647 intensity per puncta, per cell compared using Mann-Whitney U test (n = 19 (WT) and 14 (KO) cells, from 1 independent experiment) and **(E)** the mean DQ-BSA intensity per unit area per cell, compared using two-tailed unpaired t-test (n = 16 (WT) and 13 (KO) cells, from 1 independent experiment) and **(F)** the mean BSA647 intensity per unit area per cell, compared using Mann-Whitney U test (n = 16 (WT) and 12 (KO) cells, from 1 independent experiment).

Next, we wanted to test whether Rab7 was essential for other typical features of degradative lysosomes, namely acidification. Rab7 has been implicated in regulating endosomal and lysosomal pH (Bucci et al., 2000; De Luca et al., 2014; Johnson et al., 2016) though our recent work (Chapter 3) and other disparate knockout studies (Kuchitsu et al., 2018) seem to suggest otherwise. To assess acidification following acute Rab7 knockout, we loaded and chased control or knockout cells with a pH-sensitive dextran (pHRodo) and a pH-insensitive dextran (AF647dex) overnight. pHRodo increases in intensity in more acidic compartments. Both control and knockout cells displayed ample dextran containing compartments. Consistent with our previous observations, there appeared to be relatively fewer and larger dextran-containing compartments in knockouts (**Figure 6 A-B'**). However, the ratio of pHRodo to AF647dex fluorescence intensity was not altered in knockout cells. However, these data did begin to suggest an increase in acidification in knockout cells, with more replicates needed. These data suggest that Rab7 is dispensable for the acidification of lysosomal compartments, though may be important for fine tuning absolute pH.

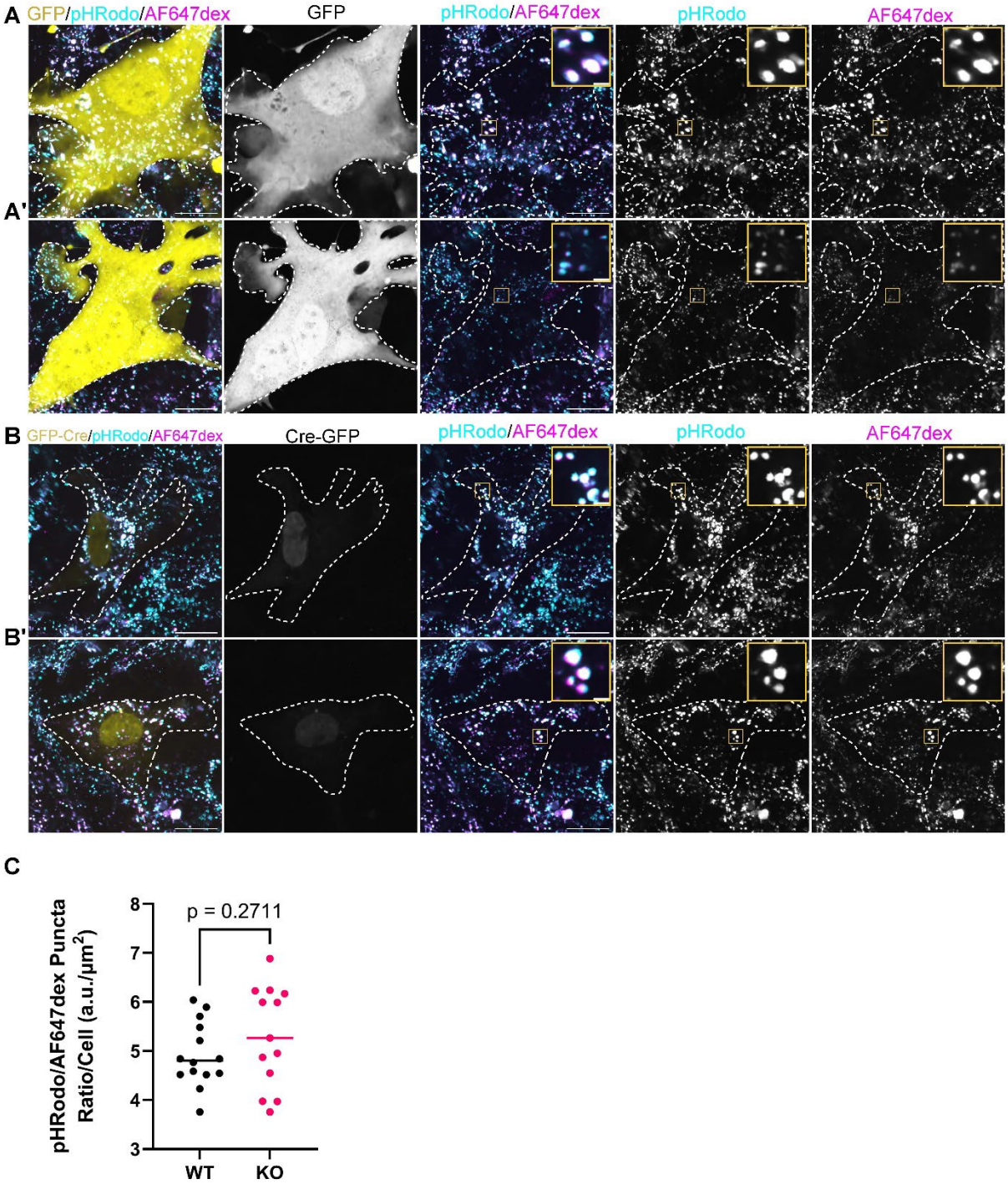

Figure 6 Endo-lysosomal acidification is unchanged in Rab7 knockout cells

(A-A') Rab7$^{fl/fl}$ MEFs were nucleofected with GFP (yellow) and expressed for two days prior to simultaneous loading with pH-sensitive pHRodo dextran (pHRodo, cyan) and pH-insensitive Alexa-Fluor 647 coupled dextran (AF647dex,

magenta) overnight for 16 hours. After overnight load, dextrans was chased to terminal compartments for 4 hours before live confocal imaging. pHRodo becomes increasingly fluorescent in more acidic compartments. Two representative still images captured from live cells are shown. (scale = 20μm, inset = 2 μm). **(B-B')** Rab7$^{fl/fl}$ MEFs were nucleofected with pCAG-GFP-Cre (yellow) and expressed for two days prior to pHRodo (cyan)/ AF647dex (magenta) acidification assay (scale = 20μm, inset = 2 μm). Two representative still images captured from live cells are shown. **(C)** Control (WT) and knockout (KO) cells were analyzed for the mean ratio of pHRodo:AF647dex intensity per puncta, per cell compared using two-tailed unpaired t-test (n = 14 (WT) and 13 (KO) cells, from 1 independent experiment).

Our data to this point suggest a problem with cathepsin-containing compartments. We thus wondered whether the upstream trafficking machinery responsible for cathepsin delivery was affected in Rab7 knockouts. Cathepsins such as cathepsin-B are trafficked to endosomes via mannose-6-phosphate receptors (M6PRs). In the more acidic lumen of endosomes, conformational changes in M6PR release cathepsins in the endosomal lumen. Cathepsins then proteolytically mature, while M6PR is retrieved from endosomes and retrogradely trafficked back to the trans-Golgi network for reuse. We thus assessed whether M6PR was perturbed in the absence of Rab7. Control MEFs displayed strong perinuclear M6PR staining that was fairly diffuse with bright puncta interspersed within (**Figure 7 A-A'**). In knockout cells, the number and perinuclear localization of M6PR was retained (**Figure 7 B-B', C, H**), however, M6PR compartments appeared much brighter and larger, similar to that of CatB (**Figure 7 B-B', D-F**). To this end, we then tested whether the relationship between CatB and M6PR immunostaining changed as result of Rab7 knockout. In control cells, CatB and M6PR are observed together on occasion (Figure 7 I). However, in knockout cells, CatB and M6PR frequently are found together within bright, enlarged compartments (**Figure 7 J**). Quantification revealed a significant increase in CatB intensity per M6PR puncta in knockout cells (**Figure 7 K**). These data suggest that M6PR trafficking is perturbed in Rab7 knockout, resulting in retention of M6PR with CatB in membraneous compartments.

Figure 7

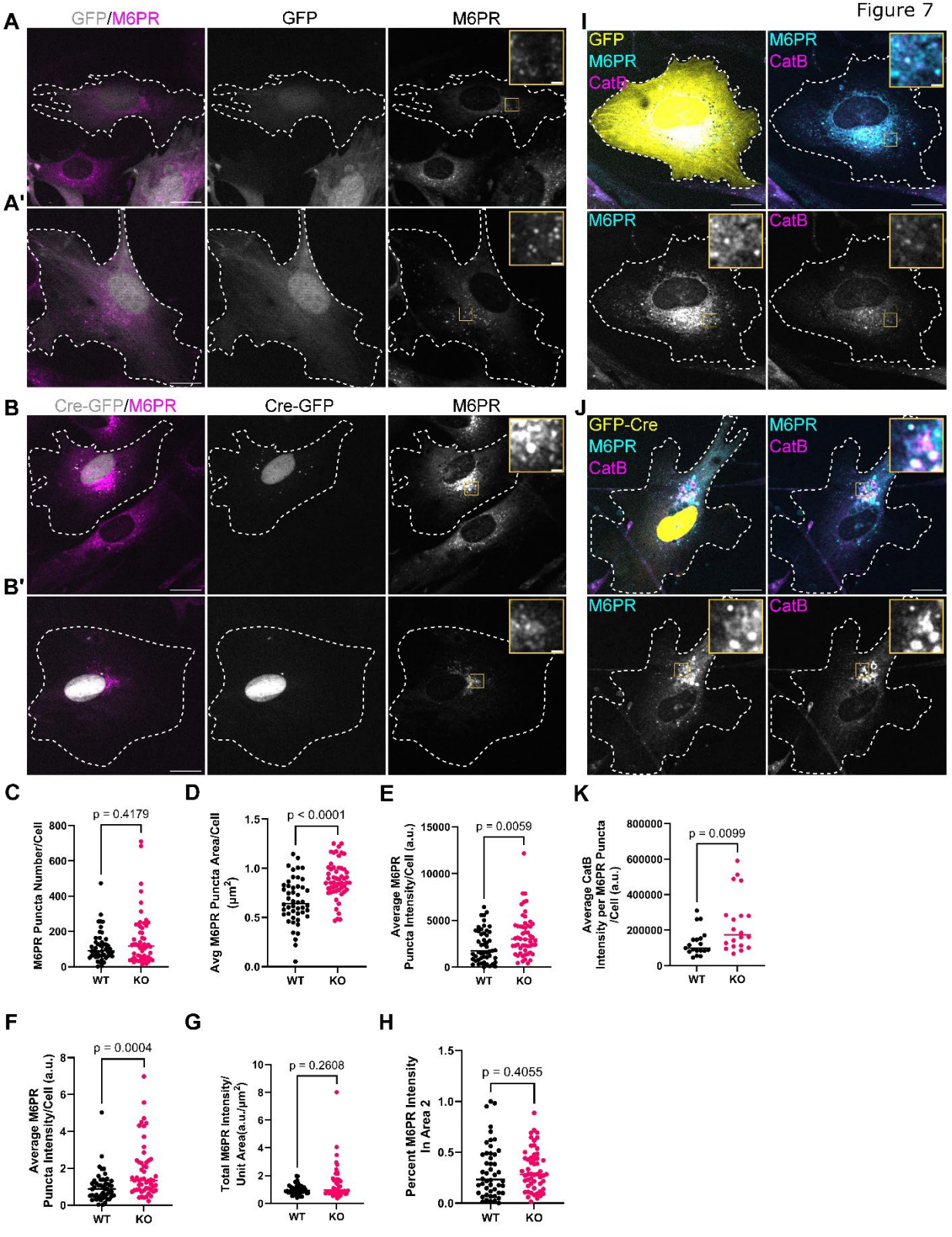
A
GFP/M6PR
GFP
M6PR
A'
B
Cre-GFP/M6PR
Cre-GFP
M6PR
B'
I
GFP
M6PR
CatB
M6PR
CatB
J
GFP-Cre
M6PR
CatB
M6PR
CatB
C
M6PR Puncta Number/Cell
p = 0.4179
D
Avg M6PR Puncta Area/Cell (µm²)
p < 0.0001
E
Average M6PR Puncta Intensity/Cell (a.u.)
p = 0.0059
K
Average CatB Intensity per M6PR Puncta /Cell (a.u.)
p = 0.0099
F
Average M6PR Puncta Intensity/Cell (a.u.)
p = 0.0004
G
Total M6PR Intensity/ Unit Area(a.u./µm²)
p = 0.2608
H
Percent M6PR Intensity In Area 2
p = 0.4055
WT
KO

Figure 7 Biosynthetic M6PR trafficking is disturbed following Rab7 knockout leading to CatBB-M6PR retention in enlarged compartments

(A-A') Rab7$^{fl/fl}$ MEFs were nucleofected with GFP (gray) and expressed for three days prior to fixation and immunostained for endogenous cation-independent mannose-6-phosphate receptor (M6PR, magenta) (scale = 20μm, inset = 2 μm). Two example widefield micrographs are shown. **(B-B')** Rab7$^{fl/fl}$ MEFs were nucleofected with pCAG-GFP-Cre (gray) and expressed for three days prior to fixation and immunostained for endogenous M6PR (magenta) (scale = 20μm, inset = 2 μm). Two example widefield micrographs are shown. WT (GFP control) and KO (pCAG-Cre-GFP) cells were analyzed for **(C)** number of M6PR puncta per cell (two-tailed Mann-Whitney U, n = 48 (WT), 54 (KO) cells, from 3 independent experiments) **(D)** average size of M6PR puncta per cell (unpaired two-tailed t-test, n = 48 (WT), 54 (KO) cells, from 3 independent experiments) and **(E)** average M6PR puncta intensity per cell (two-tailed Mann-Whitney U, n = 50 (WT), 54 (KO) cells, from 3 independent experiments). **(F)** WT and KO M6PR puncta intensity (from (E)) was also normalized to the mean each respective day and compared using two-tailed Mann-Whitney U, n = 48 (WT), 54 (KO) cells, from 3 independent experiments. **(G)** The total cellular intensity of M6PR in WT and KO cells per unit area, normalized to the mean of control on the day collected, was quantified and compared using two-tailed Mann-Whitney U test (n = 49 (WT), 56 (KO) cells, from 3 independent experiments). **(H)** The percentage of M6PR staining in the peripheral two-thirds of cells (*Area 2)* was compared with Mann-Whitney U test (n = 48 (WT), 54 (KO) cells, from 3 independent experiments). **(I)** Rab7$^{fl/fl}$ MEFs were nucleofected with GFP (yellow) and expressed for three days prior to fixation and immunostained for endogenous M6PR (cyan) and CatB (magenta) (scale = 20μm, inset = 2 μm). **(J)** Rab7$^{fl/fl}$ MEFs were nucleofected with pCAG-Cre-GFP (yellow) and expressed for three days prior to fixation and immunostained for endogenous M6PR (cyan) and CatB (magenta) (scale = 20μm, inset = 2 μm). **(K)** The average intensity of CatB per M6PR puncta, per cell was quantified and compared using Mann-Whiteny U test (n= 19 (WT) and 20 (KO) cells from 1 independent experiment).

Given M6PR is retained with CatB following Rab7 knockout, we wanted to assess whether the machinery responsible for M6PR retrieval to the Golgi was perturbed. The core retromer complex, including the previously described Rab7 interactor Vps35, have been implicated in such M6PR retrieval, but reliance of M6PR retrieval varies by cell type. We thus evaluated Vps35 in Rab7 knockout cells. In control cells, Vps35 appears as abundant, bright puncta, that often colocalize with Rab7 (**Figure 8 A-A'**). However, in knockout cells, Vps35 is less brightly associated with endosomal membranes and appears much more diffuse within the cytoplasm (**Figure 8 B-B'**). Remaining puncta appear smaller and fainter. Indeed, quantification revealed the number, area, and intensity of Vps35 puncta is significantly reduced in the absence of Rab7 (**Figure 8 D-F**), though the distribution of remaining puncta is not changed (**Figure 8 G**). Importantly, this phenotype is on target, as overexpression of mCherry-Rab7-WT in the absence of endogenous Rab7 can rescue these phenotypes (**Figure 8 C-G**). Overall, this data

suggests that Vps35 is highly sensitive to levels of Rab7, which may impact M6PR retrieval and ultimately anterograde cathepsin trafficking to lysosomal compartments.

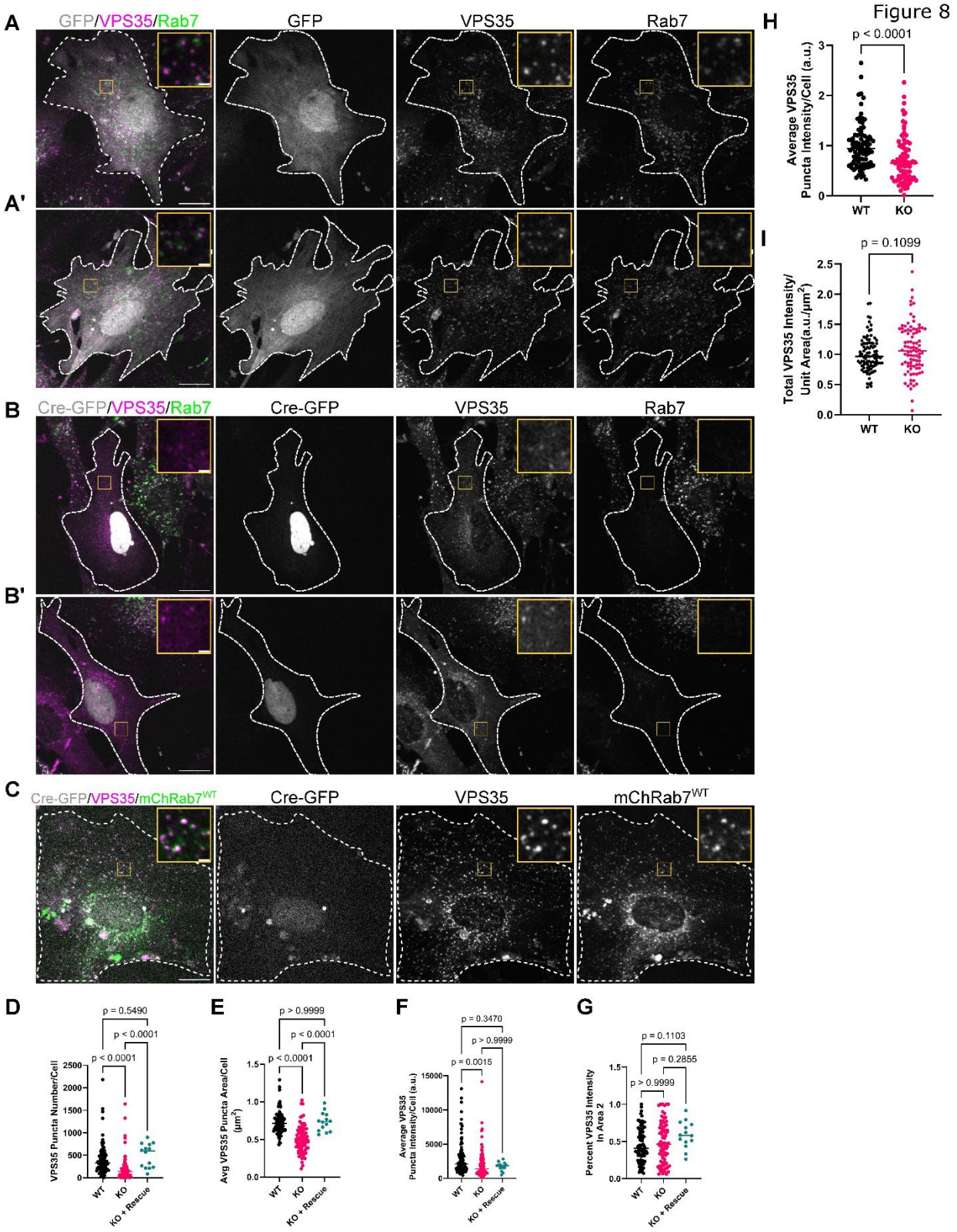

Figure 8 Rab7 knockout depletes Vps35 from endosomal compartments

(A-A') Rab7$^{fl/fl}$ MEFs were nucleofected with GFP (gray) and expressed for three days prior to fixation and immunostained for endogenous Vps35 (Vps35, magenta) and Rab7 (green) (scale = 20μm, inset = 2 μm). Two example widefield micrographs are shown. **(B-B')** Rab7$^{fl/fl}$ MEFs were nucleofected with pCAG-GFP-Cre (gray) and expressed for three days prior to fixation and immunostained for endogenous Vps35 (Vps35, magenta) and Rab7 (green) (scale = 20μm, inset = 2 μm). Two example widefield micrographs are shown. **(C)** Rab7$^{fl/fl}$ MEFs were nucleofected with pCAG-GFP-Cre (gray) and mCherry-Rab7-WT (green), and expressed for three days prior to fixation and immunostained for endogenous Vps35 (Vps35, magenta). (scale = 20μm, inset = 2 μm). WT (GFP control), KO (pCAG-Cre-GFP) and KO + Rescue (pCAG-Cre-GFP with mCh-Rab7-WT) cells were analyzed for **(D)** number of Vps35 puncta per cell (Kruskal-Wallis test, n = 94 (WT), 83 (KO), 14 (Rescue) cells) **(E)** average size of remaining Vps35 puncta per cell (Kruskal-Wallis test, n = 94 (WT), 83 (KO), 14 (Rescue) cells) **(F)** average Vps35 puncta intensity per cell (Kruskal-Wallis test, n = 94 (WT), 83 (KO), 14 (Rescue) cells) and **(G)** the percentage of Vps35 staining in the peripheral two-thirds of cells (*Area 2, left)* (Kruskal-Wallis test, n = 94 (WT), 83 (KO), 14 (Rescue) cells). **(H)** WT and KO Vps35 puncta intensity (from (F)) was also normalized to the mean each respective day and compared using two-tailed Mann-Whitney-U test (n = 94 (WT) and 83 (KO) cells) **(I)** The total cellular intensity of Vps35 in WT and KO cells per unit area, normalized to the mean of control on the day collected, was quantified and compared using two-tailed Mann-Whitney-U test (n = 94 (WT) and 90 (KO) cells). Cells counted were from 5 (WT and KO) and 1 (WT/KO/Rescue) independent experiment(s).

5.4 Discussion

In summary, this study finds perturbed morphology, including increases in size and intensity of LAMP2- and cathepsin-containing compartments following knockout of the endosomal small GTPase Rab7. However, knockout cells retained presumed lysosomal degradative capacity and acidification in the absence of endogenous Rab7. Upstream of lysosomal compartments, knockout of Rab7 lead to increases in the size and intensity of M6PR-containing compartments, which also contained more cathepsin. In alignment with this finding, the core retromer complex subunit Vps35 was depleted from endosomes in the absence of Rab7, potentially causing M6PR mis-localization (**Figure 9**).

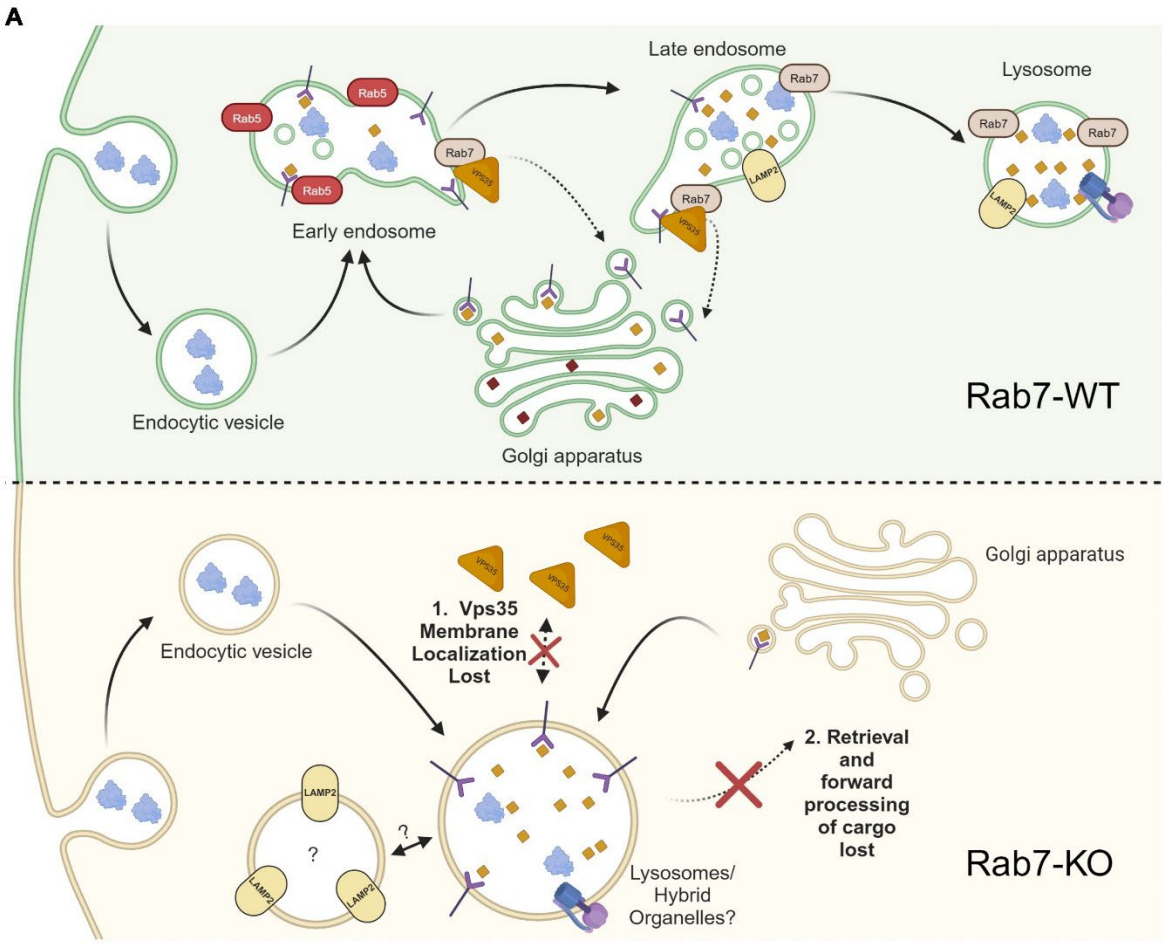

Figure 9 Loss of Rab7 reveals a Vps35 membrane association deficit that contributes to observed knockout phenotypes

(A) (*Top*) Schematic demonstrating the intersection of endocytic and biosynthetic trafficking pathways converging on endosomes, as endocytic and Golgi derived vesicles feed into Rab5-positive early endosomes. From Rab5-positive early endosomes, and Rab7-positive late endosomes, Rab7-Vps35 complexes contribute to the recycling of mannose-6-phosphate receptors (M6PRs, *purple, dashed arrows*). Lysosomal enzymes (*yellow diamonds)* and cargo (*blue globular proteins*) delivered to late endosomes are fated for degradation and traffic to acidic lysosomes. (*Bottom*) In Rab7-knockout (Rab7-KO) conditions, endocytosis of extracellular cargo proceeds normally. However, a primary deficit in Vps35 membrane localization to endosomes (1) occurs. This subsequerntly leads to the appearance of M6PRs retained in endosomes, along with lysosomal enzymes. Retained endosomes contain lysosomal markers like the cathepsins and LAMP2, and lysosomal functions like acidification and degradative capacity. These hybrid organelles are likely the result of a failure in Vps35 mediated retrieval, which subsequently leads to the loss of both retrieval and forward processing of lysosomal fated material (2).

Together these data suggest that the most Rab7-sensitive step in biosynthetic cathepsin trafficking is that which requires Vps35. In knockout cells, we observe a striking loss of Vps35 from endosomal membranes. As a consequence, the CatB pool in particular was more associated with retained M6PR in knockout cells than controls. In the absence of Rab7, and subsequently in the absence of membrane localized Vps35, our M6PR staining was in brighter and larger compartments. This data is in agreement with many foundational studies which first described such Rab7-Vps35 dependent M6PR trafficking (Rojas et al., 2008; Seaman et al., 2009). This finding is in disagreement with one previous knockout study that found M6PR levels to be greatly reduced in the absence of Rab7 (Takimoto, 2021). This may be due to increased secretion as opposed to retention of dysfunctional endosomes. Thus, our data paints a picture of Rab7-initiated Vps35-dependent CatB and M6PR trafficking. Most of the phenotypes we observe in these knockout cells can thus be explained as being downstream of this upstream deficit of Vps35-M6PR sorting, but Rab7 might have additional nodes of action elsewhere.

Such deficits in Vps35-mediated trafficking can potentially also explain the observations we note regarding the size and intensity of CatB- and CatD-containing compartments. Specifically, in the absence of Vps35 (i.e., retromer complex), sorting and tubulation out of the endosome is likely disrupted, leading to the enlarged size and increased content within endosomes of Rab7-deficient cells. We similarly observe morphologic perturbations in LAMP2-containing compartments in Rab7 knockout cells, which is in agreement with previous studies conducted both *in vivo* and *ex vivo* across many cell types (Hiragi et al., 2022; Homma et al., 2019; Kuchitsu et al., 2018; Takimoto, 2021). Whether or not enlarged LAMP2 and CatB compartments are the same compartment remains an open question that could be easily addressed in the future. Notably, enlarged LAMP2 compartments were previously noted to be distinct from other endosomal compartments in the absence of Rab7 (Homma et al., 2019), suggesting that these populations may be distinct. If this is the case, then possible future hypotheses to explore include that Rab7 directly regulates LAMP trafficking that leads to this enlarged phenotype, or that the LAMP phenotype is an indirect consequence of the primary Vps35 deficit in cathepsin trafficking, such as through a loss in fusion capability between LAMP- and Cat- carriers.

Previous studies that have also observed disrupted LAMP and cathepsin compartments are quick to conclude that these enlarged Cat-positive compartments are still lysosomes and that the morphologic changes are simply indicative of “dysfunctional lysosomes”. In my opinion, it is unclear whether these compartments are actually lysosomes, or actually are hybrid compartments as a product of failed Vps35-dependent membrane trafficking, or something else entirely. Surprisingly, despite the dysfunctional appearance of presumed lysosomes, acidification (pHRodo) and degradation (MR-B/DQ-BSA) appear intact. Our findings support other recent Rab7 knockout studies which suggest Rab7 is dispensable for endosomal acidification (Kuchitsu et al., 2018; Liang et al., 2023) and reconcile the findings of multiple other knockout studies which utilized different degradation assays (Hiragi et al., 2022; Kuchitsu et al., 2018). We find that degradation was largely not impacted in the absence of Rab7. This observation that degradation is still intact within these mystery compartments may be due the relatively large range of pH at which cathepsins can be active (Yadati et al., 2020), or due to a long half-life of the proteins essential for acidification and degradative functions, in which our three-day time course was not sufficient to deplete an already existing pool. Collectively, our findings and others thus suggest that Rab7 is not important for these bulk features of endosomes and lysosomes in contrast to what early DN-Rab7 studies suggested. Thus, the material and membranous components necessary for degradation and acidification can be localized together somewhere in a Rab7- and Vps35-independent fashion, but whether or not these are lysosomes per se is an open question.

We are operating under the current hypothesis that the primary deficit in the absence of Rab7 is loss of Vps35 from the membrane, which subsequently impacts the ability of both cargos to recycle back to the TGN (e.g., mis-localized M6PR) and for further development traffic to lysosomes (e.g., mis-localized cathepsins and LAMPs). Despite this, functional properties of lysosomes such as bulk degradation and acidification remain intact, likely due to Vps35-independent features of cathepsin and pump machinery in such hybrid compartments. One interesting alternative hypothesis to this is that in the absence of Rab7, M6PR-CatB carrier vesicles never reach the endosome to begin with and what we are observing is either TGN- or carrier vesicle-retained biosynthetic cargo. More definitive work needs to be done to support or reject this alternative, such as counterstains

with TGN markers, pulse chase experiments of cathepsins or antibody labeling and feeding of surface M6PR. If the anterograde trafficking hypothesis is better supported by these experiments, these findings would open a new avenue of exploration for Rab7-mediated anterograde sorting and trafficking at the level of TGN carriers. Given the loss of Vps35 in these conditions, additional experiments could be performed to further support a role of Vps35 in such anterograde traffic as well. For instance, does Vps35 knockout recapitulate all the phenotypes we observe?

Collectively, our data present Rab7 as essential for the proper trafficking and localization of M6PR and cathepsins, with the loss of Vps35 from endosomes being the most upstream, direct consequence of Rab7 loss. Going forward, differentiating between anterograde (TGN to endosome) and retrograde (endosome to TGN) trafficking deficits, more careful identification of accumulating compartments, and mechanistically linking Vps35 loss to the accumulation of a plethora of membrane and luminal lysosomal proteins remain open goals.

Chapter VI. Discussion, Conclusions, and Future Directions

This chapter will conclude this thesis work by summarizing key findings and advancements in the field of Rab7 biology and lysosomal membrane permeabilization. I will then offer limitations and weaknesses of these studies and future directions as direct pathways of inquiry stemming from this work. I will discuss each of the following broad contributions to the field in detail:

1) Discovered a late endosome stress response driven by Rab7 activation and Rab7-related trafficking deficits upstream of damaged lysosomes

2) Amended roles for Rab7 in endosomal maturation and biosynthetic trafficking

3) Provided foundational evidence, new questions, and consequences for the novel concept of Rab7 effector balance and ordering

4) Elucidated commonalities and differences between cell types in response to LLOMe-mediated stress

1) Discovered a late endosome stress response driven by Rab7 activation and Rab7-related trafficking deficits upstream of damaged lysosomes

One of the initial goals of this dissertation work was to elucidate the roles and/or responses of endocytic trafficking organelles and machinery to lysosomal disruption. The major advancements in the field of lysosomal membrane permeabilization to this point have largely ignored contributions from these interconnected compartments for some time, and focus has solely been placed on responses at the lysosomal membrane. Ultimately, I tried to uncover if endosomes upstream of lysosomes are perturbed similarly to lysosomes or if these endosomal organelles and machineries provide compensatory or protective responses, when their end destination (the lysosome) is dysfunctional? In Mulligan et al. 2024 (Chapter 3), I discovered a novel response in late endosomes upstream of lysosomes to a pH neutralization-driven stress, using the small, lysosome-disrupting dipeptide LLOMe. Through careful partitioning and definitions of endosomal compartments, I found that LLOMe leads to phenotypic changes in both Rab7-positive (Rab7+) late endosomes and lysosomes that

were dependent on pH neutralization but independent of LLOMe-driven membrane damage. As a result of pH stress, Rab7 is hyper-activated (GTP-bound) and membrane stabilized on these organelles, which is sufficient to disrupt tubulation events and trap biosynthetic trafficking receptors (M6PRs) in endosomes. Mechanistically, I found the hyper-stabilization of Rab7 on endosomal membranes to be dually dependent on the assembly of the endosomal V-ATPase and the molecular motor adaptor protein RILP. Either pH neutralization in the absence of V-ATPase assembly or the inability of Rab7 to bind RILP significantly decreased the hyper-stabilization of Rab7 following LLOMe. In Chapter 4, I found that trafficking events even further upstream of late endosomes were perturbed following LLOMe-mediated lysosomal perturbation using the spatial advantages of neuronal dendrites. I observed that the maturational conversion of endosomes from early to late identities was disrupted. The strongest pieces of evidence for this were the depletion of dual EEA1+Rab7+ transitioning early endosomes in the dendrite, and the trapping of dendritic cargoes (Nsg2) in early endosomes. Nsg2 depends on Rab7-mediated retrograde transport to the soma for its degradation (Yap et al., 2018; Yap et al., 2022b). I also observed a subset of Rab7 compartments that moved anterograde in response to damage, which correlated with an increase in the number of Rab7+CatB+ carriers in the medial dendrite.

Collectively, the findings from these two chapters paint a more detailed picture of the upstream deficits that arise as a result of acute lysosomal disruption. The broad array of changes we observe appear interconnected in their dependence on the localization and engagement of GTP-bound Rab7 with specific effector protein complexes and membranes. To my knowledge, the notion of upstream trafficking deficits and Rab7 control over endosomal compartments in times of stress is unprecedented within the lysosomal damage field. While one study elucidated the percentage of endosomal compartments that were damaged using galectin-9 staining (Du Rietz et al., 2020), they and others did not further explore what the behaviors of these upstream compartments may be.

Limitations to these studies

Our main limitation in studying the novel late endosomal stress response has been the inability to establish direct binding interactions between Rab7 and the V-ATPase subunits. In the literature, interactions with two different subunits have been described: a tripartite complex with the V_1G_1 subunit and RILP (De Luca et al., 2014), and a direct interaction with the V_0a_3 subunit, in osteoclasts (Nakanishi-Matsui et al., 2024). We have thus far been unable to recapitulate the V_1G_1 interaction using co-immunoprecipitation approaches in COS-7 cells. Our limitation in detecting an interaction experimentally limits the specificity in which we can state our findings. That is, we can only correlate the increased stability of membrane-bound Rab7 in LLOMe with V-ATPase pump assembly, rather than demonstrate an increased interaction of Rab7 with a particular subunit as a result of LLOMe treatment. Establishing such an interaction would further enhance our results and allow us to disturb the interaction and then study downstream consequences precisely. This is further complicated by the inherent nature of the pump itself: a single assembled pump has 29 subunits, nearly all of which Rab7 could in theory interact with, and whose delicate stoichiometry make knockout studies hard to interpret.

Collectively, our studies in both Chapters 3 and 4 are also limited by the use of LLOMe as the sole lysosomal damaging agent we employ. LLOMe both causes pH neutralization in the absence of membrane damage (in late endosomes), and pH neutralization due to membrane damage (in lysosomes). Since both of these occur simultaneously limits our interpretation of results. This is especially relevant in our conclusions in Chapter 4, as we have not yet established whether dendritic endosomes are pH-neutralized or also have holes as a result of LLOMe. As it stands, there are two interpretations: 1) LLOMe-mediated lysosomal damage impacts upstream early to late endosomal conversions. 2) LLOMe-mediated pH neutralization throughout the neuron leads to differences in somatic and dendritic responses of Rab7, including maturational conversion and motility of anterograde cathepsin carriers, because somatic and dendritic compartments have different pH profiles. For the future, consistently using LLOMe in parallel to other pH neutralizing drugs (e.g., NH_4Cl) and a non-pH dependent disrupting agent (e.g., silica particles), will allow us to better discern between pH-dependent and membrane damage-dependent effects.

Finally, our studies in neurons are also limited by the lack of suitable reagents that are essential to deducing LLOMe-driven mechanisms. For instance, we currently lack suitable detection of both endogenous and overexpressed ESCRT subunits, V-ATPase subunits, and galectins that would permit us to further study pH, or decipher membrane repair and lysophagy processes in dendrites, for instance. Identification and validation of reliable tools for these aims would bolster future investigation of these processes in neurons.

Future Directions

There remain many avenues of potential exploration following the foundational lysosomal damage response findings I have identified. Pertaining to the late endosomal stress response (Chapter 3), one key open question that remains is what effect Rab7 hyper-stabilization has on pH recovery of the acidifying endosome. That is, is Rab7 required for re-establishing the *proper* pH of the endosome? Our data support a Rab7-independent mode of V-ATPase assembly, and by extension, V-ATPase activity, but we have not established whether pH is properly restored to the correct value following LLOMe-mediated stress in a Rab7-dependent manner. One could address this question using Rab7-knockout cells loaded with pH-sensitive reagents and treated with LLOMe, or preferably, acute-inducible Rab7 inactivation systems in the presence of LLOMe with pH readouts. In fact, our preliminary data in Rab7-knockout cells (Chapter V) suggests the hypothesis that Rab7 is essential for establishing the proper pH, as knockout cells began to suggest endosomes are more acidified in the absence of Rab7, though more replicates are needed to lead to definitive conclusions. Recent literature also seems to suggest this, as LysoTracker Red Dye appeared more intense in a stable Rab7-knockout line, suggesting greater acidification (Kuchitsu et al., 2018). Thus, my working hypothesis going forward is that Rab7 activity is essential for fine tuning endosomal pH to the correct value, during normal endosomal maturation and in response to pH stressors.

The immediate next steps in regards to neuronal specific responses to LLOMe are identifying and characterizing the behavior of anterograde moving Rab7+CatB+ carriers. This population is both highly unique and reproducible, and understanding its

behavior may be an important next step in understand Rab7 biosynthetic steps in dendrites. Are these carriers normally delivered to EEA1+ early endosomes to facilitate endosomal cargo handoff, which is stalled in LLOMe conditions, or are they compensatory degraders of accumulated dendritic material in the absence of functional lysosomes? Probing residual degradative capacity of these carriers and detailed live imaging of this population relative to other endosomal pools (like EEA1) will be clarifying to these questions. We also found that LLOMe impacts endosomal maturation in dendrites. This finding suggests that the regulation of Rab5 to Rab7 conversion typical of early to late endosomal transitions (Poteryaev et al., 2010; Rink et al., 2005) is lost during LLOMe-mediated damage. Therefore, an exciting avenue of exploration is the regulation (and mis-regulation) of Rab7 activation and conversion in dendrites. We know these conversions occur, as our lab has previously observed sharp degradative gradients and gradients of endosomal subtypes within dendrites (Yap et al., 2018). How are these machineries necessary for driving such transitions, such as the Rab7 GEF Mon1-Ccz1, spatially organized in dendrites? Further, in LLOMe, is there dysregulation of Mon1-Ccz1, or any of the Rab7 GAPs in dendrites, that could explain failure of endosomal maturation? There are newer tools (e.g., Raichu-Rab7 (Cai et al., 2021)) being established that could permit one to dynamically visualize Rab7 activation using FRET. Though this does not directly visualize the GEF, it permits visualizing the dynamics of Rab7 conversions, which would be highly informative in dendrites.

Finally, I am particularly excited by a future direction that would investigate the regulation and establishment of pH gradients down dendrites. That is how are the most acidified endosome and lysosome compartments in dendrites kept most proximal, while more neutral compartments are more distal? This gradient might be important in the somatic versus dendritic response to LLOMe (as discussed in the *Limitations* section above), but we know very little about how this gradient is normally established. It may stem from differential trafficking of particular V-ATPase subunits, which may tune particular endosomes to certain pH based on composition. For example, a_1 and a_2 subunits of the V_0 domain have been described as primarily early endosomal (Nakanishi-Matsui and Matsumoto, 2022), while in neurons, the V_1G_1 and V_1G_2 subunits are uniquely polarized to somato-dendritic and axonal domains, respectively (Murata et

al., 2002). How are each of these subunits, both membranous and cytosolic, polarized in such a way in neurons?

2) Amended roles for Rab7 in endosomal maturation and biosynthetic trafficking

A central theme to my thesis work has been challenging the, in some cases poorly established, roles for Rab7 in regulating certain features of maturing endosomes. For instance, it has been suggested for over two decades due to studies using dominant-negative mutants (Bucci et al., 2000) that Rab7 is essential for acidification of the endosome. Rab7 was subsequently implicated in recruitment of the effector RILP for regulation of the stability of the V-ATPase subunit V_1G_1 to and hence pH (De Luca et al., 2014). However, more recently, knockout studies (Kuchitsu et al., 2018; Liang et al., 2023), and additional dominant negative studies (Yu et al., 2024) have suggested that Rab7 is dispensable for acidification. Indeed, we find that knockout of Rab7 does not impact localization of V_1G_1 to endosomes (Chapter 3) and does not impact the ability of endosomes to acidify (Chapter 5). In fact, our FRAP study (Chapter 3) implicates that the degree of V-ATPase assembly is upstream of and actually regulates Rab7 stability, rather than the previous notion that V-ATPase is downstream of active Rab7 as an “effector”. Thus, this work is novel in establishing an “inside-to-outside” regulatory mechanism of Rab7 activation via the V-ATPase and challenges the notion that all identified interactors of Rab7 are downstream of its activation. In fact, it is possible that many other described effectors are indeed upstream of its activation.

Further, I performed a comprehensive assessment of the effects of Rab7-knockout on biosynthetic trafficking machinery (Chapter 5). Through this work, I have identified that the most striking impact of Rab7 loss is that on the recruitment of the retromer subunit Vps35 to endosomal membranes, which we now speculate leads to the retention of both cathepsin-B and its trafficking receptor mannose-6-phosphate receptor (M6PR) in endosomes. From this finding, I am proposing that all subsequent phenotypes that have been described as result of Rab7 loss, such as cathepsin and LAMP compartment phenotype changes, early endosome changes, M6PR mis-trafficking, and cathepsin misprocessing, stem from the single loss of Vps35 from the

membrane. These collective losses likely stem from the complex functions Vps35 performs, which include both cargo sorting and tubulation, which are essential in the decision to degrade or recycle (Cullen and Steinberg, 2018). Thus, the dynamic roles of Rab7 in recycling and degradation are in part via the dynamic roles of Vps35. This concept was first proposed in (Rojas et al., 2008), though through this work I am novelly unifying all observed phenotypes under this single node.

Last, in thinking about the relationship between Rab7 and both the V-ATPase and Vps35, I speculate that active Rab7-GTP has a greater role in mediating protein complex *stability* on endosomal membranes, rather than the long-established notion that it is for effector protein *recruitment*. For instance, I speculate the engagement of active Rab7 with the V-ATPase allows for processive pumping, whereas following GTP hydrolysis of Rab7 the pump is more likely to fall apart. As another speculative example, Vps35 membrane binding and tubulation might be more stable in the presence of GTP-Rab7, and less so in the presence of GDP-Rab7, but nevertheless, the initial membrane recruitment is (partially) independent of Rab7. There is some precedent for Rab7 mediating Vps35 tubule and complex stability, independent of its role in Vps35 recruitment, from some early studies into this relationship (Rojas et al., 2008; Seaman et al., 2009). This would further explain why in our knockout study, we still detect Vps35-positive endosomes in the absence of Rab7, just that they appear to be smaller and fainter--- this might be because Vps35 is not stable and is continuously falling off and jumping back onto the membrane.

Limitations

Our limitations in studying the “inside-to-outside” mechanism of Rab7 activation via the V-ATPase are similar to those that were described in the limitation section in part 1 of this chapter. That is, we were unable to deduce the precise molecular interaction between the V-ATPase and Rab7, hindering us from further exploring the implications of their relationship. If we did know and could experimentally reproduce the molecular interaction, we could then perturb the interaction and ask whether Rab7 was still hyperactivated in LLOMe. This is further complicated by the fact the V-ATPase-Rab7 interaction may involve multiple subunits or multiple interactions, and it is likely difficult

to completely abolish V-ATPase-Rab7 interaction without compromising pump activity. In support of this possibility, interactions with two distinct subunits have already been described.

With our knockout studies, we made the conscious decision to perform acute knockdowns with GFP-Cre, rather than use stable Rab7-knockout cell lines, to avoid compensatory mechanisms that may arise in stable lines. As a result, a significant limitation is our inability to visualize more than two additional channels (markers) to elucidate more detailed evaluations of the effect of knockdown on trafficking, given we must transfect GFP-Cre in with a DAPI or Phalloidin counterstain. In experiments where we included a rescue, this was reduced down to only one endogenous marker we could visualize. As a result, we could only make limited conclusions and loose associations between phenotypes we observed, for instance, the similarities and differences between cathepsin-B and LAMP compartments in the knockout. The development of multiplexing strategies or at minimum, 5-color imaging, would greatly advance our ability to decipher more particular trafficking deficits in the absence of Rab7.

Future Directions

There is significantly more work that needs to be done to strongly rule in my unified Vps35-centric model of Rab7 function, and rule out alternative hypotheses, such as one that proposes independent roles for Rab7 in each of Vps35, cathepsin, and LAMP trafficking. One clarifying experiment would be the knockout of Vps35 in mouse embryonic fibroblasts. Does knockout of Vps35 equate to the cytosolic distribution we observe in Rab7-KO, and subsequently phenocopy all of the trafficking deficits we observe? If so, this would add great support to the model that loss of Rab7 is dysfunctional due to a primary loss of Vps35 from membranes. There is already support in many cell types for Vps35 loss contributing to features of Rab7 loss including M6PR mis-sorting, though this is not ubiquitous across cell types (Carosi et al., 2023; Cui et al., 2019; Rojas et al., 2008; Seaman, 2018; Seaman et al., 2009). Similarly, the Parkinson’s disease D620N mutation in Vps35 also leads to mis-processing of cathepsin-D (Williams et al., 2022), akin to that of Rab7 dominant negative expression (Press et al., 1998).

Further, we must also decipher whether the loss of Rab7 causes primarily retrograde or anterograde trafficking deficits. More specifically, we must deduce whether we observe increased colocalization of cathepsin-B with M6PR as a result of failed retrograde retrieval (implicating Vps35), or dysfunctional anterograde trafficking, such as TGN-based retention of M6PR-cathepsin-B complexes. Good starting options to pursue this line of inquiry include cathepsin and M6PR staining with TGN counterstains, or antibody labeling and feeding of surface M6PR and quantifying whether it can chase to the TGN or not. Another tempting option includes doing a RUSH-system based synchronous release of biosynthetic cathepsin in a Rab7 knockout cell, however due to the complex post-translational processing of cathepsins, fluorescently labeled tools are significantly lacking within the field and our previous attempts at utilizing them have demonstrated their retention in the ER and Golgi (R.M., data not shown).

Last, we could employ similar FRAP studies to those we performed using labeled fluorescently labeled versions of Rab7 effector proteins (e.g., Vps35-GFP) to probe the relationship between their stability on membranes and Rab7 activation status (using knockout, constitutively active, and dominant negative approaches). I hypothesize that either loss of Rab7 or expression of a dominant negative Rab7 would not inhibit recruitment of effectors to membranes, but if FRAP'd, would significantly increase their turnover as a result of membrane destabilization.

3) Provided foundational evidence, new questions, and consequences for the novel concept of Rab7 effector balance and ordering

In my opinion, the most impactful concept and interesting thread that connects each of the chapters in this thesis work is the concept of Rab effector balance and ordering. I have discussed in earlier chapters and sections how biosynthetic material must sequentially traffic from one organelle to another, and how endosomes undergo processes of endosomal maturation, including Rab conversions, to perform novel functions at each step. Once a particular Rab is associated with a membrane, in our case Rab7, how does it "know" which effector to bind first? How is such ordering among the cytosolic milieu accomplished, and a productive balance between all of the possible

effectors achieved? We first discuss this in Chapter 2, as it pertains to the trafficking of the NGF-TrkA survival signaling complex in Charcot-Marie Tooth 2B, a Rab7 driven disease. In that chapter, we discuss how we broadly think effectors can be grouped into “early” and “late” Rab7 effectors, dependent on their function and how a cargo would typically move through the system. Early effectors include those required for sorting (Vps35) and motility (RILP-dynein, ORP1L), while late effectors are more degradation oriented, and include those for acidification (V-ATPase) and heterotypic fusion (HOPS). In disease, disruptions in either affinity of Rab7 for a particular effector, or a change in the total amount of a particular effector (mass action) may ultimately dysregulate the balance and/or ordering needed for long range trafficking of NGF-TrkA in neurons. For example, a decreased affinity for Vps35 was described for the CMT2B K157N Rab7 mutation (Seaman et al., 2009). In this case, decreased Vps35-dependent recycling of the NGF-TrkA complex may precipitate a deficit in local axonal signaling required for axonal maintenance, as well as lead to premature degradation of signaling in somatic lysosomes.

Effector balance was then an important consideration in the interpretation of both our non-neuronal (Chapter 3) and neuronal (Chapter 4) LLOMe-based lysosomal membrane permeabilization studies. In the late endosomal stress response we describe in Chapter 3, Rab7 is hyperactivated and stabilized by the endosomal V-ATPase pump. Subsequently, tubulation behavior and recycling of M6PR to the TGN was disrupted. Are these downstream observations in trafficking and tubulation behavior due to effector binding imbalance? In my opinion, the hyperactivation and engagement of Rab7 with the pump during LLOMe-mediated stress inhibits the protein’s ability to disengage with the membrane and recycle. This in essence depletes Rab7 from other Rab7-effector complexes that perform other endosomal behaviors. This includes Vps35-Rab7 (Rojas et al., 2008; Seaman et al., 2009) for receptor recycling and Rab7-dynein for tubule generation (Mrakovic et al., 2012). In a way, we phenocopy this presumed depletion of Rab7-Vps35 complexes in LLOMe with our experiments in which we knockout Rab7 (Chapter 5), which also leads to Vps35 loss from the membrane and M6PR-dysregulation.

Our LLOMe studies in neurons (Chapter 4) provide additional evidence that Rab7 hyperactivation and engagement with particular effectors may disrupt the balance and binding with others. For example, we observe similar phenotypes of Rab7 late endosomes and lysosomes in the somata of cultured neurons treated with LLOMe to what we observe in non-neuronal cells. The assumption here is that Rab7 is similarly hyper-stabilized with these membranes and thus Rab7-GTP is depleted elsewhere. Indeed, when we look in dendrites, there is a lack of transitioning early to late endosomes, and a retention of dendritic cargo in early compartments. I speculate this is due to the lack of available Rab7 to facilitate this transition. Interestingly, we observe a novel anterograde pool of Rab7 carriers in the presence of LLOMe in neurons. It is unclear whether Rab7-GTP is similarly retained on these membranes as a result of locking with a specific motor adaptor complex, which would permit this directed movement. Further exploring this is in part complicated by the fact microtubule polarity is mixed in dendrites (Baas et al., 1988; Tas et al., 2017; Yau et al., 2016), but nevertheless this pool of carriers opens up a new avenue of investigation into Rab7 motor engagement following LLOMe-mediated stress.

Finally, in neuronal dendrites we found the Rab7-dependent trafficking cargo p19/Nsg2 is stuck in early endosomes following LLOMe. I interpret this as experimental evidence of what we initially described in Chapter 2. To elaborate, our LLOMe experiments support that notion that mis-regulation of Rab7 effector balance will disrupt the long-distance trafficking of dendritic membrane receptors, in this case p19/Nsg2, but may include NGF-TrkA or BDNF-TrkB, as well. What are the downstream consequences of this loss? In the case of NEEP21/Nsg1 or p19/Nsg2, one would hypothesize that the somatodendritic versus axonal polarization of trafficking receptors like L1/NgCAM (Yap et al., 2008) or regulation of AMPA receptors (Alberi et al., 2005) might be disrupted. It is unlikely that we see such polarization deficits in short LLOMe time courses, but perhaps long standing, low level lysosomal perturbation, such as in an aging model would allow us to detect such changes. In the case of NGF-TrkA, it appears in humans, that the consequence is a peripheral neuropathy. In the acute sense, we could monitor signaling output of NGF-TrkA following LLOMe treatment and see if the basal level of signaling is perturbed.

Future Directions

Given much of our evidence in support of the existence of a Rab7 effector order and/or balance is circumstantial, there are many lines of inquiry that could be pursued to better support this idea. For the purposes of this discussion, I will present a limited number of ideas that would be foundational in establishing such concept. The first potential experiment is to use a simple, two effector system, and investigate each effector's ability to interact with Rab7, relative to the other. For example, one could transfect and overexpress two effectors at varying stoichiometries in cells, immunoprecipitate Rab7, and probe the degree to which each effector is pulled down relative to the other. Then one could compare how the degree of pulldown changes at the different stoichiometries. This would in theory, explain how much the two effectors probed depend on abundance (or mass action) versus affinity, relative to one another, and would be enlightening as to how Rab7 "chooses" an effector. However, this experiment does not readily inform us as to whether there is an order to such interactions. Further, this experiment inherently depends on the following: the effectors chosen must be direct Rab7 interactors, they must be able to be transfected into cells without completely disrupting cell homeostasis, and we must have good tools to adequately probe each of the effectors individually. For us, Vps35 fits each of these criteria but we are currently hindered by a choice of second effector. For instance, RILP is riddled with both overexpression (Yap et al., 2022b) and tool-related problems (Yap et al., 2023), and we have had no success in probing V_1 subunits by Western blot. Therefore, the most promising effector moving forward is likely the fusion complex HOPS subunit Vps41, though we need better tools (plasmids) to complete this.

A similar experiment would be to purify Rab7 and constituent effector proteins and probe their interaction *in vitro*. One could immobilize GTP-loaded Rab7 on a column and pass different mixtures of effector proteins over the column and determine the relative binding of effectors, and how these changes with changing effector protein stoichiometries. Including a mixture of many (or all) effectors could then establish a preferential binding order, as the most abundantly captured effector could be removed from the next run, thus establishing a sequential preference in Rab7 binding. This

experiment hinges on successful purification of many proteins, and the ability of effector proteins to exist in a common buffer without denaturing or interacting among themselves, each of which are not trivial tasks. This experiment is also completely *in vitro* and thus ignores the relevant Rab7 activity regulation machinery that helps facilitate Rab7-effector interactions, like the Rab7 GEF Mon1-Ccz1 and the TBC- family of GAPs. Ultimately both this and the previous experiment could be made even more interesting by comparing the effector interaction properties of wild-type Rab7 to that of Charcot Marie Tooth 2B mutants.

One last experimental possibility, and perhaps the most comprehensive assessment of both Rab7 binding preference and ordering, is the utilization of a the APEX system for proximity-based biotinylation using neuronal specific degradative cargo to trace Rab7 interactions as cargo is trafficked (Han et al., 2019). In this experiment, we would utilize APEX-labeled p19/Nsg2 (or NEEP21/Nsg1) in neurons. Then, in brief, plasma membrane localized APEX-p19/Nsg2 would be suspended from endocytosing (cold-block) and labeled with the APEX substrate biotin-phenol (Tan et al., 2020), which is not highly cell-permeable. Then, we would release the block and chase the APEX-labeled cargo for various timepoints. We know the relative kinetics at which Nsg family proteins move through the endosomal system and that it is internalized and largely co-traffics with Rab7, from our earlier studies. We then would add hydrogen peroxide to initiate the ascorbate peroxidase activation of APEX2 and label Nsg-near proteins at acute time points post chase and quench. Downstream, we would perform streptavidin pulldowns and unique labeling for each time point, then run all samples together by mass spectrometry to generate a proteome at each endocytic step. We would then mine the mass spectrometry data for Rab7 effector proteins only. This could in theory tell us which effectors are engaged early in the endocytic pathways versus later, and at what levels relative to one another.

This experiment would be highly informative but technically challenging. We would first need to ensure we had near uniform expression of Nsg2-APEX in neuronal cultures, which would have to be via either a knock-in or viral based transduction system. Then, the success would depend on additional factors as the degree of surface

Nsg2 labeling we could accomplish during a short block, without leakage of either biotin-phenol across the membrane to label already internalized APEX-Nsg2 or premature release of labeled APEX-Nsg2 from the membrane. It is also not a direct labeling of Rab7 near proteins, but rather that of Nsg2. We could potentially address this by using a split-APEX system (one fragment on Rab7, one on Nsg2), however this would highly complicate the timing of biotin-phenol labeling and hydrogen peroxide addition, relative to the chase. This would also depend on a near enough interaction of Rab7 and Nsg2 to facilitate labeling. While they are certainly on the same membrane, to my knowledge, direct interactions have not been reported. Ideally, we would want to combine split-APEX Rab7 with a synchronously released split-APEX-Nsg2 from the ER to most tightly control chase and labeling dynamics, however, both the APEX system and current best synchronous release systems utilize biotin conjugates as substrates for their functions.

4) Elucidated commonalities and differences between cell types in response to LLOMe-mediated stress

In utilizing LLOMe as a mediator of stress across cell types in the various chapters presented within this dissertation, I have inherently established a body of work allowing the comparison of stress responses in different cell types. Important to this discussion is the following: in Chapter 3, we utilized various non-neuronal cell types, not for the purpose of comparison, but for technical reasons (e.g., NRK did not transfect well so I used COS-7; ALIX antibody did not work in NRK cells so I used MEFs). I have little reason to believe that responses between these various non-neuronal cell types are different. Therefore, I will broadly compare the findings from the collection of non-neuronal cells in Chapter 3 to that of neuronal cells in Chapter 4 (**Figure 1**).

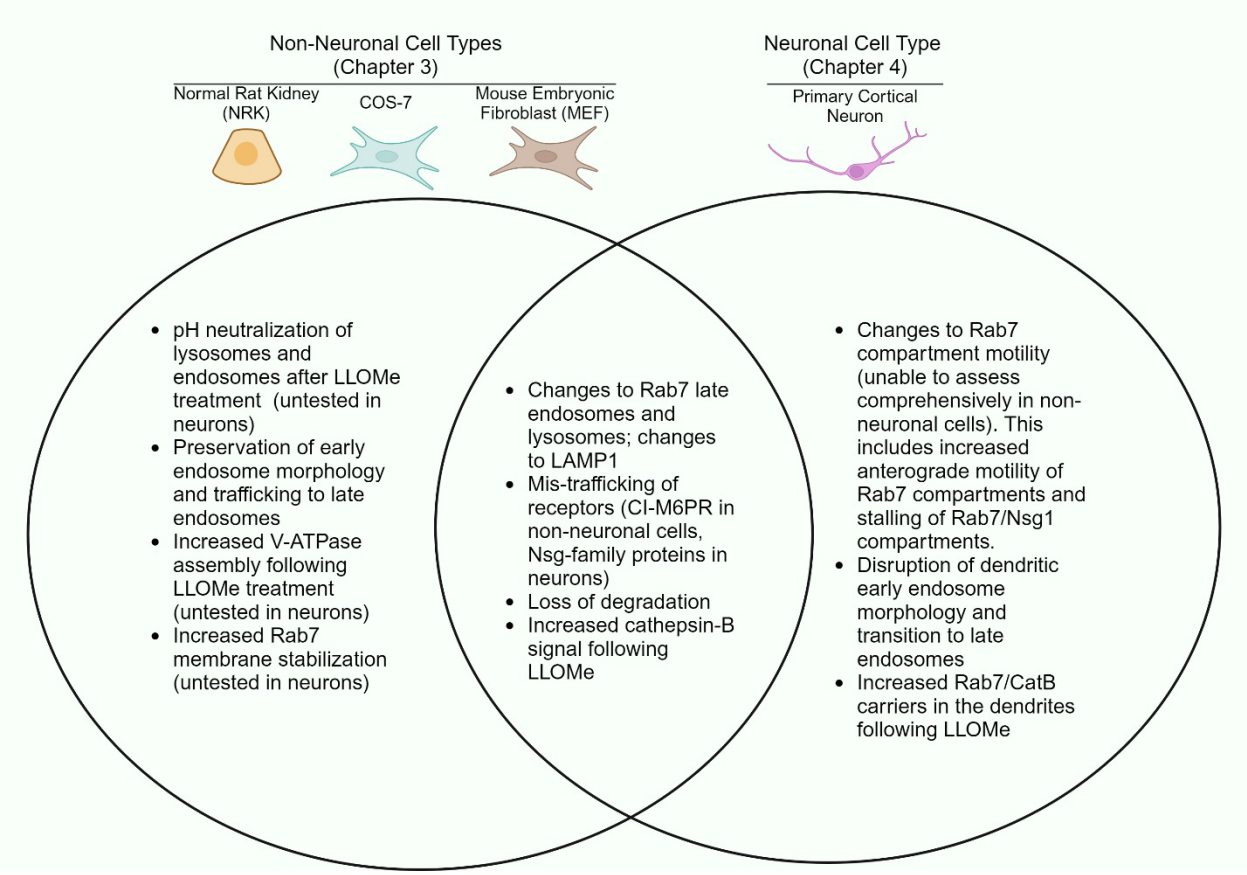

Figure 1 Venn Diagram detailing similarities and differences between cell types in response to LLOMe.

(Left) Features observed in non-neuronal cells, but not neurons. **(Middle)** Features observed in all cell types. **(Right)** Features observed in neurons but not non-neuronal cell types.

To begin, non-neuronal and neuronal cells alike exhibited similar changes in Rab7-positive late endosome and lysosome compartments. That is, the morphology of Rab7 was similarly changed (e.g., increased size, decreased number) in non-neuronal and neuronal cells. Notably, in neurons, these changes were apparently restricted to the soma and proximal dendritic regions. For that reason, I think that the somatic responses and mechanisms of Rab7 mediated changes in neurons in response to stress are akin to non-neuronal cells. This likely includes the Rab7 hyperactivation, hyper-membrane stabilization and disruption of trafficking receptors I observed in Chapter 3, though these have not yet been directly assessed in neurons. Among the non-neuronal cells, I noted that the COS-7 cells often had more subdued responses in Rab7 to LLOMe as

compared to NRK or primary MEFs. As these are a transformed cancer-like line, this may speak to adaptation as compared to more normal cells. Also common to both neurons and non-neuronal cells was the finding that membrane receptor trafficking was disrupted. In non-neuronal cells I focused on the trafficking of M6PR, which was retained in Rab7+ endosomes, whereas in neurons I focused on the Nsg-family of membrane receptors, which were retained in EEA1+ early endosomes. Other similarities include changes to degradation as a result of LLOMe treatment and a change in the phenotypic appearance of cathepsin-B. I assessed degradation differently in each cell type, but found that probing with MagicRed-Cathepsin-B after LLOMe treatment in non-neuronal cells resulted in a decrease in MR signal as compared to controls, whereas probing degradative flux using Nsg2 in neurons demonstrated a similar degradative loss.

In non-neuronal cells, I was able to more carefully elucidate mechanisms behind Rab7 changes. As such, I was able to deduce that pH neutralization, increase V-ATPase assembly, and Rab7 hyperactivation and membrane stabilization occur as a result of LLOMe treatment. I did not assess these mechanistic changes in neurons; however, I have little reason to believe that these mechanisms do not occur in neurons as other cell types. I think that these mechanisms are very much at play, specifically in the soma, though further experiments need to be performed to definitively demonstrate this. Conversely, I was able to appreciate differences in responses within the neuronal dendrites that I did not observe in non-neuronal cells. This included changes to Rab7 compartment motility, where I discovered both an anterograde-responsive pool of Rab7 compartments, and changes to the trafficking of Nsg proteins in Rab7 carriers. Similarly, I was able to appreciate a change to the morphology and maturation of early endosomal compartments within dendrites. It is currently unclear whether these changes are neuron specific, or if I am just able to appreciate these changes better given the size and spatial resolution afforded by long-range trafficking in dendrites. In other words, visualizing these dynamic changes amidst the smaller, more compact epithelial and fibroblast cell types is exceptionally difficult. Nevertheless, if these changes are unique to neurons, this could explain why they are especially susceptible to stress. As many neurodegenerative diseases, lysosomal storage diseases, and pharmacologic

treatments that affect lysosomes disproportionately lead to nervous system pathology, it is possible that the apparent susceptibility of dendritic endosomal maturation and trafficking to stress states precipitate these phenotypes. Therefore, in order to address these disease states we may need to invoke greater focus on the restoration of dendritic trafficking and degradation.

Concluding Remarks

The study of endosomal and lysosomal stress is a rapidly expanding field, with new mechanisms seemingly discovered each day. In this thesis, I have added to this field through the discovery of a novel stress response that operates through the endosomal small GTPase Rab7, both in non-neuronal and neuronal systems. In the broader sense, this stress response likely underlies many physiologic and pathologic cell processes that involve endo-lysosomal stress, most notably neurodegeneration, lysosomal storage disorders, and the use of neuropsychiatric lysosome perturbing drugs. Through this work, I have described novel control by Rab7 over intracellular membrane trafficking, challenged established notions regarding what defines a Rab7 effector, and uniformly presented the idea that Rab7 function in cells is reliant on a tight balance and ordering of effector binding. In doing so, I have more broadly contributed to our understanding of how Rab proteins may be regulated outside of nucleotide binding, but instead through interactions with effector proteins. While the experiments utilized in these studies have caveats, they have ultimately laid a foundation for further investigating Rab7 responses to stress, notably in disease model systems or in Rab7-driven Charcot Marie Tooth 2B, and opened avenues of investigation to better explore the basic principles of Rab7 biology and effector binding.

References

Al-Bassam, S., Xu, M., Wandless, T. J. and Arnold, D. B. (2012). Differential trafficking of transport vesicles contributes to the localization of dendritic proteins. *Cell Rep.* **2**, 89–100.

Alberi, S., Boda, B., Steiner, P., Nikonenko, I., Hirling, H. and Muller, D. (2005). The endosomal protein NEEP21 regulates AMPA receptor-mediated synaptic transmission and plasticity in the hippocampus. *Mol. Cell. Neurosci.* **29**, 313–319.

Allison, R., Lumb, J. H., Fassier, C., Connell, J. W., Ten Martin, D., Seaman, M. N. J., Hazan, J. and Reid, E. (2013). An ESCRT-spastin interaction promotes fission of recycling tubules from the endosome. *J. Cell Biol.* **202**, 527–543.

Arighi, C. N., Hartnell, L. M., Aguilar, R. C., Haft, C. R. and Bonifacino, J. S. (2004). Role of the mammalian retromer in sorting of the cation-independent mannose 6-phosphate receptor. *J. Cell Biol.* **165**, 123–133.

Arnandis, T., Ferrer-Vicens, I., García-Trevijano, E. R., Miralles, V. J., García, C., Torres, L., Viña, J. R. and Zaragozá, R. (2012). Calpains mediate epithelial-cell death during mammary gland involution: mitochondria and lysosomal destabilization. *Cell Death Differ.* **19**, 1536–1548.

Arrazola Sastre, A., Luque Montoro, M., Lacerda, H. M., Llavero, F. and Zugaza, J. L. (2021). Small gtpases of the rab and arf families: key regulators of intracellular trafficking in neurodegeneration. *Int. J. Mol. Sci.* **22**,.

Auer-Grumbach, M. (2004). Hereditary sensory neuropathies. *Drugs Today* **40**, 385–394.

Auer-Grumbach, M., De Jonghe, P., Wagner, K., Verhoeven, K., Hartung, H. P. and Timmerman, V. (2000). Phenotype-genotype correlations in a CMT2B family with refined 3q13-q22 locus. *Neurology* **55**, 1552–1557.

Azzedine, H., Senderek, J., Rivolta, C. and Chrast, R. (2012). Molecular genetics of charcot-marie-tooth disease: from genes to genomes. *Mol. Syndromol.* **3**, 204–214.

Baas, P. W., Deitch, J. S., Black, M. M. and Banker, G. A. (1988). Polarity orientation of microtubules in hippocampal neurons: uniformity in the axon and nonuniformity in the dendrite. *Proc. Natl. Acad. Sci. USA* **85**, 8335–8339.

Balderhaar, H. J. kleine and Ungermann, C. (2013). CORVET and HOPS tethering complexes - coordinators of endosome and lysosome fusion. *J. Cell Sci.* **126**, 1307–1316.

Balderhaar, H. J. K., Arlt, H., Ostrowicz, C., Bröcker, C., Sündermann, F., Brandt, R., Babst, M. and Ungermann, C. (2010). The Rab GTPase Ypt7 is linked to

retromer-mediated receptor recycling and fusion at the yeast late endosome. *J. Cell Sci.* **123**, 4085–4094.

Barford, K., Deppmann, C. and Winckler, B. (2017). The neurotrophin receptor signaling endosome: Where trafficking meets signaling. *Dev. Neurobiol.* **77**, 405–418.

Barford, K., Keeler, A., McMahon, L., McDaniel, K., Yap, C. C., Deppmann, C. D. and Winckler, B. (2018). Transcytosis of TrkA leads to diversification of dendritic signaling endosomes. *Sci. Rep.* **8**, 4715.

Barisic, N., Claeys, K. G., Sirotković-Skerlev, M., Löfgren, A., Nelis, E., De Jonghe, P. and Timmerman, V. (2008). Charcot-Marie-Tooth disease: a clinico-genetic confrontation. *Ann. Hum. Genet.* **72**, 416–441.

BasuRay, S., Mukherjee, S., Romero, E., Wilson, M. C. and Wandinger-Ness, A. (2010). Rab7 mutants associated with Charcot-Marie-Tooth disease exhibit enhanced NGF-stimulated signaling. *PLoS One* **5**, e15351.

BasuRay, S., Mukherjee, S., Romero, E. G., Seaman, M. N. J. and Wandinger-Ness, A. (2013). Rab7 mutants associated with Charcot-Marie-Tooth disease cause delayed growth factor receptor transport and altered endosomal and nuclear signaling. *J. Biol. Chem.* **288**, 1135–1149.

Berg, A. L., Rowson-Hodel, A., Wheeler, M. R., Hu, M., Free, S. R. and Carraway, K. L. (2022). Engaging the Lysosome and Lysosome-Dependent Cell Death in Cancer. In *Breast Cancer* (ed. Mayrovitz, H. N.), Brisbane (AU): Exon Publications.

Bhattacharya, A., Mukherjee, R., Kuncha, S. K., Brunstein, M. E., Rathore, R., Junek, S., Münch, C. and Dikic, I. (2023). A lysosome membrane regeneration pathway depends on TBC1D15 and autophagic lysosomal reformation proteins. *Nat. Cell Biol.* **25**, 685–698.

Boecker, C. A., Olenick, M. A., Gallagher, E. R., Ward, M. E. and Holzbaur, E. L. F. (2020). ToolBox: Live Imaging of intracellular organelle transport in induced pluripotent stem cell-derived neurons. *Traffic* **21**, 138–155.

Bohannon, K. P. and Hanson, P. I. (2020). ESCRT puts its thumb on the nanoscale: Fixing tiny holes in endolysosomes. *Curr. Opin. Cell Biol.* **65**, 122–130.

Boncompain, G., Divoux, S., Gareil, N., de Forges, H., Lescure, A., Latreche, L., Mercanti, V., Jollivet, F., Raposo, G. and Perez, F. (2012). Synchronization of secretory protein traffic in populations of cells. *Nat. Methods* **9**, 493–498.

Bonet-Ponce, L. and Cookson, M. R. (2022). The endoplasmic reticulum contributes to lysosomal tubulation/sorting driven by LRRK2. *Mol. Biol. Cell* **33**, ar124.

Bonet-Ponce, L., Beilina, A., Williamson, C. D., Lindberg, E., Kluss, J. H., Saez-Atienzar, S., Landeck, N., Kumaran, R., Mamais, A., Bleck, C. K. E., et al. (2020). LRRK2 mediates tubulation and vesicle sorting from lysosomes. *Sci. Adv.* **6**,.

Boonen, M., Staudt, C., Gilis, F., Oorschot, V., Klumperman, J. and Jadot, M. (2016). Cathepsin D and its newly identified transport receptor SEZ6L2 can modulate neurite outgrowth. *J. Cell Sci.* **129**, 557–568.

Borchers, A.-C., Langemeyer, L. and Ungermann, C. (2021). Who's in control? Principles of Rab GTPase activation in endolysosomal membrane trafficking and beyond. *J. Cell Biol.* **220**,.

Boyle, K. B., Ellison, C. J., Elliott, P. R., Schuschnig, M., Grimes, K., Dionne, M. S., Sasakawa, C., Munro, S., Martens, S. and Randow, F. (2023). TECPR1 conjugates LC3 to damaged endomembranes upon detection of sphingomyelin exposure. *EMBO J.* **42**, e113012.

Braulke, T. and Bonifacino, J. S. (2009). Sorting of lysosomal proteins. *Biochim. Biophys. Acta* **1793**, 605–614.

Bright, N. A., Davis, L. J. and Luzio, J. P. (2016). Endolysosomes are the principal intracellular sites of acid hydrolase activity. *Curr. Biol.* **26**, 2233–2245.

Bucci, C. and De Luca, M. (2012). Molecular basis of Charcot-Marie-Tooth type 2B disease. *Biochem. Soc. Trans.* **40**, 1368–1372.

Bucci, C., Thomsen, P., Nicoziani, P., McCarthy, J. and van Deurs, B. (2000). Rab7: a key to lysosome biogenesis. *Mol. Biol. Cell* **11**, 467–480.

Cai, C.-Z., Yang, C., Zhuang, X.-X., Yuan, N.-N., Wu, M.-Y., Tan, J.-Q., Song, J.-X., Cheung, K.-H., Su, H., Wang, Y.-T., et al. (2021). NRBF2 is a RAB7 effector required for autophagosome maturation and mediates the association of APP-CTFs with active form of RAB7 for degradation. *Autophagy* **17**, 1112–1130.

Cantalupo, G., Alifano, P., Roberti, V., Bruni, C. B. and Bucci, C. (2001). Rab-interacting lysosomal protein (RILP): the Rab7 effector required for transport to lysosomes. *EMBO J.* **20**, 683–693.

Carosi, J. M., Denton, D., Kumar, S. and Sargeant, T. J. (2023). Receptor recycling by retromer. *Mol. Cell. Biol.* **43**, 317–334.

Cason, S. E., Carman, P. J., Van Duyne, C., Goldsmith, J., Dominguez, R. and Holzbaur, E. L. F. (2021). Sequential dynein effectors regulate axonal autophagosome motility in a maturation-dependent pathway. *J. Cell Biol.* **220**,.

Castle, M. J., Gershenson, Z. T., Giles, A. R., Holzbaur, E. L. F. and Wolfe, J. H. (2014). Adeno-associated virus serotypes 1, 8, and 9 share conserved

mechanisms for anterograde and retrograde axonal transport. *Hum. Gene Ther.* **25**, 705–720.

Ceresa, B. P. and Bahr, S. J. (2006). rab7 activity affects epidermal growth factor:epidermal growth factor receptor degradation by regulating endocytic trafficking from the late endosome. *J. Biol. Chem.* **281**, 1099–1106.

Chadwick, S. R., Grinstein, S. and Freeman, S. A. (2021). From the inside out: Ion fluxes at the centre of endocytic traffic. *Curr. Opin. Cell Biol.* **71**, 77–86.

Chauhan, S., Kumar, S., Jain, A., Ponpuak, M., Mudd, M. H., Kimura, T., Choi, S. W., Peters, R., Mandell, M., Bruun, J.-A., et al. (2016). TRIMs and Galectins Globally Cooperate and TRIM16 and Galectin-3 Co-direct Autophagy in Endomembrane Damage Homeostasis. *Dev. Cell* **39**, 13–27.

Chen, C. S., Chen, W. N., Zhou, M., Arttamangkul, S. and Haugland, R. P. (2000). Probing the cathepsin D using a BODIPY FL-pepstatin A: applications in fluorescence polarization and microscopy. *J Biochem Biophys Methods* **42**, 137–151.

Chen, D., Gibson, E. S. and Kennedy, M. J. (2013). A light-triggered protein secretion system. *J. Cell Biol.* **201**, 631–640.

Chen, Y., Gershlick, D. C., Park, S. Y. and Bonifacino, J. S. (2017). Segregation in the Golgi complex precedes export of endolysosomal proteins in distinct transport carriers. *J. Cell Biol.* **216**, 4141–4151.

Cheng, X.-T., Zhou, B., Lin, M.-Y., Cai, Q. and Sheng, Z.-H. (2015). Axonal autophagosomes recruit dynein for retrograde transport through fusion with late endosomes. *J. Cell Biol.* **209**, 377–386.

Cheng, X.-T., Xie, Y.-X., Zhou, B., Huang, N., Farfel-Becker, T. and Sheng, Z.-H. (2018). Characterization of LAMP1-labeled nondegradative lysosomal and endocytic compartments in neurons. *J. Cell Biol.* **217**, 3127–3139.

Chin, M. Y., Patwardhan, A. R., Ang, K.-H., Wang, A. L., Alquezar, C., Welch, M., Nguyen, P. T., Grabe, M., Molofsky, A. V., Arkin, M. R., et al. (2021). Genetically Encoded, pH-Sensitive mTFP1 Biosensor for Probing Lysosomal pH. *ACS Sens.* **6**, 2168–2180.

Cioni, J.-M., Lin, J. Q., Holtermann, A. V., Koppers, M., Jakobs, M. A. H., Azizi, A., Turner-Bridger, B., Shigeoka, T., Franze, K., Harris, W. A., et al. (2019). Late Endosomes Act as mRNA Translation Platforms and Sustain Mitochondria in Axons. *Cell* **176**, 56–72.e15.

Clapham, D. E. (2007). Calcium signaling. *Cell* **131**, 1047–1058.

Cogli, L., Piro, F. and Bucci, C. (2009). Rab7 and the CMT2B disease. *Biochem. Soc. Trans.* **37**, 1027–1031.

Cogli, L., Progida, C., Lecci, R., Bramato, R., Krüttgen, A. and Bucci, C. (2010). CMT2B-associated Rab7 mutants inhibit neurite outgrowth. *Acta Neuropathol.* **120**, 491–501.

Cogli, L., Progida, C., Thomas, C. L., Spencer-Dene, B., Donno, C., Schiavo, G. and Bucci, C. (2013). Charcot-Marie-Tooth type 2B disease-causing RAB7A mutant proteins show altered interaction with the neuronal intermediate filament peripherin. *Acta Neuropathol.* **125**, 257–272.

Colacurcio, D. J. and Nixon, R. A. (2016). Disorders of lysosomal acidification-The emerging role of v-ATPase in aging and neurodegenerative disease. *Ageing Res Rev* **32**, 75–88.

Colecchia, D., Stasi, M., Leonardi, M., Manganelli, F., Nolano, M., Veneziani, B. M., Santoro, L., Eskelinen, E.-L., Chiariello, M. and Bucci, C. (2018). Alterations of autophagy in the peripheral neuropathy Charcot-Marie-Tooth type 2B. *Autophagy* **14**, 930–941.

Collins, M. P. and Forgac, M. (2020). Regulation and function of V-ATPases in physiology and disease. *Biochim. Biophys. Acta Biomembr.* **1862**, 183341.

Corkery, D. P., Castro-Gonzalez, S., Knyazeva, A., Herzog, L. K. and Wu, Y.-W. (2023). An ATG12-ATG5-TECPR1 E3-like complex regulates unconventional LC3 lipidation at damaged lysosomes. *EMBO Rep.* **24**, e56841.

Cross, J., Durgan, J., McEwan, D. G. and Florey, O. (2023a). Lysosome damage triggers direct ATG8 conjugation and ATG2 engagement via CASM. *BioRxiv*.

Cross, J., Durgan, J., McEwan, D. G., Tayler, M., Ryan, K. M. and Florey, O. (2023b). Lysosome damage triggers direct ATG8 conjugation and ATG2 engagement via non-canonical autophagy. *J. Cell Biol.* **222**,.

Cui, Y., Carosi, J. M., Yang, Z., Ariotti, N., Kerr, M. C., Parton, R. G., Sargeant, T. J. and Teasdale, R. D. (2019). Retromer has a selective function in cargo sorting via endosome transport carriers. *J. Cell Biol.* **218**, 615–631.

Cui, L., Zhao, L.-P., Ye, J.-Y., Yang, L., Huang, Y., Jiang, X.-P., Zhang, Q., Jia, J.-Z., Zhang, D.-X. and Huang, Y. (2020). The lysosomal membrane protein lamp2 alleviates lysosomal cell death by promoting autophagic flux in ischemic cardiomyocytes. *Front. Cell Dev. Biol.* **8**, 31.

Cullen, P. J. and Steinberg, F. (2018). To degrade or not to degrade: mechanisms and significance of endocytic recycling. *Nat. Rev. Mol. Cell Biol.* **19**, 679–696.

D'Souza, R. S., Semus, R., Billings, E. A., Meyer, C. B., Conger, K. and Casanova, J. E. (2014). Rab4 orchestrates a small GTPase cascade for recruitment of adaptor proteins to early endosomes. *Curr. Biol.* **24**, 1187–1198.

da Silva, S. and Wang, F. (2011). Retrograde neural circuit specification by target-derived neurotrophins and growth factors. *Curr. Opin. Neurobiol.* **21**, 61–67.

Daly, J. L., Danson, C. M., Lewis, P. A., Zhao, L., Riccardo, S., Di Filippo, L., Cacchiarelli, D., Lee, D., Cross, S. J., Heesom, K. J., et al. (2023). Multi-omic approach characterises the neuroprotective role of retromer in regulating lysosomal health. *Nat. Commun.* **14**, 3086.

De Jonghe, P., Timmerman, V., FitzPatrick, D., Spoelders, P., Martin, J. J. and Van Broeckhoven, C. (1997). Mutilating neuropathic ulcerations in a chromosome 3q13-q22 linked Charcot-Marie-Tooth disease type 2B family. *J. Neurol. Neurosurg. Psychiatry* **62**, 570–573.

De Luca, A., Progida, C., Spinosa, M. R., Alifano, P. and Bucci, C. (2008). Characterization of the Rab7K157N mutant protein associated with Charcot-Marie-Tooth type 2B. *Biochem. Biophys. Res. Commun.* **372**, 283–287.

De Luca, M., Cogli, L., Progida, C., Nisi, V., Pascolutti, R., Sigismund, S., Di Fiore, P. P. and Bucci, C. (2014). RILP regulates vacuolar ATPase through interaction with the V1G1 subunit. *J. Cell Sci.* **127**, 2697–2708.

Deinhardt, K., Salinas, S., Verastegui, C., Watson, R., Worth, D., Hanrahan, S., Bucci, C. and Schiavo, G. (2006). Rab5 and Rab7 control endocytic sorting along the axonal retrograde transport pathway. *Neuron* **52**, 293–305.

Delcroix, J.-D., Valletta, J. S., Wu, C., Hunt, S. J., Kowal, A. S. and Mobley, W. C. (2003). NGF signaling in sensory neurons: evidence that early endosomes carry NGF retrograde signals. *Neuron* **39**, 69–84.

Deng, Y., Rivera-Molina, F. E., Toomre, D. K. and Burd, C. G. (2016). Sphingomyelin is sorted at the trans Golgi network into a distinct class of secretory vesicle. *Proc. Natl. Acad. Sci. USA* **113**, 6677–6682.

Deppmann, C. D. and Ginty, D. D. (2006). Retrograde control of neural circuit formation. *Cell* **127**, 1306–1307.

Deschamps, A., Colinet, A.-S., Zimmermannova, O., Sychrova, H. and Morsomme, P. (2020). A new pH sensor localized in the Golgi apparatus of Saccharomyces cerevisiae reveals unexpected roles of Vph1p and Stv1p isoforms. *Sci. Rep.* **10**, 1881.

Díaz, E. and Pfeffer, S. R. (1998). TIP47: a cargo selection device for mannose 6-phosphate receptor trafficking. *Cell* **93**, 433–443.

Diering, G. H., Numata, Y., Fan, S., Church, J. and Numata, M. (2013). Endosomal acidification by Na+/H+ exchanger NHE5 regulates TrkA cell-surface targeting and NGF-induced PI3K signaling. *Mol. Biol. Cell* **24**, 3435–3448.

Dilsizoglu Senol, A., Samarani, M., Syan, S., Guardia, C. M., Nonaka, T., Liv, N., Latour-Lambert, P., Hasegawa, M., Klumperman, J., Bonifacino, J. S., et al. (2021). α-Synuclein fibrils subvert lysosome structure and function for the propagation of protein misfolding between cells through tunneling nanotubes. *PLoS Biol.* **19**, e3001287.

Dong, X., Shen, D., Wang, X., Dawson, T., Li, X., Zhang, Q., Cheng, X., Zhang, Y., Weisman, L. S., Delling, M., et al. (2010). PI(3,5)P(2) controls membrane trafficking by direct activation of mucolipin Ca(2+) release channels in the endolysosome. *Nat. Commun.* **1**, 38.

Doray, B., Bruns, K., Ghosh, P. and Kornfeld, S. (2002). Interaction of the cation-dependent mannose 6-phosphate receptor with GGA proteins. *J. Biol. Chem.* **277**, 18477–18482.

Du Rietz, H., Hedlund, H., Wilhelmson, S., Nordenfelt, P. and Wittrup, A. (2020). Imaging small molecule-induced endosomal escape of siRNA. *Nat. Commun.* **11**, 1809.

Eapen, V. V., Swarup, S., Hoyer, M. J., Paulo, J. A. and Harper, J. W. (2021). Quantitative proteomics reveals the selectivity of ubiquitin-binding autophagy receptors in the turnover of damaged lysosomes by lysophagy. *Elife* **10**,.

Ebstrup, M. L., Sønder, S. L., Fogde, D. L., Heitmann, A. S. B., Dietrich, T. N., Dias, C., Jäättelä, M., Maeda, K. and Nylandsted, J. (2023). Annexin A7 mediates lysosome repair independently of ESCRT-III. *Front. Cell Dev. Biol.* **11**, 1211498.

Ecard, J., Lian, Y.-L., Divoux, S., Gouveia, Z., Vigne, E., Perez, F. and Boncompain, G. (2024). Lysosomal membrane proteins LAMP1 and LIMP2 are segregated in the Golgi apparatus independently of their clathrin adaptor binding motif. *Mol. Biol. Cell* mbcE23060251.

Elkin, S. R., Lakoduk, A. M. and Schmid, S. L. (2016). Endocytic pathways and endosomal trafficking: a primer. *Wien. Med. Wochenschr.* **166**, 196–204.

Eriksson, I., Wäster, P. and Öllinger, K. (2020). Restoration of lysosomal function after damage is accompanied by recycling of lysosomal membrane proteins. *Cell Death Dis.* **11**, 370.

Farfel-Becker, T., Roney, J. C., Cheng, X.-T., Li, S., Cuddy, S. R. and Sheng, Z.-H. (2019). Neuronal Soma-Derived Degradative Lysosomes Are Continuously Delivered to Distal Axons to Maintain Local Degradation Capacity. *Cell Rep.* **28**, 51–64.e4.

Feng, S. and Arnold, D. B. (2016). Techniques for studying protein trafficking and molecular motors in neurons. *Cytoskeleton (Hoboken)* **73**, 508–515.

Flavin, W. P., Bousset, L., Green, Z. C., Chu, Y., Skarpathiotis, S., Chaney, M. J., Kordower, J. H., Melki, R. and Campbell, E. M. (2017). Endocytic vesicle rupture is a conserved mechanism of cellular invasion by amyloid proteins. *Acta Neuropathol.* **134**, 629–653.

Florey, O. (2023). TECPR1 helps bridge the CASM during lysosome damage. *EMBO J.* **42**, e115210.

Freeman, D., Cedillos, R., Choyke, S., Lukic, Z., McGuire, K., Marvin, S., Burrage, A. M., Sudholt, S., Rana, A., O'Connor, C., et al. (2013). Alpha-synuclein induces lysosomal rupture and cathepsin dependent reactive oxygen species following endocytosis. *PLoS One* **8**, e62143.

Freeman, S. A., Grinstein, S. and Orlowski, J. (2023). Determinants, maintenance, and function of organellar pH. *Physiol. Rev.* **103**, 515–606.

Gallagher, E. R. and Holzbaur, E. L. F. (2023). The selective autophagy adaptor p62/SQSTM1 forms phase condensates regulated by HSP27 that facilitate the clearance of damaged lysosomes via lysophagy. *Cell Rep.* **42**, 112037.

Gao, Y., Xiong, J., Chu, Q.-Z. and Ji, W.-K. (2022). PDZD8-mediated lipid transfer at contacts between the ER and late endosomes/lysosomes is required for neurite outgrowth. *J. Cell Sci.* **135**,.

Ghosh, P., Dahms, N. M. and Kornfeld, S. (2003). Mannose 6-phosphate receptors: new twists in the tale. *Nat. Rev. Mol. Cell Biol.* **4**, 202–212.

Gillooly, D. J., Morrow, I. C., Lindsay, M., Gould, R., Bryant, N. J., Gaullier, J. M., Parton, R. G. and Stenmark, H. (2000). Localization of phosphatidylinositol 3-phosphate in yeast and mammalian cells. *EMBO J.* **19**, 4577–4588.

Giudetti, A. M., Guerra, F., Longo, S., Beli, R., Romano, R., Manganelli, F., Nolano, M., Mangini, V., Santoro, L. and Bucci, C. (2020). An altered lipid metabolism characterizes Charcot-Marie-Tooth type 2B peripheral neuropathy. *Biochim. Biophys. Acta Mol. Cell Biol. Lipids* **1865**, 158805.

Goldman, R. and Kaplan, A. (1973). Rupture of rat liver lysosomes mediated by l-amino acid esters. *Biochimica et Biophysica Acta (BBA) - Biomembranes* **318**, 205–216.

Grant, B. D. and Donaldson, J. G. (2009). Pathways and mechanisms of endocytic recycling. *Nat. Rev. Mol. Cell Biol.* **10**, 597–608.

Griffiths, G., Hoflack, B., Simons, K., Mellman, I. and Kornfeld, S. (1988). The mannose 6-phosphate receptor and the biogenesis of lysosomes. *Cell* **52**, 329–341.

Grosshans, B. L., Ortiz, D. and Novick, P. (2006). Rabs and their effectors: achieving specificity in membrane traffic. *Proc. Natl. Acad. Sci. USA* **103**, 11821–11827.

Gu, Y., Guerra, F., Hu, M., Pope, A., Sung, K., Yang, W., Jetha, S., Shoff, T. A., Gunatilake, T., Dahlkamp, O., et al. (2022). Mitochondria dysfunction in Charcot Marie Tooth 2B Peripheral Sensory Neuropathy. *Commun. Biol.* **5**, 717.

Guerra, F. and Bucci, C. (2016). Multiple roles of the small gtpase rab7. *Cells* **5**,.

Han, Y., Branon, T. C., Martell, J. D., Boassa, D., Shechner, D., Ellisman, M. H. and Ting, A. (2019). Directed evolution of split APEX2 peroxidase. *ACS Chem. Biol.* **14**, 619–635.

Hancock-Cerutti, W., Wu, Z., Xu, P., Yadavalli, N., Leonzino, M., Tharkeshwar, A. K., Ferguson, S. M., Shadel, G. S. and De Camilli, P. (2022). ER-lysosome lipid transfer protein VPS13C/PARK23 prevents aberrant mtDNA-dependent STING signaling. *J. Cell Biol.* **221**,.

Hangen, E., Cordelières, F. P., Petersen, J. D., Choquet, D. and Coussen, F. (2018). Neuronal activity and intracellular calcium levels regulate intracellular transport of newly synthesized AMPAR. *Cell Rep.* **24**, 1001–1012.e3.

Harding, A. E. and Thomas, P. K. (1980). The clinical features of hereditary motor and sensory neuropathy types I and II. *Brain* **103**, 259–280.

Harrington, A. W., St Hillaire, C., Zweifel, L. S., Glebova, N. O., Philippidou, P., Halegoua, S. and Ginty, D. D. (2011). Recruitment of actin modifiers to TrkA endosomes governs retrograde NGF signaling and survival. *Cell* **146**, 421–434.

Harrison, M. S., Hung, C.-S., Liu, T., Christiano, R., Walther, T. C. and Burd, C. G. (2014). A mechanism for retromer endosomal coat complex assembly with cargo. *Proc. Natl. Acad. Sci. USA* **111**, 267–272.

Helms, J. B. and Rothman, J. E. (1992). Inhibition by brefeldin A of a Golgi membrane enzyme that catalyses exchange of guanine nucleotide bound to ARF. *Nature* **360**, 352–354.

Henry, M. E., Schmidt, M. E., Hennen, J., Villafuerte, R. A., Butman, M. L., Tran, P., Kerner, L. T., Cohen, B. and Renshaw, P. F. (2005). A comparison of brain and serum pharmacokinetics of R-fluoxetine and racemic fluoxetine: A 19-F MRS study. *Neuropsychopharmacology* **30**, 1576–1583.

Herbst, S., Campbell, P., Harvey, J., Bernard, E. M., Papayannopoulos, V., Wood, N. W., Morris, H. R. and Gutierrez, M. G. (2020). LRRK2 activation controls the repair of damaged endomembranes in macrophages. *EMBO J.* **39**, e104494.

Hiragi, S., Matsui, T., Sakamaki, Y. and Fukuda, M. (2022). TBC1D18 is a Rab5-GAP that coordinates endosome maturation together with Mon1. *J. Cell Biol.* **221**,.

Ho, R. and Stroupe, C. (2015). The HOPS/class C Vps complex tethers membranes by binding to one Rab GTPase in each apposed membrane. *Mol. Biol. Cell* **26**, 2655–2663.

Hoflack, B. and Kornfeld, S. (1985). Lysosomal enzyme binding to mouse P388D1 macrophage membranes lacking the 215-kDa mannose 6-phosphate receptor: evidence for the existence of a second mannose 6-phosphate receptor. *Proc. Natl. Acad. Sci. USA* **82**, 4428–4432.

Homma, Y., Kinoshita, R., Kuchitsu, Y., Wawro, P. S., Marubashi, S., Oguchi, M. E., Ishida, M., Fujita, N. and Fukuda, M. (2019). Comprehensive knockout analysis of the Rab family GTPases in epithelial cells. *J. Cell Biol.* **218**, 2035–2050.

Homma, Y., Hiragi, S. and Fukuda, M. (2021). Rab family of small GTPases: an updated view on their regulation and functions. *FEBS J.* **288**, 36–55.

Hooper, K. M., Jacquin, E., Li, T., Goodwin, J. M., Brumell, J. H., Durgan, J. and Florey, O. (2022). V-ATPase is a universal regulator of LC3-associated phagocytosis and non-canonical autophagy. *J. Cell Biol.* **221**,.

Houlden, H., King, R. H. M., Muddle, J. R., Warner, T. T., Reilly, M. M., Orrell, R. W. and Ginsberg, L. (2004). A novel RAB7 mutation associated with ulcero-mutilating neuropathy. *Ann. Neurol.* **56**, 586–590.

Howe, C. L. and Mobley, W. C. (2005). Long-distance retrograde neurotrophic signaling. *Curr. Opin. Neurobiol.* **15**, 40–48.

Hoyer, M. J., Swarup, S. and Harper, J. W. (2022). Mechanisms controlling selective elimination of damaged lysosomes. *Curr. Opin. Physiol.* **29**,.

Hoyle, J. C., Isfort, M. C., Roggenbuck, J. and Arnold, W. D. (2015). The genetics of Charcot-Marie-Tooth disease: current trends and future implications for diagnosis and management. *Appl Clin Genet* **8**, 235–243.

Hraběta, J., Belhajová, M., Šubrtová, H., Merlos Rodrigo, M. A., Heger, Z. and Eckschlager, T. (2020). Drug sequestration in lysosomes as one of the mechanisms of chemoresistance of cancer cells and the possibilities of its inhibition. *Int. J. Mol. Sci.* **21**,.

Hung, Y.-H., Chen, L. M.-W., Yang, J.-Y. and Yang, W. Y. (2013). Spatiotemporally controlled induction of autophagy-mediated lysosome turnover. *Nat. Commun.* **4**, 2111.

Huotari, J. and Helenius, A. (2011). Endosome maturation. *EMBO J.* **30**, 3481–3500.

Hurtado-Lorenzo, A., Skinner, M., El Annan, J., Futai, M., Sun-Wada, G.-H., Bourgoin, S., Casanova, J., Wildeman, A., Bechoua, S., Ausiello, D. A., et al. (2006). V-ATPase interacts with ARNO and Arf6 in early endosomes and regulates the protein degradative pathway. *Nat. Cell Biol.* **8**, 124–136.

Hutagalung, A. H. and Novick, P. J. (2011). Role of Rab GTPases in membrane traffic and cell physiology. *Physiol. Rev.* **91**, 119–149.

Ikonomov, O. C., Sbrissa, D. and Shisheva, A. (2001). Mammalian cell morphology and endocytic membrane homeostasis require enzymatically active phosphoinositide 5-kinase PIKfyve. *J. Biol. Chem.* **276**, 26141–26147.

Jakobs, M. A., Dimitracopoulos, A. and Franze, K. (2019). KymoButler, a deep learning software for automated kymograph analysis. *Elife* **8**,.

Janssens, K., Goethals, S., Atkinson, D., Ermanoska, B., Fransen, E., Jordanova, A., Auer-Grumbach, M., Asselbergh, B. and Timmerman, V. (2014). Human Rab7 mutation mimics features of Charcot-Marie-Tooth neuropathy type 2B in Drosophila. *Neurobiol. Dis.* **65**, 211–219.

Jia, J., Claude-Taupin, A., Gu, Y., Choi, S. W., Peters, R., Bissa, B., Mudd, M. H., Allers, L., Pallikkuth, S., Lidke, K. A., et al. (2020a). Galectin-3 Coordinates a Cellular System for Lysosomal Repair and Removal. *Dev. Cell* **52**, 69–87.e8.

Jia, J., Claude-Taupin, A., Gu, Y., Choi, S. W., Peters, R., Bissa, B., Mudd, M. H., Allers, L., Pallikkuth, S., Lidke, K. A., et al. (2020b). MERIT, a cellular system coordinating lysosomal repair, removal and replacement. *Autophagy* **16**, 1539–1541.

Jiang, P., Nishimura, T., Sakamaki, Y., Itakura, E., Hatta, T., Natsume, T. and Mizushima, N. (2014). The HOPS complex mediates autophagosome-lysosome fusion through interaction with syntaxin 17. *Mol. Biol. Cell* **25**, 1327–1337.

Jimenez, A. J., Maiuri, P., Lafaurie-Janvore, J., Divoux, S., Piel, M. and Perez, F. (2014). ESCRT machinery is required for plasma membrane repair. *Science* **343**, 1247136.

Jimenez-Orgaz, A., Kvainickas, A., Nägele, H., Denner, J., Eimer, S., Dengjel, J. and Steinberg, F. (2018). Control of RAB7 activity and localization through the retromer-TBC1D5 complex enables RAB7-dependent mitophagy. *EMBO J.* **37**, 235–254.

Johannes, L., Jacob, R. and Leffler, H. (2018). Galectins at a glance. *J. Cell Sci.* **131**,.

Johansson, M., Lehto, M., Tanhuanpää, K., Cover, T. L. and Olkkonen, V. M. (2005). The oxysterol-binding protein homologue ORP1L interacts with Rab7 and alters functional properties of late endocytic compartments. *Mol. Biol. Cell* **16**, 5480–5492.

Johansson, M., Rocha, N., Zwart, W., Jordens, I., Janssen, L., Kuijl, C., Olkkonen, V. M. and Neefjes, J. (2007). Activation of endosomal dynein motors by stepwise assembly of Rab7-RILP-p150Glued, ORP1L, and the receptor betalll spectrin. *J. Cell Biol.* **176**, 459–471.

Johnson, D. E., Ostrowski, P., Jaumouillé, V. and Grinstein, S. (2016). The position of lysosomes within the cell determines their luminal pH. *J. Cell Biol.* **212**, 677–692.

Jongsma, M. L., Bakker, J., Cabukusta, B., Liv, N., van Elsland, D., Fermie, J., Akkermans, J. L., Kuijl, C., van der Zanden, S. Y., Janssen, L., et al. (2020). SKIP-HOPS recruits TBC1D15 for a Rab7-to-Arl8b identity switch to control late endosome transport. *EMBO J.* **39**, e102301.

Jordens, I., Fernandez-Borja, M., Marsman, M., Dusseljee, S., Janssen, L., Calafat, J., Janssen, H., Wubbolts, R. and Neefjes, J. (2001). The Rab7 effector protein RILP controls lysosomal transport by inducing the recruitment of dynein-dynactin motors. *Curr. Biol.* **11**, 1680–1685.

Kallunki, T., Olsen, O. D. and Jäättelä, M. (2013). Cancer-associated lysosomal changes: friends or foes? *Oncogene* **32**, 1995–2004.

Kametaka, S. and Waguri, S. (2012). Visualization of TGN-endosome trafficking in mammalian and Drosophila cells. *Meth. Enzymol.* **504**, 255–271.

Kavčič, N., Butinar, M., Sobotič, B., Hafner Česen, M., Petelin, A., Bojić, L., Zavašnik Bergant, T., Bratovš, A., Reinheckel, T. and Turk, B. (2020). Intracellular cathepsin C levels determine sensitivity of cells to leucyl-leucine methyl ester-triggered apoptosis. *FEBS J.* **287**, 5148–5166.

Kawamura, N., Sun-Wada, G.-H., Aoyama, M., Harada, A., Takasuga, S., Sasaki, T. and Wada, Y. (2012). Delivery of endosomes to lysosomes via microautophagy in the visceral endoderm of mouse embryos. *Nat. Commun.* **3**, 1071.

Kawamura, N., Takaoka, K., Hamada, H., Hadjantonakis, A.-K., Sun-Wada, G.-H. and Wada, Y. (2020). Rab7-Mediated Endocytosis Establishes Patterning of Wnt Activity through Inactivation of Dkk Antagonism. *Cell Rep.* **31**, 107733.

Khatter, D., Raina, V. B., Dwivedi, D., Sindhwani, A., Bahl, S. and Sharma, M. (2015). The small GTPase Arl8b regulates assembly of the mammalian HOPS complex on lysosomes. *J. Cell Sci.* **128**, 1746–1761.

Khobrekar, N. V., Quintremil, S., Dantas, T. J. and Vallee, R. B. (2020). The dynein adaptor RILP controls neuronal autophagosome biogenesis, transport, and clearance. *Dev. Cell* **53**, 141–153.e4.

Kinchen, J. M. and Ravichandran, K. S. (2010). Identification of two evolutionarily conserved genes regulating processing of engulfed apoptotic cells. *Nature* **464**, 778–782.

Kirkegaard, T., Roth, A. G., Petersen, N. H. T., Mahalka, A. K., Olsen, O. D., Moilanen, I., Zylicz, A., Knudsen, J., Sandhoff, K., Arenz, C., et al. (2010).

Hsp70 stabilizes lysosomes and reverts Niemann-Pick disease-associated lysosomal pathology. *Nature* **463**, 549–553.

Klionsky, D. J., Elazar, Z., Seglen, P. O. and Rubinsztein, D. C. (2008). Does bafilomycin A1 block the fusion of autophagosomes with lysosomes? *Autophagy* **4**, 849–850.

Klumperman, J. and Raposo, G. (2014). The complex ultrastructure of the endolysosomal system. *Cold Spring Harb. Perspect. Biol.* **6**, a016857.

Koerver, L., Papadopoulos, C., Liu, B., Kravic, B., Rota, G., Brecht, L., Veenendaal, T., Polajnar, M., Bluemke, A., Ehrmann, M., et al. (2019). The ubiquitin-conjugating enzyme UBE2QL1 coordinates lysophagy in response to endolysosomal damage. *EMBO Rep.* **20**, e48014.

Kreuzaler, P. A., Staniszewska, A. D., Li, W., Omidvar, N., Kedjouar, B., Turkson, J., Poli, V., Flavell, R. A., Clarkson, R. W. E. and Watson, C. J. (2011). Stat3 controls lysosomal-mediated cell death in vivo. *Nat. Cell Biol.* **13**, 303–309.

Krzystek, T. J., White, J. A., Rathnayake, R., Thurston, L., Hoffmar-Glennon, H., Li, Y. and Gunawardena, S. (2023). HTT (huntingtin) and RAB7 co-migrate retrogradely on a signaling LAMP1-containing late endosome during axonal injury. *Autophagy* **19**, 1199–1220.

Kuchitsu, Y. and Fukuda, M. (2018). Revisiting rab7 functions in mammalian autophagy: rab7 knockout studies. *Cells* **7**,.

Kuchitsu, Y., Homma, Y., Fujita, N. and Fukuda, M. (2018). Rab7 knockout unveils regulated autolysosome maturation induced by glutamine starvation. *J. Cell Sci.* **131**,.

Kuijpers, M., Nguyen, P. T. and Haucke, V. (2023). The endoplasmic reticulum and its contacts: emerging roles in axon development, neurotransmission, and degeneration. *Neuroscientist* 10738584231162810.

Kulkarni, V. V., Stempel, M. H., Anand, A., Sidibe, D. K. and Maday, S. (2022). Retrograde axonal autophagy and endocytic pathways are parallel and separate in neurons. *J. Neurosci.* **42**, 8524–8541.

Kumar, S., Chauhan, S., Jain, A., Ponpuak, M., Choi, S. W., Mudd, M., Peters, R., Mandell, M. A., Johansen, T. and Deretic, V. (2017). Galectins and TRIMs directly interact and orchestrate autophagic response to endomembrane damage. *Autophagy* **13**, 1086–1087.

Kuwahara, T., Funakawa, K., Komori, T., Sakurai, M., Yoshii, G., Eguchi, T., Fukuda, M. and Iwatsubo, T. (2020). Roles of lysosomotropic agents on LRRK2 activation and Rab10 phosphorylation. *Neurobiol. Dis.* **145**, 105081.

Kuzu, O. F., Toprak, M., Noory, M. A. and Robertson, G. P. (2017). Effect of lysosomotropic molecules on cellular homeostasis. *Pharmacol. Res.* **117**, 177–184.

Kvainickas, A., Jimenez-Orgaz, A., Nägele, H., Hu, Z., Dengjel, J. and Steinberg, F. (2017). Cargo-selective SNX-BAR proteins mediate retromer trimer independent retrograde transport. *J. Cell Biol.* **216**, 3677–3693.

Kwon, J. M., Elliott, J. L., Yee, W. C., Ivanovich, J., Scavarda, N. J., Moolsintong, P. J. and Goodfellow, P. J. (1995). Assignment of a second Charcot-Marie-Tooth type II locus to chromosome 3q. *Am. J. Hum. Genet.* **57**, 853–858.

Lakpa, K. L., Khan, N., Afghah, Z., Chen, X. and Geiger, J. D. (2021). Lysosomal stress response (LSR): physiological importance and pathological relevance. *J Neuroimmune Pharmacol* **16**, 219–237.

Lamber, E. P., Siedenburg, A.-C. and Barr, F. A. (2019). Rab regulation by GEFs and GAPs during membrane traffic. *Curr. Opin. Cell Biol.* **59**, 34–39.

Langemeyer, L., Fröhlich, F. and Ungermann, C. (2018). Rab gtpase function in endosome and lysosome biogenesis. *Trends Cell Biol.* **28**, 957–970.

Lasiecka, Z. M. and Winckler, B. (2016). Studying endosomes in cultured neurons by live-cell imaging. *Methods Cell Biol.* **131**, 389–408.

Lasiecka, Z. M., Yap, C. C., Caplan, S. and Winckler, B. (2010). Neuronal early endosomes require EHD1 for L1/NgCAM trafficking. *J. Neurosci.* **30**, 16485–16497.

Lee, S., Sato, Y. and Nixon, R. A. (2011). Lysosomal proteolysis inhibition selectively disrupts axonal transport of degradative organelles and causes an Alzheimer's-like axonal dystrophy. *J. Neurosci.* **31**, 7817–7830.

Lennon, N. J., Kho, A., Bacskai, B. J., Perlmutter, S. L., Hyman, B. T. and Brown, R. H. (2003). Dysferlin interacts with annexins A1 and A2 and mediates sarcolemmal wound-healing. *J. Biol. Chem.* **278**, 50466–50473.

Levin-Konigsberg, R., Montaño-Rendón, F., Keren-Kaplan, T., Li, R., Ego, B., Mylvaganam, S., DiCiccio, J. E., Trimble, W. S., Bassik, M. C., Bonifacino, J. S., et al. (2019). Phagolysosome resolution requires contacts with the endoplasmic reticulum and phosphatidylinositol-4-phosphate signalling. *Nat. Cell Biol.* **21**, 1234–1247.

Liang, W., Sagar, S., Ravindran, R., Najor, R. H., Quiles, J. M., Chi, L., Diao, R. Y., Woodall, B. P., Leon, L. J., Zumaya, E., et al. (2023). Mitochondria are secreted in extracellular vesicles when lysosomal function is impaired. *Nat. Commun.* **14**, 5031.

Lie, P. P. Y. and Nixon, R. A. (2019). Lysosome trafficking and signaling in health and neurodegenerative diseases. *Neurobiol. Dis.* **122**, 94–105.

Lie, P. P. Y., Yang, D.-S., Stavrides, P., Goulbourne, C. N., Zheng, P., Mohan, P. S., Cataldo, A. M. and Nixon, R. A. (2021). Post-Golgi carriers, not lysosomes, confer lysosomal properties to pre-degradative organelles in normal and dystrophic axons. *Cell Rep.* **35**, 109034.

Lin, X., Yang, T., Wang, S., Wang, Z., Yun, Y., Sun, L., Zhou, Y., Xu, X., Akazawa, C., Hong, W., et al. (2014). RILP interacts with HOPS complex via VPS41 subunit to regulate endocytic trafficking. *Sci. Rep.* **4**, 7282.

Lipsky, N. G. and Pagano, R. E. (1983). Sphingolipid metabolism in cultured fibroblasts: microscopic and biochemical studies employing a fluorescent ceramide analogue. *Proc. Natl. Acad. Sci. USA* **80**, 2608–2612.

Lipton, P. (2013). Lysosomal membrane permeabilization as a key player in brain ischemic cell death: a “lysosomocentric” hypothesis for ischemic brain damage. *Transl. Stroke Res.* **4**, 672–684.

Liu, G. Y. and Sabatini, D. M. (2020). mTOR at the nexus of nutrition, growth, ageing and disease. *Nat. Rev. Mol. Cell Biol.* **21**, 183–203.

Liu, H. and Wu, C. (2017). Charcot marie tooth 2B peripheral sensory neuropathy: how rab7 mutations impact NGF signaling? *Int. J. Mol. Sci.* **18**,.

Liu, E. A., Schultz, M. L., Mochida, C., Chung, C., Paulson, H. L. and Lieberman, A. P. (2020). Fbxo2 mediates clearance of damaged lysosomes and modifies neurodegeneration in the Niemann-Pick C brain. *JCI Insight*.

Loison, F., Zhu, H., Karatepe, K., Kasorn, A., Liu, P., Ye, K., Zhou, J., Cao, S., Gong, H., Jenne, D. E., et al. (2014). Proteinase 3–dependent caspase-3 cleavage modulates neutrophil death and inflammation. *J. Clin. Invest.*

Lönn, P., Kacsinta, A. D., Cui, X.-S., Hamil, A. S., Kaulich, M., Gogoi, K. and Dowdy, S. F. (2016). Enhancing endosomal escape for intracellular delivery of macromolecular biologic therapeutics. *Sci. Rep.* **6**, 32301.

Lund, V. K., Lycas, M. D., Schack, A., Andersen, R. C., Gether, U. and Kjaerulff, O. (2021). Rab2 drives axonal transport of dense core vesicles and lysosomal organelles. *Cell Rep.* **35**, 108973.

Ma, X., Liu, K., Li, J., Li, H., Li, J., Liu, Y., Yang, C. and Liang, H. (2018). A non-canonical GTPase interaction enables ORP1L-Rab7-RILP complex formation and late endosome positioning. *J. Biol. Chem.* **293**, 14155–14164.

Maday, S. and Holzbaur, E. L. F. (2016). Compartment-Specific Regulation of Autophagy in Primary Neurons. *J. Neurosci.* **36**, 5933–5945.

Maejima, I., Takahashi, A., Omori, H., Kimura, T., Takabatake, Y., Saitoh, T., Yamamoto, A., Hamasaki, M., Noda, T., Isaka, Y., et al. (2013). Autophagy sequesters damaged lysosomes to control lysosomal biogenesis and kidney injury. *EMBO J.* **32**, 2336–2347.

Malik, B. R., Maddison, D. C., Smith, G. A. and Peters, O. M. (2019). Autophagic and endo-lysosomal dysfunction in neurodegenerative disease. *Mol. Brain* **12**, 100.

Maranda, B., Brown, D., Bourgoin, S., Casanova, J. E., Vinay, P., Ausiello, D. A. and Marshansky, V. (2001). Intra-endosomal pH-sensitive recruitment of the Arf-nucleotide exchange factor ARNO and Arf6 from cytoplasm to proximal tubule endosomes. *J. Biol. Chem.* **276**, 18540–18550.

Markworth, R., Dambeck, V., Steinbeck, L. M., Koufali, A., Bues, B., Dankovich, T. M., Wichmann, C. and Burk, K. (2021). Tubular microdomains of Rab7-endosomes retrieve TrkA, a mechanism disrupted in Charcot-Marie-Tooth 2B. *J. Cell Sci.*

Marshansky, V. (2007). The V-ATPase a2-subunit as a putative endosomal pH-sensor. *Biochem. Soc. Trans.* **35**, 1092–1099.

Martin, O. C. and Pagano, R. E. (1994). Internalization and sorting of a fluorescent analogue of glucosylceramide to the Golgi apparatus of human skin fibroblasts: utilization of endocytic and nonendocytic transport mechanisms. *J. Cell Biol.* **125**, 769–781.

Martina, J. A., Chen, Y., Gucek, M. and Puertollano, R. (2012). MTORC1 functions as a transcriptional regulator of autophagy by preventing nuclear transport of TFEB. *Autophagy* **8**, 903–914.

Maruzs, T., Lőrincz, P., Szatmári, Z., Széplaki, S., Sándor, Z., Lakatos, Z., Puska, G., Juhász, G. and Sass, M. (2015). Retromer ensures the degradation of autophagic cargo by maintaining lysosome function in drosophila. *Traffic* **16**, 1088–1107.

Matsumoto, N. and Nakanishi-Matsui, M. (2019). Proton pumping V-ATPase inhibitor bafilomycin A1 affects Rab7 lysosomal localization and abolishes anterograde trafficking of osteoclast secretory lysosomes. *Biochem. Biophys. Res. Commun.* **510**, 421–426.

Matsumoto, N., Sekiya, M., Tohyama, K., Ishiyama-Matsuura, E., Sun-Wada, G.-H., Wada, Y., Futai, M. and Nakanishi-Matsui, M. (2018). Essential Role of the a3 Isoform of V-ATPase in Secretory Lysosome Trafficking via Rab7 Recruitment. *Sci. Rep.* **8**, 6701.

Matsumoto, N., Sekiya, M., Sun-Wada, G.-H., Wada, Y. and Nakanishi-Matsui, M. (2022). The lysosomal V-ATPase a3 subunit is involved in localization of Mon1-

Ccz1, the GEF for Rab7, to secretory lysosomes in osteoclasts. *Sci. Rep.* **12**, 8455.

Maxfield, F. R. and Yamashiro, D. J. (1987). Endosome acidification and the pathways of receptor-mediated endocytosis. *Adv. Exp. Med. Biol.* **225**, 189–198.

McCray, B. A., Skordalakes, E. and Taylor, J. P. (2010). Disease mutations in Rab7 result in unregulated nucleotide exchange and inappropriate activation. *Hum. Mol. Genet.* **19**, 1033–1047.

McGuire, C. M. and Forgac, M. (2018). Glucose starvation increases V-ATPase assembly and activity in mammalian cells through AMP kinase and phosphatidylinositide 3-kinase/Akt signaling. *J. Biol. Chem.* **293**, 9113–9123.

McNally, K. E. and Cullen, P. J. (2018). Endosomal retrieval of cargo: retromer is not alone. *Trends Cell Biol.* **28**, 807–822.

Meggouh, F., Bienfait, H. M. E., Weterman, M. A. J., de Visser, M. and Baas, F. (2006). Charcot-Marie-Tooth disease due to a de novo mutation of the RAB7 gene. *Neurology* **67**, 1476–1478.

Méresse, S. and Hoflack, B. (1993). Phosphorylation of the cation-independent mannose 6-phosphate receptor is closely associated with its exit from the trans-Golgi network. *J. Cell Biol.* **120**, 67–75.

Mesaki, K., Tanabe, K., Obayashi, M., Oe, N. and Takei, K. (2011). Fission of tubular endosomes triggers endosomal acidification and movement. *PLoS One* **6**, e19764.

Miranda, A. M., Lasiecka, Z. M., Xu, Y., Neufeld, J., Shahriar, S., Simoes, S., Chan, R. B., Oliveira, T. G., Small, S. A. and Di Paolo, G. (2018). Neuronal lysosomal dysfunction releases exosomes harboring APP C-terminal fragments and unique lipid signatures. *Nat. Commun.* **9**, 291.

Modica, G. and Lefrancois, S. (2020). Post-translational modifications: How to modulate Rab7 functions. *Small GTPases* **11**, 167–173.

Mrakovic, A., Kay, J. G., Furuya, W., Brumell, J. H. and Botelho, R. J. (2012). Rab7 and Arl8 GTPases are necessary for lysosome tubulation in macrophages. *Traffic* **13**, 1667–1679.

Mukherjee, S. and Maxfield, F. R. (2004). Lipid and cholesterol trafficking in NPC. *Biochim. Biophys. Acta* **1685**, 28–37.

Müller, M. P. and Goody, R. S. (2018). Molecular control of Rab activity by GEFs, GAPs and GDI. *Small GTPases* **9**, 5–21.

Mulligan, R. J. and Winckler, B. (2023). Regulation of Endosomal Trafficking by Rab7 and Its Effectors in Neurons: Clues from Charcot-Marie-Tooth 2B Disease. *Biomolecules* **13**,.

Mulligan, R. J., Yap, C. C. and Winckler, B. (2023). Endosomal Transport to Lysosomes and the Trans-Golgi Network in Neurons and Other Cells: Visualizing Maturational Flux. *Methods Mol. Biol.* **2557**, 595–618.

Muraleedharan, A. and Vanderperre, B. (2023). The Endo-lysosomal System in Parkinson's Disease: Expanding the Horizon. *J. Mol. Biol.* **435**, 168140.

Murata, Y., Sun-Wada, G.-H., Yoshimizu, T., Yamamoto, A., Wada, Y. and Futai, M. (2002). Differential localization of the vacuolar H+ pump with G subunit isoforms (G1 and G2) in mouse neurons. *J. Biol. Chem.* **277**, 36296–36303.

Nagano, M., Toshima, J. Y., Elisabeth Siekhaus, D. and Toshima, J. (2019). Rab5-mediated endosome formation is regulated at the trans-Golgi network. *Commun. Biol.* **2**, 419.

Nakada-Tsukui, K., Saito-Nakano, Y., Ali, V. and Nozaki, T. (2005). A retromerlike complex is a novel Rab7 effector that is involved in the transport of the virulence factor cysteine protease in the enteric protozoan parasite Entamoeba histolytica. *Mol. Biol. Cell* **16**, 5294–5303.

Nakamura, S., Shigeyama, S., Minami, S., Shima, T., Akayama, S., Matsuda, T., Esposito, A., Napolitano, G., Kuma, A., Namba-Hamano, T., et al. (2020). LC3 lipidation is essential for TFEB activation during the lysosomal damage response to kidney injury. *Nat. Cell Biol.* **22**, 1252–1263.

Nakanishi-Matsui, M. and Matsumoto, N. (2022). V-ATPase a3 Subunit in Secretory Lysosome Trafficking in Osteoclasts. *Biol. Pharm. Bull.* **45**, 1426–1431.

Nakanishi-Matsui, M., Matsumoto, N., Sun-Wada, G.-H. and Wada, Y. (2024). Role of the Cytosolic Domain of the a3 Subunit of V-ATPase in the Interaction with Rab7 and Secretory Lysosome Trafficking in Osteoclasts. *Biol. Pharm. Bull.* **47**, 339–344.

Nakatsu, F. and Kawasaki, A. (2021). Functions of Oxysterol-Binding Proteins at Membrane Contact Sites and Their Control by Phosphoinositide Metabolism. *Front. Cell Dev. Biol.* **9**, 664788.

Nanayakkara, R., Gurung, R., Rodgers, S. J., Eramo, M. J., Ramm, G., Mitchell, C. A. and McGrath, M. J. (2023). Autophagic lysosome reformation in health and disease. *Autophagy* **19**, 1378–1395.

Nassal, J. P., Murphy, F. H., Toonen, R. F. and Verhage, M. (2022). Differential axonal trafficking of Neuropeptide Y-, LAMP1-, and RAB7-tagged organelles in vivo. *Elife* **11**,.

Niekamp, P., Scharte, F., Sokoya, T., Vittadello, L., Kim, Y., Deng, Y., Südhoff, E., Hilderink, A., Imlau, M., Clarke, C. J., et al. (2022). Ca2+-activated sphingomyelin scrambling and turnover mediate ESCRT-independent lysosomal repair. *Nat. Commun.* **13**, 1875.

Nordmann, M., Cabrera, M., Perz, A., Bröcker, C., Ostrowicz, C., Engelbrecht-Vandré, S. and Ungermann, C. (2010). The Mon1-Ccz1 complex is the GEF of the late endosomal Rab7 homolog Ypt7. *Curr. Biol.* **20**, 1654–1659.

O'Sullivan, M. J. and Lindsay, A. J. (2020). The Endosomal Recycling Pathway-At the Crossroads of the Cell. *Int. J. Mol. Sci.* **21**,.

Olson, L. J., Hindsgaul, O., Dahms, N. M. and Kim, J.-J. P. (2008). Structural insights into the mechanism of pH-dependent ligand binding and release by the cation-dependent mannose 6-phosphate receptor. *J. Biol. Chem.* **283**, 10124–10134.

Olson, L. J., Peterson, F. C., Castonguay, A., Bohnsack, R. N., Kudo, M., Gotschall, R. R., Canfield, W. M., Volkman, B. F. and Dahms, N. M. (2010). Structural basis for recognition of phosphodiester-containing lysosomal enzymes by the cation-independent mannose 6-phosphate receptor. *Proc. Natl. Acad. Sci. USA* **107**, 12493–12498.

Ouyang, Q., Lizarraga, S. B., Schmidt, M., Yang, U., Gong, J., Ellisor, D., Kauer, J. A. and Morrow, E. M. (2013). Christianson syndrome protein NHE6 modulates TrkB endosomal signaling required for neuronal circuit development. *Neuron* **80**, 97–112.

Overly, C. C. and Hollenbeck, P. J. (1996). Dynamic organization of endocytic pathways in axons of cultured sympathetic neurons. *J. Neurosci.* **16**, 6056–6064.

Özkan, N., Koppers, M., van Soest, I., van Harten, A., Jurriens, D., Liv, N., Klumperman, J., Kapitein, L. C., Hoogenraad, C. C. and Farías, G. G. (2021). ER - lysosome contacts at a pre-axonal region regulate axonal lysosome availability. *Nat. Commun.* **12**, 4493.

Pagano, R. E., Martin, O. C., Kang, H. C. and Haugland, R. P. (1991). A novel fluorescent ceramide analogue for studying membrane traffic in animal cells: accumulation at the Golgi apparatus results in altered spectral properties of the sphingolipid precursor. *J. Cell Biol.* **113**, 1267–1279.

Palmieri, M., Impey, S., Kang, H., di Ronza, A., Pelz, C., Sardiello, M. and Ballabio, A. (2011). Characterization of the CLEAR network reveals an integrated control of cellular clearance pathways. *Hum. Mol. Genet.* **20**, 3852–3866.

Papadopoulos, C., Kirchner, P., Bug, M., Grum, D., Koerver, L., Schulze, N., Poehler, R., Dressler, A., Fengler, S., Arhzaouy, K., et al. (2017). VCP/p97 cooperates with YOD1, UBXD1 and PLAA to drive clearance of ruptured lysosomes by autophagy. *EMBO J.* **36**, 135–150.

Papadopoulos, C., Kravic, B. and Meyer, H. (2020). Repair or Lysophagy: Dealing with Damaged Lysosomes. *J. Mol. Biol.* **432**, 231–239.

Papini, E., Satin, B., Bucci, C., de Bernard, M., Telford, J. L., Manetti, R., Rappuoli, R., Zerial, M. and Montecucco, C. (1997). The small GTP binding protein rab7 is essential for cellular vacuolation induced by Helicobacter pylori cytotoxin. *EMBO J.* **16**, 15–24.

Peng, W., Schröder, L. F., Song, P., Wong, Y. C. and Krainc, D. (2023). Parkin regulates amino acid homeostasis at mitochondria-lysosome (M/L) contact sites in Parkinson's disease. *Sci. Adv.* **9**, eadh3347.

Perdigão, C., Barata, M. A., Araújo, M. N., Mirfakhar, F. S., Castanheira, J. and Guimas Almeida, C. (2020). Intracellular trafficking mechanisms of synaptic dysfunction in alzheimer's disease. *Front. Cell Neurosci.* **14**, 72.

Pescosolido, M. F., Ouyang, Q., Liu, J. S. and Morrow, E. M. (2021). Loss of christianson syndrome na+/h+ exchanger 6 (NHE6) causes abnormal endosome maturation and trafficking underlying lysosome dysfunction in neurons. *J. Neurosci.* **41**, 9235–9256.

Plemel, R. L., Lobingier, B. T., Brett, C. L., Angers, C. G., Nickerson, D. P., Paulsel, A., Sprague, D. and Merz, A. J. (2011). Subunit organization and Rab interactions of Vps-C protein complexes that control endolysosomal membrane traffic. *Mol. Biol. Cell* **22**, 1353–1363.

Podinovskaia, M., Prescianotto-Baschong, C., Buser, D. P. and Spang, A. (2021). A novel live-cell imaging assay reveals regulation of endosome maturation. *Elife* **10**,.

Polanco, J. C. and Götz, J. (2022). Exosomal and vesicle-free tau seeds-propagation and convergence in endolysosomal permeabilization. *FEBS J.* **289**, 6891–6907.

Polanco, J. C., Li, C., Durisic, N., Sullivan, R. and Götz, J. (2018). Exosomes taken up by neurons hijack the endosomal pathway to spread to interconnected neurons. *Acta Neuropathol. Commun.* **6**, 10.

Polanco, J. C., Hand, G. R., Briner, A., Li, C. and Götz, J. (2021). Exosomes induce endolysosomal permeabilization as a gateway by which exosomal tau seeds escape into the cytosol. *Acta Neuropathol.* **141**, 235–256.

Pols, M. S., van Meel, E., Oorschot, V., ten Brink, C., Fukuda, M., Swetha, M. G., Mayor, S. and Klumperman, J. (2013). hVps41 and VAMP7 function in direct TGN to late endosome transport of lysosomal membrane proteins. *Nat. Commun.* **4**, 1361.

Ponomareva, O. Y., Eliceiri, K. W. and Halloran, M. C. (2016). Charcot-Marie-Tooth 2b associated Rab7 mutations cause axon growth and guidance defects during vertebrate sensory neuron development. *Neural Dev.* **11**, 2.

Ponsford, A. H., Ryan, T. A., Raimondi, A., Cocucci, E., Wycislo, S. A., Fröhlich, F., Swan, L. E. and Stagi, M. (2021). Live imaging of intra-lysosome pH in cell lines and primary neuronal culture using a novel genetically encoded biosensor. *Autophagy* **17**, 1500–1518.

Poteryaev, D., Datta, S., Ackema, K., Zerial, M. and Spang, A. (2010). Identification of the switch in early-to-late endosome transition. *Cell* **141**, 497–508.

Pratt, M. R., Sekedat, M. D., Chiang, K. P. and Muir, T. W. (2009). Direct measurement of cathepsin B activity in the cytosol of apoptotic cells by an activity-based probe. *Chem. Biol.* **16**, 1001–1012.

Press, B., Feng, Y., Hoflack, B. and Wandinger-Ness, A. (1998). Mutant Rab7 causes the accumulation of cathepsin D and cation-independent mannose 6-phosphate receptor in an early endocytic compartment. *J. Cell Biol.* **140**, 1075–1089.

Priya, A., Kalaidzidis, I. V., Kalaidzidis, Y., Lambright, D. and Datta, S. (2015). Molecular insights into Rab7-mediated endosomal recruitment of core retromer: deciphering the role of Vps26 and Vps35. *Traffic* **16**, 68–84.

Progida, C., Malerød, L., Stuffers, S., Brech, A., Bucci, C. and Stenmark, H. (2007). RILP is required for the proper morphology and function of late endosomes. *J. Cell Sci.* **120**, 3729–3737.

Radulovic, M., Schink, K. O., Wenzel, E. M., Nähse, V., Bongiovanni, A., Lafont, F. and Stenmark, H. (2018). ESCRT-mediated lysosome repair precedes lysophagy and promotes cell survival. *EMBO J.* **37**,.

Radulovic, M., Wenzel, E. M., Gilani, S., Holland, L. K., Lystad, A. H., Phuyal, S., Olkkonen, V. M., Brech, A., Jäättelä, M., Maeda, K., et al. (2022). Cholesterol transfer via endoplasmic reticulum contacts mediates lysosome damage repair. *EMBO J.* **41**, e112677.

Rahman, A. A. and Morrison, B. E. (2019). Contributions of VPS35 mutations to parkinson's disease. *Neuroscience* **401**, 1–10.

Ratto, E., Chowdhury, S. R., Siefert, N. S., Schneider, M., Wittmann, M., Helm, D. and Palm, W. (2022). Direct control of lysosomal catabolic activity by mTORC1 through regulation of V-ATPase assembly. *Nat. Commun.* **13**, 4848.

Rink, J., Ghigo, E., Kalaidzidis, Y. and Zerial, M. (2005). Rab conversion as a mechanism of progression from early to late endosomes. *Cell* **122**, 735–749.

Rocha, N., Kuijl, C., van der Kant, R., Janssen, L., Houben, D., Janssen, H., Zwart, W. and Neefjes, J. (2009). Cholesterol sensor ORP1L contacts the ER protein

VAP to control Rab7-RILP-p150 Glued and late endosome positioning. *J. Cell Biol.* **185**, 1209–1225.

Roczniak-Ferguson, A., Petit, C. S., Froehlich, F., Qian, S., Ky, J., Angarola, B., Walther, T. C. and Ferguson, S. M. (2012). The transcription factor TFEB links mTORC1 signaling to transcriptional control of lysosome homeostasis. *Sci. Signal.* **5**, ra42.

Rohrer, J. and Kornfeld, R. (2001). Lysosomal hydrolase mannose 6-phosphate uncovering enzyme resides in the trans-Golgi network. *Mol. Biol. Cell* **12**, 1623–1631.

Rojas, R., van Vlijmen, T., Mardones, G. A., Prabhu, Y., Rojas, A. L., Mohammed, S., Heck, A. J. R., Raposo, G., van der Sluijs, P. and Bonifacino, J. S. (2008). Regulation of retromer recruitment to endosomes by sequential action of Rab5 and Rab7. *J. Cell Biol.* **183**, 513–526.

Romano, R., Rivellini, C., De Luca, M., Tonlorenzi, R., Beli, R., Manganelli, F., Nolano, M., Santoro, L., Eskelinen, E.-L., Previtali, S. C., et al. (2021). Alteration of the late endocytic pathway in Charcot-Marie-Tooth type 2B disease. *Cell Mol. Life Sci.* **78**, 351–372.

Romano, R., Del Fiore, V. S., Saveri, P., Palamà, I. E., Pisciotta, C., Pareyson, D., Bucci, C. and Guerra, F. (2022). Autophagy and lysosomal functionality in CMT2B fibroblasts carrying the RAB7K126R mutation. *Cells* **11**,.

Romero Rosales, K., Peralta, E. R., Guenther, G. G., Wong, S. Y. and Edinger, A. L. (2009). Rab7 activation by growth factor withdrawal contributes to the induction of apoptosis. *Mol. Biol. Cell* **20**, 2831–2840.

Sanyal, A., Scanavachi, G., Somerville, E., Saminathan, A., Nair, A., Oikonomou, A., Hatzakis, N. S. and Kirchhausen, T. (2024). Constitutive Endolysosomal Perforation in Neurons allows Induction of α-Synuclein Aggregation by Internalized Pre-Formed Fibrils. *BioRxiv*.

Sardiello, M., Palmieri, M., di Ronza, A., Medina, D. L., Valenza, M., Gennarino, V. A., Di Malta, C., Donaudy, F., Embrione, V., Polishchuk, R. S., et al. (2009). A gene network regulating lysosomal biogenesis and function. *Science* **325**, 473–477.

Sargeant, T. J., Lloyd-Lewis, B., Resemann, H. K., Ramos-Montoya, A., Skepper, J. and Watson, C. J. (2014). Stat3 controls cell death during mammary gland involution by regulating uptake of milk fat globules and lysosomal membrane permeabilization. *Nat. Cell Biol.* **16**, 1057–1068.

Saric, A., Hipolito, V. E. B., Kay, J. G., Canton, J., Antonescu, C. N. and Botelho, R. J. (2016). mTOR controls lysosome tubulation and antigen presentation in macrophages and dendritic cells. *Mol. Biol. Cell* **27**, 321–333.

Sassone, J., Reale, C., Dati, G., Regoni, M., Pellecchia, M. T. and Garavaglia, B. (2021). The role of VPS35 in the pathobiology of parkinson's disease. *Cell Mol. Neurobiol.* **41**, 199–227.

Saveri, P., De Luca, M., Nisi, V., Pisciotta, C., Romano, R., Piscosquito, G., Reilly, M. M., Polke, J. M., Cavallaro, T., Fabrizi, G. M., et al. (2020). Charcot-Marie-Tooth Type 2B: A New Phenotype Associated with a Novel RAB7A Mutation and Inhibited EGFR Degradation. *Cells* **9**,.

Saxena, S., Bucci, C., Weis, J. and Kruttgen, A. (2005). The small GTPase Rab7 controls the endosomal trafficking and neuritogenic signaling of the nerve growth factor receptor TrkA. *J. Neurosci.* **25**, 10930–10940.

Scharf, B., Clement, C. C., Wu, X.-X., Morozova, K., Zanolini, D., Follenzi, A., Larocca, J. N., Levon, K., Sutterwala, F. S., Rand, J., et al. (2012). Annexin A2 binds to endosomes following organelle destabilization by particulate wear debris. *Nat. Commun.* **3**, 755.

Scheffer, L. L., Sreetama, S. C., Sharma, N., Medikayala, S., Brown, K. J., Defour, A. and Jaiswal, J. K. (2014). Mechanism of Ca^{2+}-triggered ESCRT assembly and regulation of cell membrane repair. *Nat. Commun.* **5**, 5646.

Schleinitz, A., Pöttgen, L.-A., Keren-Kaplan, T., Pu, J., Saftig, P., Bonifacino, J. S., Haas, A. and Jeschke, A. (2023). Consecutive functions of small GTPases guide HOPS-mediated tethering of late endosomes and lysosomes. *Cell Rep.* **42**, 111969.

Schröder, L. F., Peng, W., Gao, G., Wong, Y. C., Schwake, M. and Krainc, D. (2024). VPS13C regulates phospho-Rab10-mediated lysosomal function in human dopaminergic neurons. *J. Cell Biol.* **223**,.

Scott-Solomon, E. and Kuruvilla, R. (2018). Mechanisms of neurotrophin trafficking via Trk receptors. *Mol. Cell. Neurosci.* **91**, 25–33.

Seals, D. F., Eitzen, G., Margolis, N., Wickner, W. T. and Price, A. (2000). A Ypt/Rab effector complex containing the Sec1 homolog Vps33p is required for homotypic vacuole fusion. *Proc. Natl. Acad. Sci. USA* **97**, 9402–9407.

Seaman, M. N. J. (2004). Cargo-selective endosomal sorting for retrieval to the Golgi requires retromer. *J. Cell Biol.* **165**, 111–122.

Seaman, M. N. J. (2018). Retromer and the cation-independent mannose 6-phosphate receptor-Time for a trial separation? *Traffic* **19**, 150–152.

Seaman, M. N. J. (2021). The retromer complex: from genesis to revelations. *Trends Biochem. Sci.* **46**, 608–620.

Seaman, M. N. J., Harbour, M. E., Tattersall, D., Read, E. and Bright, N. (2009). Membrane recruitment of the cargo-selective retromer subcomplex is catalysed

by the small GTPase Rab7 and inhibited by the Rab-GAP TBC1D5. *J. Cell Sci.* **122**, 2371–2382.

Seaman, M. N. J., Mukadam, A. S. and Breusegem, S. Y. (2018). Inhibition of TBC1D5 activates Rab7a and can enhance the function of the retromer cargo-selective complex. *J. Cell Sci.* **131**,.

Serrano-Puebla, A. and Boya, P. (2016). Lysosomal membrane permeabilization in cell death: new evidence and implications for health and disease. *Ann. N. Y. Acad. Sci.* **1371**, 30–44.

Settembre, C. and Perera, R. M. (2023). Lysosomes as coordinators of cellular catabolism, metabolic signalling and organ physiology. *Nat. Rev. Mol. Cell Biol.*

Shao, E. and Forgac, M. (2004). Involvement of the nonhomologous region of subunit A of the yeast V-ATPase in coupling and in vivo dissociation. *J. Biol. Chem.* **279**, 48663–48670.

Shinde, S. R. and Maddika, S. (2016). PTEN modulates EGFR late endocytic trafficking and degradation by dephosphorylating Rab7. *Nat. Commun.* **7**, 10689.

Shukla, S., Larsen, K. P., Ou, C., Rose, K. and Hurley, J. H. (2022). In vitro reconstitution of calcium-dependent recruitment of the human ESCRT machinery in lysosomal membrane repair. *Proc. Natl. Acad. Sci. USA* **119**, e2205590119.

Simonetti, B., Danson, C. M., Heesom, K. J. and Cullen, P. J. (2017). Sequence-dependent cargo recognition by SNX-BARs mediates retromer-independent transport of CI-MPR. *J. Cell Biol.* **216**, 3695–3712.

Skowyra, M. L., Schlesinger, P. H., Naismith, T. V. and Hanson, P. I. (2018). Triggered recruitment of ESCRT machinery promotes endolysosomal repair. *Science* **360**,.

Sønder, S. L., Boye, T. L., Tölle, R., Dengjel, J., Maeda, K., Jäättelä, M., Simonsen, A. C., Jaiswal, J. K. and Nylandsted, J. (2019). Annexin A7 is required for ESCRT III-mediated plasma membrane repair. *Sci. Rep.* **9**, 6726.

Song, P., Trajkovic, K., Tsunemi, T. and Krainc, D. (2016). Parkin Modulates Endosomal Organization and Function of the Endo-Lysosomal Pathway. *J. Neurosci.* **36**, 2425–2437.

Spang, A. (2016). Membrane tethering complexes in the endosomal system. *Front. Cell Dev. Biol.* **4**, 35.

Spinosa, M. R., Progida, C., De Luca, A., Colucci, A. M. R., Alifano, P. and Bucci, C. (2008). Functional characterization of Rab7 mutant proteins associated with Charcot-Marie-Tooth type 2B disease. *J. Neurosci.* **28**, 1640–1648.

Steiner, P., Sarria, J.-C. F., Glauser, L., Magnin, S., Catsicas, S. and Hirling, H. (2002). Modulation of receptor cycling by neuron-enriched endosomal protein of 21 kD. *J. Cell Biol.* **157**, 1197–1209.

Stransky, L. A. and Forgac, M. (2015). Amino Acid Availability Modulates Vacuolar H+-ATPase Assembly. *J. Biol. Chem.* **290**, 27360–27369.

Stroupe, C. (2018). This is the end: regulation of rab7 nucleotide binding in endolysosomal trafficking and autophagy. *Front. Cell Dev. Biol.* **6**, 129.

Strous, G. J., van Kerkhof, P., van Meer, G., Rijnboutt, S. and Stoorvogel, W. (1993). Differential effects of brefeldin A on transport of secretory and lysosomal proteins. *J. Biol. Chem.* **268**, 2341–2347.

Sugii, S., Lin, S., Ohgami, N., Ohashi, M., Chang, C. C. Y. and Chang, T.-Y. (2006). Roles of endogenously synthesized sterols in the endocytic pathway. *J. Biol. Chem.* **281**, 23191–23206.

Takahashi, K., Mashima, H., Miura, K., Maeda, D., Goto, A., Goto, T., Sun-Wada, G.-H., Wada, Y. and Ohnishi, H. (2017). Disruption of small gtpase rab7 exacerbates the severity of acute pancreatitis in experimental mouse models. *Sci. Rep.* **7**, 2817.

Takáts, S., Pircs, K., Nagy, P., Varga, Á., Kárpáti, M., Hegedűs, K., Kramer, H., Kovács, A. L., Sass, M. and Juhász, G. (2014). Interaction of the HOPS complex with Syntaxin 17 mediates autophagosome clearance in Drosophila. *Mol. Biol. Cell* **25**, 1338–1354.

Takimoto, A. (2021). Rab7-Dependent Endocytic Pathways Play an Important Role in Nutrient Absorption during Pre-Weaning Growth. *BPB Reports* **4**, 27–35.

Tan, J. X. and Finkel, T. (2022). A phosphoinositide signalling pathway mediates rapid lysosomal repair. *Nature* **609**, 815–821.

Tan, B., Peng, S., Yatim, S. M. J. M., Gunaratne, J., Hunziker, W. and Ludwig, A. (2020). An optimized protocol for proximity biotinylation in confluent epithelial cell cultures using the peroxidase APEX2. *STAR Protocols* **1**, 100074.

Tas, R. P., Chazeau, A., Cloin, B. M. C., Lambers, M. L. A., Hoogenraad, C. C. and Kapitein, L. C. (2017). Differentiation between Oppositely Oriented Microtubules Controls Polarized Neuronal Transport. *Neuron* **96**, 1264–1271.e5.

Teranishi, H., Tabata, K., Saeki, M., Umemoto, T., Hatta, T., Otomo, T., Yamamoto, K., Natsume, T., Yoshimori, T. and Hamasaki, M. (2022). Identification of CUL4A-DDB1-WDFY1 as an E3 ubiquitin ligase complex involved in initiation of lysophagy. *Cell Rep.* **40**, 111349.

Thiele, D. L. and Lipsky, P. E. (1990). Mechanism of L-leucyl-L-leucine methyl ester-mediated killing of cytotoxic lymphocytes: dependence on a lysosomal thiol

protease, dipeptidyl peptidase I, that is enriched in these cells. *Proc. Natl. Acad. Sci. USA* **87**, 83–87.

Uchimoto, T., Nohara, H., Kamehara, R., Iwamura, M., Watanabe, N. and Kobayashi, Y. (1999). Mechanism of apoptosis induced by a lysosomotropic agent, L-Leucyl-L-Leucine methyl ester. *Apoptosis* **4**, 357–362.

Uhlen, M., Bandrowski, A., Carr, S., Edwards, A., Ellenberg, J., Lundberg, E., Rimm, D. L., Rodriguez, H., Hiltke, T., Snyder, M., et al. (2016). A proposal for validation of antibodies. *Nat. Methods* **13**, 823–827.

van der Kant, R., Fish, A., Janssen, L., Janssen, H., Krom, S., Ho, N., Brummelkamp, T., Carette, J., Rocha, N. and Neefjes, J. (2013). Late endosomal transport and tethering are coupled processes controlled by RILP and the cholesterol sensor ORP1L. *J. Cell Sci.* **126**, 3462–3474.

Vance, J. M., Speer, M. C., Stajich, J. M., West, S., Wolpert, C., Gaskell, P., Lennon, F., Tim, R. M., Rozear, M. and Othmane, K. B. (1996). Misclassification and linkage of hereditary sensory and autonomic neuropathy type 1 as Charcot-Marie-Tooth disease, type 2B. *Am. J. Hum. Genet.* **59**, 258–262.

Vanlandingham, P. A. and Ceresa, B. P. (2009). Rab7 regulates late endocytic trafficking downstream of multivesicular body biogenesis and cargo sequestration. *J. Biol. Chem.* **284**, 12110–12124.

Verhoeven, K., De Jonghe, P., Coen, K., Verpoorten, N., Auer-Grumbach, M., Kwon, J. M., FitzPatrick, D., Schmedding, E., De Vriendt, E., Jacobs, A., et al. (2003). Mutations in the small GTP-ase late endosomal protein RAB7 cause Charcot-Marie-Tooth type 2B neuropathy. *Am. J. Hum. Genet.* **72**, 722–727.

Verma, S., Dixit, R. and Pandey, K. C. (2016). Cysteine proteases: modes of activation and future prospects as pharmacological targets. *Front. Pharmacol.* **7**, 107.

Vietri, M., Radulovic, M. and Stenmark, H. (2020). The many functions of ESCRTs. *Nat. Rev. Mol. Cell Biol.* **21**, 25–42.

Vitelli, R., Santillo, M., Lattero, D., Chiariello, M., Bifulco, M., Bruni, C. B. and Bucci, C. (1997). Role of the small GTPase Rab7 in the late endocytic pathway. *J. Biol. Chem.* **272**, 4391–4397.

Waguri, S., Dewitte, F., Le Borgne, R., Rouillé, Y., Uchiyama, Y., Dubremetz, J.-F. and Hoflack, B. (2003). Visualization of TGN to endosome trafficking through fluorescently labeled MPR and AP-1 in living cells. *Mol. Biol. Cell* **14**, 142–155.

Waguri, S., Tomiyama, Y., Ikeda, H., Hida, T., Sakai, N., Taniike, M., Ebisu, S. and Uchiyama, Y. (2006). The luminal domain participates in the endosomal trafficking of the cation-independent mannose 6-phosphate receptor. *Exp. Cell Res.* **312**, 4090–4107.

Wandinger-Ness, A. and Zerial, M. (2014). Rab proteins and the compartmentalization of the endosomal system. *Cold Spring Harb. Perspect. Biol.* **6**, a022616.

Wang, X., Han, C., Liu, W., Wang, P. and Zhang, X. (2014). A novel RAB7 mutation in a Chinese family with Charcot-Marie-Tooth type 2B disease. *Gene* **534**, 431–434.

Wang, F., Gómez-Sintes, R. and Boya, P. (2018). Lysosomal membrane permeabilization and cell death. *Traffic* **19**, 918–931.

Wang, S., Zhao, Z. and Rodal, A. A. (2019). Higher-order assembly of Sorting Nexin 16 controls tubulation and distribution of neuronal endosomes. *J. Cell Biol.* **218**, 2600–2618.

Wang, R., Wang, J., Hassan, A., Lee, C.-H., Xie, X.-S. and Li, X. (2021). Molecular basis of V-ATPase inhibition by bafilomycin A1. *Nat. Commun.* **12**, 1782.

Wang, J., Daniszewski, M., Hao, M. M., Hernández, D., Pébay, A., Gleeson, P. A. and Fourriere, L. (2023a). Organelle mapping in dendrites of human iPSC-derived neurons reveals dynamic functional dendritic Golgi structures. *Cell Rep.* **42**, 112709.

Wang, X., Bondar, V. V., Davis, O. B., Maloney, M. T., Agam, M., Chin, M. Y., Cheuk-Nga Ho, A., Ghosh, R., Leto, D. E., Joy, D., et al. (2023b). Rab12 is a regulator of LRRK2 and its activation by damaged lysosomes. *Elife* **12**,.

Webb, B. A., Cook, J., Wittmann, T. and Barber, D. L. (2020). pHLARE: A Genetically Encoded Ratiometric Lysosome pH Biosensor. *BioRxiv*.

Webb, B. A., Aloisio, F. M., Charafeddine, R. A., Cook, J., Wittmann, T. and Barber, D. L. (2021). pHLARE: a new biosensor reveals decreased lysosome pH in cancer cells. *Mol. Biol. Cell* **32**, 131–142.

Wenzel, E. M., Elfmark, L. A., Stenmark, H. and Raiborg, C. (2022). ER as master regulator of membrane trafficking and organelle function. *J. Cell Biol.* **221**,.

Wijdeven, R. H., Janssen, H., Nahidiazar, L., Janssen, L., Jalink, K., Berlin, I. and Neefjes, J. (2016). Cholesterol and ORP1L-mediated ER contact sites control autophagosome transport and fusion with the endocytic pathway. *Nat. Commun.* **7**, 11808.

Williams, E. T., Chen, X., Otero, P. A. and Moore, D. J. (2022). Understanding the contributions of VPS35 and the retromer in neurodegenerative disease. *Neurobiol. Dis.* **170**, 105768.

Winckler, B., Faundez, V., Maday, S., Cai, Q., Guimas Almeida, C. and Zhang, H. (2018). The endolysosomal system and proteostasis: from development to degeneration. *J. Neurosci.* **38**, 9364–9374.

Windelborn, J. A. and Lipton, P. (2008). Lysosomal release of cathepsins causes ischemic damage in the rat hippocampal slice and depends on NMDA-mediated calcium influx, arachidonic acid metabolism, and free radical production. *J. Neurochem.* **106**, 56–69.

Wong, Y. C., Ysselstein, D. and Krainc, D. (2018). Mitochondria-lysosome contacts regulate mitochondrial fission via RAB7 GTP hydrolysis. *Nature* **554**, 382–386.

Wong, Y. C., Kim, S., Peng, W. and Krainc, D. (2019a). Regulation and Function of Mitochondria-Lysosome Membrane Contact Sites in Cellular Homeostasis. *Trends Cell Biol.* **29**, 500–513.

Wong, Y. C., Peng, W. and Krainc, D. (2019b). Lysosomal Regulation of Inter-mitochondrial Contact Fate and Motility in Charcot-Marie-Tooth Type 2. *Dev. Cell* **50**, 339–354.e4.

Wood, S. A. and Brown, W. J. (1992). The morphology but not the function of endosomes and lysosomes is altered by brefeldin A. *J. Cell Biol.* **119**, 273–285.

Wu, M., Wang, T., Loh, E., Hong, W. and Song, H. (2005). Structural basis for recruitment of RILP by small GTPase Rab7. *EMBO J.* **24**, 1491–1501.

Wurmser, A. E., Sato, T. K. and Emr, S. D. (2000). New component of the vacuolar class C-Vps complex couples nucleotide exchange on the Ypt7 GTPase to SNARE-dependent docking and fusion. *J. Cell Biol.* **151**, 551–562.

Xu, Y., Zhou, P., Cheng, S., Lu, Q., Nowak, K., Hopp, A.-K., Li, L., Shi, X., Zhou, Z., Gao, W., et al. (2019). A Bacterial Effector Reveals the V-ATPase-ATG16L1 Axis that Initiates Xenophagy. *Cell* **178**, 552–566.e20.

Yacobi-Sharon, K., Namdar, Y. and Arama, E. (2013). Alternative germ cell death pathway in Drosophila involves HtrA2/Omi, lysosomes, and a caspase-9 counterpart. *Dev. Cell* **25**, 29–42.

Yadati, T., Houben, T., Bitorina, A. and Shiri-Sverdlov, R. (2020). The ins and outs of cathepsins: physiological function and role in disease management. *Cells* **9**,.

Yamamoto, H., Zhang, S. and Mizushima, N. (2023). Autophagy genes in biology and disease. *Nat. Rev. Genet.* **24**, 382–400.

Yamauchi, J., Torii, T., Kusakawa, S., Sanbe, A., Nakamura, K., Takashima, S., Hamasaki, H., Kawaguchi, S., Miyamoto, Y. and Tanoue, A. (2010). The mood stabilizer valproic acid improves defective neurite formation caused by Charcot-Marie-Tooth disease-associated mutant Rab7 through the JNK signaling pathway. *J. Neurosci. Res.* **88**, 3189–3197.

Yang, H. and Tan, J. X. (2023). Lysosomal quality control: molecular mechanisms and therapeutic implications. *Trends Cell Biol.* **33**, 749–764.

Yap, C. C. and Winckler, B. (2012). Harnessing the power of the endosome to regulate neural development. *Neuron* **74**, 440–451.

Yap, C. C. and Winckler, B. (2022). Spatial regulation of endosomes in growing dendrites. *Dev. Biol.* **486**, 5–14.

Yap, C. C., Wisco, D., Kujala, P., Lasiecka, Z. M., Cannon, J. T., Chang, M. C., Hirling, H., Klumperman, J. and Winckler, B. (2008). The somatodendritic endosomal regulator NEEP21 facilitates axonal targeting of L1/NgCAM. *J. Cell Biol.* **180**, 827–842.

Yap, C. C., Digilio, L., McMahon, L. and Winckler, B. (2017). The endosomal neuronal proteins Nsg1/NEEP21 and Nsg2/P19 are itinerant, not resident proteins of dendritic endosomes. *Sci. Rep.* **7**, 10481.

Yap, C. C., Digilio, L., McMahon, L. P., Garcia, A. D. R. and Winckler, B. (2018). Degradation of dendritic cargos requires Rab7-dependent transport to somatic lysosomes. *J. Cell Biol.* **217**, 3141–3159.

Yap, C. C., Mason, A. J. and Winckler, B. (2022a). Dynamics and distribution of endosomes and lysosomes in dendrites. *Curr. Opin. Neurobiol.* **74**, 102537.

Yap, C. C., Digilio, L., McMahon, L. P., Wang, T. and Winckler, B. (2022b). Dynein Is Required for Rab7-Dependent Endosome Maturation, Retrograde Dendritic Transport, and Degradation. *J. Neurosci.* **42**, 4415–4434.

Yap, C. C., Digilio, L., McMahon, L. and Winckler, B. (2023). Disruption of Golgi markers by two RILP-directed shRNAs in neurons: A new role for RILP or a neuron-specific off-target phenotype? *J. Biol. Chem.* **299**, 104916.

Yau, K. W., Schätzle, P., Tortosa, E., Pagès, S., Holtmaat, A., Kapitein, L. C. and Hoogenraad, C. C. (2016). Dendrites In Vitro and In Vivo Contain Microtubules of Opposite Polarity and Axon Formation Correlates with Uniform Plus-End-Out Microtubule Orientation. *J. Neurosci.* **36**, 1071–1085.

Ye, M., Lehigh, K. M. and Ginty, D. D. (2018). Multivesicular bodies mediate long-range retrograde NGF-TrkA signaling. *Elife* **7**,.

Yim, W. W.-Y., Yamamoto, H. and Mizushima, N. (2022). Annexins A1 and A2 are recruited to larger lysosomal injuries independently of ESCRTs to promote repair. *FEBS Lett.*

Yoshida, Y., Yasuda, S., Fujita, T., Hamasaki, M., Murakami, A., Kawawaki, J., Iwai, K., Saeki, Y., Yoshimori, T., Matsuda, N., et al. (2017). Ubiquitination of exposed glycoproteins by SCFFBXO27 directs damaged lysosomes for autophagy. *Proc. Natl. Acad. Sci. USA* **114**, 8574–8579.

Yu, L., McPhee, C. K., Zheng, L., Mardones, G. A., Rong, Y., Peng, J., Mi, N., Zhao, Y., Liu, Z., Wan, F., et al. (2010). Termination of autophagy and reformation of lysosomes regulated by mTOR. *Nature* **465**, 942–946.

Yu, Y., Chen, D., Farmer, S. M., Xu, S., Rios, B., Solbach, A., Ye, X., Ye, L. and Zhang, S. (2024). Endolysosomal trafficking controls yolk granule biogenesis in vitellogenic Drosophila oocytes. *PLoS Genet.* **20**, e1011152.

Zhang, K., Fishel Ben Kenan, R., Osakada, Y., Xu, W., Sinit, R. S., Chen, L., Zhao, X., Chen, J.-Y., Cui, B. and Wu, C. (2013). Defective axonal transport of Rab7 GTPase results in dysregulated trophic signaling. *J. Neurosci.* **33**, 7451–7462.

Zhitomirsky, B., Yunaev, A., Kreiserman, R., Kaplan, A., Stark, M. and Assaraf, Y. G. (2018). Lysosomotropic drugs activate TFEB via lysosomal membrane fluidization and consequent inhibition of mTORC1 activity. *Cell Death Dis.* **9**, 1191.

Zoncu, R. and Perera, R. M. (2022). Built to last: lysosome remodeling and repair in health and disease. *Trends Cell Biol.* **32**, 597–610.

Züchner, S. and Vance, J. M. (2006). Mechanisms of disease: a molecular genetic update on hereditary axonal neuropathies. *Nat. Clin. Pract. Neurol.* **2**, 45–53.

Appendix I. Endosomal Transport to Lysosomes and the Trans-Golgi Network in Neurons and Other Cells: Visualizing Maturational Flux

This Appendix is published as a Methods Chapter as “Endosomal Transport to Lysosomes and the Trans-Golgi Network in Neurons and Other Cells: Visualizing Maturational Flux”. Mulligan RJ, Yap CC, Winckler B. Endosomal Transport to Lysosomes and the Trans-Golgi Network in Neurons and Other Cells: Visualizing Maturational Flux. Methods Mol Biol. 2023;2557:595-618. doi: 10.1007/978-1-0716-2639-9_36. PMID: 36512240.

A1.A. Abstract

High-level microscopy enables the comprehensive study of dynamic intracellular processes. Here we describe a toolkit of combinatorial approaches for fixed cell imaging and live cell imaging to investigate the interactions along the trans-Golgi network (TGN)-endosome-lysosome transport axis, which underlie the maturation of endosomal compartments and degradative flux. For fixed cell approaches, we specifically highlight how choices of permeabilization conditions, antibody selection, and antibody multiplexing affect interpretation of results. For live cell approaches, we emphasize the use of sensors that read out pH and degradative capacity in combination with endosomal identity for elucidating dynamic compartment changes.

A1.1. Introduction

Endosomes facilitate intracellular membrane trafficking and transport of cargo for degradation in lysosomes. Proper flux of cargos along the endosomal-lysosomal axis ensures proper signaling from endocytosed ligand-receptor complexes throughout the organism's lifespan (Barford et al., 2017; Yap and Winckler, 2012) and maintenance of protein homeostasis (proteostasis) (Winckler et al., 2018). Disturbances in proteostasis due to defective endosomal-lysosomal or endosomal-trans-Golgi (TGN) trafficking result in numerous diseases in many organs, including the nervous system. Notably many neurodegenerative diseases like Alzheimer's and Parkinson's disease have been linked to accumulation of toxic aggregates which fail to be degraded by the cell (Arrazola Sastre et al., 2021; Lie and Nixon, 2019; Malik et al., 2019; Perdigão et al., 2020; Winckler et al., 2018). In order to ensure adequate endosomal-lysosomal capacity, proteins needed to build lysosomes originate from the secretory system (ER-to-Golgi-to TGN) and are transported through endosomal compartments to lysosomes. The trafficking of newly synthesized lysosomal components from the TGN intersects with endocytic machinery at the level of the early endosome (Grant and Donaldson, 2009; Huotari and Helenius, 2011; Nagano et al., 2019). TGN-derived biosynthetic cargos include lysosomal resident hydrolases, endosomal membrane proteins, and transport receptors, which together contribute to the overall function of the endo-lysosomal system. Furthermore, bi-directional TGN-endosomal trafficking is vitally important for the retrieval of TGN-endosome trafficking proteins, such as mannose-6-phosphate receptors (M6PRs), which deliver lysosomal hydrolases to endosomes and are then transported back to the TGN for re-use (Cui et al., 2019; Huotari and Helenius, 2011; Kvainickas et al., 2017; McNally and Cullen, 2018; Simonetti et al., 2017). Thus, initial steps of endo-lysosomal biosynthesis and protein trafficking rely heavily on endosomal and TGN compartment communication. Altogether, elucidating how endosomes and the TGN interact is important for overall understanding of intracellular membrane transport, cellular cargo degradation, and maintenance of endo-lysosomal homeostasis.

Given the dynamic nature of intracellular membrane trafficking, precise experimental approaches are needed to adequately study system function. Experimentation must be capable of capturing the endosomal maturational process, a

process by which endosomes fuse and acquire new functional properties, such as low pH, degradative capacity, and motility. Studying these endosomal processes, and their relationship with TGN machinery, requires combinatorial fixed and live imaging techniques to fully capture system maturation and interactions. Fixed imaging offers highly detailed snapshots of compartment relationships that can be analyzed efficiently with high replicability and spatial resolution. In addition, the localization of the endogenous, untagged protein can be determined. Conversely, only live imaging is capable of capturing the dynamic TGN-endosomal events, such as maturational steps and functional changes. New advances in live imaging are capable of maintaining much of the spatial resolution of fixed imaging and while providing temporal information. Indeed, many recent publications, including our own, have described novel endosomal-related findings through powerful imaging approaches, which include supplementing standard imaging approaches with pulse-chase of cargos, or endosomal loading with sensors or probes to better define pH and degradative changes as endosomes mature (Bright et al., 2016; Cui et al., 2019; Farfel-Becker et al., 2019; Lie et al., 2021; Yap et al., 2018).

Within this chapter we provide guidance on how to (1) visualize endosomal compartments that derive from Golgi/TGN biosynthetic pathways and are sources for endosome-to-TGN retrieval, through fixed and live methodologies, (2) characterize specific functional properties of endosomal compartments, such as pH and degradative capacity, (3) provide caveats to these approaches with alternative imaging techniques and, (4) analyze results.

A1.2. Materials

2.1 Materials A (for *Methods 3.1)*

1. Micropipettes (P2, P10, P200, P1000)
2. Cells of interest plated on coverslips (Recommended thickness 0.17mm, #1.5)
3. Tissue culture grade treated 24 well plates
4. 1X Phosphate buffered saline (PBS)
5. 4% Paraformaldehyde solution (PFA), stored at 4°C

6. Normal donkey serum (NDS) (100%) (Jackson ImmunoResearch, #017-000-121)
7. Triton X-100: stock solution prepared at 10% in 1X PBS, stored at 4°C once prepared (*see* **Note 1**)
8. Saponin: stock solution prepared at 5% in 1X PBS, stored at 4°C once prepared (*see* **Note 1**)
9. Permeabilization solution: 0.1% saponin OR 0.2% Triton X-100/5% Normal Donkey Serum/1X PBS to volume (*see* **Note 4**)
10. Bovine serum albumin (BSA): prepared at 1% in 1X PBS, stored at 4°C once prepared (*see* **Note 1**)
11. 10 mM glycine, prepared in 1X PBS
12. Desired primary antibodies (for suggestions, *see* **Note 5**)
13. AlexaFluor-conjugated secondary antibodies (ThermoFisher, *for suggestions see* **Note 6**)
14. Prolong Gold Antifade Mounting Medium (ThermoFisher, #36930)
15. Glass microscope slides
16. Sterile glass Pasteur pipettes
17. Kim Wipes

2.2 Materials B (for *Methods 3.2-3.5*)

1. Complete DMEM medium: GlutaMax DMEM (ThermoFisher, #105566-016)/10% fetal bovine serum/1X penicillin-streptomycin (ThermoFisher, #15070063)
2. Complete DMEM medium, phenol red free: GlutaMax DMEM - phenol red (ThermoFisher, #31053-028)/10% fetal bovine serum/1X penicillin-streptomycin (ThermoFisher, #15070063)
3. Lysotracker Red DND-99 (Invitrogen, #L7528), for *Method 3.2*
4. Magic Red Substrate (ImmunoChemistry Technologies, #937), for *Method 3.3*
5. DQ-BSA (Invitrogen, #12051), for *Method 3.4*
6. Bodipy-Pepstatin (ThermoFisher, #P12271), for *Method 3.5*
7. 1X DPBS (Sigma, #D8537)
8. Tissue culture grade incubator and culture hood

9. Temperature and CO_2 controlled live imaging microscopy set-up

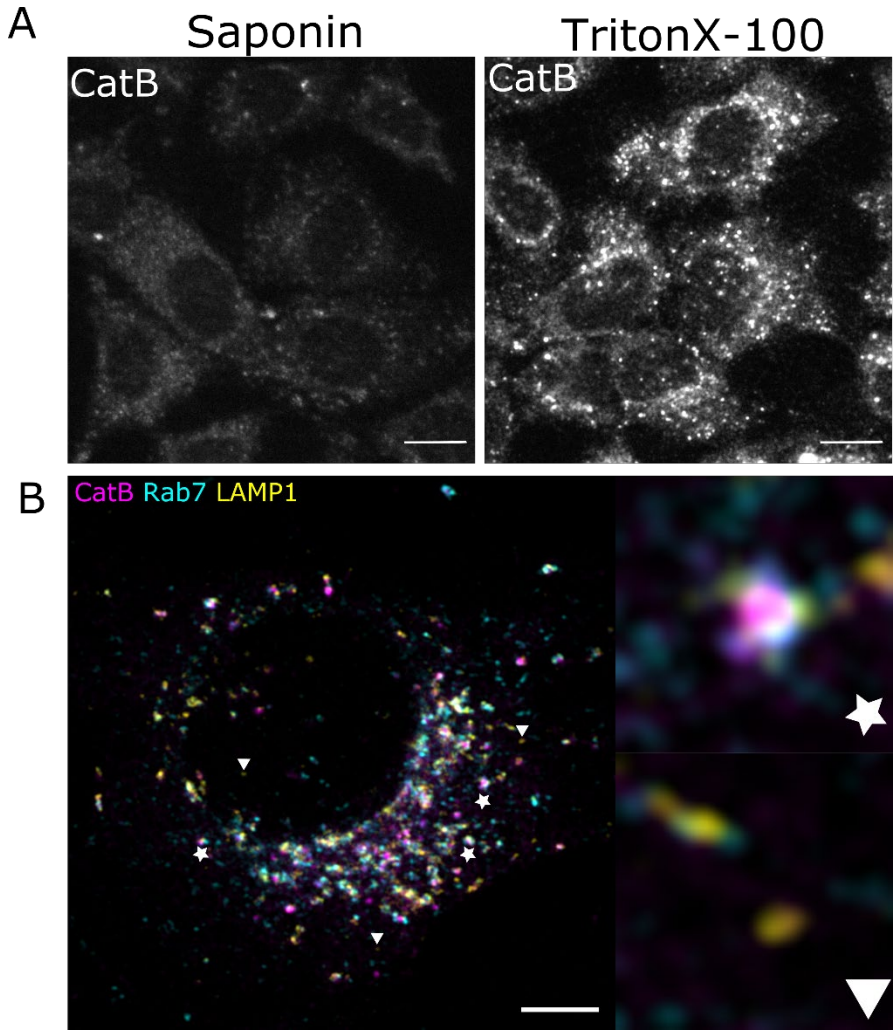

Figure 1 Choice of permeabilization technique and marker combination influences interpretations.

(A) Wide-field micrographs imaged on equivalent settings of normal rat kidney (NRK) cells immunostained for cathepsin-B (CatB) following 0.1% saponin (*left*) or 0.2% Triton X-100 (*right*) permeabilization methods. Significant improvements in immunostaining can be appreciated for this protein when Triton X-100 is used. Scale bars=10μm **(B)** Airyscan2 super resolution micrograph of an NRK cell sample sequentially immunostained for lysosomal associated membrane protein 1 (LAMP1) using 0.1% saponin, followed by immunostaining for Rab7 and CatB using 0.2% Triton X-100. Arrowheads indicate LAMP1 only compartments (*LAMP carriers*), and Stars indicate LAMP1+CatB+Rab7+ compartments (*lysosomes*), which would be indistinguishable if only LAMP1 was used. Scale bar= 5μm.

A1.3. Methods

3.1 Fixed Imaging (reference 2.1 Materials A)

In this *Methods* sub-section, we describe methods for visualization of TGN-endosomal interactions using fixed imaging techniques based on standard immunocytochemistry (ICC). This method allows visualization of various compartmental steps in endosomal compartment maturation based on using combinations of multiple markers simultaneously. Since most compartments cannot be unequivocally identified with a single marker, multiplexing of markers is needed to distinguish trans-Golgi network (TGN), early endosomes (EE), recycling endosomes (RE), late endosomes (LE), and lysosomes (Lys). By choosing appropriate marker combinations, one can also visualize and characterize endosomal compartments that contain TGN derived-membrane proteins, most prominently mannose-6-phosphate receptors (M6PRs) and retrieval machinery such as vacuolar protein sorting-associated protein 35 (Vps35), a retromer subunit. The protocol described below is optimized for normal rat kidney (NRK) cells prepared on glass coverslips in a cell culture model, but can be used for other specimen (such as cultured neurons and tissue sections) with minor modifications.

a. When experimental manipulations are complete, begin preparation of fixed samples for imaging by gentle aspiration of culture medium present in wells with a Pasteur pipette fitted to a vacuum flask (*see* **Note 2**). Gently wash off residual medium with one wash with 1X PBS.
b. Following wash, fix cells for 15 mins at room temperature with 4% paraformaldehyde (PFA) (*see* **Note 3**), with enough fixative to cover cellular material. Remove fixative manually using a pipette and dispose of it properly in a proper institutionally regulated hazardous material container. Wash coverslips adequately three times with 1X PBS.
    i. Optional: Quench for 10-30 minutes with 10 mM glycine (in PBS) after PFA fixation to reduce autofluorescence
c. Prepare permeabilization solution: Prepare enough permeabilization solution to adequately cover coverslips. Prepare 5% normal donkey serum (NDS)/0.2% Triton X-100 in 1X PBS and/or 5% normal donkey serum (NDS)/0.1% saponin

in 1X PBS, depending on needs. (For selecting an appropriate permeabilization method, *see* **Note 4** and **Figure 1A)**. Permeabilize cells for 15 minutes at room temperature using an appropriately selected solution.

d. Selecting and preparing antibody dilutions: For details on choosing appropriate endosomal and Golgi markers, *see* **Note 5.** All antibodies should first be validated (Uhlen et al., 2016). Dilute appropriate volume of chosen antibodies in prepared 1% BSA solution. Prepare enough antibody/BSA solution such that the surface of each coverslip can be adequately covered (for 12 mm diameter coverslips fitting in 24-well plates, this is about 50 µL per coverslip). We recommend using manufacturers' recommended dilutions to start and optimize dilutions through subsequent experiments. Incubate cells in the primary antibody solution for 1 hour at room temperature.
    i. Reminder: if 0.1% saponin based permeabilization was selected, subsequent primary and secondary antibody dilutions should also be prepared in 1% BSA + 0.1% saponin (in PBS).
e. Wash off excess primary antibody with three washes of 1X PBS.
f. Dilute appropriate AlexaFluor secondary antibody conjugates (*see* **Note 6**) in 1% BSA solution. Similar to primary antibody preparation, prepare enough secondary antibody dilution in 1% BSA such that the surface of the coverslip can be adequately covered. Incubate coverslips with secondary antibodies for 30 minutes at room temperature in the dark.
g. Wash off excess secondary antibodies with three washes of 1X PBS. Replace the final wash with sterile water to wash off potential excess PBS derived crystalline salts prior to mounting to microscope slides.
h. Place a drop of Prolong Antifade Gold mounting medium on glass microscope slides using a P200 pipette. Transfer coverslip from well plate and place cellular material side down on drop of mounting medium, dabbing off excess water before placement. Incubate in the dark overnight at room temperature. The following day, coverslip surfaces can be cleaned with a moist Kim Wipe.

i. Samples are now ready for imaging in various microscopy settings. For recommendations and caveats regarding these fixed imaging techniques, *see* **Notes 7-8**. For recommendations on analysis, *see* **Note 21.**

3.2 Live Imaging of Compartment Specific Dyes (Reference Materials.B)

Within this *Methods* subsection, we present an approach for visualizing TGN-endosomal maturational flux by live imaging by investigating endosome acidification using an endosomal compartment specific dye. Operational sensors such as these are vital live imaging tools which can readout functional properties of compartments, such as pH, which change with endosomal compartment maturation over space and time. The most readily used compartment specific dyes in our lab include the LysoTrackers from Life Technologies (e.g., LysoTracker Red DND-99, LysoTracker Green DND-26, LysoSensor Yellow/Blue DND-160), which accumulate following protonation in the lumen of acidified organelles, most brightly in lysosomes. Dyes like LysoTracker Red can be used to both rapidly visualize acidified/lysosomal compartments and provide information on luminal acidification status. Conceptually similar to GFP/RFP-dually tagged proteins of interest (discussed at length in **Note 18**), more specific dyes such as LysoSensor Yellow/Blue can ratiometrically read out specific pH of lysosomal compartments. We would like to emphasize that these dyes cannot be used after fixation, as collapse of the pH gradient through fixative use eliminates the driver for dye localization and its utility in reading pH.

Beyond discussion of compartment specific dyes and its associated protocol below, we discuss the essentials of successful live imaging in **Note 17.** We further discuss the power in using compartment dyes (and other operational sensors) in combination with labeled proteins of interest in **Note 18**. This allows simultaneous read outs of compartment identity and function of that same compartment, and how these properties may change over time and space. We acknowledge other bulk endocytic tracers and pulse chase techniques in **Notes 19** and **20**, respectively.

A recommended protocol for the use of the compartment specific dye LysoTracker Red DND-99 is as follows:

a. Prepare cells for live imaging on glass bottom live imaging dishes as desired.

b. On day of imaging, dilute Lysotracker Dye DND-99 to ~70nM (1:15,000 from 1mM stock) in complete DMEM medium
c. Incubate cells in CO_2 controlled incubator at 37°C for, at maximum, 15 minutes in diluted LysoTracker medium (*see* **Note 9**).
d. Wash cells sufficiently with multiple washes of 1X DPBS for one minute each, or fresh complete medium, and replace in complete DMEM without phenol red, for live imaging.
e. Equilibrate LysoTracker loaded cells in 37°C for, at maximum, 5 minutes before imaging (*see* **Note 10**), OR image immediately at lowest exposure. Do not image for more than 15 minutes post loading (*see* **Note 9**). For recommendations on analysis, *see* **Note 21**.

3.3 Live Imaging of Endosomal Degradation: Magic Red (MR)

Onset of compartment degradative capacity is a fundamental component of endosomal

maturation. With increasing acidification of maturing endosomal compartments, proteases (e.g., cathepsins) dissociate from TGN-derived trafficking receptors (e.g., M6PRs) within endosomal compartments, where proteolytic activity is subsequently activated. Tracking where this activation occurs and the relative degradative abilities of endosomal compartments is important in understanding endosomal compartment function, especially following experimental manipulation or in disease models. Magic Red (MR) is a cathepsin B target sequence linked to cresyl violet fluorophore. Upon cathepsin B mediated cleavage (*see* **Note 11**), the fluorophore generates red fluorescence when excited at 550-590nm. It is most useful for quick assessments of cathepsin B activity within the live cell and thus we recommend its use for short time courses.

a. Prepare cells for live imaging on glass bottom live imaging dishes as desired.

b. On day of imaging, dilute 1000X of MR stock prepared as described in the manufacturer's protocol in complete DMEM medium and incubate with cells at 37°C for 20 minutes.
c. Wash dishes sufficiently with 1X DPBS or fresh complete DMEM medium for 3X with 1 minute per wash.
d. Replace final wash with complete DMEM medium without phenol red, to reduce background noise when imaging live.
e. Image MR loaded cells immediately or after equilibrating loaded cells at 37°C for no more than 5 minutes (*see* **Note 12**). For recommendations on analysis, *see* **Note 21**.

3.4 Live Imaging of Endosomal Degradation: DQ-BSA (DQ)

DQ-BSA is a quenched Bodipy fluorophore coupled to a BSA molecule that is de-quenched upon cathepsin mediated proteolytic cleavage of BSA into smaller peptides (*see* **Note 13**). Therefore, DQ-BSA is another useful tool in visualizing onset of cathepsin mediated degradation. As a BSA conjugate, it must be loaded via endocytic mechanisms and chased within target cells. Depending on needs, loading and chase times can be altered to enrich DQ-BSA in particular compartments of interest. Due to both the stability of BSA and the coupled Bodipy fluorophore, DQ-BSA is extremely useful for extended imaging experiments.

a. Prepare cells for live imaging on glass bottom live imaging dishes as desired.
b. For loading and imaging of DQ-BSA on the same day, load cells with 25ug/mL DQ-BSA in complete DMEM at 37°C for 2 hours. For use the following day, load cells with 5ug/mL DQ-BSA in complete DMEM at 37°C overnight. We see comparable loading of DQ-BSA using these two methods.
c. Wash cells sufficiently with multiple washes of 1X DPBS or fresh complete medium, and replace in complete DMEM without phenol red.
d. Chase loaded DQ-BSA for desired duration of time at 37°C and then image on an appropriate scope OR image immediately after addition of fresh

complete media (*see* **Notes 14-15**). For recommendations on analysis, *see* **Note 21**.

3.5 Live Imaging of Endosomal Degradation: Bodipy-Pepstatin (BPA)

BPA is a Bodipy fluorophore coupled to pepstatin A (*see* **Note 16**), a competitive inhibitor of the cathepsin D catalytic site. Thus, BPA is useful in tracking the onset of cathepsin D degradation and subsequent trafficking in the cell, as it binds irreversibly in the catalytic site. As cathepsin D is a TGN-derived endocytically targeted cargo, BPA is a useful tool for studying onset of cathepsin D activity and subsequent localization as it emerges from TGN compartments. As previously described *(Chen et al., 2000)*, BPA binds selectively and specifically to cathepsin D at pH 4.5, and thus traditionally it is thought that BPA will only bind active cathepsin D in acidic compartments. Similar to DQ-BSA, BPA can be fixed in paraformaldehyde at the expense of a ~60 to 80% reduction in signal.

a. Prepare cells for live imaging on glass bottom dishes as desired.
b. On day of imaging, incubate cells with 1 μM of BPA (ThermoFisher, #P12271) in complete DMEM medium at 37°C for 45 minutes.
c. Wash dishes sufficiently with 1X DPBS or fresh complete DMEM medium for 3X with 1 minute per wash.
d. Replace final wash with complete DMEM medium <u>without phenol red</u>, to reduce background noise when imaging live.
e. Image BPA loaded cells immediately, or proceed to fixation with PFA. For recommendations on analysis, *see* **Note 21**.

A1.4. Notes

<u>Note 1. Stock solution preparations</u>: For preparation of 10% Triton X-100 solution, dilute 1 mL 100% Triton X-100 into 9 mL of 1X PBS. Given the viscosity of the Triton X-100 solution it is recommended to clip the end of a P1000 pipette tip at an angle using sterile scissors, and pipette slowly to accurately deliver a 1 mL volume. For 5% saponin solution, weigh out and dissolve 0.25 g saponin in 5 mL of 1X PBS. Similarly, for 1% BSA solution, weigh out and dissolve 0.1 g BSA in 10 mL of 1X PBS. Prepared 10%

Triton X-100 solution can be stored at 4°C for many months. Prepared 5% saponin and 1% BSA solutions should not be stored for longer than 1 month at 4°C before preparing again.

Note 2. It is recommended for this step and all subsequent aspiration steps to outfit the end of the Pasteur pipette with a 200 µL disposable pipette tip to ensure gentle aspiration.

Note 3. If applying this protocol to neuronal cultures specifically, we recommend fixing in 2% PFA by addition of cold 4% PFA directly into existing culture medium at a 1:1 (4% PFA: existing medium) ratio. Alternative fixatives, such as cold 100% methanol, may be needed depending on the antibody.

Note 4. Choice of detergent for permeabilization: Depending on the proteins of interest and specific epitopes recognized by certain antibodies, the strength of the detergent used within the permeabilization buffer step can influence the success and quality of the cellular staining. For most applications, use of 0.2% Triton X-100 is appropriate and not detrimental to staining success, and thus we suggest this as an appropriate starting point for investigation of a new protein of interest or antibody. However, for some proteins or antibodies, most often integral membrane proteins on intracellular compartments such as the lysosomal associated membrane proteins (LAMPs), the strength of Triton X-100 leads to suboptimal staining. For these more difficult proteins or antibodies, we recommend using a 0.1% saponin based permeabilization solution instead of Triton X-100. 0.1% saponin should then also be included in the subsequent primary and secondary antibody incubation steps. We have found great success in visualizing LAMPs using this technique. The subsequent caveat to this approach is that antibodies that work well in 0.2% Triton X-100, such as cytosolic proteins or membrane associated proteins, are not necessarily compatible with 0.1% saponin (**Figure 1A**). Thus, permeabilization conditions must be optimized for each antibody. To circumvent differences in permeabilization requirements in co-staining experiments, we often perform two sequential staining on the same sample (i.e., the above staining protocol twice). In this method, samples are fixed, permeabilized with 0.1% saponin and then stained with primary antibodies that require a gentler

permeabilization step (such as the LAMPs), followed by an appropriate secondary antibody. Then samples are re-fixed, re-permeabilized with 0.2% Triton X-100, and stained with the remainder of the necessary primary antibodies, followed by labeling with appropriate secondary antibodies, and mounting. Using this technique, we can visualize LAMP proteins, which require 0.1% saponin, with other endo-lysosomal proteins, such as cathepsin-B (CatB) and Rab7, which require 0.2% Triton X-100, on the same coverslip (**Figure 1B**). Alternative detergents used for permeabilization may include the likes of Tween-20, NP-40 etc. though we do not routinely use these for our purposes.

Note 5. Choice of markers: We would like to emphasize how choice of endosomal compartment markers are vital to fully understanding compartment identity and thus informing function. Lack of well-informed or comprehensive marker panels can easily lead to mis-interpretation of results and mis-identification of compartments. For example, while many researchers use the lysosomal associated membrane proteins (LAMPs) exclusively as markers of lysosomes, these membrane proteins are trafficked from the Golgi to their recipient compartment like all other membrane proteins. In fact, we and others have identified and discussed non-lysosomal LAMP carrier compartments by various microscopy techniques (Cheng et al., 2018; Lie et al., 2021; Pols et al., 2013; Yap et al., 2018). Hence, a certain population of LAMPs will be localized to membrane bound compartments other than the lysosome, and thus may lead to misleading conclusions if LAMPs are used as a sole lysosomal marker (**Figure 1B)**. Overexpression of endo-lysosomal membrane proteins can also be misleading, as saturation of the biosynthetic system with exogenous protein will increase the presence of that protein throughout the entire maturational pathway (e.g., overexpression of LAMP1-GFP in our hands leads to increased localization of LAMP1 in non-lysosomal compartments such as TGN and early endosomes).

Further, use of operational markers (Magic Red, Lysostracker Red DND-99 etc.) are not appropriate to use in the fixed setting to define compartments, as fixation and permeabilization greatly reduces signal leading to significant loss of data (**Figure 2**). The exceptions to this are DQ-BSA and Bodipy-Pepstatin A (BPA), which can be fixed

so long as 0.1% saponin based permeabilization is used. Even still, retained DQ-BSA or BPA signal following fixation is only 20-40%, and thus significant “real” signal is lost. Uses and drawbacks of operational markers for Golgi-endosomal study in live imaging experimentation are discussed at length in *Methods 3.2-3.5* and **Notes** *9-16.*

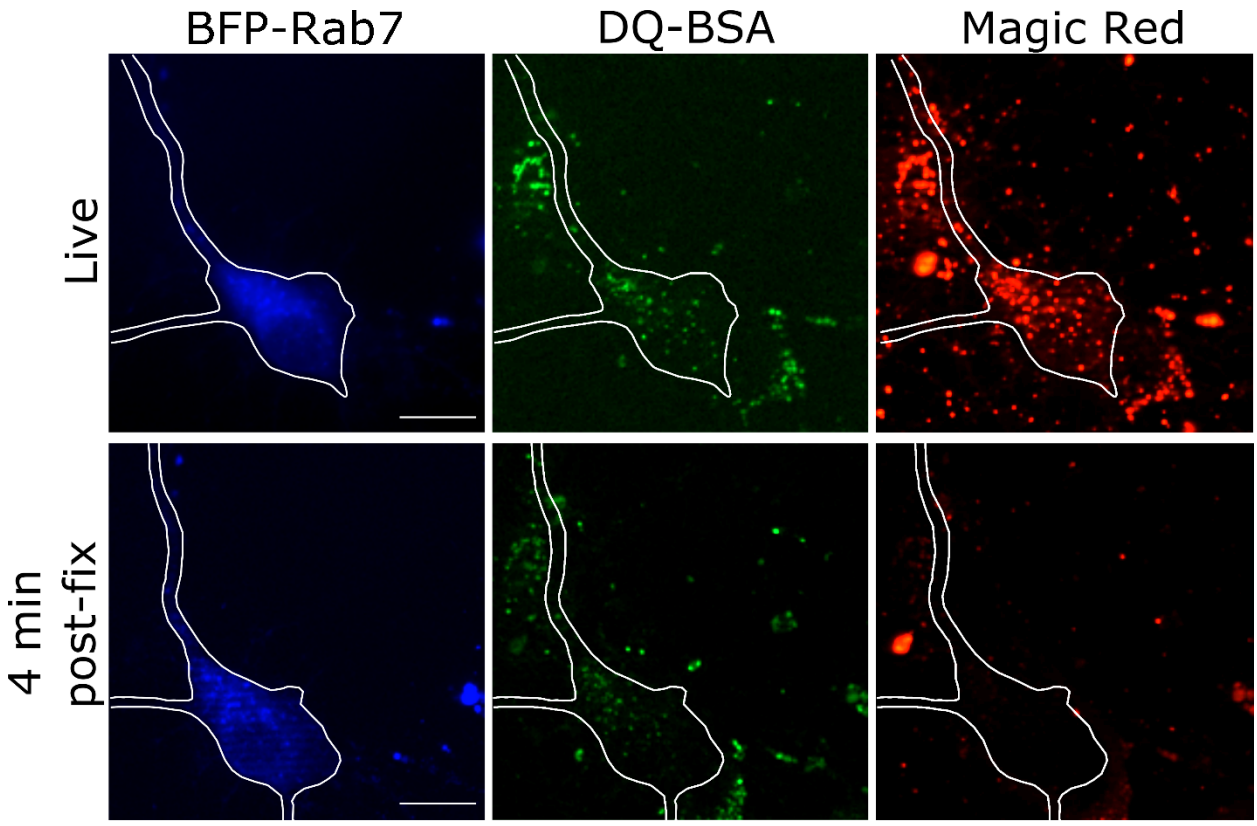

Figure 2 Fixation abolishes signal of endosomal operational markers.

Wide-field micrographs of *in vitro* hippocampal rat neurons transfected with BFP tagged Rab7 and loaded with DQ Green-BSA and Magic Red degradative sensors. Images of the same field were taken live (*top*) and following four minutes of fixation with 4% paraformaldehyde (PFA) (*bottom*). While Rab7-BFP signal is enhanced by fixation, appreciable loss of both DQ-BSA and Magic Red signal can be appreciated. Scale bar=20μm.

In summary, for compartment classification, we encourage comprehensive labeling of endogenous compartments with primary antibodies in the absence of overexpression or operational markers. This is accomplished by combinatorial marker approaches and consistent use of, at minimum, 3-color imaging. For example, we would be most convinced by work that defines lysosomes as LAMP, Rab7, and

lysosomal hydrolase (such as cathepsins B/D) triple positive compartments (**Figure 1B**). Our specific recommendations for each endosomal compartment are as follows:

(1) Early endosomal/TGN: Early endosomes (EE) can be most easily and accurately defined with labeling of Rab5 in conjunction with its EE-specific effector early endosome antigen 1 (EEA1). Traditional endocytic related receptors such as transferrin receptor (TfR) or epidermal growth factor receptor (EGFR) could also be used in conjunction with either Rab5 or EEA1, though these will frequently be found populating other endocytic compartments, such as recycling endosomes as well. Choices of TGN derived markers that can be used in conjunction with EE markers to investigate TGN-EE interacting compartments are abundant. Endo-lysosomal destined hydrolases are transported by Golgi derived receptors such as mannose-6-phosphate receptors (M6PRs) and SEZ6L2 (Boonen et al., 2016; Ghosh et al., 2003; Griffiths et al., 1988; Hoflack and Kornfeld, 1985; Méresse and Hoflack, 1993; Olson et al., 2010; Rohrer and Kornfeld, 2001; Waguri et al., 2006), which exist predominantly in the trans-Golgi network at steady state. These serve as good choices for investigating initial TGN-endosomal trafficking steps and endosomal-TGN recycling pathways. Retrieval pathways for these receptors include retromer complex (including Vps35) and sorting nexin (SNX) proteins, which are also good candidates for endosome to TGN trafficking studies (Cui et al., 2019; Kvainickas et al., 2017; McNally and Cullen, 2018; Rojas et al., 2008; Seaman, 2021; Simonetti et al., 2017) . Alternative endosome-to-TGN retrieval pathways have been demonstrated to be clathrin and AP-1 dependent (Ghosh et al., 2003; Waguri et al., 2003). Therefore, use of either of these markers in conjunction with EEA1 or Rab5 offer alternative choices for study of initial trafficking steps if more specific alternatives are not available or exhibit species incompatibilities.

(2) Late endosomal/TGN: Late endosomes are typically more difficult to elucidate, with Rab7 often considered the defining maker. Rab7, however, is also present on mature lysosomes, autophagic compartments and

transitional early endosomes, and thus co-staining with other markers is essential when utilizing Rab7. Thus, we recommend approaching a definition of late endosomes as a definition of exclusion (i.e., true Rab7+ late endosomes are likely EEA1-, and may or may not include LAMP1). While a small amount of TGN-derived M6PR may be found in late endosomal compartments, relevant TGN proteins found here will largely comprise retrieval machinery. This, like early endosomes, can include retromer components like Vps35, but also late endosomal specific retrieval machinery such as Rab9 and TIP47 (Díaz and Pfeffer, 1998; Ghosh et al., 2003).

(3) Lysosomal markers: As stated previously, we believe the most accurate definition of lysosomes to be LAMP1+, Rab7+ and lysosomal hydrolase+ (such as cathepsins B/D). The earliest definitions of lysosomes are founded on their exclusion of TGN resident M6PRs, and thus there is not significant overlap between TGN and lysosomal compartments. However, we would recommend using the above definition of lysosomes when they are being considered in fixed imaging studies that may involve the TGN, especially if a disrupted TGN-endosomal axis is suspected.

Note 6. We most commonly use AlexaFluor and Dylight conjugated secondary antibodies in our staining and imaging protocol. All secondary antibodies are used at a concentration of 1:400, with the exception of those in the “far red/near IR” wavelengths (generally AlexaFluor647/Cy5 antibodies), which are used at 1:600, to significantly reduce the risk of spectral bleed-through into the “orange/red” wavelengths. Otherwise, fine tuning of excitation spectra should be considered to further reduce bleed-through risk.

Note 7. Imaging Techniques: We utilize a wide variety of microscopy techniques and microscopes to capture relevant data from fixed samples. Notable interactions, phenotypes and trends are first explored on a widefield light microscope and then subsequently on higher resolution microscopes, such as traditional confocal microscopy or various super resolution microscopes, as available. The intricacies of performing high quality fixed imaging differ between microscopes and manufacturers, and thus it is

difficult to provide comprehensive suggestions on how to optimally image in all of these settings. However, we would like to emphasize that high quality staining usually permits the use of any power of microscope for capturing relevant data (i.e., any clear phenotype should be observable on any microscope). Given the size of most endosomal compartments, moving to higher resolution microscopy does not often change our interpretation of the data. However, higher resolution microscopy does offer the ability to better resolve individual domains on larger intracellular compartments. In our experience, some techniques (such as Airyscan super resolution microscopy) aid in teasing apart true boundaries of multiple compartments from independent domains on a singular larger compartment. Other techniques (e.g., STED) often result in large number of non-overlapping small dots with our markers, which makes interpretation of compartment boundaries problematic. This may be due to the lack of resolution of very small, faint transport carriers by most standard microscopes. This provides the additional challenge of distinguishing staining of very small structures from background staining, which also often appears as small dots. Thus, extraordinary care needs to be taken to distinguish “background staining” from “real but faint staining” of small compartments. Together, while application of high-resolution microscopy has its benefits it does not always help interpretations and tends to complicate analysis. Such considerations must increasingly be taken into account as imaging continues to move toward increases in resolving power.

Note 8. Pitfalls and caveats: The pros of utilizing a fixed approach to investigating endogenous TGN-endosomal maturational elements include the ability to screen a wide variety of markers, especially in combination, at high resolutions. This can be accomplished without fears of photobleaching or significant background noise. It is also easier to achieve satisfactory sample sizes using fixed approaches. Simply, prepared fixed samples on microscope slides are more manageable to work with, both in preparation and imaging. However, this ease comes with significant downsides. Fixed samples offer only a snapshot in time of a highly dynamic TGN-endosomal axis. As such, most temporal resolution of any changes that may occur is lost unless stringent time courses are performed. Further, the harsh conditions of fixation can often result in the loss of fine membranous compartment detail. For example, the process of endo-

lysosomal tubulation is frequently reported (Allison et al., 2013; Bonet-Ponce et al., 2020; Mesaki et al., 2011; Saric et al., 2016; Wang et al., 2019; Yu et al., 2010), however, tubules can rarely be seen in fixed settings, likely due to both their fleeting and fragile nature. Since operational makers such as Lysotracker Red or Magic Red cannot be fixed (*see* **Figure 2** and **Notes 9-12**, compartments identified by endogenous markers cannot be probed for functional properties, such as acidification and degradative capacity.

Note 9. Extended loading and imaging times are detrimental to the utility of LysoTracker dyes, as dye accumulation will inevitably alter luminal pH itself (i.e., lead to alkalinization) (Bright et al., 2016), with compensatory responses by lysosomal resident hydrogen ion pumps. Therefore, short imaging windows should be considered with LysoTrackers. We do not recommend them for tracing changes to lysosomal pH over long term experiments. Additionally, even on gentle live imaging set-ups with minimal exposure times, such as spinning disk confocal microscopes, LysoTrackers have the propensity to rapidly photo bleach and thus short imaging windows are optimal.

Note 10. An additional equilibration step, followed by one more wash, can be used to further eliminate any residual LysoTracker dye that may have leaked across membranes in the time immediately following loading and washing.

Note 11. MR signal may also arise due to extracellular cleavage of cresyl violet linked substrate, as considerable amounts of cathepsin-B can be secreted from some cell lines into the medium and cathepsin-B is active over a broad range of pH, 4 to 7 (Pratt et al., 2009).

Note 12. Caveats to MR usage include its propensity to rapidly photo-bleach, and a wide spectral emission profile, which leads to significant bleed-through into adjacent fluorescent channels, most often Far Red/IR channels (Alexa Fluor 635, 647). Short imaging times with careful considerations to neighboring channels must be made. We do not recommend using MR in fixed settings (**Figure 2**).

Note 13. The fate of cleaved fluorescent BSA fragments is unclear. For instance, mildly degradative compartments can, over an extended incubation, cleave a considerable

amount of BSA. Whether cleaved fluorescent fragments continue to traffic or are stored as non-degradable cargo in terminal compartments is wholly unclear. This is an important consideration when ascribing where degradative activity is primarily taking place within the endo-lysosomal system

Note 14. Short chases (<30 mins) will enrich in earlier endosomal compartments, where the most likely interaction with TGN-derived material will occur. Traditionally, these compartments are not very acidic or degradatively active, so DQ-BSA signals here are likely dim or close to undetectable. Longer chases will result in delivery of DQ-BSA to late endosome (>1 hour) and lysosomal (>2 hour) compartments. Immediate imaging following DQ-BSA loading will permit precise determination of the onset of degradation, with the note that movement of DQ-BSA cannot be traced until degradative activity has commenced. Similar to MR, DQ-BSA could potentially be cleaved in the extracellular environment by cathepsins, and then subsequently endocytosed.

Note 15. Unlike LysoTrackers and MR, DQ-BSA can be used fixed, although still best utilized live. 0.1% saponin based permeabilization must be used. This is with the important caveat that considerable signal loss (60-80%) will occur and thus, significant populations of fainter, less degradative compartments cannot be appreciated with this approach (**Figure 2**). Further, due to loss of signal, fixed DQ-BSA samples cannot be used to adequately compare degree of cathepsin presence in a compartment to degradative activity. Any correlations between the presence or intensity of cathepsin staining and DQ-BSA fluorescence would need to be conducted live.

Note 16. Pepstatin A is a cathepsin D inhibitor. Thus, with extensive incubations with BPA, secondary effects on endosomal biosynthesis and trafficking may occur due to continuous inhibition of proteolytic activity.

Note 17. Endosome Live Imaging Essentials: Ultimately, the crux of successful live imaging experimentation is balancing exposure time and resolution. When investigating the endosomal system, this is further complicated by the often-small size of compartments of interest, which can be difficult to sufficiently resolve, and the compartments propensity to photo-bleach. We discuss optimal live imaging set up for visualization of endosomes, imaging conditions and acquisition practices at length in

(Lasiecka and Winckler, 2016). While the conditions referenced here are ideal for endosomes within neurons, they are equally applicable to other cell types and intracellular compartments, such as the Golgi/TGN.

Note 18. Protein of Interest Visualization: Following preparation of desired cells for live imaging on glass bottomed dishes, the next step in live imaging experimentation is selecting and executing a mode of protein visualization, which most often relies on plasmid introduction into cells. Notably, expression of fluorescent proteins fused to the protein of interest is the most technically approachable and therefore widely used. It is important to remember that plasmid overexpression does not always accurately represent endogenous distribution and can cause overexpression phenotypes. Overexpression artifacts thus may muddle interpretations. For detailed methods on our most commonly used strategies for introducing exogenous plasmid DNA into recipient cells to express a fluorescent version of a protein of interest, we refer you to (Lasiecka and Winckler, 2016). While the strategies referenced here are optimized for neurons, they can easily be applied to other cellular culture models, such as immortalized cell lines.

Not previously discussed is the power of dually-tagged integral transmembrane proteins in live imaging approaches for reading out the pH of compartments. In this approach, the luminal/extracellular domain of the protein of interest is tagged with a pH-sensitive fluorophore (such as GFP and its derivatives), while the cytoplasmic terminus is tagged with a pH-insensitive fluorophore (such as RFP and its derivatives). The fluorescence of the two fluorescent tags can be ratio'ed to offer a functional readout of luminal pH. If desired, specific pH values can be determined by calibrating the intracellular sensor with a range of pH solutions. Selection of a transmembrane protein unique to a specific Golgi or endosomal compartment can thus read out pH of that compartment, while selection of a transmembrane cargo that is trafficked from Golgi to endosomes or vice versa can trace relative (or quantitative, if calibrated) pH changes as membrane trafficking steps occur. As pH in these compartments are closer to neutral cytosolic pH, and the differences between Golgi and endosomal pH are not always considerable, a notable caveat to this approach is the sensitivity of the sensor in

detecting small pH changes. Further, selection of a transmembrane protein to tag for these purposes often poses a significant hurdle, as adding tags on both termini increases chances of disrupting normal function, trafficking or folding of the protein of interest. Nevertheless, a growing number of pH sensors are currently being developed and utilized for these purposes, which offer significant upsides in understanding properties of both the Golgi/TGN and endosomal maturational steps alike (Chin et al., 2021; Deschamps et al., 2020; Ponsford et al., 2021; Webb et al., 2020; Webb et al., 2021).

Finally, with the now widespread presence of commercially available compartment specific reagents, the need for using specific fluorescently tagged proteins to label every compartment of interest is lessened. Use of these reagents in concert with a tagged protein of interest eliminates the need for dual or triple transfection conditions. For example, an endosomal resident protein tagged with a green fluorescent protein can be paired with a red Golgi specific reagent, and thus intra-compartment interactions could be traced this way. While this method clearly eliminates the ability to look at a specific protein, it offers a way to easily visualize a bulk compartment. Fortunately, there are many live imaging compatible reagents, primarily from Life Technologies, for Golgi and lysosomal compartments, yet specific endocytic reagents for compartments such as early or recycling endosomes are still lacking. CellLite-Golgi specific reagents (Invitrogen), which themselves are fluorescent fusion proteins of Golgi resident enzymes, are most useful for live imaging studies in labeling bulk Golgi. Further, available fluorescently conjugated ceramide and sphingomyelin reagents are useful in labeling TGN in live cells, whose utility has been long established (Deng et al., 2016; Lipsky and Pagano, 1983; Pagano et al., 1991). In addition to these lipid-based reagents, use of specific lectin conjugates, such as wheat germ agglutinin (WGA), can be used for labeling TGN compartments of fixed samples. However, for both WGA and lipid conjugates, the cell surface is readily labeled in addition to the Golgi and might obscure intracellular structures, which is an important consideration when deciding to utilize one of these tools (Martin and Pagano, 1994). Carbohydrate based conjugates such as this take advantage of native biology of Golgi based carbohydrate modifications to readily label specific Golgi stacks. Given the range of Golgi conjugates available,

each may need to be individually optimized in a given cellular system under live conditions.

Note 19. Use of Bulk Endocytic Tracers: Degradative probes described in *Methods 3.3-3.5* rely on cellular endocytic activity to navigate to sites of use. Other endocytic tracers introduced via dilution in cell culture medium can also be used to enrich endosomal compartments with a cargo, thus labeling them. Indeed, certain endocytic cargos can be labeled with pH or calcium sensitive fluorophores and thus can also provide functional information regarding the compartment they are contained in. There is a wide range of commercially available endocytic cargoes for use, each available as conjugates to numerous different fluorophores. Bulk endocytic cargos such as fluorescent dextrans are useful in labeling all steps of endosomal maturation. Upon prolonged chases, dextrans will accumulate in lysosomal compartments. The diverse endocytic labeling that dextrans provide can prove useful in studying spatial relationships between endosomal compartments and labeled Golgi/TGN, such as compartment contact sites. Importantly, dextrans themselves will not label the TGN, as there has not been descriptions of appreciable retrograde traffic of this cargo from early endosomes to the trans Golgi network. Cells take up dextran via fluid phase endocytosis, and thus rapidity of dextran uptake and uptake efficiency are correlated with bulk endocytic or phagocytic activity of the cells. In cells with low fluid phase endocytosis, it can take hours to load enough dextran to detect. This is an important consideration when deciding if dextrans are a suitable tool for a specific experiment, especially if acute time windows are desired.

For studying TGN-endosome interactions, the most suitable endocytic tracers are those that are quickly endocytosed and are enriched in early endosomal compartments, as the early endosome is the site of convergence for endocytic and Golgi biosynthesis pathways. Two suitable options that would fit these criteria are fluorescently labeled transferrin and EGF. Both are natural ligands with plasma membrane receptors that can be loaded for 5-15 minutes at 37°C and enriched in early endosomal compartments in a matter of minutes. In early endosomes, labeled ligands interact heavily with TGN-delivered cargos. Thus, utilization of pH or calcium reporter fluorophores coupled to

endocytosed ligands such as transferrin or EGF can provide tools that read out early endosomal function and maturation as TGN-derived cargo is delivered.

Note 20. Alternative Strategies for TGN-to-endosome release: The relationship between TGN and endosomes cannot be entirely captured by the use of operational sensors (*Methods 3.2-3.5*) or labeled proteins of interest (**Note 18**) alone. There are numerous alternative live imaging strategies that can be used in concert with compartment or protein labeling strategies to more specifically study TGN vesicle release events. The classic approaches to stall biosynthetic cargos is through the use of brefeldin A (BFA), which inhibits vesicle formation and general protein transport (Helms and Rothman, 1992; Strous et al., 1993)**,** or by temperature block. Both blocks can be reversed to allow more or less synchronous resumption of forward trafficking. Use of BFA or temperature block is combined with a fluorescently labeled cargo originating in the Golgi which is temporarily stalled and can be released after reversal of the block. The transit of the fluorescent cargo can then be followed in time and space by live imaging. Timing of BFA treatments and release have to be optimized because extended BFA incubations lead to gross morphologic changes of Golgi/TGN and endosomal compartments (Wood and Brown, 1992). Our lab has used BFA and temperature blocks in cultured neurons in the past (Yap et al., 2008), but more specific blocks have since become available which only block TGN export of the protein of interest. These include membrane proteins tagged with tetramerization domains that block ER exit, but can be released by adding specific reagents (Al-Bassam et al., 2012; Feng and Arnold, 2016; Hangen et al., 2018). The RUSH system can also be used to trap and release cargo proteins of interest from the Golgi (Boncompain et al., 2012; Chen et al., 2017). RUSH relies on a streptavidin conjugated Golgi resident hook, and a streptavidin binding protein (SBP)-conjugated fluorescent protein of interest. Upon the addition of biotin, biotin outcompetes SBP for streptavidin binding and releases the protein of interest from the Golgi in a tightly controlled and synchronous manner. Finally, at the level of imaging, fluorescence recovery after photobleaching (FRAP) is a powerful tool to isolate specific pools of TGN-endosomal trafficked proteins (Kametaka and Waguri, 2012; Waguri et al., 2006). High intensity laser application to bleach a compartment of interest allows studying newly delivered fluorescent material to that compartment. For

TGN-endosomal relationships, this allows bleaching of the TGN pool and studying subsequent fluorescent recovery, providing information regarding retrieval pathways. Conversely, bleaching of a peripheral pool of endosomal compartments allows precise study of TGN-derived fluorescent vesicles being delivered to the bleached compartment. Alternatively, use of photoactivatable or photoconvertible fluorophores can be used to follow a specific subpopulation of a cargo of interest (Chen et al., 2013). Together, these strategies, combined with operational sensors and labeled proteins of interest, provide capabilities for highly powerful live imaging experiments to study protein and membrane trafficking.

Note 21. Data Analysis: Rigorous post-imaging analysis allows extraction of a plethora of qualitative and quantitative data from fixed and live imaging experiments. Powerful image analysis software is available to carry out detailed analyses, ranging from free software such as ImageJ/FIJI and CellProfiler, to pricier high-powered software, like Imaris, Metamorph, or Volocity, as well as software packages attached to many microscopes.

Due to their static nature, fixed image analysis hinges on taking advantage of high spatial resolutions to analyze colocalization between cellular structures. First, qualitative descriptions of compartment relationships are important foundational steps before quantitative analysis is undertaken. This may be extended further to formulating line-scan analyses of markers to supplement quantitative findings and provide detailed spatial information between markers. However, orientation of the selected line must be standardized in some fashion.

Quantitative approaches can range from simple calculations to complex object-based approaches. On the simpler side, most programs offer calculations of correlation coefficients such as Pearson correlation and Mander's correlation coefficients. Correlation coefficients are great for getting quick, mathematical understandings of the relationships between the intensities of markers of interest, and are widely used for describing compartment relationships. One downside, particularly in the case of Pearson coefficients, is the artificial inflation of correlation coefficient values given substantial black space in a field of view. Further to this point, the absolute values of the

correlation coefficients themselves have little inherent meaning and provide only rough insights to the biological relationships between two markers. Most useful are the relative changes in Pearson correlation coefficients that may occur following a treatment or experimental manipulation to demonstrate that the relationship between two markers has changed. Our lab's preference is to use more object-based approaches to understanding endosomal and Golgi relationships as opposed to coefficient calculations, which we accomplish primarily using the Imaris software. In general, our co-localization workflow in Imaris is as follows: (1) threshold images to eliminate background and define real signal, (2) use the built in "Spots" tool to define compartments of interest in each channel, allowing for different sized spots and (3) Run co-localizes spots functions to generate additional channels that detail which compartments are colocalized versus not, for each channel of interest. From there, raw percentages of the number of colocalized spots are calculated. Additional functions include the ability to look at triple colocalized spots; data of which simple coefficients cannot provide. Advantages of this approach are the capability to accurately define compartments of interest and compare them to one another, and as result, get a more easily interpretable answer. On the other side, the work is considerably more time-consuming than simple coefficients, and can become prohibitive with large data sets. Further, the "Spots" function is optimal for small, well-defined compartments, and is difficult to use for more amorphous, or clustered structures. When working with high or super resolution images in this workflow, defining complete membrane bound compartments versus specific domains on a larger compartment becomes a significant issue, and is thus a drawback of using object-based techniques.

Live imaging permits extraction of detail not afforded by fixed, single time point images. However, with that come additional challenges. Live imaging tends to have increased noise and background as compared to fixed imaging. Further, as cells are alive, they often move in any plane. Fortunately, most post-imaging analysis software are capable of performing drift and bleach corrections to correct for common imperfections in movies. Beyond this, there is a great deal of data and information that can be extracted. Endosomal and Golgi compartments, labeled with fluorescent proteins of interest, endocytic tracers, or operational sensors, can be characterized for a list of

behavioral properties over time including: (1) motility, including speed and directionality, (2) intensity, (3) fusion/fission events, and (4) cellular localization. High powered software, such as Imaris and its “Spots” function (or the equivalent on other commercial software), permit the quick assignment and extraction of most of this data. However, with careful processing in free shareware programs such as ImageJ, equivalent data can be extracted using functions such as “Analyze Particles”. Plugins for ImageJ are constantly added to increase the versatility and power of this analysis platform. More specific analyses can be conducted for experiments such as FRAP, such as measuring the fluorescence intensity of the bleached compartment over time, while simultaneously monitoring compensatory activity of other Golgi-endosomal axis compartments.